A Superconducting Flux QuBit: Measurement, Noise and Control

by

Lin Tian
M.S. in Physics, Beijing University, 1997

Submitted to the Department of Physics
in partial fulfillment of the requirements for the degree of
Doctor of Philosophy
at the
MASSACHUSETTS INSTITUTE OF TECHNOLOGY
June 2002

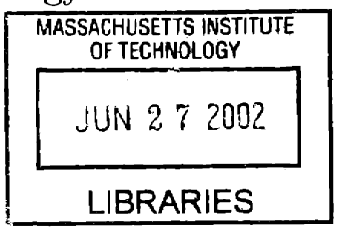

ARCHIVES

Author .....
Department of Physics
May 1st, 2002

Certified by.....
Mildred S. Dresselhaus
Institute Professor
Thesis Supervisor

Certified by..
Seth Lloyd
Professor of Mechanical Engineering
Thesis Supervisor

Certified by.....
Terry P. Orlando
Professor of Electrical Engineering
Thesis Supervisor

Accepted by.....
Thomas J. Greytak
Chairman, Departmental Committee on Graduate Students

A Superconducting Flux QuBit: Measurement, Noise and Control

by

Lin Tian

M.S. in Physics, Beijing University, 1997

Submitted to the Department of Physics
on May 1st, 2002, in partial fulfillment of the
requirements for the degree of
Doctor of Philosophy

Abstract

A superconducting quantum bit can be made with three nano-scale Josephson junctions connected in series. In this thesis, various aspects of this qubit are studied. It is shown numerically that the qubit behaves as a giant magnetic dipole with quantum tunneling between the two qubit states. The natural coupling between qubits plus the manipulation on a single qubit state provides the building blocks for universal quantum computing. The state of the qubit can be determined by measuring its flux with a SQUID. The measurement efficiency and measurement-induced decoherence are investigated. A coherent transition assisted scheme is designed for a projective measurement on the qubit. A general method is developed to study qubit decoherence by environmental noise. The dynamic control approach is applied for preventing off-resonant leakage during gate operations and for de-coupling the qubit from noise.

Thesis Supervisor: Mildred S. Dresselhaus
Title: Institute Professor

Thesis Supervisor: Seth Lloyd
Title: Professor of Mechanical Engineering

Thesis Supervisor: Terry P. Orlando
Title: Professor of Electrical Engineering

Acknowledgments

I would like to thank one of my advisors, Terry Orlando, for guiding me through my thesis. He not only introduced me to an exciting and upgrowing field of research, but also provided encouragement and wisdom throughout my graduate career. Following his guidance, I closely collaborated with experimentalists in his group. This experience will be most precious to me in my future career.

I would like to thank my other advisor, Seth Lloyd, whose physical insight always fascinates me. I treasure the many hours of discussions and physical inspirations in his office. He has the talent of finding the easiest yet accurate solutions to problems. His way of thinking influenced me greatly throughout my thesis.

Special thanks to my co-adviser, Millie Dresselhaus, for her guidance, encouragement and her many suggestions on my career.

I would like to thank my thesis committee for reading my thesis.

I would like to thank my collaborators: Leonya Levitov, Hans Mooij, Ken Segall, Juan Mazo, Enrique Trias, Donald Crankshaw, Daniel Nakada, Bill Kaminsky, Frank Wilhelm, Caspar van der Wal and many others for stimulating discussions during Ph.D. work.

I would like to thank my friends for encouraging me, entertaining me and tolerating me. They brought more fun to my graduate life. I would like to thank my parents for their constant support.

This research was supported by NSA and ARDA under ARO grant DAAG55-98-1-0369.

Contents

List of Figures

List of Tables

Chapter 1

Introduction

The theory of quantum computation provides a novel approach to speed up some classically hard problems, such as the factoring problem[1] and the search problem in a random database[2, 3]. Physical media have to be built to carry out these algorithms and test the theory[4]. In this thesis, a superconducting implementation of quantum computation is studied theoretically.

1.1 Physical Implementation

Quantum computers store and process information on quantum variables such as spins, photons, and atoms. Typically, these variables consist of two-state quantum systems called quantum bits or "qubits". By manipulating the quantum states of those variables in a way that preserves quantum coherence, quantum algorithms can be implemented with the qubits. To perform a quantum computation, one must be able to prepare qubits in a desired initial state, coherently and to accurately manipulate superpositions of a qubit's two states, couple qubits together, measure their state, and keep them relatively free from interactions that induce noise and decoherence [5, 6, 7, 8, 9, 10]. To perform quantum communication, one needs to coherently transmit a qubit state from one place to another, which requires the design of a "flying qubit"[4].

Qubit designs have been proposed in a variety of physical systems, such as trapped

ions[11, 12], cavity QED[13], electron spins in quantum dots[14] and nuclear spins[15, 16], to name but a few. Essentially any two-state quantum system that can be addressed, controlled, measured, coupled to its neighbors and decoupled from the environment, is potentially useful for quantum computation and quantum communications[17]. In the trapped ion qubit, two internal states of the ion are chosen as the qubit. A single qubit operation is implemented by addressing the individual ions with laser pulses. Two-qubit controlled gates are implemented via collective motional modes of the ions. Detection is possible by applying laser pulses and observing spontaneous emission. In the liquid state nuclear magnetic resonance quantum computing, qubits are interacting spins in molecules. By microwave pulsing, an ensemble of molecules can be prepared into a pseudo-pure state as the initial state. Qubit operations are implemented by a selective re-coupling technique in NMR. By detecting the NMR signal of the ensemble, the qubit information is measured.

Nano-scale electrical systems which can be produced by modern lithography, such as quantum dots and tunnel junctions, are attractive candidates for constructing qubits: a wide variety of potential designs for qubits and their couplings are available, and the qubits are easily scaled to large arrays which can be integrated in electronic circuits [7, 18]. A distinguishing property of these designs is the flexibility in the qubit characters: the physical size and property of these artificial systems can be adjusted in a very wide range. For this reason mesoscopic superconducting circuits of ultra-small Josephson junctions have been proposed as qubits[19, 20, 21, 22, 23, 24]. When the Josephson energy of the junction dominates over the charge energy of the junction, the qubit is said to be in the flux regime where qubit states are local flux states. When the charge energy of the junction dominates over the Josephson energy of the junction, the qubit is said to be in the charge regime where qubit states are easily discussed by discrete charge states. Qubits in both regimes have been intensively studied both theoretically and experimentally in recent years.

In this thesis, a superconducting flux qubit—the persistent-current qubit (pc-qubit)[20, 25], is studied. Both the physical properties of the pc-qubit and the quantum computing related problems such as manipulation, decoherence, control and

measurement, are covered. Most of these studied are single qubit problems. They are a useful step in building large-scale superconducting quantum computers.

1.1.1 Josephson Junction and Macroscopic Quantum Tunneling

An attractive feature of the superconducting flux qubits compared with other solid state designs is that the flux qubits are macroscopic, or more accurately, mesoscopic quantum systems[26, 27]. For example, the pc-qubit has a micron scale superconducting loop and a submicron size Josephson junction. There are more than 10 billion electrons in the superconducting loop. The electrons move together coherently in some collective mode. The collective state of these electrons are described by the complete superconductor, where the gauge-invariant phase determines the qubit states selected for quantum computing. By quantizing the gauge-invariant phase, the collective states can be easily calculated. For the pc-qubit, the qubit states have a magnetic dipole 10^6 times the electron dipole.

The macroscopic qubit has the advantage that it is easy to manipulate, easy to couple different qubits together, and easy to measure. When the character of the qubit is of macroscopic size, it is easy to couple the qubit degree of freedom to other quantum systems. The pc-qubit has a flux of 10^{-3} flux quantum which can be easily resolved by a regular SQUID magnetometer. The coupling energy between pc-qubits can be as strong as 2 GHz which gives a built-in method for two-qubit control gates. Of course, the macroscopic nature of the qubit that results in these advantages also results in a disadvantage. The qubit degree of freedom is not very well isolated from environmental noise. The qubit is subjected to stronger environmental fluctuation and tends to decohere faster than qubits in microscopic systems. Hence, serious experimental studies on these qubits are necessary to show that these qubits can operate coherently.

Various proposals for superconducting flux qubits have been implemented experimentally recently. Among them are the double junction rf-SQUID loop[28], the three

junction persistent-current qubit[29], and the current ramped tunnel junction[30]. In all these experiments, the gauge-invariant phase is the quantum variable being explored. One often describes the dynamics as that of a "phase particle" in some potential landscape, which is controlled by external flux and currents. In the rf SQUID experiment[28], the phase particle is designed to be in a double well potential. The quantum tunneling between the localized phase states is probed via microwave spectroscopic experiments. In the pc-qubit experiment[29], the three junction circuit is described as a "phase particle" in a two dimensional periodical potential. The qubit states are nearly localized phase states. The quantum tunneling between nearby local minima is probed. Microwave data show a qubit energy dependence on the magnetic flux in the qubit loop and the tunneling induced anti-crossing. In the current-ramped junction experiment[30], the quantum tunneling of a "phase particle" in a washboard potential is studied where the tilting of the washboard is controlled by the ramping current. In this experiment, coherent oscillations between two quantum states that are localized in the potential well are observed by measuring the escape probability of the particle from the metastable potential well.

Not only is the superconducting system a promising candidate for implementing large-scale quantum computation, but it is also a good system for testing fundamental problems in physics. One interesting question is whether quantum mechanics is valid for macroscopic/ mesoscopic quantum systems[26, 27] and if not, where is the boundary between quantum mechanical and classical behavior. The superconducting system is macroscopic in the sense that large number of electrons are involved. By verifying quantum mechanic behavior in this system, it will help to answer the first question. Another interesting topic of study is the dynamics of a system in a dissipative environment [31, 32]. The superconducting system often has a double well potential or a metastable potential well in phase space[33, 34, 35]. This potential can be adjusted by various means of external control. As a result, the phase particle in the potential can be studied at various conditions by adjusting the potential and also by manipulating the environment of the system. This is then a good experimental system for testing the dissipative behavior of quantum systems. This behavior de-

pends on the small-scale of the junctions and on the coherent behavior of the circuit. As the fabrication technology advances, the control of the system and the environment advances so that more and more of the fundamental studies can be tested in the laboratory in superconducting systems.

1.1.2 Comparison with Other Implementations

In the following, we discuss the advantages and disadvantages of solid-state qubit designs in comparison with other systems, such as trapped ions, cavity QED systems, liquid-state NMR and solid-state NMR.

Compared with the photonic, atomic, and nuclear qubits already constructed, solid state proposals based on lithography such as the one described here have two considerable disadvantages and one considerable advantage. The first disadvantage is noise and decoherence [7, 9, 10]: the solid state environment has a higher density of states and is typically more strongly coupled to the degrees of freedom that make up the qubit than is the environment for photons in cavities, ions in ion traps, and nuclear spins in a molecule or crystal. Extra care must be taken in solid state systems to decouple the qubit from sources of noise and decoherence in its environment. The second disadvantage is manufacturing variability[10]: each ion in an ion trap is identical by nature, while each lithographically defined Josephson junction in an integrated circuit will have slightly different properties. Solid-state designs must either be insensitive to variations induced by the manufacturing process, or must include a calibration step in which the parameters of different sub-circuits are measured and compensated for [18].

The advantage of solid-state lithographically defined circuits is their flexibility: the layout of the circuit with Josephson junctions or quantum dots is determined by the designer, and its parameters can be adjusted continuously over a wide range. As the results presented in this thesis demonstrate, this flexibility allows the design of circuits in which the variables that register the qubits are only weakly coupled to their environment. In addition, the flexibility in circuit layout allows many possible options for coupling qubits together, and for calibrating and adjusting the qubits'

parameters. That is, the advantage of flexibility in design can compensate for the disadvantages of decoherence and manufacturing variability.

The flexibility in design afforded by lithography conveys a further advantage to constructing quantum computers. As noted above, a qubit has to accomplish at least five functions: it has to be addressed, controlled, measured, coupled to its neighbors and decoupled from the environment. One of the axioms of design, is that the number of parameters that characterize a system's design should be at least as great as the number of parameters that characterize the system's function[36]. The problem of having too few design parameters available is particularly acute in the design of quantum computers and qubits : a quantum computer is a device in which essentially every physical degree of freedom is used to register information and to perform the computation. Degrees of freedom that are not used to compute are sources of noise and must be isolated from the computing degrees of freedom. Designs for quantum computers are accordingly more constrained by fundamental physics than are designs for conventional computers: if one is storing information on a cesium atom, then the "design parameters" of the cesium atom —its energy levels, decoherence times, interaction strengths, etc. —are fixed by nature once and for all. In the lithographically defined Josephson junction circuits proposed here, by contrast, it is possible to make qubits that have a variety of different design parameters, each of which can be adjusted to optimize different functions.

Various physical systems for quantum computing are listed in Table 1.1 with a summary given for each type of qubit on its physical carrier, method of manipulation, qubit interaction, and the advantage and disadvantage of each type of qubit.

	ion trap, atom trap	cavity QED	liquid NMR	nuclear spin in solid	spin in quantum dot	superconduting qubits
qubit	internal state of trapped ions, atoms	atom in cavity	nuclear spin ensemble	nuclear spin	electron spin	Josephson junction circuit
single-qubit gate	light radiation	atom-photon interaction	microwave radiation	microwave or optics via e-n int.	light radiation	microwave, adiabatic operation
coupling	int. via collective mode	atom-photon interaction	pulse selective coupling	via electron spin	exchange int by gate control	magnetic or electric gate
pros and cons	isolated from noise, scalable, hard to couple	isolated from noise, hard to couple, require single photon	existing tech. ensemble control and detection, not scalable	scalable, identical spins, fabrication difficulty	scalable, single-qubit gate hard, fabrication hard	macroscopic, easy to control, noise strong

Table 1.1: The comparison between several qubits.

1.2 Flux Based Superconducting Quantum Bits

The main topic of this thesis is to study the superconducting persistent-current qubit (pc-qubit)[20, 25], Fig. 1-1. This qubit is made of three small Josephson junctions connected in a superconducting loop. The quantum mechanical variables being studied in this circuit are the superconducing gauge-invariant phases. The circuit can be controlled by varying the magnetic flux in the loop or by varying the gate voltage on the metallic islands. A recent experiments[29, 37] have shown the quantum mechanical properties of this circuit and its possibility for being a quantum bit. In this thesis, our studies on the pc-qubit are summarized, which include the basic structures of the qubit state and its manipulation[20, 25], measurement-related issues such as improving the resolution[38] and measurement-induced noise[39, 40], the study of the environmental noise on the qubit[41], quantum control of off-resonant transitions to higher energy states[42] and on the decoupling of the qubit from noise. These results are described in more detail in the subsequent chapters of this thesis. However, the main results are summarized below.

1.2.1 The Persistent-Current Qubit (PC-Qubit)

In chapter II, the circuit of the pc-qubit is studied both numerically and with a tight-binding approximation. The three gauge-invariant phases of the Josephson junctions obey the flux quantization relation; and, hence supply two independent variables. After quantizing the phase variables, the circuit behaves as a particle in a two-dimensional periodic potential, Fig. 1-2.

By discretizing the phase variables, we numerically calculated the energy spectrum of the pc-qubit versus the magnetic flux in the superconducting loop and versus the gate voltage. Our results show that the pc-qubit circuit behaves as a giant spin $S = 1/2$ magnetic dipole when the magnetic flux ($\Phi = f_1\Phi_0$) in the superconducting loop is biased away from $\Phi_0/2$ ($f_1 = 1/2$). The lowest two eigenstates of the pc-qubit resemble the spin states and have a Zeeman splitting proportional to the flux. A contour map of the pc-qubit wave-function shows that the lowest two eigenstates are

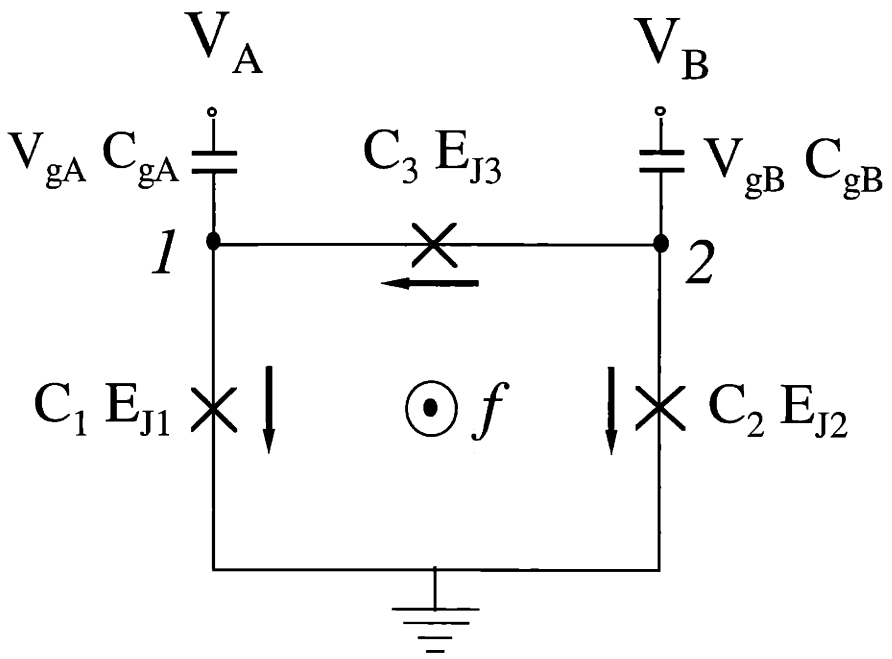

Figure 1-1: The three-junction qubit. Josephson junctions 1 and 2 both have Josephson energies E_J and capacitance C and Josephson junction 3 has a Josephson energy and capacitance α times larger. The nodes 1 and 2 represent the superconducting islands (nodes) which are coupled by gate capacitors $C_g = \gamma C$ to gate voltages V_A and V_B. The arrows define the direction of the currents. The flux is taken out of the page.

nearly localized flux states with opposite circulating currents. When the magnetic flux in the loop is near $f_1 = 1/2$, the situation is different. The Zeeman term becomes smaller than (or even disappears at $f_1 = 1/2$ when the double well potential is symmetric to $f_1 = 1/2$) another term which is due to the quantum tunneling between local minima in Fig. 1-2 and is a completely quantum mechanical effect. When the Zeeman splitting is described as an σ_z term, the tunneling is described as an σ_x term. The effective two-level Hamiltonian is $\mathcal{H}_0 = \frac{\epsilon_0}{2}\sigma_z + \frac{t_0}{2}\sigma_x$, when $\epsilon_0 \propto (f_1 - 1/2)$ and t_1 is the tunneling matrix element. Numerical calculation shows that $t_1 \approx 10^{-3}E_J$ with parameters from the experimental sample. The energy spectrum of the pc-qubit versus flux is shown in Fig. 1-3 with the arrows indicating the qubit states at the selected operating point with $f_1 = 0.495$. The qubit state generates a flux of 10^{-3} flux quanta which facilitates coupling between qubits and the detection of qubit states.

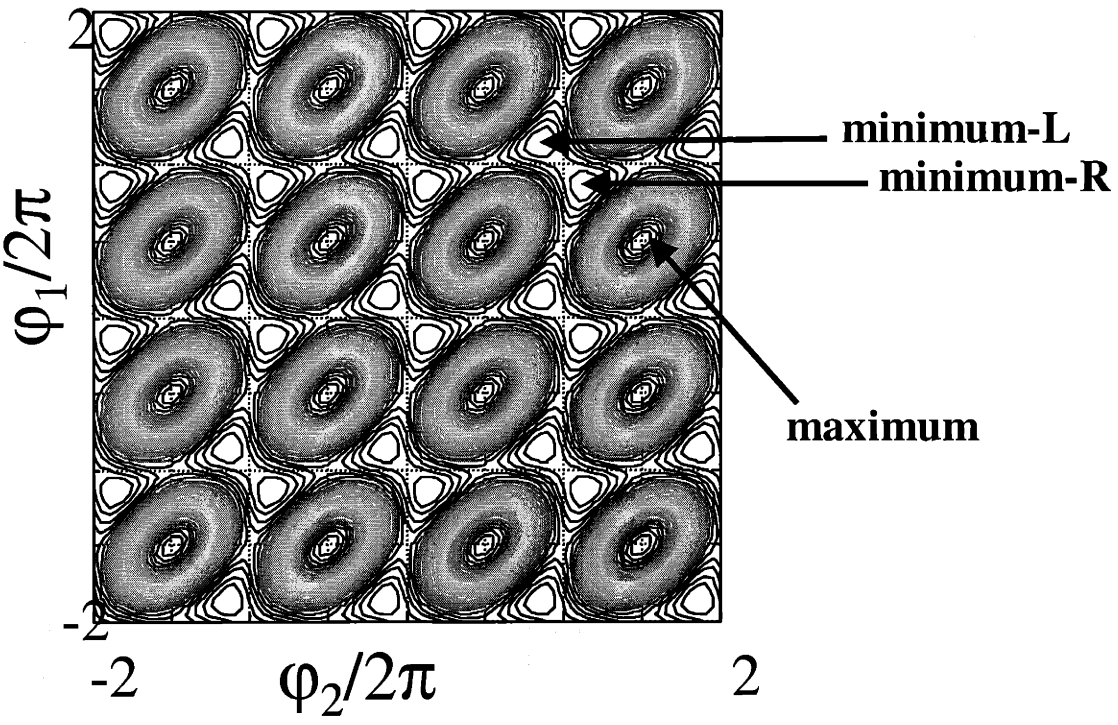

Figure 1-2: Two dimensional potential of the pc-qubit.

The lowest energy states of the pc-qubit can also be calculated by a tight-binding type of calculation. Starting from the local state in the potential wells of the two-dimensional potential, the tunneling rate from one local minumum to other minuma can be calculated with a WKB approach. Considering only nearest neighbour tunneling, the most important tunneling terms are: (1). the tunneling between the two minima within the unit cell t_1, and (2). the tunneling from a minimum to one of the two closest minima outside the unit cell t_2. In the pc-qubit configuration, both t_1 and t_2 depend exponentially on E_J/E_c and are determined by $e^{-\sqrt{E_J/E_c}}$. The total tunneling is $t_0 = t_1 + t_2 e^{-i\pi q_1/e} + t_2 e^{i\pi q_2/e}$ where q_1 and q_2 are charges on gates. Calculation shows that $t_1 > 10^3 t_2$, and hence $t_0 = t_1$. The tight-binding Hamiltonian is then

$$\mathcal{H}_0 = \begin{pmatrix} \varepsilon_0/2 & t_0(q_1,q_2) \\ t_0^*(q_1,q_2) & -\varepsilon_0/2 \end{pmatrix}, \tag{1.1}$$

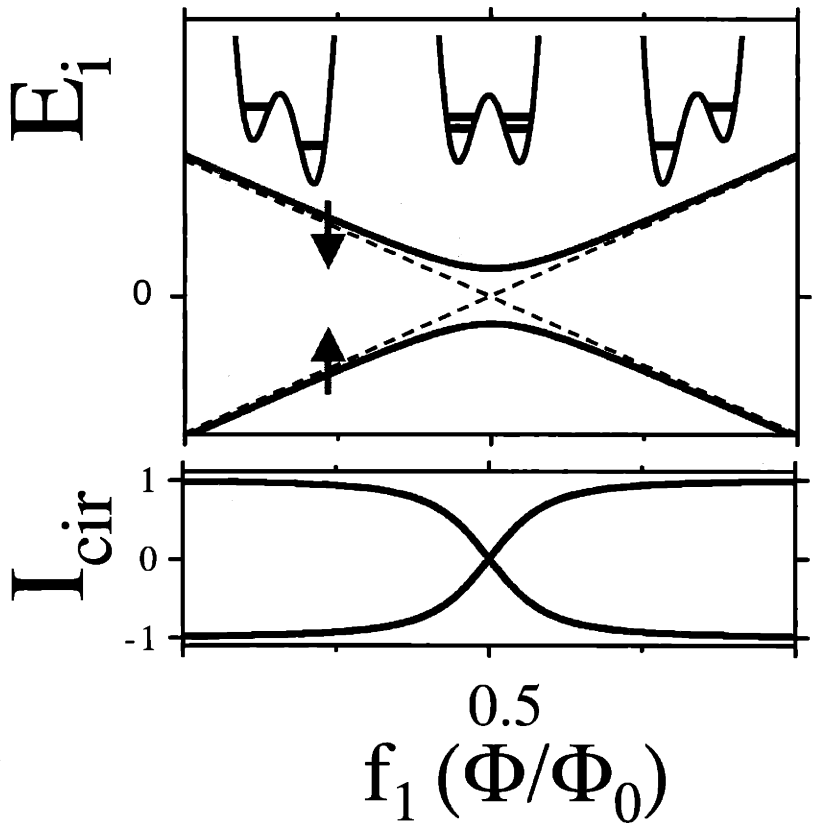

Figure 1-3: The energy of the pc-qubit versus the magnetic flux in the superconducting loop. The arrows indicate the qubit states at $f_1 = 0.495$. The two states have opposite circulating currents and generate a flux of 10^{-3} flux quantum.

This is exactly the same as the effective Hamiltonian for the lowest two states.

This approach also shows that the pc-qubit is insensitive to charge fluctuations from the background. The charge degrees of freedom couple to the pc-qubit through the t_2 tunneling term in the tight-binding Hamiltonian. As $t_1 \gg t_2$ and the effect of t_2 is neglected, the charge noise has no effect on the dynamics of the qubit. This agrees with the numerical results on the gate dependence of the energy spectrum of the pc-qubit. Fig. 1-4 shows the qubit energy versus the gate voltage. The energy bands are almost flat lines in the spectrum which shows the insensitivity of the qubit to charge noise.

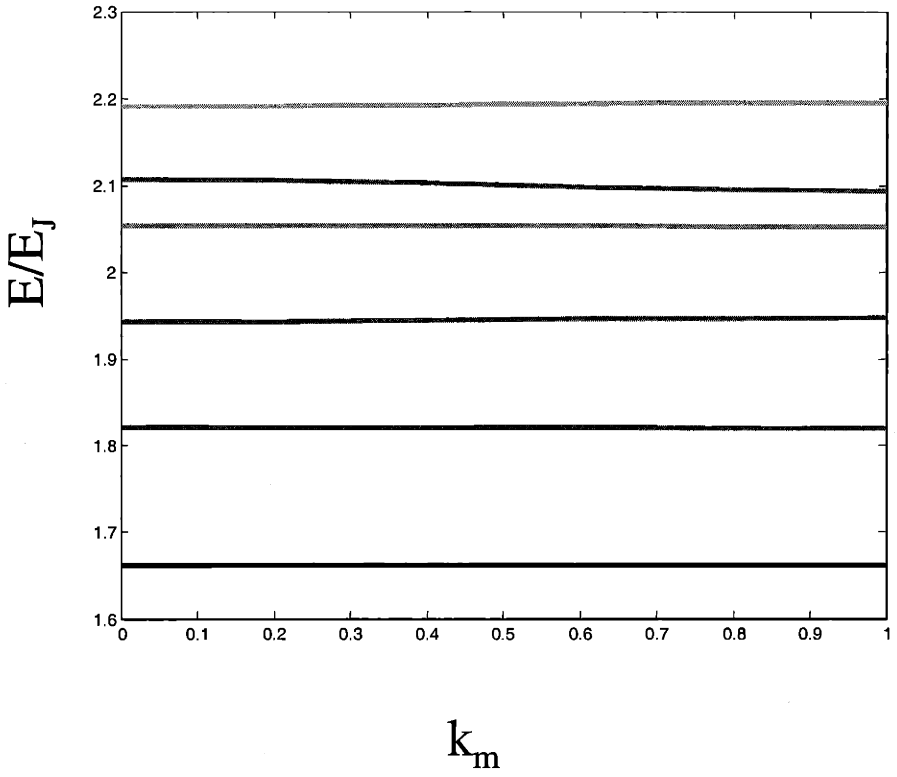

Figure 1-4: The energy of the pc-qubit versus the voltage on the gates.

Single qubit gate operation and two qubit controlled operation can be easily implemented with the above circuit, both according to magnetic coupling. The easiest way to perform a single qubit rotation is by applying pulses of microwave radiation to the pc-qubit circuit. The radiation induces a term $\mathcal{H}_1 = \Delta_1 \sigma_z \cos \omega_0 t$ where Δ_1 is the amplitude of the radiation and ω_0 is the frequency of the qubit. This term induces transitions between the two qubit states with a Rabi frequency of $\Omega_R = \frac{\Delta_1}{\hbar} \frac{t_1}{\epsilon_0}$. Note that there is a large overhead factor $\frac{\epsilon_0}{t_1}$ for the Rabi frequency. A typical value for the Rabi frequency is 100 MHz. Another way for performing a single-qubit rotation is by making the third junction in the circuit a SQUID and irradiating the SQUID. This radiation induces a σ_x-rotation term instead.

The two-qubit operation is implemented via the inductive interaction between neighbouring qubits. The circulating current in the loop of the pc-qubit generates

a magnetic flux of 10^{-3} flux quantum. This flux couples to other pc-qubits via the mutual inductances. The induced coupling is a dipole-dipole type of coupling. This coupling gives additional two-qubit interaction terms

$$H_{AB}^{\text{int}} = \kappa_1 \, \sigma_z^A \sigma_z^B + \kappa_2 \sigma_z^A \sigma_x^B + + \kappa_3 \sigma_x^A \sigma_z^B \tag{1.2}$$

where κ_1, κ_2 and κ_3 are interaction strengths. The σ_z coupling is from the modulation of the flux in the qubit loop. The σ_x coupling is from the modulation of the flux in the SQUID loop of the third junction. Each of the interaction strengths can be adjusted by designing the pc-qubit differently. When two qubits are located close to one another, the interaction can be about 2 GHz.

1.2.2 Measurement on PC-Qubit

The detection of quantum bits is an important step in quantum information processing. Detection relies on coupling the qubit to a detector at least part of which is another quantum system. The extraction of qubit information is determined by the way the two quantum systems interact with each other. In chapter III of this thesis, we are going to discuss the effect of the interaction between the qubit and the detector on the qubit state and on the detector states. The major issues studied are: (1). The interaction between the qubit and the detector transmits qubit information to the detector, and eventually to the observer. How does this interaction affect the detector state and how does it affect the measurement efficiency? (2). The detector is always subjected to stronger noise than the qubit, which is designed to be well-isolated from the environment. Through the interaction between the two systems, noise can be transmitted to the qubit during measurement. How is the noise affected when it is transmitted to the qubit? Both of these issues will be discussed in detail.

In a recent experiment on the persistent-current qubit, an underdamped dc SQUID measures the pc-qubit by inductively coupling with the qubit (Fig. 1-5). The flux of the qubit is coupled into the dc-SQUID loop and affects the effective critical current of the dc SQUID. During the measurement, a dc current is ramped through the dc

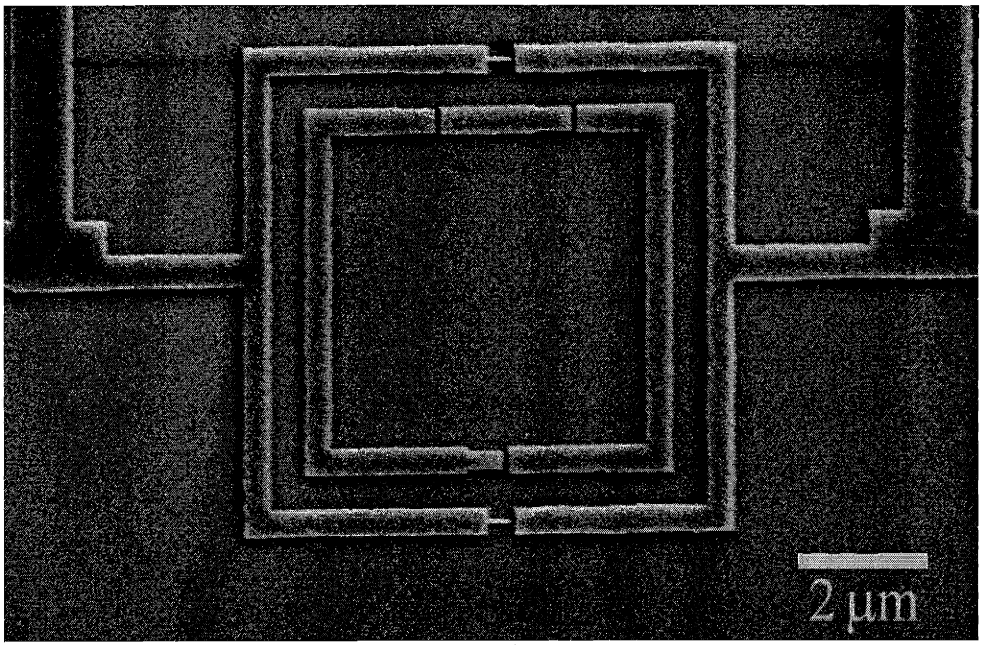

Figure 1-5: The fabricated sample of a pc-qubit measured by a dc SQUID. The inner loop is the pc-qubit with three Josephson junctions. The external loop is the underdamped dc SQUID with two Josephson junctions. Current can be ramped into the dc SQUID via the leads connected with the SQUID.[29]

SQUID. When this current is close to the effective critical current, the dc SQUID switches from the supercurrent phase to the finite voltage phase. The switching current is then recorded. Due to quantum and thermal fluctuations, the switching current has a finite width distribution. The distribution histogram contains information about the qubit's state and is recorded in the experiment.

To study this measurement in detail, we modeled the dc SQUID as a linear quantum system with two variables, the inner oscillator and the external oscillator. The qubit interacts only directly with the inner oscillator. The external oscillator is a particle in a washboard potential, the tilting of which is determined by the ramping current. The external oscillator gets entangled with the qubit indirectly through its entanglement with the inner oscillator. As a result, instead of measuring the two

qubit eigenstates directly, the inner oscillator state that is entangled with the qubit is measured. Our analysis shows that the inner oscillator states are highly overlapped states which are hard to resolve by any single measurement process. This is reflected in the fact that the splitting of the switching histogram due to the qubit flux is much smaller than the width of the histogram. This explains the large number of repetitions that are required in the experiment.

To improve the situation, we designed a new measurement scheme that by adding an ancilla qubit significantly improves the measurement efficiency and is, in a general sense, a von Neumann type of measurement. In this proposal, we add an ancilla qubit that is initially at state $|0\rangle$ and stays at state $|0\rangle$ during the regular qubit operation time. The interaction between the two qubits doesn't affect the ancilla state during regular qubit operation as long as the interaction commutes with the ancilla qubit Hamiltonian. On the other hand, the interaction modifies the level splitting between the ancilla states and makes the splitting when the qubit state is at $|1\rangle$ different from the splitting when the qubit state is at $|0\rangle$. Proper design can make this difference large enough to make off-resonant transitions impossible. During the measurement, an rf pulse with a frequency at resonance with the ancilla splitting when the qubit is at state $|1\rangle$ is applied to the ancilla qubit. The ancilla qubit then flips conditionally according to the qubit states and the two systems become entangled with each other. The ancilla is selected to be a system that is easily measured by some standard device. After the entanglement, the ancilla state is measured projectively (hence efficiently). Combining the entanglement and the measurement on the ancilla results in a measurement process for the qubit that is projective and doesn't induce extra noise. To realize this scheme experimentally, we choose an rf SQUID to be the ancilla. The rf SQUID is a qubit with a short decoherence time but has a very large flux signal. The schematic figure of the realization is shown in Fig. 1-6.

The measurement process not only extracts information from the qubit, but also opens the channel for noise from the detector's environment to be transmitted to the qubit. The transmitted noise can be an important source for qubit decoherence. It turns out that the detector acts as a quantum mechanical filter that tailors the noise

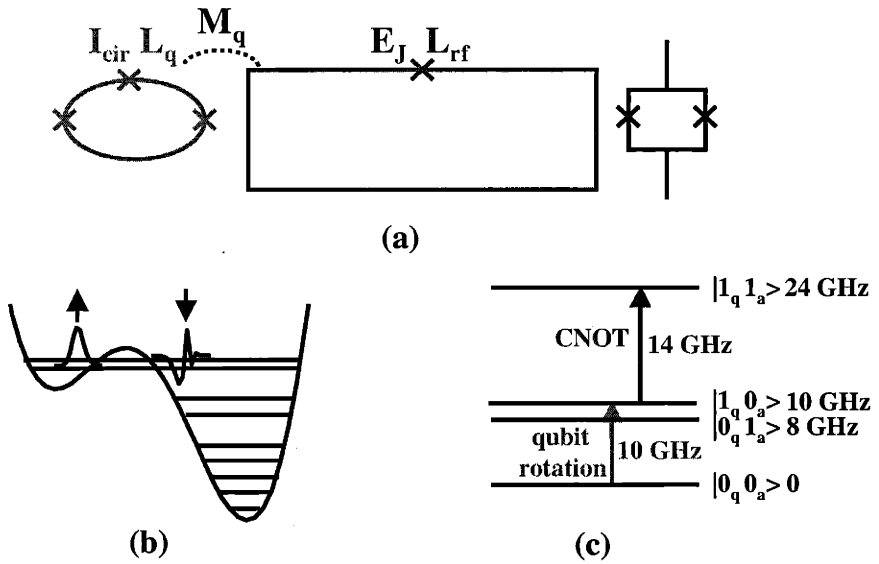

Figure 1-6: The experimenal realization of the improved measurement circuit.

transmitted to the qubit. In chapter III, we develop a general method to calculate the transmitted noise based on the spin-boson type of model for the noise reservoir, given the noise spectral density on the detector. The method is presented with an equivalent circuit approach. In this approach, the Hamiltonian of the qubit and the detector is mapped into an equivalent circuit; the transmitted noise can then be directly derived from the effective circuit impedance following the fluctuation-dissipation theorem. Our method is an efficient way to study the transmitted noise for interacting quantum systems and can be generalized to study systems such as a qubit coupled to a radiation source. In the qubit-dc SQUID interaction system, the dc SQUID can be studied as two interacting oscillators. The reservoir of the dc SQUID is described by a spin-boson model with the noise spectral density $J_0(\omega)$. As a result, the qubit has an effective environment with two discrete oscillators plus the reservoir. The equivalent circuit has three independent loops, corresponding to the qubit and the two oscillators. The spectral density of the effective noise is:

$$J_{eff}(\omega) \approx \frac{4(eI_{cir}I_bM_q)^2}{C_s^2\hbar^3 R_s} \frac{\omega}{(\omega^2-\omega_p^2)^2+(\omega/R_sC_s)^2} \tag{1.3}$$

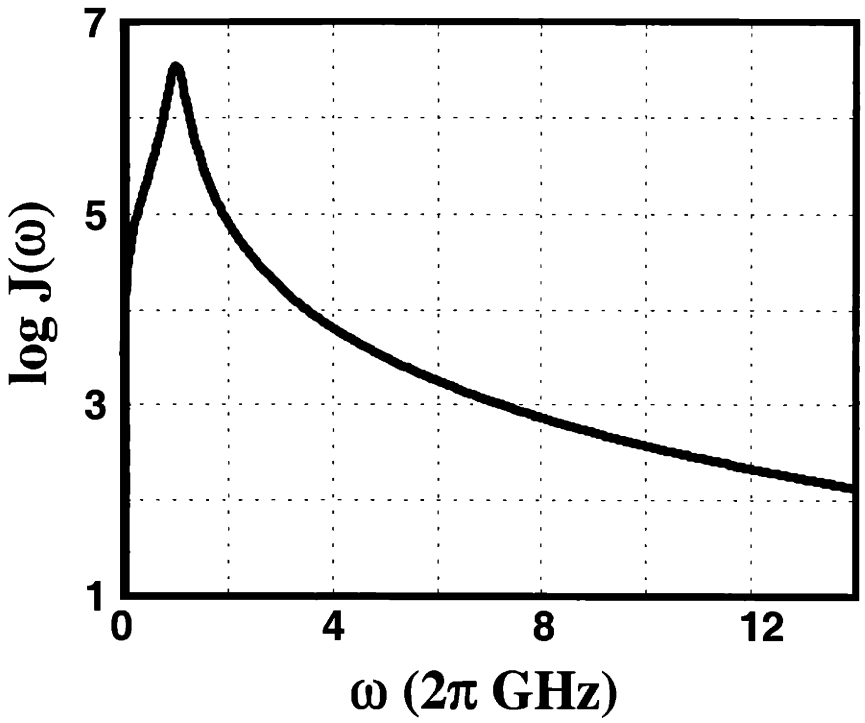

Figure 1-7: The spectral density of the effective noise transmitted to the pc-qubit during measurement.

where I_{cir} is the circulating current of the qubit, I_b is the ramping current, M_q is the mutual inductance, C_s is the shunt capacitance of the SQUID, and R_s is the resistance of the SQUID. ω_p is the frequency of the external oscillator. $J_{eff}(\omega)$ increases with the square of the mutual inductance and the square of the ramping current.

The effect of the transmitted noise on the qubit can be studied with a master equation approach. At finite temperature, the noise spectral density has an extra factor of $\coth \frac{\hbar\omega}{2k_BT}$ at frequency ω. The evolution of the density matrix of the qubit is perturbed by the reservoir modes to second order in the coupling. There is a direct correspondence between the T_1 (damping time) and T_2 (decoherence time) and the noise spectral density at certain frequencies under a Markovian approximation:

$$\begin{aligned} T_1^{-1} &= \frac{t_0^2}{2\omega_0^2} J_{eff}(\omega) \coth \frac{\hbar\omega}{2k_BT}|_{\omega=\omega_0} \\ T_2^{-1} &= \frac{\epsilon_0^2}{2\omega_0^2} J_{eff}(\omega) \coth \frac{\hbar\omega}{2k_BT}|_{\omega\to 0} + \frac{t_0^2}{4\omega_0^2} J_{eff}(\omega) \coth \frac{\hbar\omega}{2k_BT}|_{\omega=\omega_0} \end{aligned} \tag{1.4}$$

Due to the reduction factor ω_p^4/ω_0^4 in the spectral density at high frequency, relaxation is slowed by the filtering of the SQUID. With the system parameters, we calculate the damping time as $T_1 = 0.15\,\text{sec}$ and the decoherence time as $T_2 = 2\,\mu\text{sec}$ at $I_b = 0.8I_c^{eff}$. The decoherence time is much shorter than the estimated intrinsic decoherence[41]; while relaxation is slow enough that it will not hinder the extraction of qubit information. The noise transferred to the qubit is negligible at $I_b = 0$ when no measurement is being conducted.

1.2.3 Environmental Noise

The superconducting qubit is a macroscopic quantum system where billions of electrons behave collectively under superconducting phases. The qubit's quantum mechanical variable is a collective degree of freedom of the system instead of individual electrons. Such a system has the advantage that it can be easily detected and be easily coupled to other qubits. On the other hand, there are many other degrees of freedom in the superconductor that interact with the qubit degree of freedom and cause stochastic dynamics in the qubit. These degrees of freedom become an important source of decoherence. In chapter IV, we develop a general theory for studying the effect of environmental noise on the qubit dynamics. This theory is then applied to the pc-qubit to study the effect of the major noise sources, including charge fluctuations, nuclear spins *etc.* We also go beyond this theory to calculate the effect of electromagnetic emission with a golden rule approach. The electromagnetic field is treated quantum mechanically. Besides the environmental noise, interactions between qubits also induce random phases for qubit. We studied this effect by analyzing the dipole interaction between the pc-qubits.

Because the interaction between the qubit and the environment is weak, the environment can be treated as classical fluctuating fields. To study the effect of the environment on the qubit dynamics, we study the dynamics of a spin in a classical fluctuating field. The Fourier transform of the correlation function classical field is the noise spectrum of the field and contains all the effects the field has on the

spin: $\mathcal{H}_{\text{total}} = \mathcal{H}_{\text{Q}}(\vec{\sigma}) + \mathcal{H}_{\text{bath}}(\{\xi_\alpha\})$, where $\mathcal{H}_{\text{Q}} = \frac{\hbar}{2}\left(\vec{\Delta}(t) + \vec{\eta}(t)\right)\cdot\vec{\sigma}$ is the coupling Hamiltonian and the fluctuating field is $\vec{\eta} = \sum_\alpha \vec{A}_\alpha \hat{\xi}_\alpha$ due to coupling to the bath variables ξ_α. $\vec{\sigma} = (\sigma_x, \sigma_y, \sigma_z)$ is the vector of Pauli matrices acting on the qubit states. The vector $\vec{\Delta}$ represents external control: $\Delta_z = -\varepsilon_0$, $\Delta_x - i\Delta_y = t(q_1, q_2)$. This stochastic field induces decoherence for the qubit. The calculation shows that the decoherence includes pure dephasing from the σ_z coupling and spin-flip dephasing from the σ_x and σ_y couplings, which can be calculated from: $\phi_{\|}(t) = \int_0^t \eta_{\|}(t')dt'$ and $\phi_\perp(t) = \int_0^t e^{-i\Delta t'}\eta_\perp(t')dt'$ where $\langle ... \rangle$ stands for ensemble average, and the decoherence rate is

$$R(t) = \max\left[\langle\phi_{\|}^2(t)\rangle,\ \langle|\phi_\perp(t)|^2\rangle\right], \tag{1.5}$$

by calculating the ensemble averages for related physical noise. This theory is then applied to the major noise sources for the pc-qubit, including charge fluctuations, quasi-particle tunneling, nuclear spin fluctuations *etc.* The estimation of this noise shows that the decoherence is longer than 0.1 msec.

Electromagnetic emission is another important source of decoherence. In vacuum, the electromagnetic field is:

$$\begin{aligned} E(r) &= \textstyle\sum_{\sigma,k} \hat{i}_\sigma \sqrt{\frac{\hbar\omega_k}{2\epsilon_0 L^3}}\left[\hat{a}_{k,\sigma}e^{ik\dot{r}} + \hat{a}^\dagger_{k,\sigma}e^{-ik\dot{r}}\right] \\ H(r) &= -i\textstyle\sum_{\sigma,k} \hat{i}_k \times \hat{i}_\sigma \sqrt{\frac{\hbar\omega_k}{2\mu_0 L^3}}\left[\hat{a}_{k,\sigma}e^{ik\dot{r}} - \hat{a}^\dagger_{k,\sigma}e^{-ik\dot{r}}\right] \end{aligned} \tag{1.6}$$

where r is the position of the field, and k is the wave vector. $\hat{a}_{k,\sigma}$ and $\hat{a}^\dagger_{k,\sigma}$ are field operators for corresponding photon modes. Following this expression, the interaction between the qubit and the magnetic component of the field is $\delta\mathcal{H}_M = \hat{I}_{cir}R^2\delta B(t)$ where R is the size of the qubit circuit and is about 5 times the size of the junction p. $\hat{I}_{cir}$ is the circulating current operator of the pc-qubit. The decay is estimated by Fermi's Golden rule: $\Gamma_M = \frac{\mu_0\omega_0^3 R^4}{3\pi c^3\hbar}|\langle\Psi_1|\hat{I}|\Psi_2\rangle|^2$, where $\rho(\hbar\omega_0)$ is the density of states at the energy ω_0 that is the resonant frequency between the two qubit states under the stable bias f_{ex}^0. Also $\rho(\hbar\omega) = L^3\omega^2/3\pi^2\hbar c^3$, where L is

the size of the cavity. The interaction between the qubit and the electric component of the field is $\delta\mathcal{H}_E = \frac{\gamma R}{2(1+\gamma)}\hat{Q}_p\delta E_p + \frac{\gamma R}{2(1+2\alpha+\gamma)}\hat{Q}_m\delta E_m$. $\hat{Q}_p$ and $\hat{Q}_m$ are charges conjugated to the phase variables. The decay rates for the two variables are $\Gamma_E^{(p)} = \left(\frac{\gamma}{1+\gamma}\right)^2 \frac{4e^2\omega_0^3R^2}{12\pi\epsilon_0\hbar^3c^3}|\langle\Psi_1|\hat{P}_p|\Psi_2\rangle|^2$ and $\Gamma_E^{(m)} = \left(\frac{\gamma}{1+2\alpha+\gamma}\right)^2 \frac{4e^2\omega_0^3R^2}{12\pi\epsilon_0\hbar^3c^3}|\langle\Psi_1|\hat{P}_m|\Psi_2\rangle|^2$, where $\hat{P}_m$ and $\hat{P}_p$ are the momenta of the phase variables. Both the magnetic decay and electric decay increases with the size of the qubit loop R. For the pc-qubit, the decoherence time from the radiation decays is calculated to be longer than a few seconds. The size dependence also gives a good reason to make superconducting qubits smaller.

When many qubits are integrated into a chip, the interaction between qubits becomes a substantial source of decoherence. For the pc-qubit, the qubits interact by a dipolar type of interaction due to the circulating current in the superconducting loop:

$$\mathcal{H}_{\text{coupling}} = \sum_{i,j} \hbar\lambda_{ij}\sigma_z^{(i)} \otimes \sigma_z^{(j)} , \qquad \hbar\lambda_{ij} \approx \frac{\mu_i\mu_j}{|r_i - r_j|^3} \tag{1.7}$$

where the dipole moment $|\vec{\mu}| = I.A \approx 0.2\mu A \times \mu m^2$. If qubits are distributed homogeneously on the chip, the decoherence time from the dipole interaction is $15\mu s$, significantly shorter than decoherence time from other environmental noise. There are several ways to get around with this problem. One method is to intentionally pair qubits together to cancel the dipole moments of the qubit pair. The remaining interaction is the higher order (and weaker) quadrupole interaction. It can be shown that this method improves the situation greatly for the pc-qubit.

1.2.4 Quantum Control on PC-Qubit

Dynamic control is a useful tool in quantum information processing. It can be applied to achieve both accurate quantum gate operation and the decoupling of the qubit from environmental noise. The theory of dynamic control is based on a group theoretic approach on the Hilbert space of the quantum mechanical system. By applying appropriate quantum operations according to the group theoretic properties of the

operators, a desired unitary operation is implemented and the effective Hamiltonian of the system over a finite time interval is derived. In chapter V, we apply this method to improving the pc-qubit's resistance to quantum errors. The following problems are solved: (1). The control of the off-resonant transitions to higher states in the pc-qubit during a qubit gate operation; and (2). The decoupling of the qubit from the environmental noise by fast pulses. The two problems are different aspects of the application of the dynamic control method.

The pc-qubit is a multi-level quantum system, the lowest two states of which are selected to be an effective qubit. Calculation shows that the higher states are separated from the qubit states by energy differences of the same order as the qubit energy. During a single qubit gate operation, the pc-qubit is irradiated by a microwave pulse with a frequency in resonance with the qubit energy. This radiation implements the single qubit rotation between the qubit states. At the same time, it also causes transitions between the qubit states to the higher energy states of the pc-qubit circuit. For example, the transition amplitude for the off-resonant transition between state 1 and state 3 is $P(1 \rightarrow 3) = \frac{|\gamma_{13}|^2}{\omega_r^2} \sin^2 \omega_r t$, where $\omega_r = \sqrt{|\gamma_{13}|^2 + (\omega_{31} - \omega_0)^2}$ is the oscillation frequency for the off-resonant transition. The transition amplitude can hence be estimated to be 0.01 which presents a very strong source of gate error. This also agrees with the result of a numerical simulation. Note that the quantum error from leakage to other states in a quantum system is a ubiquitous effect in the physical implementation of quantum computation. Similar effects happen in the ion trap systems and many other systems.

Group theory shows that the qubit's original Hamiltonian and the radiation operator together form a complete operator set for the pc-qubit, meaning that by applying the radiation operator alternatively with not applying the radiation operator (with only the original Hamiltonian), any unitary transformation on the multi-level pc-qubit circuit can be constructed. As a result, an operation which is block diagonal between the qubit states and the rest of the states is possible by applying the radiation pulse in some manner. In this thesis, we demonstrate a way to design a sequence of radiation pulses for a perfect two-level operation with an $O(2N)$ number of pulses, N being the

number of states of the pc-qubit. Each pulse is in resonance with $E_k - E_1$ or $E_k - E_2$, respectively, with $k > 2$. Our method works by expanding the pulse amplitude in ascending order of relevant parameters:

$$\begin{aligned} \alpha_{31}e^{i\phi_{31}} &= \alpha_{31}^{(1)}e^{i\phi_{31}^{(1)}} + \alpha_{31}^{(2)}e^{i\phi_{31}^{(2)}} + \cdots \\ \alpha_{32}e^{i\phi_{32}} &= \alpha_{32}^{(1)}e^{i\phi_{32}^{(1)}} + \alpha_{32}^{(2)}e^{i\phi_{32}^{(2)}} + \cdots \end{aligned} , \tag{1.8}$$

where each of the higher order terms can be derived from the result of the lower order terms. It can be proved that with this method, perfect two-level operations are possible with arbitrary accuracy. In fact, the $O(2N)$ pulses can be further simplified into one pulse with sophisticated parameters. As each pulse in the sequence has the same duration, the pulse amplitude has no singularity. The pulse method has been experimentally explored in the NMR systems and accurate control of pulses can achieve desired gate operations to very high accuracy. [150]

Another application of the dynamic control method is to apply pulse sequences to the qubit to effectively decouple the qubit from its environment. By applying fast pulses to the qubit, the dynamics of the system is perturbed by the incoming pulses. At the end of one pulse sequence, the system evolution is described by an averaged Hamiltonian which can be manipulated by the pulse sequences. Each of the pulses can be viewed as a transformation which can rotate (e.g., flip) certain terms in the Hamiltonian. After each pulse, the system can be viewed as evolving under the rotated Hamiltonian. Hence, certain terms in the Hamiltonian, either the original qubit term or the term of the qubit coupling to the environment, can be canceled out at the end of the pulse sequence. We discuss the possibility of applying this method to the pc-qubit to deal with the general type of noise. By "general", we mean that the noise includes σ_z, σ_x and σ_y coupling to the pc-qubit. This requires a pulse sequence that cancels all the Pauli matrices. Our study shows that it is marginally possible to decouple the pc-qubit by applying a 0.5 psec short pulse at 2.5 nsec intervals between the pulses. As this sequence cancels all the Pauli operators, it decouples the qubit from noise sources whose correlation time is longer than $\sim 1\,\mu$sec. On the other hand, this sequence also averages out any non-trivial dynamics for the qubit. To

achieve a gate operation together with the decoupling process, the gate pulse should be designed in coordination with the symmetry of the decoupling pulses. Under this condition, a Rabi rotation of $\Omega_R = 5\,\mathrm{MHz}$ can be achieved.

Chapter 2

The Persistent-Current Quantum Bit

To implement quantum algorithms to achieve the exponential speed-up promised by theory, a physical carrier is needed—the algorithm has to be realized in a concrete physical system. The first step in realizing quantum computing is to build a quantum bit (qubit). There have been many proposals on using various systems to build a qubit, including ion traps[11, 12], cavity QED systems[13], nuclear spins[15, 16, 18], quantum dots[14], and superconducting systems[20, 21, 22, 23, 25].

In this chapter, we investigate the properties of the superconducting persistent-current qubit (pc-qubit). We will start the chapter by quantizing the Hamiltonian of the pc-qubit. Numerical methods are then applied to calculate the band structure of the qubit versus both the flux in the qubit loop and the gate voltage on the qubit. Basis logic gates including single qubit rotation and the two-qubit controlled-not gate (CNOT) are constructed. Then we discuss several simple quantum computing models in this superconducting system. The decoherence of the qubit is discussed briefly.

2.1 Josephson-Junction Qubits

The superconducting Josephson tunnel junction is described by a critical current I_o and a capacitance C. (We will assume that the resistive channel of the junction is

negligibly small.) For superconducting circuits the geometrical loop inductance L_s is also important if $\Lambda = L_J/L_s < 1$, where $L_J = \Phi_o/2\pi I_o$ is the inductance associated with a Josephson junction in the loop. Here $\Phi_o = h/2e$ is the superconducting flux quantum. Josephson circuits can be divided into two general categories. Circuits of the first type have $\Lambda \gg 1$ so that the induced flux in the loop is not important. These circuits are typically made of aluminum, and the mesoscopic nature of their electronic transport has been studied in nano-scaled circuits. Circuits of the second type have $\Lambda \ll 1$ and induced flux caused by circulating currents is important. These circuits are typically made of niobium, and the macroscopic nature of the tunneling of flux has been studied in small-scaled circuits.

The prospects of using superconducting circuits of the first type as qubits is encouraging because extensive experimental and theoretical work has already been done on mesoscopic superconducting circuits. (For a review of this work see Chapter 7 in [43] and in Ref. [44].) In circuits of the first type ($\Lambda \gg 1$), two energy scales determine the quantum mechanical behavior: The Josephson coupling energy, $E_J = I_o\Phi_o/2\pi$, and the Coulomb energy for single charges, $E_c = e^2/2C$. The energies can be determined by the phases of the Cooper pair wave function of the nodes (islands) and the number of excess Cooper pairs on each node. The phase and the number can be expressed as quantum mechanical conjugate variables[45].

In the "superconducting" limit $E_J > E_c$, the phase is well defined and the charge fluctuates. In the "charging" limit, the charges on the nodes are well defined and the phase fluctuates strongly. When E_J and E_c are within a few orders of magnitude of each other, the eigenstates must be considered as quantum mechanical superpositions of either charge states or phase states. Such superposition states are important in designing qubits. Experimental studies have been performed by several groups with aluminum tunnel junctions with dimensions below 100 nm[43, 44]. Superposition of charge states in circuits in the charging regime have been demonstrated[46, 47, 48] and are in quantitative agreement with theory[49, 50]. The Heisenberg uncertainty principle has been demonstrated when $E_J \approx E_c$[47, 51]. When $E_J > E_c$ topological excitations known as vortices exists and quantum mechanical interference of these

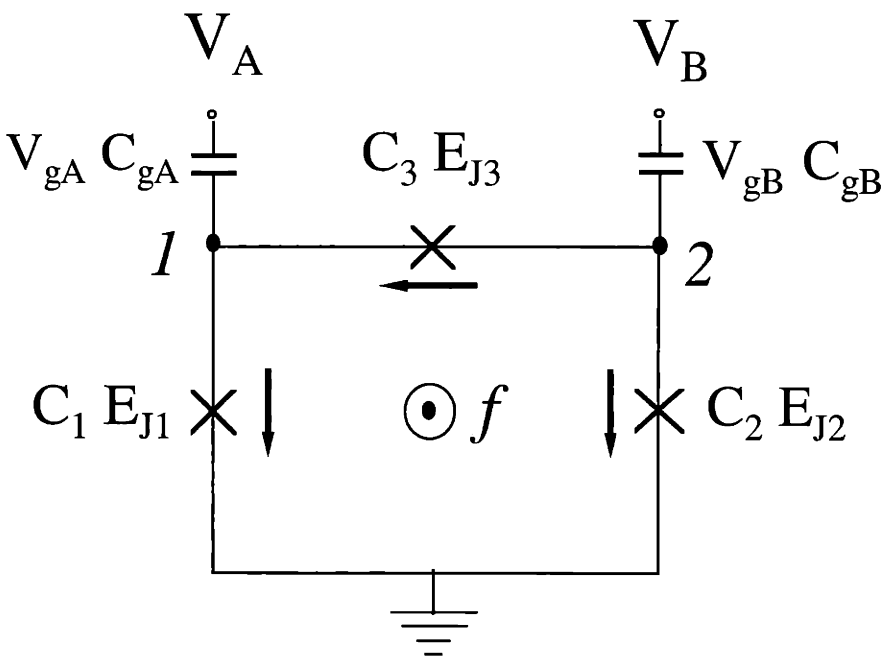

Figure 2-1: The three-junction qubit. Josephson junctions 1 and 2 both have Josephson energies E_J and capacitance C and Josephson junction 3 has a Josephson energy and capacitance α times larger. The nodes 1 and 2 represent the superconducting islands (nodes) which are coupled by gate capacitors $C_g = \gamma C$ to gate voltages V_A and V_B. The arrows define the direction of the currents. The flux is taken out of the page.

quantities has been observed[52]. Unfortunately, circuits of the first type in the charging regime are sensitive to fluctuating off-set charges that are present in the substrate [53, 54]. These random off-set charges make difficult the design of a controllable array of quantum circuits and introduce a strong source of decoherence.

In circuits of the second type ($\Lambda \ll 1$), the quantum variables can be related to the flux in the loops and their time derivatives. For a superconducting loop with a single Josephson junction, known as an rf SQUID, thermal activation of macroscopic quantum states[55] has been observed as well as macroscopic quantum tunneling between states and the discrete nature of the quantum states[56]. One of the advantages of these rf SQUID systems is that the two states have circulating currents of opposite sign and, hence, produce a readily measurable flux of opposite signs. To date no superposition of states have been demonstrated in niobium circuits, although the improving quality of the niobium tunnel junctions may allow such a demonstration[57, 58].

The goal of this section is to present the design of a qubit using circuits of the first type with aluminum, yet to have states (like in circuits of the second type) that are circulating currents of opposite sign. These circulating current states create a magnetic flux of about $10^{-3}\Phi_o$ and we refer to these as "persistent current (PC) states." These states obey all five functional requirements for a quantum bit. The five requirements are: (1). well defined qubit states in a scalable physical system; (2). universal quantum logic operations; (3). the initiation of qubit states; (4). the readout of qubit states; (5). sufficiently slow decoherence on qubit states. The superconducting circuit is at a sufficiently low temperature that the PC states can be made insensitive to background charges and effectively de-coupled from their electrostatic environment. The magnetic coupling to the PC states and the environment can also be made sufficiently weak.

2.1.1 The Circuit of a PC-Qubit

The circuit of the qubit is shown in Fig. 2-1. Each junction is marked by an "x" and is modeled[43, 59] by a parallel combination of an ideal Josephson junction and a capacitor C_i. The parallel resistive channel is assumed negligible. The ideal Josephson junction has a current-phase relation, $I_i = I_o \sin\varphi_i$ where φ_i is the gauge-invariant phase of junction i.

For the calculation of the energy the inductance of the loop is considered negligible $\Lambda \gg 1$ so that the total flux is the external flux. In this case, fluxoid quantization around the loop containing the junctions, gives $\varphi_1 - \varphi_2 + \varphi_3 = -2\pi f$. Here f is the magnetic frustration and is the amount of external magnetic flux in the loop in units of the flux quantum Φ_o.

The Josephson energy due to each junction is $E_{Jn}(1-\cos\varphi_n)$. The total Josephson energy is then $U = \sum_i E_{Ji}(1-\cos\varphi_i)$. Combined with the flux quantization condition, the Josephson energy is[60]

$$\frac{U}{E_J} = 2 + \alpha - \cos\varphi_1 - \cos\varphi_2 - \alpha\cos(2\pi f + \varphi_1 - \varphi_2)\,. \tag{2.1}$$

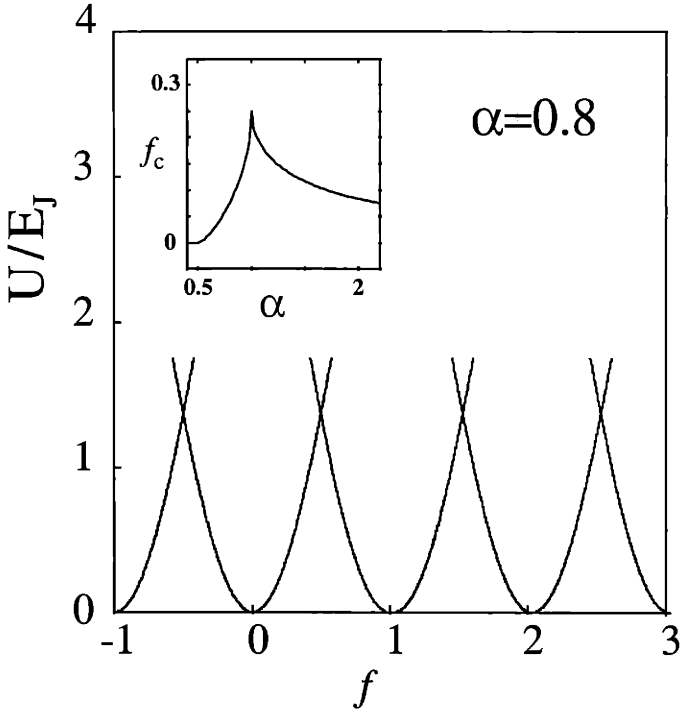

Figure 2-2: U/E_J vs. f for $\alpha = 0.8$ and for minimum energy phase configuration. The energy is periodic with period $f = 1$ and is symmetric about $f = 1/2$. Near $f = 1/2$, there is a region $[1/2 - f_c, 1/2 + f_c]$ where there are two stable solutions. The inset plots f_c as a function of α.

where α is the ratio between the Josephson current of third junction and the Josephson current of the first and the second junctions. The important feature of this Josephson energy is that it is a function of two phases [61]. For a range of magnetic frustration f, these two phases, φ_1 and φ_2, permit two stable configurations which correspond to dc currents flowing in opposite directions. We illustrate this in Fig. 2-2, where we plot the energy of the minimum of the system as a function of f for $\alpha = 0.8$. The energy is periodic with period $f = 1$ and is symmetric about $f = 1/2$. Near $f = 1/2$, there is a region $[1/2 - f_c, 1/2 + f_c]$ where there are two stable solutions. The inset plots f_c as a function of α. These two solutions have circulating currents of opposite direction and are degenerate at $f = 1/2$. The calculation of the energy for the stable solutions and f_c is given in Appendix A.

These two states of opposite current are the two states of the qubit studied in this thesis. By adding the charging energy (the capacitive energy) of the junctions and considering the circuit quantum mechanically, we can adjust the parameters of the circuit so that the two lowest states of the system near $f = 1/2$ will correspond to these two classical states of opposite circulating currents. Moreover, we will show that these two states can be made insensitive to the gate voltages and the random off-set charges. The quantum mechanics of the circuit will be considered in detail in the next section.

The stable classical solutions correspond to energy minima in $U(\varphi_1, \varphi_2)$. Let's consider the case of $f = 1/2$. For $\alpha \leq 1/2$, U has only one minimum at $\varphi_1 = \varphi_2 = 0 \bmod 2\pi$. Above the critical value of $\alpha = 1/2$, this minimum bifurcates into two degenerate minima at $\varphi_1 = -\varphi_2 = \pm\varphi^* \bmod 2\pi$ where $\cos\varphi^* = 1/2\alpha$. The minima form a two-dimensional pattern with the two minima at $(\varphi^*, -\varphi^*)$ and $(-\varphi^*, \varphi^*)$ repeated in a two-dimensional square lattice. This pattern can be seen in Fig. 2-3 which is a contour plot of the Josephson energy as a function of the phase variables for $\alpha = 0.8$. The nested nearly circular contours mark the maxima in the potential. The figure-eight shaped contour encloses two minima. Fig. 2-3b shows the potential along φ_m, the phase between the two minima in a unit cell; that is, along the line $\varphi_2 = -\varphi_1$. The upper curve is for $\alpha = 1.0$ and the lower for $\alpha = 0.8$. Fig. 2-3c shows the potential vs φ_n, which connects one minimum (say at $(-\varphi^*, \varphi^*)$) to its next nearest neighbor (at $(\varphi^*, 2\pi - \varphi^*)$). For $\alpha = 0.8$ the energy barrier between the two minima is much lower than the energy barrier from the minimum in one unit cell to the neighboring unit cell. For $\alpha = 1.0$ the energy barrier from unit cell to unit cell is nearly the same as the barrier within the unit cell. The ability to manipulate the potential landscape by changing α will be important in designing the qubit.

We now consider the electric energy T stored in the five capacitors in the circuit. Each capacitor C_j has a voltage V_j across it so that

$$T = \frac{1}{2}\sum_j C_j V_j^2 - Q_{gA}V_A - Q_{gB}V_B\,. \tag{2.2}$$

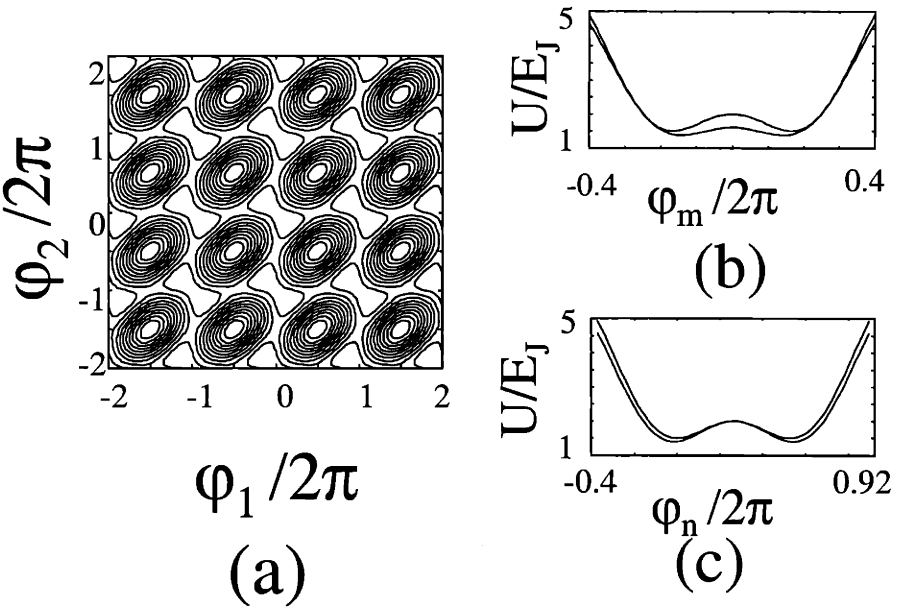

Figure 2-3: (a) A contour plot of the Josephson energy (potential energy) $U(\varphi_1, \varphi_2)$ for $f = 1/2$ for $\alpha = 0.8$. The nested nearly circular shapes mark the maxima in the potential, and the figure-eight shaped contours enclose two minima. (b) A plot of the potential vs. φ_m, the phase along the direction between these two minimum in the same unit cell, (c) A plot of the potential vs. φ_n, the phase along direction from one minima to its next nearest neighbor. Note that the barrier is a saddle point. The upper curve in each figure is for $\alpha = 1.0$ and the lower for $\alpha = 0.8$.

Here $j = 1, 2, 3$. gA and gB are the two metallic gate contacts. The last two terms subtract the work done by the voltage source to give the available electric (free) energy[62]. The voltage across each Josephson junction is given by the Josephson voltage-phase relation $V_n = (\Phi_o/2\pi)\dot{\varphi}_n$, where the over-dot indicates a partial time derivative. The ground in the circuit labels the zero of potential and is a virtual ground.

The voltage across the gate capacitor gA is $V_{gA} = V_A - V_1$ and similarly for $V_{gB} = V_B - V_2$. The electric energy can then be written in terms of the time derivatives of the phases as

$$T = \frac{1}{2}\left(\frac{\Phi_0}{2\pi}\right)^2 \dot{\vec{\varphi}}^T \cdot \mathbf{C} \cdot \dot{\vec{\varphi}}. \tag{2.3}$$

The constant term $-\frac{1}{2}\vec{V}_g^T \cdot \mathbf{C}_g \cdot \vec{V}_g$ has been neglected and

$$\vec{\dot{\varphi}} = \begin{pmatrix} \dot{\varphi}_1 \\ \dot{\varphi}_2 \end{pmatrix} \qquad \mathbf{C} = C \begin{pmatrix} 1+\alpha+\gamma & -\alpha \\ -\alpha & 1+\alpha+\gamma \end{pmatrix} \tag{2.4}$$

and

$$\vec{V}_g = \begin{pmatrix} V_A \\ V_B \end{pmatrix} \qquad \mathbf{C}_g = \gamma C \begin{pmatrix} 1 & 0 \\ 0 & 1 \end{pmatrix} . \tag{2.5}$$

The classical equations of motion can be found from the Lagrangian $\mathcal{L} = T - U$. We take the electrical energy as the kinetic energy and the Josephson energy as the potential energy [63].The canonical momenta are $P_i = \partial\mathcal{L}/\partial\dot{\varphi}_i$. To attach a more physical meaning to the canonical momentum, we shift the Lagrangian by a Galilean-like transformation to

$$\mathcal{L} = T - U - \left(\frac{\Phi_o}{2\pi}\right) \vec{\dot{\varphi}}^T \cdot \mathbf{C}_g \cdot \vec{V}_g \, . \tag{2.6}$$

The canonical momentum is then

$$\vec{P} = \left(\frac{\Phi_o}{2\pi}\right)^2 \mathbf{C} \cdot \vec{\dot{\varphi}} - \left(\frac{\Phi_o}{2\pi}\right) \mathbf{C}_g \cdot \vec{V}_g \tag{2.7}$$

and is directly proportional to the charges at the islands at nodes 1 and 2 in Fig. 2-1 as

$$\vec{Q} = \frac{2\pi}{\Phi_o} \vec{P} \, . \tag{2.8}$$

(For any Josephson circuit it can be shown that there exist linear combinations of the phases across the junctions such that these linear combination can be associated with each node, and the corresponding conjugate variable is proportional to the charge at that node[64, 65]. If self and mutual inductances are need to be included in the circuit (as we argue does not need to be done in our case), then additional conjugate pairs would be needed[65].)

The classical Hamiltonian, $H = \sum_i P_i \dot{\varphi}_i - \mathcal{L}$, is

$$H = \frac{1}{2}\left(\vec{P} + \frac{\Phi_o}{2\pi}\vec{Q}^I\right)^T \cdot \mathbf{M}^{-1} \cdot \left(\vec{P} + \frac{\Phi_o}{2\pi}\vec{Q}^I\right) + U(\vec{\varphi}) \tag{2.9}$$

where the effective mass $\mathbf{M} = (\Phi_o/2\pi)^2\mathbf{C}$ is anisotropic and the induced charge on the island is $\vec{Q}^I = \mathbf{C}_g \cdot \vec{V}_g$. The " ^{T} " operation is the transposition of the corresponding operators. When driven by an additional external current source, the classical dynamics of this system has been studied in recent years both theoretically[66, 67] and experimentally.[68, 69]

Note that the kinetic energy part of this Hamiltonian is

$$T = \frac{1}{2}\left(\vec{Q} + \vec{Q}^I\right)^T \cdot \mathbf{C}^{-1} \cdot \left(\vec{Q} + \vec{Q}^I\right) \tag{2.10}$$

which is just the electrostatic energy written is terms of the charges and induced charges on the islands. Often this is the method used in discussing the charging part of the Hamiltonian. See for example Reference [64] and the references therein. A characteristic charge is e and a characteristic capacitance is C so that the characteristic electric energy is the so-called charging energy, $E_c = e^2/2C$.

2.1.2 Quantization of the Classical Hamiltonian

The transition to treating a circuit quantum mechanically is to consider the classically conjugate variables in a classical Hamiltonian as quantum mechanical operators[70, 71]. For example, the momenta can be written as $P_1 = -i\hbar\partial/\partial\varphi_1$ and $P_2 = -i\hbar\partial/\partial\varphi_2$ and the wave function can then be considered as $|\Psi> = \Psi(\varphi_1, \varphi_2)$.

In this representation the plane-wave solutions, such as $\psi = \exp\{-i(\ell_1\varphi_1 + \ell_2\varphi_2)\}$ correspond to a state that has ℓ_1 Cooper pairs on island (node) 1 and ℓ_2 Cooper pairs on island 2. These plane-wave states are the so-called charging states of the system[49, 72]. Since a single measurement of the number of Cooper pairs on each island must be an integer, then so should the ℓ's be here. (Note the expectation value of the number of Cooper pairs is not restricted to an integer.) Furthermore, an eigen

function $\Psi(\varphi_1, \varphi_2)$ can be written as a weighted linear combination of these charge states. This means that $\Psi(\varphi_1, \varphi_2)$ is periodic when each of the phases are changed by 2π, as in the physical pendula[73].

By considering

$$\Psi(\varphi_1,\, \varphi_2) = \exp\{i(k_1'\varphi_1 + k_2'\varphi_2)\}\chi(\varphi_1,\, \varphi_2) \tag{2.11}$$

with $[k_1', k_2'] = -(\gamma C/2e)[V_A, V_B]$, the Hamiltonian for $\chi(\varphi_1, \varphi_2)$ is almost the same but the induced charges are now transformed out of the problem, and we refer to this new Hamiltonian as the transformed Hamiltonian H_t, where[74]

$$\begin{aligned} H_t = \quad & \frac{1}{2}\vec{P}^T \cdot \mathbf{M}^{-1} \cdot \vec{P} + E_J\{2 + \alpha - \cos\varphi_1 - \cos\varphi_2 \\ & -\alpha\cos(2\pi f + \varphi_1 - \varphi_2)\}\,. \end{aligned} \tag{2.12}$$

The resulting equation $H_t\chi(\varphi_1, \varphi_2) = E\chi(\varphi_1, \varphi_2)$ is the same as for an anisotropic, two-dimensional particle in the periodic potential U. The solutions are Bloch waves with the "crystal momentum" $\mathbf{k}$-values corresponding to $-\mathbf{k}'$, which is proportional to the applied voltages. This choice of crystal momentum insures that $\Psi(\varphi_1, \varphi_2)$ is periodic in the phases.

2.2 Qubit Properties

The Hamiltonian of this three junction circuit describes a particle in a two-dimensional periodic potential. We choose the lowest two energy levels as the states of the qubit—the effective two-level system that is well separated from the other states. These two states have opposite circulating currents and the qubit behaves as a giant magnetic dipole. The dipole moment is exploited as a means for implementing two-qubit coupling and for qubit detection. In our design, the qubit states are insensitive to background charge noise as will be shown below.

In this section, we numerically study the energy structure of the qubit and plot the energy spectrum versus the magnetic flux and the gate voltages. We analyze the

physical origin of the insensitivity to background charges and compare our analysis with the numerical result of the energy spectrum. A tight-binding model is also applied to study the qubit states in addition to the numerical method.

2.2.1 Numerical Results

We will first present the numerical results of the energy levels and wave functions for the circuit. Then we will use a tight-binding approach to understand the results semi-quantitatively.

The eigenvalues and eigenwave functions for the transformed Hamiltonian H_t are determined numerically by expanding the wave functions in terms of states of constant charge or states of constant phase. The states of constant charge result in the standard central equation for Bloch functions and are computationally efficient when $E_c > E_J$. The states of constant phase are solved by putting the phases on a discrete lattice and the numerics are more efficient when $E_J > E_c$. Since the Josephson energy dominates, we will show results computed using the constant phase states. (However, when we used the constant charge states, we obtained the same results.)

The numerical calculations are done in a rotated coordinate system which diagonalizes the capacitance matrix $\mathbf{C}$ by choosing as coordinates the sum and difference of the phases, $\varphi_p = (\varphi_1 + \varphi_2)/2$ and $\varphi_m = (\varphi_1 - \varphi_2)/2$. The resulting reduced Hamiltonian is

$$\begin{aligned} H_t = \quad & \frac{1}{2}\frac{P_p^2}{M_p} + \frac{1}{2}\frac{P_m^2}{M_m} + E_J\{2+\alpha \\ & -2\cos\varphi_p\cos\varphi_m - \alpha\cos(2\pi f + 2\varphi_m)\} \end{aligned} \tag{2.13}$$

where the momenta can be written as $P_p = -i\hbar\partial/\partial\varphi_p$ and $P_m = -i\hbar\partial/\partial\varphi_m$. The mass terms are $M_p = (\Phi_o/2\pi)^2 2C(1+\gamma)$ and $M_m = (\Phi_o/2\pi)^2 2C(1+2\alpha+\gamma)$. In this coordinate system the full wave function $\Psi(\varphi_p,\varphi_m) = \exp\{i(k'_p\varphi_p + k'_m\varphi_m)\}\chi(\varphi_p,\varphi_m)$ with $[k'_p, k'_m] = -(\gamma C/2e)[V_A + V_B, V_A - V_B]$ and $H_t\chi(\varphi_p,\varphi_m) = E\chi(\varphi_p,\varphi_m)$. Also the two minima of the potential $U(\varphi_p,\varphi_m)$ within a unit cell form a periodic two-dimensional centered cubic lattice with lattice constants $\mathbf{a}_1 = 2\pi\mathbf{i}_x$ and $\mathbf{a}_2 = \pi\mathbf{i}_x + \pi\mathbf{i}_y$.

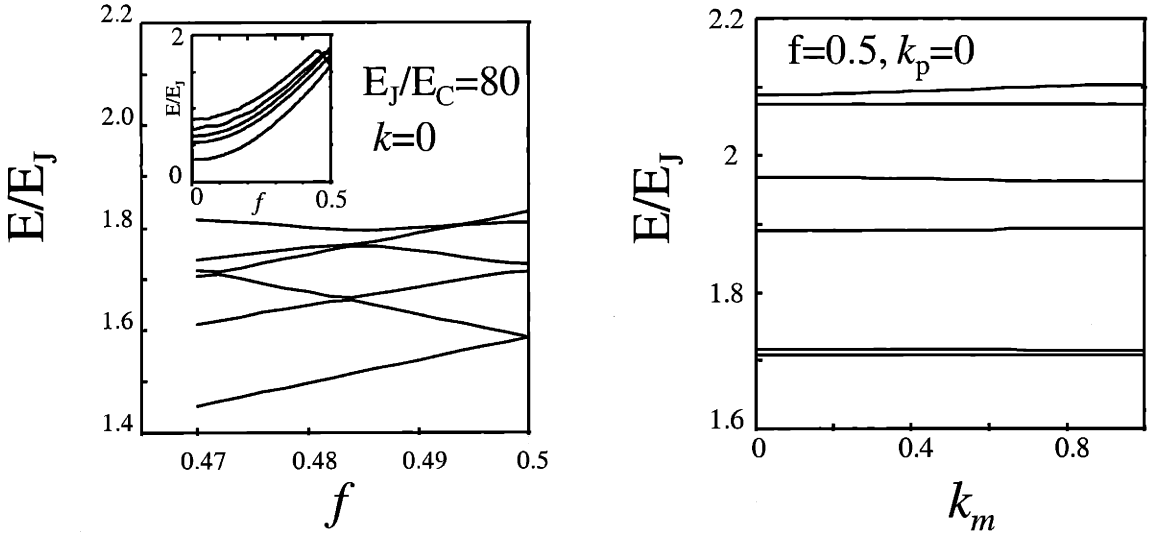

Figure 2-4: The energy levels E vs. frustration and gate voltage for $E_J/E_c = 80$, $\alpha = 0.8$, and $\gamma = 0.02$. The gate voltage is related to the $\vec{\mathbf{k}}$ values by $[k_p, k_m] = (\gamma C/2e)[V_A + V_B, V_A - V_B]$. Left: E/E_J vs f near $f = 1/2$ for $[k_p, k_m] = [0, 0]$. Right: E/E_J vs k_m for $k_p = 0$ and $f = 1/2$.

Fig. 2-4 shows the energy levels as a function of f and as a function of the gate voltage which is given in terms of $\mathbf{k}$. We have taken $E_J/E_c = 80$, $\alpha = 0.8$, and $\gamma = 0.02$ in this example. The energy levels are symmetric about $f = 1/2$. In the left hand side of Fig. 2-4, we see that the two lowest energy levels near $f = 1/2$, have opposite slopes, indicating that the circulating currents are of opposite sign. We also see that there is only a small range of $0.485 < f < 0.5$ where the qubit can be operated between these states of opposite circulating current. This range is consistent with the range $[\frac{1}{2} \pm f_c]$ from the classical stability as shown in Fig. 2-2. At $f = 0.49$ direct calculation of the average circulating current, $< \Psi | I_o \sin \varphi_1 | \Psi >$ gives that the circulating current for the lower level is $I_1/I_o = -0.70$ and for the upper level is $I_2/I_o = +0.70$. (A calculation of the circulating current from the thermodynamic relation $-\Phi_o^{-1} \partial E_n / \partial f$ gives the same result.) For a loop of diameter of $d = 10\,\mu$m, the loop inductance is of the order $\mu_o d \approx 10\,$pH[75]. For $I_o \approx 400\,$nA ($E_J = 200\,$GHz), the flux due to the circulating current is $LI_1 \approx 10^{-3}\Phi_o$, which is detectable by an external SQUID. Nevertheless, the induced flux is small enough, that we are justified

in neglecting its effect when calculating the energy levels.

The difference in energy between the lower and upper levels at the operating point of $f = 0.485$ is about $0.1\,E_J \approx 20\,\mathrm{GHz}$. Moreover, in the right hand side of Fig. 2-4 shows that the energies of these levels is very insensitive to the gate voltages, or equivalently, to the random off-set charges. The numerical results show that the bands are flat to better than one part in a thousand, especially at $f = 0.48$. To understand the underlying physics, a tight-binding model is developed.

In Table. 2.1 and Table. 2.2, the numerical calculations on the gate voltage dependence of the qubit states are shown. These results are calculated by varying the wave vectors $[k_p, k_m]$ in the qubit Hamiltonian. The wave vectors directly correspond to the charge fluctuations on the qubit gates. Table. 2.1 is for $f_1 = 1/2$ where the double well potential is symmetric to each other and where the energy splitting of the two qubits states is equal to the quantum tunneling t_0. Table. 2.2 is for $f_1 = 0.48$ where the Zeemann energy due to the external flux dominates over the quantum tunneling. In both situations, it is shown that the variation in energy due to wave vectors is very small and the pc-qubit is insensitive to background charge fluctuations in the environment.

The insensitivity can be explained by the tight-binding approach which will be detailed in the next subsection. In the two-dimensional potential, a particle at each local minimum can tunnel to three other minima: the tunneling to its nearest neighbour characterized by t_1 and the tunneling to the two next nearest neighbours characterized by t_2. Physically, the gate voltage affects the qubit states via the tunneling between the next nearest neighbours. The total tunneling term in the tight-binding Hamiltonian is $t_0 = t_1 + t_2 e^{-i\pi q_1/e} + t_2 e^{i\pi q_2/e}$. As $t_2 \ll t_1$ in the pc-qubit, the effect of the charge fluctuations on the qubit is also negligible.

2.2.2 Tight-Binding Model

Consider the case near the degeneracy point $f = 1/2$. The minima in energy occurs when $\varphi_p^* = 0$ and $\varphi_m = \pm\varphi_m^*$ where $\cos\varphi_m^* = 1/2\alpha$. Near the minimum at $[\varphi_m, \varphi_p] = [\varphi_m^*, 0]$, the potential looks like a double potential well repeated at lattice points

$[k_p, k_m]$	[0, 0]	[0.1, 0.1]	[0.2, 0.2]	[0.3, 0.3]	[0.4, 0.4]	[0.5, 0.5]
E_1	1.7076	1.7076	1.7077	1.7078	1.7079	1.7080
E_2	1.7163	1.7163	1.7161	1.7160	1.7159	1.7158
E_3	1.8904	1.8905	1.8908	1.8912	1.8915	1.8916
I_1	0	0	0	0	0	0
I_2	0	0	0	0	0	0
I_3	0	0	0	0	0	0
$[kp, km]$	[0, 0]	[0, 0.2]	[0, 0.4]	[0, 0.6]	[0, 0.8]	[0, 1]
E_1	1.7076	1.7076	1.7078	1.7081	1.7083	1.7083
E_2	1.7163	1.7162	1.7160	1.7157	1.7155	1.7154
E_3	1.8904	1.8906	1.8912	1.8919	1.8926	1.8928
I_1	0	0	0	0	0	0
I_2	0	0	0	0	0	0
I_3	0	0	0	0	0	0
$[k_p, k_m]$	[1, 0]	[0.8, 0.2]	[0.6, 0.4]	[0.4, 0.6]	[0.2, 0.8]	[0, 1]
E_1	1.7083	1.7082	1.7080	1.7080	1.7082	1.7083
E_2	1.7154	1.7155	1.7158	1.7158	1.7155	1.7154
E_3	1.8928	1.8924	1.8917	1.8917	1.8924	1.8928
I_1	0	0	0	0	0	0
I_2	0	0	0	0	0	0
I_3	0	0	0	0	0	0

Table 2.1: Qubit energy dependence on gate voltage at $f = 1/2$.

$\mathbf{a}_1 = 2\pi\mathbf{i}_x$ and $\mathbf{a}_2 = \pi\mathbf{i}_x + \pi\mathbf{i}_y$. Fig. 2-5 shows the two eigen functions in a unit cell. The wave function for the lower level (Ψ_1) is symmetric and the wave function for the upper level (Ψ_2) is antisymmetric. Both of the wave functions are localized near the two minima in U in the unit cell.

To find an approximate tight-binding solution, let $u(\varphi_m, \varphi_p)$ be the wave function for the ground state on one side of the double potential wells, and $v(\varphi_m, \varphi_p)$ be the wave function on the other side. The tight-binding solution for H_t in Eqn. 2.13 is $\Phi = c_u u + c_v v$ and satisfies

$$\begin{pmatrix} H_{uu} & H_{uv} \\ H_{vu} & H_{vv} \end{pmatrix} \begin{pmatrix} c_u \\ c_v \end{pmatrix} = E \begin{pmatrix} c_u \\ c_v \end{pmatrix} \tag{2.14}$$

Because the double well is symmetric at $f = 1/2$, each wave function has the same energy ϵ_0 and so $H_{uu} = H_{vv} = \epsilon_0$. Let t_1 be the tunneling matrix element between these two minima in the same unit cell and t_2 between nearest neighbor minima in

$[k_p, k_m]$	[0, 0]	[0.1, 0.1]	[0.2, 0.2]	[0.3, 0.3]	[0.4, 0.4]	[0.5, 0.5]
E_1	1.6281	1.6281	1.6281	1.6281	1.6281	1.6281
E_2	1.7942	1.7942	1.7941	1.7940	1.7940	1.7940
E_3	1.8605	1.8606	1.8608	1.8611	1.8613	1.8614
I_1	-0.6634	-0.6634	-0.6635	-0.6635	-0.6635	-0.6635
I_2	0.6168	0.6164	0.6153	0.6139	0.6128	0.6124
1_3	-0.3604	-0.3602	-0.3598	-0.3593	-0.3590	-0.3588
$[kp, km]$	[0, 0]	[0, 0.2]	[0, 0.4]	[0, 0.6]	[0, 0.8]	[0, 1]
E_1	1.6281	1.6281	1.6281	1.6281	1.6281	1.6281
E_2	1.7942	1.7942	1.7940	1.7939	1.7938	1.7937
E_3	1.8605	1.8607	1.8611	1.8616	1.8621	1.8622
I_1	-0.6634	-0.6634	-0.6635	-0.6635	-0.6636	-0.6636
I_2	0.6168	0.6159	0.6137	0.6109	0.6087	0.6079
I_3	-0.3604	-0.3600	-0.3591	-0.3581	-0.3574	-0.3571
$[k_p, k_m]$	[1, 0]	[0.8, 0.2]	[0.6, 0.4]	[0.4, 0.6]	[0.2, 0.8]	[0, 1]
E_1	1.6281	1.6281	1.6281	1.6281	1.6281	1.6281
E_2	1.7937	1.7938	1.7939	1.7939	1.7938	1.7937
E_3	1.8622	1.8619	1.8614	1.8614	1.8619	1.8622
I_1	-0.6636	-0.6636	-0.6635	-0.6635	-0.6636	-0.6636
I_2	0.6079	0.6094	0.6120	0.6120	0.6094	0.6079
I_3	-0.3571	-0.3577	-0.3587	-0.3587	-0.3577	-0.3571

Table 2.2: Qubit energy dependence on gate voltage at $f = 0.48$.

the adjacent unit cells. Then $H_{uv} = H_{vu}^* = -t_1 - t_2 e^{i\mathbf{k}\cdot\mathbf{a}_2} - t_2 e^{i\mathbf{k}\cdot(\mathbf{a}_1-\mathbf{a}_2)}$. The eigen energy levels are $E = \epsilon_0 \mp |H_{uv}|$. The effect of t_1 is to split the degeneracy of the two states so that at $k = 0$, the energy is $\epsilon_0 \mp (2t_2 + t_1)$ for the symmetric and antisymmetric states, respectively. The effect of t_2 is to give dispersion in k, that is, in gate voltage and off-set charges, to the energy levels. Because we want to minimize the gate-voltage (and off-set charge) dependence, we seek to minimize the tunneling t_2 from one unit cell to another. Likewise, we want the two localized states in the two wells to interact, so that we want t_1 to be non-zero. This is why the potential landscape in Fig. 2-3 was chosen to have $\alpha \approx 0.8$: The potential has a much lower barrier between states in the double well, but a large barrier between states from one double well to the next.

An estimate of t_i can be obtained from calculating the action S_i between the two minima and using $t_i \approx (\hbar\omega_i/2\pi)e^{-S_i/\hbar}$ where ω_i is the attempt frequency of escape in

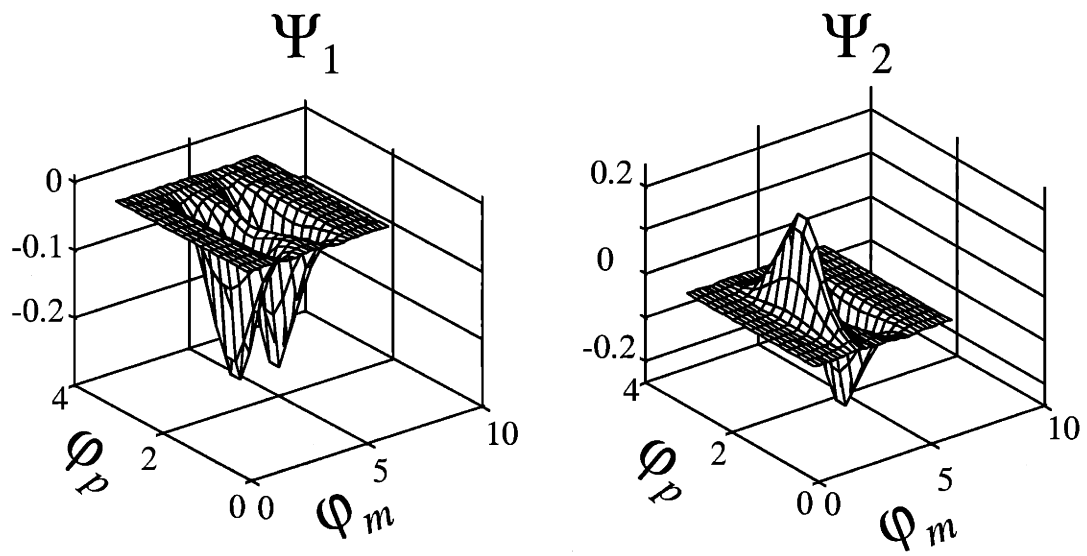

Figure 2-5: The eigen wave functions for the lower (Ψ_1) and upper (Ψ_2) energy levels at $f = 1/2$ as a function of the phases.

the potential well. The action from point $\vec{\varphi}_a$ to $\vec{\varphi}_b$ is

$$S = \int_{\vec{\varphi}_a}^{\vec{\varphi}_b} \left(2M_{nn}(E-U)\right)^{1/2} |d\varphi_n| \,. \tag{2.15}$$

Here $\mathbf{n}$ is a unit vector along the path of integration, $d\varphi_n$ the differential path length, and $M_{nn} = \mathbf{n}^T \cdot \mathbf{M} \cdot \mathbf{n}$ is the component of the mass tensor along the path direction. In both cases we will approximate the energy difference $E - U$ as the difference in the potential energy ΔU from the minima along the path.

First, consider the calculation of t_1, the tunneling matrix element within the unit cell. The path of integration is taken from $(-\varphi_m^*, 0)$ to $(\varphi_m^*, 0)$ along the direction $\mathbf{n} = \mathbf{i}_x$, so that $M_{nn} = M_m$ for this path. The potential energy at the minima is $U_{min} = 2 - 1/2\alpha$. The difference in the potential energy from the minima at $(-\varphi_m^*, 0)$ along this path is can we written as $\Delta U_1 = E_J\{2\alpha\left(\cos\varphi_m - 1/2\alpha\right)^2\}$. The action along this path is then

$$S_1 = \int_{-\varphi_m^*}^{\varphi_m^*} \left(4M_m \alpha E_J\right)^{1/2} \left(\cos\varphi_m - \frac{1}{2\alpha}\right) d\varphi_m \tag{2.16}$$

which yields

$$S_1 = \hbar \left[4\alpha(1+2\alpha+\gamma)E_J/E_c\right]^{1/2} \left(\sin\varphi_m^* - \frac{1}{2\alpha}\varphi_m^*\right) . \tag{2.17}$$

Now consider t_2, the tunneling from unit cell to unit cell. For example, take the integration to be from $(\varphi_m^*, 0)$ to one of its nearest neighbor minima at $(\pi - \varphi_m^*, \pi)$. We will take the path of integration to be a straight line joining these two points in the φ_m-φ_p plane. This path is not the optimal trajectory, but the difference of this straight line path from the optimal trajectory is quadratic in the small deviations of these two paths. The straight line path is described by $\varphi_m = \varphi_m^* + \lambda\varphi_p$ where $\lambda = (\pi - 2\varphi_m^*)/\pi$; it has a direction of $\mathbf{n} = \lambda\mathbf{i}_x + \mathbf{i}_y$ and a path length of $ds = \sqrt{1+\lambda^2}\, d\varphi_p$. The mass on this direction is $M_2 = (M_p + \lambda^2 M_m)/(1+\lambda^2)$. The difference of the potential energy along this path from the minima energy is $\Delta U_2/E_J = -2\cos\varphi_p \cos(\varphi_m^* + \lambda\varphi_p) + 2\alpha\cos^2(\varphi_m^* + \lambda\varphi_p) + 1/2\alpha$. The action is then

$$S_2 = \left[2M_2E_J(1+\lambda^2)\right]^{1/2} \int_0^{\pi} \left(\frac{\Delta U_2}{E_J}\right)^{1/2} d\varphi_p \, . \tag{2.18}$$

The integrand is not analytically integrable, but it is zero at the end points of the integration and is well approximated by $\sqrt{\Delta U_2/E_J} \approx (1/\sqrt{2\alpha})\cos(\varphi_p - \pi/2)$. With this approximation, $S_2 = (4M_2E_J(1+\lambda^2)/\alpha)^{1/2}$, which is

$$S_2 = \hbar\sqrt{\frac{E_J}{E_c}\left(\frac{(1+\gamma)(1+\lambda^2)}{\alpha} + 2\lambda^2\right)} . \tag{2.19}$$

To compare the tunneling rates we would first need the attempt frequencies in the two directions. However, we can consider the attempt frequencies to be of the same order of magnitude and thus $t_2/t_1 \sim e^{-(S_2-S_1)/\hbar}$. For $\alpha = 0.8$, we find that $S_1/(\hbar\sqrt{E_J/E_c}) \approx 0.6$ and $S_2/(\hbar\sqrt{E_J/E_c}) \approx 1.4$. For $E_J/E_c \sim 100$, then $t_2/t_1 \sim 10^{-4} \ll 1$. We are therefore able to ignore t_2, the tunneling from unit cell to unit cell. This means that there is little dispersion in the energy levels with $\mathbf{k}$ and consequently, with the voltage or off-set charges. In fact, using the action one can show that for α smaller than about 0.85, $t_1 > t_2$ for $E_J/E_c \approx 80$. Throughout the rest of the paper

we will choose parameters so that the effects of t_2 can be ignored.

We now obtain an approximate solution for the energy levels and tunneling matrix elements by modeling each side of the double potential. Near the minimum at $[\varphi_m, \varphi_p] = [\varphi_m^*, 0]$, the potential looks like an anisotropic two-dimensional harmonic oscillator. The Hamiltonian in the vicinity of the minimum is approximately, (with $Q_i^I = 0$)

$$\mathcal{H} \approx \frac{1}{2}\frac{P_p^2}{M_p} + \frac{1}{2}M_p\omega_p^2\varphi_p^2 + \frac{1}{2}\frac{P_m^2}{M_m} + \frac{1}{2}M_m\omega_m^2(\varphi_m - \varphi_m^*)^2 + U_0 \tag{2.20}$$

where

$$\frac{\hbar\omega_p}{E_J} = \sqrt{\frac{4}{\alpha(1+\gamma)(E_J/E_c)}} \tag{2.21}$$

and

$$\frac{\hbar\omega_m}{E_J} = \sqrt{\frac{4(4\alpha^2-1)}{\alpha(1+2\alpha+\gamma)(E_J/E_c)}} \tag{2.22}$$

and $U_o = 2 - 1/2\alpha$. The ground state ϕ_o of the single harmonic well has energy $\epsilon_0 = \hbar(\omega_p + \omega_m)/2 + U_o$. Let's now use this approximation to understand the energy levels, first at $f = 1/2$ and then near this point.

At $f = 1/2$ we expect the four lowest energy levels of the two-dimensional harmonic oscillator to be with $\omega_m < \omega_p$, $E_1 = \epsilon_0 - t_1$, $E_2 = \epsilon_0 + t_1$, $E_3 = \epsilon_0 - t_1 + \hbar\omega_m$, $E_4 = \epsilon_0 + t_1 + \hbar\omega_m$. Table 2.3 compares the results and we also list the small anharmonic corrections to the simple harmonic energy levels. We have chosen to compare $(E_1 + E_2)/2$ and $(E_3 + E_4)/2$ so that the tunneling term is absent and a direct comparison with the simple harmonic oscillators can be made. The agreement between

	$\hbar\omega_m$	$\hbar\omega_p$	E_0	$(E_1+E_2)/2$	$(E_3+E_4)/2$
Harmonic	0.193	0.247	1.60	1.79	1.84
Anharmonic	0.183	0.238	1.59	1.77	1.83
Numerical	0.154	0.226	1.58	1.74	1.81

Table 2.3: A comparison of the energy levels with the approximate harmonic oscillator levels (with harmonic and anharmonic terms) with the numerical calculations.Here, $f = 1/2$, $\alpha = 0.8$, $\gamma = 0.02$, and and $E_J/E_c = 80$. Also $U_o = 1.38$ and $U_{\text{bar}} = 0.225$ for the harmonic and anharmonic estimations. All the energies are in units of E_J.

this tight-binding approximation and the numerical calculations is good. We have also included the barrier height from one minimum to the other one in the same unit cell.

If we estimate the attempt frequency for t_1 as ω_m, then we find that for the parameters in Table 2.3, the action calculation gives $t_1 = 10^{-4}E_J$. From the full wave functions, we estimate $t_1 = (E_2 - E_1)/2 \approx 10^{-3}E_J$. This discrepancy can be made smaller by noting that in the calculation of the action, we could more accurately integrate from the classical turning points in the potential rather than from the minima [76]. However, for our purposes, the action expression will be sufficient for qualitative discussions, and we will use the full numerical calculations when estimating actual numbers.

So far we have estimated the energy levels and tunneling matrix elements when $f = 1/2$. As f is decreased from $f = 1/2$ the potential U changes such that one well becomes higher than the other, and the barrier height also changes. For the qubit we are mainly interested in the lowest two energy states of the system, so we now estimate the terms in the tight-binding expression of Eqn. 2.14. By defining the zero of energy as the average of the two lowest energy states at $f = 1/2$, we find that the Hamiltonian for these two states is

$$H = \begin{pmatrix} F & -t \\ -t & -F \end{pmatrix} \tag{2.23}$$

Here F is the energy the change of each of the wells measured with respect to the energy of the wells at the degeneracy point; that is, $F = (\partial U/\partial f)\delta f$ where U is the potential energy. Note that since we will be operating the qubit just below the degeneracy point $f = 1/2$, then $F < 0$. Also, $t = t_1 + \Delta t$, where t_1 is the intra-cell tunneling matrix element calculated at the degeneracy point and Δt is the change. The eigen values are $\lambda_{1,2} = \mp\sqrt{F^2 + t^2}$ where we have explicitly assumed that F is negative and t is positive.

The eigen vectors are given as the columns in the rotation matrix

$$D(\theta) = \begin{pmatrix} \cos\theta/2 & -\sin\theta/2 \\ \sin\theta/2 & \cos\theta/2 \end{pmatrix} \tag{2.24}$$

where $\theta = -\arctan t/F$. For example, at the degeneracy point, $F = 0$, so that $E = \mp t$ and the eigen vectors are $(1/\sqrt{2}, 1/\sqrt{2})^T$ and $(-1/\sqrt{2}, 1/\sqrt{2})^T$. These are just symmetric and antisymmetric combinations of the single well wave functions, as expected. For f slightly below $1/2$, we have $|F| \gg t$, so $\theta \approx 0$, and the energies are $E = \mp\sqrt{F^2 + t^2} \approx \pm F$. The eigen vectors are approximately $(1, 0)^T$ and $(0, 1)^T$, so that the eigen states are nearly localized in each well.

It is more convenient to discuss the Hamiltonian and eigen states in the rotated coordinate system such that $H_D = D^T(\theta) H D(\theta)$. In the rotated coordinate system, the Hamiltonian is diagonal with

$$H_D = -\sqrt{F^2 + t^2}\,\sigma_z \tag{2.25}$$

and the eigen energies are $E = \pm\sqrt{F^2 + t^2}$ and the eigen states are then simply spin down $|0> = (1, 0)^T$ and spin up $|1> = (0, 1)^T$ vectors. In other words, no matter what the operating field is, we can always go to a diagonal representation; but the rotation matrix must be used to relate the simple spin up and down vectors to the linear combinations of the wave functions in the well.

2.3 Manipulation Qubit

Universal quantum logic[5, 7, 77] can be realized by constructing a discrete set of elementary quantum gates[78]. A convenient choice of the discrete set consists of single qubit rotations and a two-qubit CNOT gate. With these building blocks, any unitary transformation in the state space can be constructed polynomially. In this section, we discuss how to implement these elementary gates for the persistent-current qubit by applying radio-frequency pulse and by inductive coupling between different

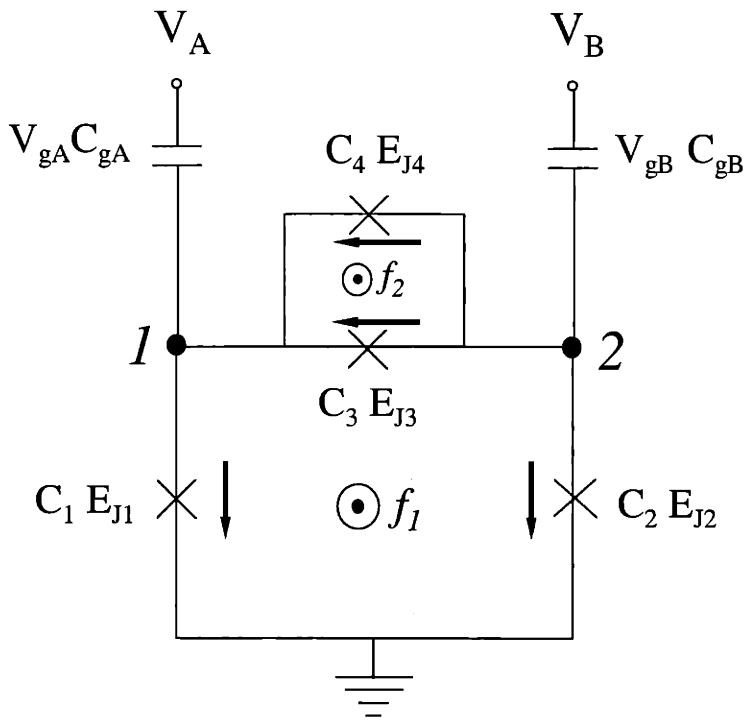

Figure 2-6: The four-junction qubit. Two junctions form a SQUID loop and have Josephson Energies and capacitance β times larger than the other junctions 1 and 2 which both have Josephson energies E_J and capacitance C. The nodes A and B represent the superconducting islands which are coupled by gate capacitors $C_g = \gamma C$ to gate voltages V_A and V_B. The arrows define the direction of the currents. The flux is out of the page.

qubits.

As noted in the previous sections, the flexibility of the design of Josephson junction circuits affords a variety of methods for manipulating and controlling the state of qubits. In this section we show how the basic qubit circuit can be modified to allow precise control of its quantum states. To manipulate the states of the qubit, we need control over the properties of the qubit. For example, control over f, the magnetic field, allows one to change the operating point and F, the value of the energy difference between the two states. Control over the potential barrier height allows changing of the tunneling through t. For example, if the operating point of F_o and t_o are changed

by ΔF and Δt, then the Hamiltonian in the rotated coordinate system is

$$H_D = -\sqrt{F_o^2 + t_o^2}\,\sigma_z + \Delta H_D \tag{2.26}$$

where with $\theta_o = -\arctan t_o/F_o$,

$$\Delta H_D = \Delta F(\cos\theta\,\sigma_z - \sin\theta\,\sigma_x) - \Delta t(\sin\theta\,\sigma_z + \cos\theta\,\sigma_x)\,. \tag{2.27}$$

2.3.1 Single Qubit Rotation

The control over F can be done by changing f. The control over t can be done by changing the barrier heights. To control the barrier heights by external parameters, we replace the third junction by a SQUID which acts like a variable strength junction. The modified circuit of the qubit is shown in Fig. 2-6.

We now analyze this circuit since it will be used in all subsequent discussions of the qubit. Flux quantization around each of the two loops, gives $\varphi_1 - \varphi_2 + \varphi_3 = -2\pi f_1$ and $\varphi_4 - \varphi_3 = -2\pi f_2$. The Josephson energy due to each junction is $E_{Jn}(1 - \cos\varphi_n)$. The total Josephson energy U is then

$$\frac{U}{E_J} = 2 + 2\beta - 2\cos\varphi_p\cos\varphi_m - 2\beta\cos(\pi f_a)\cos(2\pi f_b + 2\varphi_m)\,, \tag{2.28}$$

where $\varphi_p = (\varphi_1 + \varphi_2)/2$ and $\varphi_m = (\varphi_1 - \varphi_2)/2$, and also $f_a = f_2$ and $f_b = f_1 + f_2/2$. Hence we see that $2\beta\cos(\pi f_a)$ plays the role of α in the three junction qubit, but now this term can be changed by changing $f_a = f_2$, the flux in the top SQUID loop. Likewise, $f_b = f_1 + f_2/2$ plays the role of f in the three-junction qubit. The reduced Hamiltonian is then

$$\begin{aligned} H_t = \quad & \frac{1}{2}\frac{P_p^2}{M_p} + \frac{1}{2}\frac{P_m^2}{M_m} + E_J\{2 + 2\beta \\ & -2\cos\varphi_p\cos\varphi_m - 2\beta\cos(\pi f_a)\cos(2\pi f_b + 2\varphi_m)\} \end{aligned} \tag{2.29}$$

where $M_p = (\Phi_o/2\pi)^2 2C(1+\gamma)$ and $M_m = (\Phi_o/2\pi)^2 2C(1+4\beta+\gamma)$.

To manipulate the parameters in the Hamiltonian let the magnetic fields change very slightly away from the same degeneracy point of f_1^* and f_2^* to a new operating point $f_1^o = f_1^* + \epsilon_1$ and $f_2^o = f_2^* + \epsilon_2$. Then F changes from zero to $F_o = r_1\epsilon_1 + r_2\epsilon_2$ and t changes to $t_o = t_1 + s_1\epsilon_1 + s_2\epsilon_2$, where r_i and s_i are constants and t_1 is the tunneling matrix element at the degeneracy point as found in the previous section. We take the operating point to be effectively in the regime where $f < 1/2$ in Fig. 2-4, so that $\epsilon_{1,2} < 0$. Hence, $F_o < 0$. Also, t_o is assumed to remain positive. In the new rotated frame with $\theta_o = -\arctan t_o/F_o$, the Hamiltonian given by Eqn. 2.25 is $H_D = -\sqrt{F_o^2 + t_o^2}\,\sigma_z$.

Away from this new operating point, let $f_1 = f_1^o + \delta_1$ and $f_2 = f_2^o + \delta_2$. In the operation of the qubit, $|\delta_i| \ll |\epsilon_i|$ and δ_i usually will usually have a sinusoidal time dependence. Then $F = F_o + r_1\delta_1 + r_2\delta_2$ and $t = t_o + s_1\delta_1 + s_2\delta_2$, so that $\Delta F = r_1\delta_1 + r_2\delta_2$ and $\Delta t = s_1\delta_1 + s_2\delta_2$. Then the Hamiltonian in the rotated system with $\theta_o = -\arctan t_o/F_o$ is

$$H_D = -\sqrt{F_o^2 + t_o^2}\,\sigma_z + \Delta H_D \tag{2.30}$$

where

$$\begin{aligned}\Delta H_D = \quad & (r_1\delta_1 + r_2\delta_2)(\cos\theta_o\,\sigma_z - \sin\theta_o\,\sigma_x) \\ - \quad & (s_1\delta_1 + s_2\delta_2)(\sin\theta_o\,\sigma_z + \cos\theta_o\,\sigma_x)\,.\end{aligned} \tag{2.31}$$

Hence we see that changes in the magnetic field from the operating point of f_1^o and f_2^o cause both σ_z and σ_x types of interactions.

To find the magnitude of these changes, we calculate the coefficients of change (r_1, r_2, s_1 and s_2) most simply at the degeneracy point where $\epsilon_i = 0$; that is, at the degeneracy point $f_i^o = f_i^*$. We choose the degeneracy point for the four-junction qubit at $f_1^* = 1/3$ and $f_2^* = 1/3$. This results in classically doubly degenerate levels. In fact, any choice which satisfies $2f_1^* + f_2^* = 1$ when the classical energy U has two minima, will also result in doubly degenerate levels. For example $f_1^* = 1/2$ and $f_2^* = 0$

is also a possible and convenient choice. However, we prefer $f_1^* = f_2^* = 1/3$ for the following reason. The change in potential energy with f_a gives (with $f_b = 1/2$)

$$\begin{aligned} \frac{\partial U}{\partial f_a} &= -2\pi\beta \sin \pi f_a^0 \cos 2\varphi_m^o \\ \frac{\partial^2 U}{\partial f_a^2} &= -2\pi^2\beta \cos \pi f_a^0 \cos 2\varphi_m^o \end{aligned} \tag{2.32}$$

The first order terms vanishes if $f_2^o = 0$, resulting in the potential barrier always decreasing with changes in f_2. On the other hand, if $f_2^o = 1/3$, then the barrier height can be made to increase and decrease with changes in f_2, thus allowing more control of the qubit.

Now the coefficients of change (r_1, r_2, s_1 and s_2) can be estimated both from the numerical calculations and from the tight-binding model as shown in Appendix B. We find that at the degeneracy point of $f_1 = f_2 = 1/3$,

$$\frac{r_1}{E_J} = 2\pi\sqrt{1 - 1/(4\beta^2)}\,. \tag{2.33}$$

For our example with $\beta = 0.8$, we have $r_1/E_J = 4.90$. Estimates obtained from the numerical calculations done by changing f_1 and f_2, give $r_1/E_J = 4.8$ and $r_2/E_J = 2.4$ in good agreement with Eqn. B.6 in Appendix B.

Likewise, from Appendix B we have that $s_1 = 0$ and $s_2 = \eta t\sqrt{E_J/E_c}$ where η is of the order of unity. For the operating point we find $\eta \sim 3.5$. Therefore, changes in H due to changes in t_1 go like σ_x. These tight-binding estimates for $\beta = 0.8$ give $s_1 = 0$ and $s_2/E_J = 0.03$. Full numerical calculations for our example with $s_1 = 0$ and $s_2/E_J = 0.20$. The agreement with the tight-binding results are good, although the tight-binding underestimates s_2 with for these parameters.

In summary, from the degeneracy point of $f_1^* = f_2^* = 1/3$, let the operating point be $f_1^o = f_1^* + \epsilon_1$ and $f_2^o = f_2^* + \epsilon_2$, so that $F_o = r_1(\epsilon_1\epsilon_2/2)$ and $t_o = t_1 + s_2\epsilon_2$. Now consider the changes in field about the operating point such that $f_1 = f_1^* + \delta_1$ and

$f_2 = f_2^* + \delta_2$. In the rotated frame where $\theta_o = -\arctan t_o/F_o$, the Hamiltonian is

$$H_D = -\sqrt{F_o^2 + t_o^2}\,\sigma_z + \Delta H_D \tag{2.34}$$

where

$$\begin{aligned} \Delta H_D = \quad & r_1(\delta_1 + \frac{\delta_2}{2})(\cos\theta_o\,\sigma_z - \sin\theta_o\,\sigma_x) \\ - \quad & s_2\delta_2(\sin\theta_o\,\sigma_z + \cos\theta_o\,\sigma_x)\,. \end{aligned} \tag{2.35}$$

and $r_1/E_J = 2\pi\sqrt{1 - 1/(4\beta^2)}$ and $s_2 = \eta t_o\sqrt{E_J/E_c}$.

A typical design for a qubit will have $E_J/E_c = 80$, $\beta = 0.8$, $\gamma = 0.02$. We find from numerical calculations that $t_o \approx 0.005E_J$ and $\eta \approx 3.5$, which agree well with our tight-binding estimates. We operate at $f_1 = f_2 = 0.33$ so that $\epsilon_1 = \epsilon_2 = -1/300$. (This is equivalent to operating the three-junction qubit at $f = f_1 + f_2/2 = 0.495$ in Fig. 2-4.) Writing the energies as $E_i = h\nu_i$, we have taken typical values of $E_J = 200\,\mathrm{GHz}$ and $E_c = 2.5\,\mathrm{GHz}$, and we find that $t_o = 1\,\mathrm{GHz}$ and $F_o = 5\,\mathrm{GHz}$ (which gives a splitting between the two states of about 10 GHz). The Hamiltonian is found to be

$$\frac{H_D}{E_J} = -0.025\sigma_z + (4.0\delta_1 + 2.1\delta_2)\,\sigma_z - (0.46\delta_1 + 0.41\delta_2)\,\sigma_x\,. \tag{2.36}$$

The numerical values used are from numerical calculations. These values agree well with the estimates used in Eqns. 2.34 and 2.35 for the level splitting and the terms proportional to r_1; the terms proportional to s_2 match to about 50%, due to the more sensitive nature of estimating the tunneling terms.

The terms containing σ_x can be used to produce Rabi oscillations between the two states by modulating δ_1 and δ_2 with microwave pulses of the frequency of the level splitting of $2F_o = 10\,\mathrm{GHz}$. One could arrange the values of δ_1 and δ_2 to make the time-varying σ_z-term vanish. Then the operation of the qubit would be isomorphic to the NMR qubit. However, our simulations show that such an arrangement couples higher energy levels and invalidates the simple two-state approximation. This is due to the large matrix element between the ground state and the second excited state given

by the change in potential due to varying δ_2. (It is interesting to note that similar coupling to higher levels occurs in qubits based on the RF SQUID and on simple charge states.) We propose to manipulate the qubit by varying δ_1 which causes a Rabi oscillation through the σ_x term as well as a strong modulation of the Larmor precession through the time varying σ_z term. Because the Rabi frequency is much smaller than the Larmor frequency, the precession causes no problem for manipulating the qubit. For $\delta_1 = 0.001$ and $\delta_2 = 0$, the Rabi frequency is about 90 MHz. We note that this mode of operation is also possible with the three-junction qubit. Of course, it will not be possible to completely eliminate the deleterious effects of the δ_2 coupling, but the effect of this coupling can be greatly reduced if δ_2 is restricted below 0.0001.

The varying magnetic fields δ_1 and δ_2 can be applied locally to the qubit by using a control line to inductively couple to the qubit. Moreover, if the control line is driven by an Josephson oscillator, then the coupling circuit could be fabricated on the same chip.

2.3.2 Interaction between Qubits

The qubits interact with each other via the mutual inductance between the superconducting loops. The qubit behaves as giant magnetic dipoles and to first order, the interaction between qubits is the dipole interaction. This interaction strongly depends on the geometry of the qubit layouts. In a planar layout, where qubits distribute on the same surface, the interaction goes away with $1/r^3$, where r is the distance between the two qubits. A variety of methods are available for coupling qubits together. As noted in [77, 79], essentially any interaction between qubits, combined with the ability to manipulate qubits individually, suffices to construct a universal quantum logic gate. Here we present two methods for coupling qubits inductively as shown in Fig. 2-7. The inductive coupling could either be permanent, or could be turned on and off at will by inserting Josephson junctions in the coupling loops.

Fig. 2-7a shows one way of coupling two identical qubits. The lower portions of each qubit (the loops that contain the circulating currents) are inductively coupled. To a first approximation we model the coupling as changing the flux in each of the

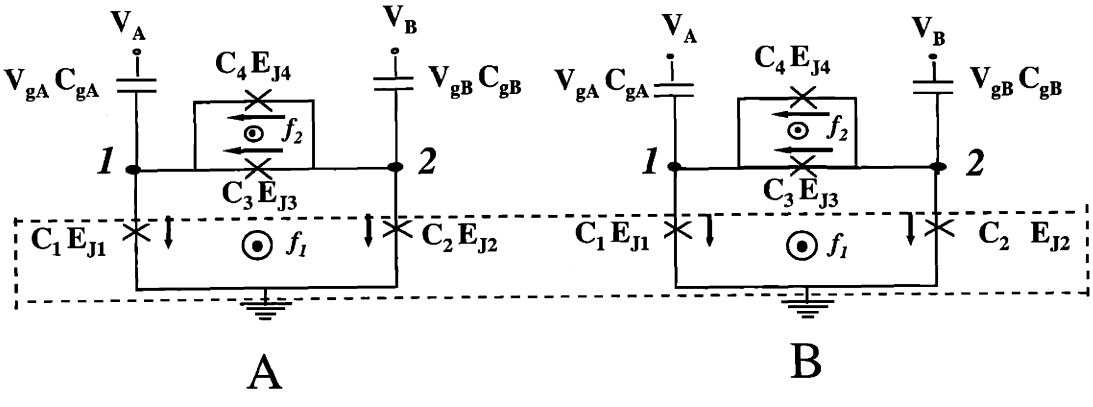

(a)

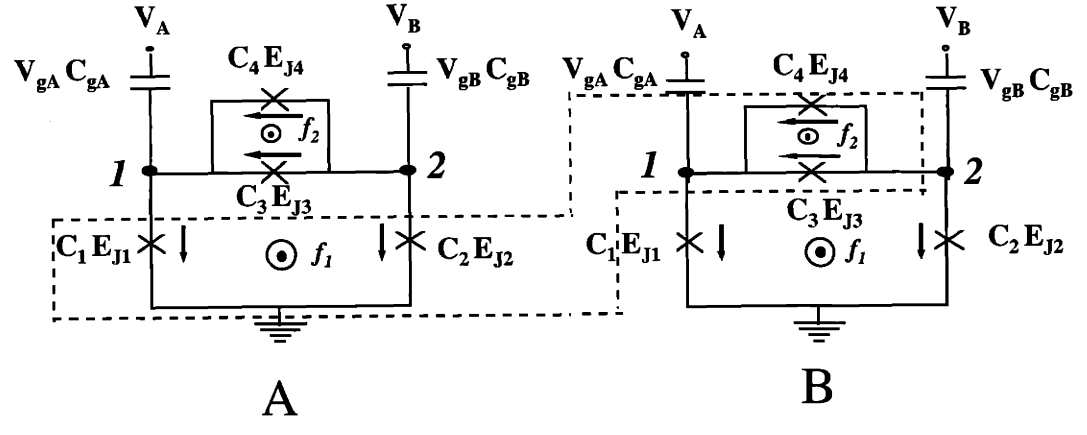

(b)

Figure 2-7: Coupling of qubits A and B through the mutual inductance between (a) the lower regions of both, and (b) the lower region of A and the upper region of B.

two lower rings only through the mutual inductive coupling. (We ignore the the self-inductance which can easily be included.) The effective frustration in the lower loop of A, $\tilde{f}_1^A$, is changed over the applied frustration f_1^A to $\tilde{f}_1^A = f_1^A + MI_1^B/\Phi_o$. Here the current in the lower loop of B is I_1^B. Similarly, $\tilde{f}_1^B = f_1^B + MI_1^A/\Phi_o$. The coupled Hamiltonian is

$$H_{AB} = H^A(\tilde{f}_1^A) + H^B(\tilde{f}_1^B) + MI_1^A I_1^B \tag{2.37}$$

which is the sum of the Hamiltonians for each system plus a term due to the mutual inductive coupling.

The inductively coupled contribution to the frustration is estimated to be of the order of $10^{-3}\Phi_o$ which is much smaller than the applied frustration. Since each persistent current will inductively couple into the other qubit, this will produce changes in the Hamiltonian of the σ_z and σ_x type and these changes will be proportional to the sign of the circulating currents in the qubit. Hence, we expect the coupling to be described by an interaction Hamiltonian of the form,

$$H_{AB}^{\text{int}} = \kappa_1\, \sigma_z^A \sigma_z^B + \kappa_2 \sigma_z^A \sigma_x^B + +\kappa_3 \sigma_x^A \sigma_z^B \tag{2.38}$$

Hence we see that this interaction has both $\sigma_z^A\sigma_z^B$ and $\sigma_z^A\sigma_x^B$ types of coupling. We have an estimated magnitude of $\kappa_i \approx 0.01 E_J$.

As Eqn. 2.36 shows, the inductive coupling between the qubits can be made to be a substantial fraction of the qubit Larmor frequency. This is an attractive feature, as the coupling between two qubits sets the speed limit for how rapidly two qubit quantum logic operations can be performed in principle. In practice, it may be desirable to sacrifice speed of operation for enhanced accuracy: in this case, the inductive coupling could be designed to be smaller by decreasing the overlap of the inductive loops with the circuits.

Coupling between qubits is similar to the coupling we envision between the qubit and the measurement circuits containing SQUID-like detectors. In its usual configuration, the SQUID is biased in the voltage state which produces a voltage related to the flux through its detector loop. However, such a strong, continuous measurement

on a qubit would destroy the superposition of states in the qubit and project out only one of the states. This problem can be circumvented by designing a SQUID such that it is current biased in the superconducting state and hence is not measuring the flux in its detector loop. When one needs to measure the qubit, the SQUID can be switched to its voltage state, for example, by applying a pulse of bias. The coupling from mutual inductance between the SQUID and the qubit will also have to be controlled. Other measurement schemes using SQUIDs which are weakly coupled to the macroscopically coherent system have been proposed [80, 81, 82].

Detailed discussion on how to calculate the energy states of the interacting two qubit system is presented in Appendix C.

2.4 Computing with A PC-Qubit

All the ingredients for quantum computation are now available. We have qubits that can be addressed, manipulated, coupled to each other, and read out (chapter 3). As will be indicated later in this thesis (chapter 4, 5), the particular qubits that we have chosen are well insulated from their environment as well. The flexibility of design for collections of qubits now allows a wide variety of overall designs for quantum computers constructed from such qubits. In this section, we will illustrate the implementation of several simple quantum logic elements, including single qubit rotation and a two-qubit CNOT gate. Then we will introduce the computation with a linear chain of qubits and a network of quantum bits.

Before discussing various superconducting quantum computer architectures, let us review some basic ideas about quantum logic and see how to implement quantum logic using our superconducting qubits. A quantum logic gate is a unitary operation on one or more qubits. Quantum computations are typically accomplished by building up quantum logic circuits out of many quantum logic gates. Just as in the case of classical computers, certain sets of quantum logic gates are universal in the sense that any quantum computation can be performed by wiring together members of the set. In fact, almost any interaction between two or more qubits is universal [77, 79]; but a

convenient universal set of quantum logic gates widely used in the design of quantum algorithms consists of single qubit rotations and the quantum controlled-NOT gate, or CNOT [78].

2.4.1 One-Qubit Rotation

An arbitrary one qubit rotation can be written as $e^{-i\sigma t} = \cos t - i \sin t\, \sigma$ for some Pauli matrix $\sigma = a\sigma_x + b\sigma_y + c\sigma_z$, where $a^2 + b^2 + c^2 = 1$. There are many ways of accomplishing a one qubit rotation: the ability to rotate the qubit by a precise amount around any two orthogonal axes suffices. Pursuing the analog with NMR, we choose a method that involves applying an oscillatory field applied at the qubit's resonant frequency to rotate the qubit.

The Hamiltonian for a single qubit (A) can be gotten from Eqn. 2.36. Here we assume $E_J = 200\,\mathrm{GHz}$, $\delta_1 = 0.001 \cos \omega t$ and $\delta_2 = 0$, and the level splitting is $\omega = 10\,\mathrm{GHz}$. Then, the Hamiltonian is

$$H_D(\mathrm{GHz}) = 5\,\sigma_z + 0.80\,(\cos \omega t)\,\sigma_z - 0.09\,(\cos \omega t)\,\sigma_x \tag{2.39}$$

The Rabi frequency is $90\,MHz$ so that the duration of a π pulse would be about 20 nsec.

2.4.2 Two-Qubit Controlled NOT

A controlled NOT is a two qubit quantum logic gate that flips the value of the second qubit if and only if the value of the first qubit is 1. That is, it takes: $|00\rangle \rightarrow |00\rangle$, $|01\rangle \rightarrow |01\rangle$, $|10\rangle \rightarrow |11\rangle$, and $|11\rangle \rightarrow |10\rangle$. A controlled NOT can be combined with single qubit rotations to give arbitrary quantum logic operations. A controlled NOT can be straightforwardly implemented in the superconducting qubit system by exploiting the analogy with NMR. Suppose that two qubits A and B have been constructed with an inductive coupling between their lower loops as in the first part of the previous section. Then the level splitting of qubit B depends on the state of qubit A, with values $\Delta E_{A,0}$ for A in the $|0>$ state and $\Delta E_{A,1}$ for A in the $|1>$

state. When a resonant pulse corresponding of $\Delta E_{A,1}/\hbar$ is applied to qubit B, it will only change if qubit A is in its $|1>$ state. Since the coupling between the qubits is considerably larger than the Rabi frequency, the amount of time that it takes to perform the controlled NOT operation is equal to the amount of time it takes to perform a π rotation of a single qubit.

So the basic quantum logic operations can be performed on our superconducting qubits in a straightforward fashion. Accordingly, it is possible in principle to wire groups of qubits together to construct a quantum computer. A variety of architectures for quantum computers exist, usually consisting of regular arrays of quantum systems that can be made to interact either with their neighbors or with a quantum "bus" such as a cavity photon field or a phonon field in an ion trap that communicates equally with all the systems in the array. Because of the flexibility inherent in laying out the integrated Josephson junction circuit, a wide variety of architectures are possible. A particularly simple architecture for a quantum computer can be based on the proposal of Lloyd[5] for arrays of quantum systems such as spins or quantum dots.

2.4.3 Linear Chain of Qubits

Consider a linear array of qubits $ABABABAB\ldots$. Let the bottom of each qubit be inductively coupled to the top of the neighbor to the left. Also let each type of qubit, A and B, have a slightly different Josephson energy. Each qubit also has the area of the top loop which is half that of the bottom loop. In the absence of the driving electromagnetic fluxes (the δ_i^j), the Hamiltonian for the system can be generalized to be written as

$$H = -\hbar \sum_k \left(\omega_k \sigma_k^z + 2J_{k,k+1} \sigma_k^z \sigma_{k+1}^z \right) \tag{2.40}$$

where $\hbar\omega_k = \sqrt{F_k^2 + t_k^2}$ and $J_{k,k+1} = \kappa_{k,k+1}(r_{1,k} + r_{1,k+1})/2$. This problem then maps on the linear chain of nuclear spins which was shown by Lloyd to be a universal quantum computer. The coupling needed to perform $\pi/2$ pulses is provided by the terms containing the δ_i^j's. The nice feature of this linear chain is that separate control lines for AC fields are not needed. The whole linear array can sit in a microwave cavity

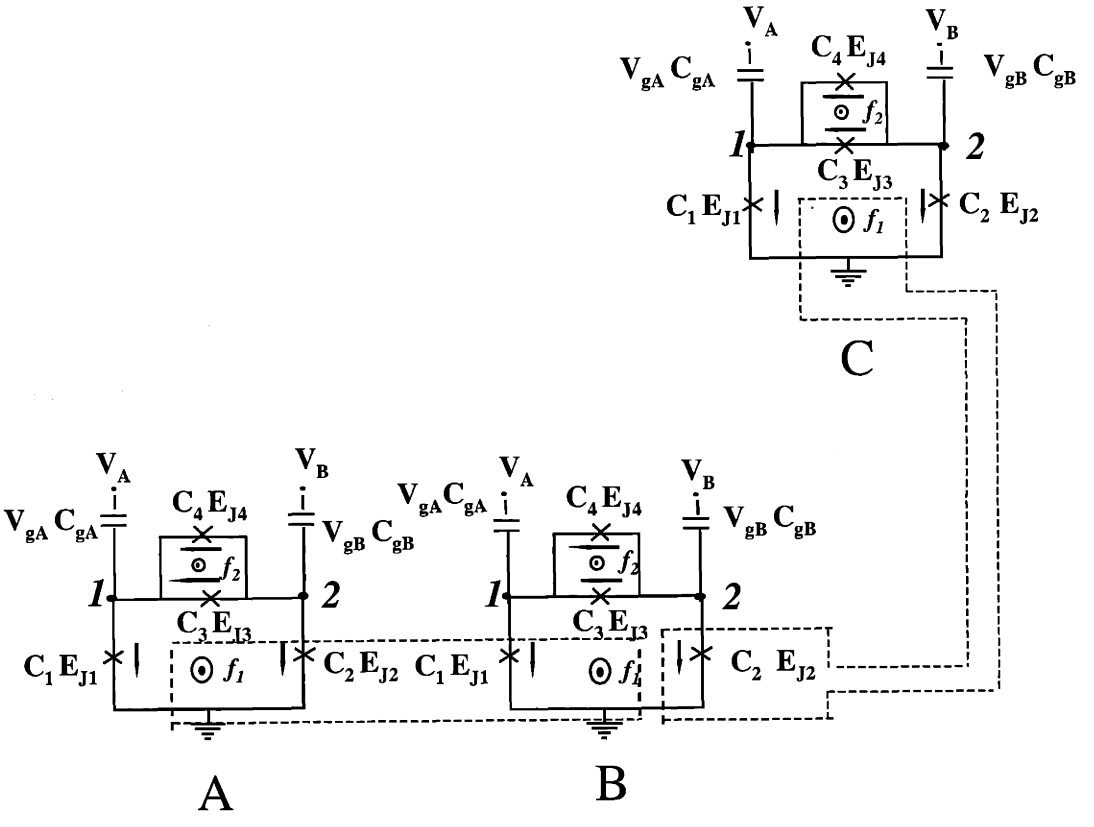

Figure 2-8: A method for coupling a single qubit to other qubits.

and be pulsed at the desired frequency. (The dc bias fields to ensure $f_1 = f_2 = 1/3$ will require at least two dc control lines). The frequencies needed are around 10—25 GHz with intervals of 1 GHz (and with a resolution of about 0.1 GHz). We could make these numbers larger or smaller if needed.

Details of computing with this are given in various references, see for examples Ref. [83] and Chapter 20 of Ref. [84].

2.4.4 Superconducting Quantum Integrated Circuits

There is no reason why the inductive loops cannot couple qubits that are far apart. In addition, a single qubit can be coupled to several other qubits as shown in Fig. 2-8. This arrangement requires separate AC control lines for each of the qubits, which

then demands localized on-chip oscillators. One can build up essentially arbitrary integrated circuits of superconducting qubits by this method. This flexibility in the construction of quantum computer architectures is one of the benefits of using superconducting Josephson junction circuits to perform quantum computation. The quantum integrated circuit could be set up to provide a number of useful features. For example [85], one might be able to design the circuit and interactions in such a way that it automatically implements an intrinsically fault-tolerant quantum computer architecture such as those proposed by Kitaev[86] and Preskill[87]. In addition, since the circuits are parallelizable in that different quantum logic operations can be performed in different places simultaneously, the circuit could be designed to provide the maximum possible parallelization of a particular problem such as factoring[1], database search[2, 3], or computing a discrete quantum Fourier transform[1, 88].

2.5 Decoherence

We have shown how superconducting circuits can be used to construct qubits and quantum logic circuits. These superconducting qubits have been idealized in the sense that we have ignored the effects of manufacturing variability, noise and decoherence. Manufacturing variability can be compensated for as discussed above: before performing any quantum computations, the properties of individual qubits can be measured, recorded in a look-up table in a conventional computer, and used either to supply compensating calibration fields or to alter the frequencies with which control pulses are supplied to the qubits.

The sources of decoherence can be divided into categories: the fluctuations of the environment and the coherent error during gate operation, interaction with other qubits, and leakage to other energy levels. The error can be probabilistic, continuous and discrete. It can be shown that the evolution of the density matrix of the qubit can be described by an operator method where possible qubit errors can be completely described by $n \times n$ Hermitian operators as $\epsilon(\rho_0)(t) = \sum_1^{n^2} E_i \rho E_i^\dagger$, n being the dimension of the quantum system, and $E_i, i = 1 \cdots n$ are the error operators. As

a result, even continuous error on the 2-level qubit can be described by the discrete Pauli operators. The qubit error then includes the phase flip error which adds a -1 to the phase of state $|1\rangle$, the state flip error which flips the state $|0\rangle$ to $|1\rangle$ and vice versa, and the combination of these two errors.

From the point of view of the ultimate performance of a superconducting computer, a more pressing issue is that of environmentally induced noise and decoherence. In real systems the performance of a qubit will be limited by dissipative mechanisms which cause the quantum state to decohere in time τ_d. The 'quality factor' for a qubit is the decoherence time divided by the amount of time it takes to perform fundamental quantum logic operations[7]. The quality factor gives the number of quantum logic operations that can be performed before the computation decoheres, and should be 10^4 or greater for the quantum computer to be able to perform arbitrarily long quantum computations by the use of error-correction techniques[89, 90, 91, 92, 93].

Decoherence can be due to "internal" dissipation (quasiparticle resistance), or coupling to an environmental degree of freedom. It is also possible to couple to an environmental degree of freedom, without a dissipative mechanism, that will still lead to decoherence[94]

We will now discuss some of the major sources of decoherence.

Normal state quasi-particles can cause dissipation and energy relaxation at finite temperatures in Josephson junctions. However, mesoscopic aluminum junctions have been shown to have the BCS temperature dependence for the density of quasiparticles. At low temperatures this density is exponentially small[81], so quasi-particle tunneling will be strongly suppressed at low temperatures and at low voltages, as was seen in a system with multiple superconducting islands in Ref. [95]. We estimate a lower bound of 10^4 for the quality factor, given a sub-gap resistance of $10^{10}\,\Omega$[81].

The qubit can also decohere by emitting photons. We estimate this by classically estimating the rate photons are emitted by magnetic dipole radiation from oscillating current in the loop defining the qubit. For a loop with radius R with an alternating current of frequency ν and rms amplitude of I_m, the power transmitted to free space is $P_m = K_m R^4 I_m^2 \nu^4$ where $K_m = 8\mu_o\pi^5/3c^3$. A typical rate for pho-

ton emission is $1/t_m = P_m/h\nu$, which gives an estimate of the decoherence time of $t_m = h/K_m R^4 I_m^2 \nu^3$. An estimate for the frequency is the Larmor frequency, (other characteristic frequencies such as the Rabi frequency are even smaller). For our qubit $R \approx 1\,\mu$m, $\nu \approx 10\,$GHz and $I_m = 1\,$nA, we find that $t_m \sim 10^7\,$s, so that this is not a serious source of decoherence. However, it should be noted that proposals for using RF SQUIDs for qubits, involve currents of the order of $1\,\mu$A and and loops of the order of $10\,\mu$m. These RF SQUIDs have $t_m \approx 10^{-3}\,$sec, which is substantially lower than for our qubits which can be made much smaller and have much less current. However, by making the rf SQUID loop in a gradiometer geometry, the dipolar radiation can be greatly reduced[28].

Inhomogeneity in the magnetic flux distribution can also be a source of decoherence. This is similar to T_2 in NMR systems. We estimate this for our system by calculating the amount of flux a $1\,\mu\text{m} \times 1\,\mu$m wire carrying 100 nA of current induces in a loop of the same size which has its center $3\,\mu$m away. We find that the induced frustration is about $\delta f = 10^{-7}$. If this is taken as an estimate of the typical variance of the frustration that different qubits experience, then there will be a spread of operating frequencies among the loops. An estimate of t_d is the time for the extremes of this frequency to differ by π. This results in $t_d \approx \pi/(2r_1\delta f)$, where we have taken the larger value from Eqn. 2.36. With $r_1/\hbar \approx 600\,$GHz, we find $t_d \approx 1.5\,$msec. The dipole-dipole interaction between qubits gives a time of the same order.

We have also estimated the magnetic coupling between the dipole moment of the current loops and the magnetic moments of the aluminum nuclei in the wire. At low temperatures where the quasi-particles are frozen out, the decoherence time for a single qubit is of the order of T_1 which is exponentially large in the low-temperature superconducting state. For an ensemble of qubits, the decoherence time may be of the order of milliseconds due to the different configurations of nuclear spins in the different qubits. However, this effect may be reduced by aligning the spins or by applying compensating pulse sequences.

Coupling to Ohmic dissipation in the environment has been modeled for superconducting qubits operating in the charging regime[22]. These authors found that the

source of decoherence could be made sufficiently small such that the quality factor is large enough. Similar calculations for qubits in the superconducting regime of circulating currents have not yet been done. Experiments to measure this decoherence time in our circuits are underway. In practice, electromagnetic coupling to the normal state ground plane can limit coherence[56]; however, a superconducting ground plane can greatly reduce this coupling.

Other possible sources of decoherence are the effects of the measuring circuit, the arrangement and stability of the control lines for the magnetic fields, the ac dielectric losses in the substrate at microwave frequencies. These and other source of decoherence will have to be estimated in a real circuit environment and measured.

Taking 0.1 msec as a lower bound on the decoherence time and 10 nsec as a switching time, we find that the quality factor is of the order of 10^4. Furthermore, if the proper set of topological excitations is used to store information, the decoherence time for quantum computation can be made substantially longer than the minimum decoherence time for an individual junction circuit[86].

2.6 Summary

In this chapter we have discussed a superconducting qubit which has circulating currents of opposite sign as its two logic states. The circuit consist of three nano-scale Josephson junctions connected in a superconducting loop and controlled by magnetic fields. One of the three junctions is a variable junction made as a SQUID loop. This qubit has quantum states which are analogous to a particle with an anisotropic mass moving in a two-dimensional periodic potential. The Josephson junctions have much larger Josephson energy E_J than the charging energy E_c $E_J \gg E_c$, so that the qubit states are close to localized flux states. The circuit is intrinsically insensitive to background charge fluctuations which is a serious problem in the Single-Cooper-Pair-Box qubit (SCPB). This insensitivity comes from the almost zero tunneling between the local minima in different unit cells of the potential energy.

We numerically calculated the energy band structure for this circuit versus the

external flux in the superconducting loop. The numerical result gives a convenient way to derive the tunneling between the local flux states and can be compared with that from the WKB calculation. We also numerically calculated the transition matrix elements between the qubit states when microwave radiation is applied. The result shows a Rabi oscillation frequency of 100 MHz when the applied radiation amplitude is about 0.001 flux quantum. We studied the inductively coupled qubits by a mean-field method (see Appendix C). In this simulation, the interaction operator from one qubit to the other is substituted by the average of the corresponding operators, and the qubit states under this average are calculated. Then, the calculated results are substituted to the next round of the iteration. Eventually the calculation converges.

We have applied the properties of the pc-qubit to implementing basic quantum logic gates including single qubit rotation, a two-qubit CNOT gate, a one-dimensional qubit chain, and qubit networks. Simply by applying microwave radiation to a qubit, all these computations can be realized. These simple logic operations are the building blocks of large scale quantum computing, and are a sufficient set of gates for universal quantum computing.

In this chapter, we also briefly mentioned the readout of the qubit and the decoherence of the qubit. As was shown the readout can be simply achieved by a magnetometer. In Chapter 3, we will study the measurement process in detail, including the interaction between the qubit and the detector, the noise related to the measurement process and the built-in limit to the measurement efficiency. We mentioned the major sources of qubit errors in this chapter. The decoherence by environmental noise will be discussed further in Chapter 4 and quantum control on gate error will be discussed in chapter 5.

Chapter 3

Measurement of the PC-Qubit

Measurement is a crucial step in quantum information processing. In the first experiments on the superconducting persistent-current qubit (pc-qubit), a dc SQUID magnetometer was used to detect the flux of the qubit and the switching current histogram of the SQUID was analyzed to obtain information about the qubit state. In this chapter, we study this measurement procedure in detail by modeling the dc SQUID as two interacting harmonic oscillators during the premeasurement entanglement process. Two questions are answered regarding this study: (1). the spectrum of the noise propagated to the qubit from the environment of the dc SQUID; (2). the limitation on measurement efficiency in this qubit-magnetometer setup. We also calculate the tunneling rate of the metastable SQUID state from the washboard potential and compare the theoretical histogram with the experiment.

In this chapter we study the pc-qubit measured by a dc SQUID. Both the information obtained during the measurement and the noise transferred to the qubit during the measurement are calculated. The decoherence and relaxation of the qubit are then estimated with the calculated noise spectrum. In section 3.1, we study the interacting system of the qubit and the SQUID in detail and derive the static response of the SQUID to the qubit. Then, we analyze the measurement process for this qubit-SQUID system in section 3.2 and derive an upper bound to the mutual information that could be achieved during one measurement. In section 3.3, we apply the Caldeira-Leggett formalism to calculate the spectrum of the noise transferred to

the qubit from the SQUID's environment by mapping the qubit-SQUID Hamiltonian to a linear circuit. Relaxation and decoherence rates due to this transferred noise are then estimated in terms of the noise spectral density in section 3.4. In section 3.5, the switching current histogram is calculated by taking the quantum fluctuation into account. To improve measurement efficiency, a coherent transition assisted measurement is designed in section 3.6. Finally, conclusions are given in section 3.7.

3.1 Qubit-SQUID interaction Hamiltonian

The superconducting persistent-current qubit (pc-qubit) is a solid-state Josephson junction device that stores quantum information on circulating currents[20, 25]. pc-qubits have been successfully fabricated and measured[29]. These measurements are not only the first steps in realizing solid state quantum computers, but also invoke fundamental studies on verifying quantum mechanics at macroscopic scales[26, 28]. In the experiments the SQUID interacts with the qubit and influences the qubit's dynamics. To interpret experimental data correctly, we need to study the interaction between the qubit and the detector carefully to analyze the influence of the detector on the qubit, and to extract from the measured data the features that are due to the qubit's behavior.

3.1.1 Circuit

The superconducting persistent-current qubit[20, 25] is a single superconducting loop that has three Josephson junctions in series as is studied in the previous chapter. One junction has a slightly different critical current from that of the others. A magnetic flux $f_q\Phi_0$ is applied in the loop, where Φ_0 is the flux quantum. At f_q near 1/2, the lowest two energy levels of this quantum system are nearly localized flux states with opposite circulating currents, and are chosen as the qubit states. The two qubit states are analogous to spin states and can be described by $SU(2)$ algebra of the Pauli matrices. By identifying the localized flux states as eigenstates of σ_z, the qubit Hamiltonian is $\mathcal{H}_q = \frac{\epsilon_0}{2}\sigma_z + \frac{t_0}{2}\sigma_x$, where $\epsilon_0 \propto (f_q - 1/2)$ is controlled by flux f_q in

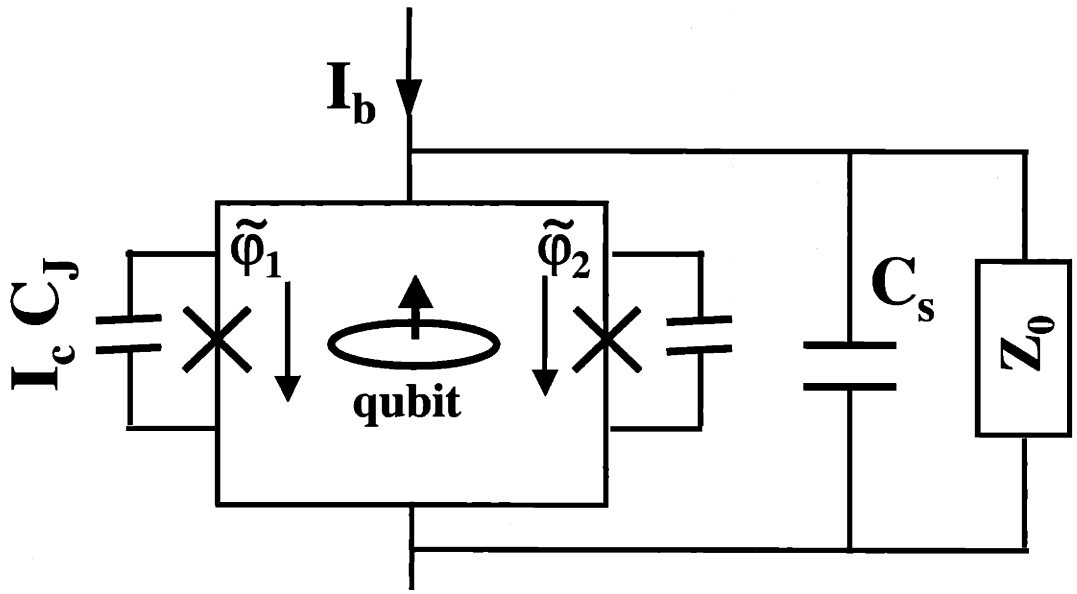

Figure 3-1: Persistent-current qubit measured by a dc SQUID. The qubit is in the SQUID loop. I_c is the critical current of the Josephson junctions in the SQUID; C_J is the junction capacitances. $\tilde{\varphi}_1$ and $\tilde{\varphi}_2$ are the gauge invariant phases of the junctions with their directions indicated by an arrow beside the junction. The SQUID is shunted by a capacitance C_s. Z_0 is the environment of the dc SQUID. The SQUID is biased by ramping the current I_b.

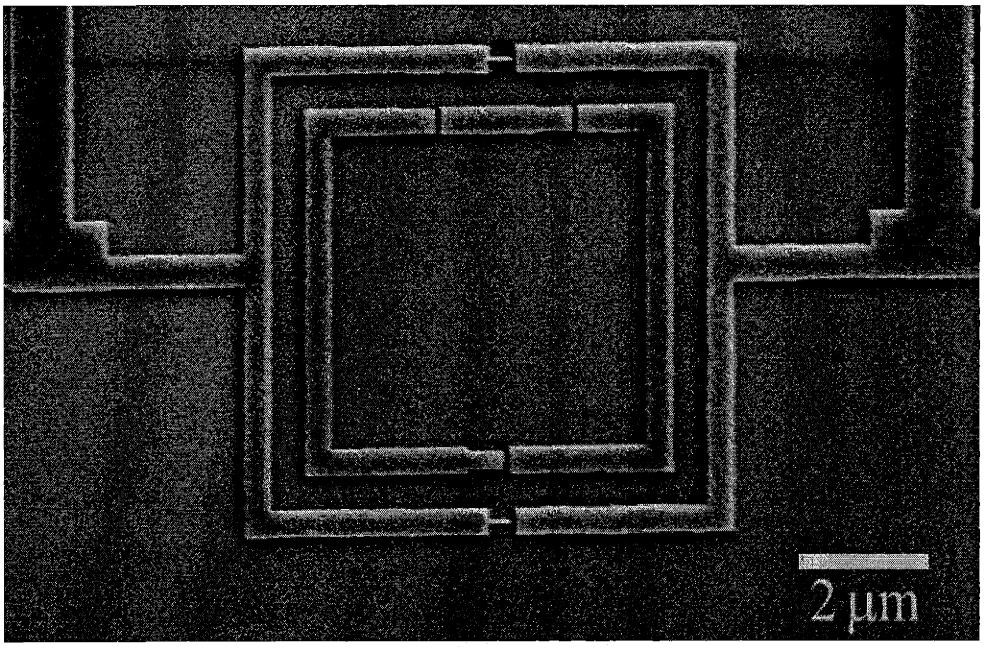

Figure 3-2: The STM image of the fabricated sample of the pc-qubit inside a dc SQUID. The inner loop is the pc-qubit with three Josephson junctions. The external loop is the under-damped dc SQUID with two Josephson junctions. Current can be ramped into the dc SQUID via the leads connected with the SQUID.[29]

the qubit loop and t_0 is the tunneling between the two localized flux states. Typical parameters are $\epsilon_0 = 10\,\text{GHz}$ at $f = 0.495$ and $t_0 = 1\,\text{GHz}$.

The qubit state can be measured by inductively coupling the qubit to a dc SQUID[29] as shown in Fig. 3-1. The flux of the qubit shifts the flux in the SQUID loop, and hence the effective critical current of the SQUID. During measurement, a bias current I_b is ramped through the SQUID; and the switching current, where the SQUID switches to a finite voltage state, is measured. Due to quantum fluctuations and thermal activation, the SQUID switches before the critical current and has a finite distribution. The average switching current shifts with the effective critical current and reflects the probability of the two qubit states. In practice, a large capacitance shunts the SQUID to suppress fluctuations and reduce the width of switching current

distribution.

The sample of the superconducting pc-qubit being measured by a dc SQUID has been fabricated and tested in the Delft group. Fig.3-2 is the STM image of the fabricated sample, and Fig.3-3 is the current verses voltage character of the dc SQUID.

3.1.2 Hamiltonian

When taking into account the self inductance, the SQUID has two independent variables: the inner variable phase $\tilde{\varphi}_m$ that represents the circulating current of the SQUID loop; and the external variable phase $\tilde{\varphi}_p$ that represents a quantum particle in a washboard potential that is tilted by ramping current I_b. The external variable is in a metastable state when the potential is tilted by I_b. A detailed study on the quantization of SQUID's Hamiltonian can be found in [98]. Here we only consider the case when the two junctions are symmetric.

After linearizing the potential energy near the energy minimum, the SQUID variables behave as harmonic oscillators interacting with each other. We have the following approximate Hamiltonian for the qubit-SQUID system:

$$\mathcal{H}_t = \mathcal{H}_q + \frac{\mathrm{P}_m^2}{2m_m} + \frac{1}{2}m_m\omega_m^2(\varphi_m + \delta\varphi_0\sigma_z)^2 + \frac{\mathrm{P}_p^2}{2m_p} + \frac{1}{2}m_p\omega_p^2\varphi_p^2 + J_1\varphi_m\varphi_p \qquad (3.1)$$

where $\mathcal{H}_q$ is the qubit Hamiltonian. The phases $\varphi_m = \tilde{\varphi}_m - \tilde{\varphi}_m^0$ and $\varphi_p = \tilde{\varphi}_p - \tilde{\varphi}_p^0$ are the oscillator coordinates relative to the energy minimum $(\tilde{\varphi}_m^0, \tilde{\varphi}_p^0)$. P_m, P_p are the momenta of the inner and the external oscillators, and are conjugate operators of the corresponding phases. The oscillator masses are $m_m = 2C_J(\frac{\Phi_0}{2\pi})^2$ and $m_p = (\frac{\Phi_0}{2\pi})^2(C_s + 2C_J)$, where C_J is the capacitance of the junctions and C_s is the shunt capacitance as shown in Fig. 3-1. The inner oscillator frequency ω_m depends on the self inductance of the SQUID L_{dc} and the critical current of the junctions I_c as $\omega_m = \sqrt{2/L_{dc}C_J}$. In the experiment, the self inductance of the SQUID is weak with $\beta_L = 2\pi L_{dc}I_c/\Phi_0 = 0.004$. Hence $\omega_m \approx 10^3$ GHz is higher than all the other relevant

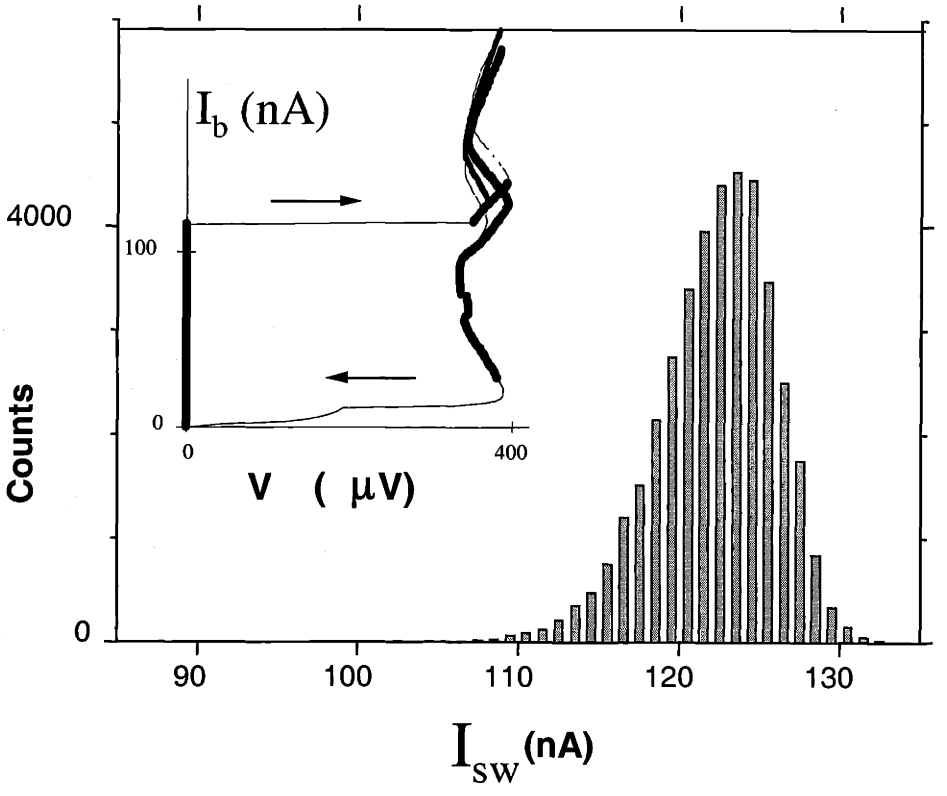

Figure 3-3: Main figure: the distribution of the switching current I_{sw}; Inset: the I-V character of the dc SQUID. The left arrow and the right arrow in the inset indicate the switching directions of the SQUID state for increasing current and decreasing current, respectively. The wigglings about the critical current on the I-V character are possibly due to nonlinearity of the circuit and don't have a definite theoretical explanation yet.

energies in the qubit-SQUID system. As a result, the inner oscillator is slaved to the qubit and follows the qubit's dynamics even during qubit operation. The external oscillator frequency depends on the ramping current as $\omega_p = \omega_p^0 [1 - (\frac{I_b}{I_c^{eff}})^2]^{1/4}$ where $\omega_p^0 = \sqrt{2\pi I_c^{eff}/C_s\Phi_0}$ is the oscillator frequency at zero current and I_c^{eff} is the effective critical current of the SQUID under external flux. The inner oscillator offset $\pm\delta\varphi_0\sigma_z$ originates from the inductive interaction between the qubit and the SQUID with $\delta\varphi_0 = \pi M_q I_{cir}/\Phi_0$, where I_{cir} is the circulating current of the localized states of the qubit and M_q is the mutual inductance. The J_1 term is the bilinear coupling between φ_m and φ_p at the potential energy minimum and is determined by the ramping current I_b. We have $J_1 = |\tan\tilde{\varphi}_m^0| I_b\Phi_0/2\pi$. When the ramping current is turned off, J_1 coupling disappears, and φ_m and φ_p interact via a higher order term $\varphi_m\varphi_p^2$ which brings negligible entanglement with the qubit state. Typical numbers for the SQUID are: $E_J^{dc} = 40\,\text{GHz}$ with $I_c^{dc} = 80\,\text{nA}$, $C_J = 2\,\text{fF}$, $C_s = 5\,\text{pF}$, $L_{dc} = 16\,\text{pH}$ and $M_q = 8\,\text{pH}$. And $\delta\varphi_0 \approx 0.002$; $\omega_p^0 = 1.3\,\text{GHz}$ and $\omega_p = 1.0\,\text{GHz}$ at $I_b = 0.8 I_c^{eff}$.

This linear model omits the escape of the particle from the washboard potential which becomes stronger as I_b increases. As we mainly use this model to discuss the decoherence and relaxation of the qubit by the SQUID's environment during the "pre-escape" entanglement process, this model is valid as far as ω_p is much smaller than the energy barrier (which is true until $I_b \approx 0.95$). We want to point out that the escape from the washboard potential, which is a crucial step in this measurement and will be discussed in the next section, is not included in this model.

When the qubit stays in an eigenstate of σ_z, the response of the SQUID can be derived by a perturbation approach. Assuming the qubit in state $|\uparrow\rangle$ and taking the J_1 term as a perturbation, the unperturbed eigenstates are: $|\uparrow, n_m^{\uparrow}, n_p\rangle$, where $|n_p\rangle$ are the external oscillator's number states, $|n_m^{\uparrow}\rangle = e^{\delta\varphi_0 \frac{\partial}{\partial\varphi_m}} |n_m\rangle$ are the inner oscillator's number states shifted by $\delta\varphi_0$ by interacting with the qubit. The perturbed ground state of the qubit-SQUID system is:

$$|\psi_g^{\uparrow}\rangle = |\uparrow, 0_m^{\uparrow}, 0_p\rangle - \frac{J_1\delta\varphi_0 x_p}{\hbar\omega_p}|\uparrow, 0_m^{\uparrow}, 1_p\rangle - \frac{J_1 x_m x_p}{\hbar\omega_m}|\uparrow, 1_m^{\uparrow}, 1_p\rangle \qquad (3.2)$$

where $x_m = \sqrt{\frac{\hbar}{2m_m\omega_m}}$ and $x_p = \sqrt{\frac{\hbar}{2m_p\omega_p}}$ are the widths of the ground state wave functions. The state includes contributions from $|1_p\rangle$. Hence, the average of φ_p increases linearly with I_b as: $\langle\varphi_p\rangle_0 = L_J J_1(\frac{2\pi}{\Phi_0})^2\delta\varphi_0$, where $L_J = (C_s\omega_p^2)^{-1}$ is the dynamic inductance of the external oscillator. When the ramping current is off, $\varphi_p = 0$, the external oscillator responds negligibly to the inner oscillator and is effectively decoupled from the inner oscillator. When the ramping current is on, the external oscillator becomes entangled with the inner oscillator. Given the parameters from the experiment and at $I_b = 0.8I_c^{eff}$, we get $\langle\varphi_p\rangle_0 \approx 0.002$.

Compared with the Stern-Gerlach experiment, the qubit-inner oscillator system acts as the spin of a particle passing through the gradient field. The external oscillator acts as the spatial degree of freedom of this particle. As the particle passes the field, the spatial wave function of the particle becomes separated for the two spin states; by recording the spatial distribution, the probability of different spin states can be obtained. In the SQUID, as the ramping current increases, the states of the external oscillator become separated in its coordinate space in correlation with the two qubit states; by detecting the switching current of the SQUID, the qubit state is detected.

3.2 Limits to Measurement Optimization

In the above measurement, the same measurement needs to be repeated many times to obtain a satisfactory switching current histogram that can resolve the two qubit states. It is thus crucial to analyze the limit to the mutual information gained in the measurement. This will help the design of optimized experiments to approach this limit within the flux-measuring configuration of qubit-SQUID coupling.

3.2.1 Efficiency of the experiment

In the experiment, the qubit interacts with the SQUID's inner oscillator via mutual inductance all the time and the flux of the qubit is detected by the inner oscillator even when the measurement is not on; while the switching current histogram is the directly observed physical quantity. We can divide the qubit-SQUID system into two

parts: the measured system that includes the qubit and the inner oscillator of the SQUID; and the "meter" that is the external oscillator of the SQUID. The current ramping process entangles the system with the meter. When the SQUID switches, the meter variable escapes from the supercurrent state to the finite voltage state, and a macroscopically distinguishable record is obtained; in this process, the coherence of the system is completely destroyed by quasiparticle excitations at gap voltage.

The histogram of the switching current is affected by many factors: the critical current of the SQUID, fluctuations, and the time dependence of the ramping current *etc.* Flux in the SQUID loop changes by $\pm\delta\varphi_0$ due to the qubit states; as a result, the effective critical current I_c^{eff} is shifted by $\Delta I_c = \pm I_c^{eff}\delta\varphi_0|\tan\tilde{\varphi}_m^0| \simeq \pm 10^{-3} I_c^{eff}$ respectively, which results in a shift of the same order in the histogram. Due to strong quantum fluctuations and thermal activation, this shift is much smaller than the width of the histogram [99], and hence the switching current in any given measurement is not perfectly correlated with the state of the qubit. In other words the measurement is not strictly speaking a von Neumann measurement, but rather a more general positive operator valued measurement (POVM)[100].

The probability for the SQUID to switch at current I_b and qubit state $|s\rangle$ is $P(I_b|s) = tr(\hat{A}_{I_b}|\phi_s\rangle\langle\phi_s|)$, where $\hat{A}_{I_b}$ is the positive operator in the POVM corresponding to the result I_b and $|\phi_s\rangle$ is the SQUID state when the qubit state is $|s\rangle$. Assuming a qubit state of $\alpha|\uparrow\rangle + \beta|\downarrow\rangle$, the density matrix of the SQUID is $\rho_{sq} = |\alpha|^2|\phi_\uparrow\rangle\langle\phi_\uparrow| + |\beta|^2|\phi_\downarrow\rangle\langle\phi_\downarrow|$. The probability that the SQUID switches at I_b is $P(I_b) = tr(\hat{A}_{I_b}\rho_{sq}) = |\alpha|^2 P(I_b|\uparrow) + |\beta|^2 P(I_b|\downarrow)$. By the Bayesian theorem, we can derive the conditional probability of the qubit state when switching occurs at I_b: $P(\uparrow|I_b) = |\alpha|^2 P(I_b|\uparrow)/P(I_b)$ and $P(\downarrow|I_b) = |\beta|^2 P(I_b|\downarrow)/P(I_b)$. If the histograms for the two qubit states are well separated, given a switching at I_b, one can clearly infer what the qubit state is after the measurement. But when the histograms for the two qubit states are largely overlapped, which is the case in the experiment[29], it is hard to decide the qubit state after switching. The mutual information gained in the measurement is $I_1 = H_1 - H_{sw}$, where $H_1 = -|\alpha|^2\log|\alpha|^2 - |\beta|^2\log|\beta|^2$ is the Shannon entropy for the SQUID and $H_{sw} = -\sum_{I_b} P(I_b)(P(\uparrow|I_b)\log P(\uparrow|I_b) + P(\downarrow|I_b)\log P(\downarrow$

$|I_b\rangle)$ is the ensemble averaged Shannon entropy after the switching event [101]. For $|\alpha|^2 = |\beta|^2 = 1/2$, the mutual information can be estimated to be $I_1 \approx 10^{-4}$ given the experimental parameters[99], which indicates each measurement only provides very limited information and the same measurement has to be repeated many times to resolve the qubit states.

3.2.2 Limit to the efficiency

Now let us look at the best we can achieve for this flux-measuring scheme. The measurement process (ramping the current) is the detection of the inner oscillator states by the external oscillator instead of the direct detection of the qubit state. In other words, the "meter" switches according to the inner oscillator states instead of the qubit state. As a result, with the qubit-SQUID coupling scheme, measurement optimization is limited by how different the inner oscillator states corresponding to the two qubit states are.

The inner oscillator entangles with the qubit even when the ramping current is not on; furthermore, as $\omega_m \gg \omega_0, \omega_p$, the inner oscillator follows the dynamics of the qubit faithfully even during qubit operation. The inner oscillator is slaved by the qubit just as an electron is slaved by the atomic nucleus in a solid. Due to the inductive coupling with the qubit, the inner oscillator states are coherent states $|\alpha\rangle$ and $|-\alpha\rangle$ for the two qubit states respectively, where $|\alpha\rangle = e^{\delta\varphi_0 \frac{\partial}{\partial \varphi_m}} |0_m\rangle$ and $\alpha = \delta\varphi_0/2x_m$. Written explicitly, the coherent state parameter α is determined by the ratio between $\delta\varphi_0 = \pi M_q I_{cir}/\Phi_0$, the coordinate space shift of the oscillator ground state due to coupling with the qubit, and $x_m = \sqrt{\frac{\hbar}{2M_m\omega_m}}$, the width of the ground state wave function. In the experiment, $\delta\varphi_0 \approx 0.002$ and $x_m \approx 0.1$, we have $\alpha \approx 0.01$ and the overlap of the two coherent states is $\langle -\alpha|\alpha\rangle = 1 - 2 \times 10^{-4}$. Hence, the two states are highly non-orthogonal, which means it is very hard to distinguish them with any possible measurement. Let the density matrix of the inner oscillator be $\rho_m = \frac{1}{2}[|\alpha\rangle\langle\alpha| + |-\alpha\rangle\langle-\alpha|]$ with equal probability for the two states. In any measurement to resolve these two states, the mutual information is limited by an upper bound[102]: $I_1 \leq S$, where $S = -tr(\rho_m \log \rho_m)$ is the von Neumann entropy of

ρ_m. When α is given, this entropy can be calculated. At large α, which indicates well separated states, the entropy goes to 1; at $\alpha \approx 0.01$, the entropy is very small with $S \approx 0.0015$. With this analysis, in the qubit-SQUID coupling, the most information we could achieve in one measurement is $I_1 \approx 0.0015$, which is also very limited but one order higher than that in the present experiment.

This analysis indicates that it is possible to improve the measurement by exploring the potential of the SQUID measurement and keeping the same qubit and SQUID parameters as in the present experiments. Meanwhile, by adjusting the qubit or SQUID designs to increase α, better measurement can be expected. Another approach which will be explored in future work is to go beyond the flux-measuring scheme to exploit the orthogonality of the qubit states without measuring the small flux of the qubit.

3.3 Induced Noise During Measurement

Quantum computers store and process information on quantum bits. Any coherent controllable two-state quantum system[5, 7] can register a quantum bit, or "qubit", and qubit has been realized in a wide variety of physical systems[11, 12, 13, 14, 15, 16, 18, 20, 25]. To collect, manipulate or transfer information from a qubit, we need to entangle the qubit to an external quantum system such as a detector, a radiation source or another qubit. The external quantum system acts as an information transmission channel that performs an operation on the qubit state and collects its information. In addition to the intrinsic decoherence of the qubit, this operation transmits noise from the environment of the external system to the qubit and decoheres the qubit. The stronger the interaction between the qubit and the external system is, the more information is obtained by one measurement, and at the same time, the more noisy the qubit will be. Because the external system typically contains macroscopic, non-coherent elements, it is often exposed to strong environmental noise and becomes a crucial noise source for the qubit. This raises the problem of designing optimized quantum circuits that can maximize the signal-to-noise ratio during infor-

mation transmission. In this chapter we will study the information obtained in the measurement of the persistent-current qubit by a dc SQUID and present a method to derive the noise transferred to the qubit from the detector's environment.

During a measurement, the detector entangles with the qubit and collects information from the qubit; it then transfers this information into macroscopic distinguishable states that are recorded. Meanwhile, via the same coupling, the detector transmits noise from the output parts of the circuit, which are usually exposed to stronger environmental noise, to the input parts where the qubit is located. The transferred noise will damage the qubit state when it takes a long time to collect the information. This problem exists in many kinds of qubits. In the pc-qubit experiment, the detector is an underdamped dc SQUID, whose critical current is offset by the flux of the two qubit states towards opposite directions. For the offsets to be large enough to resolve the two qubit states, stronger qubit-SQUID coupling is preferred. But noise from SQUID's environment is transmitted to the qubit by the same inductive coupling; moreover, this noise increases with the square of the coupling strength while the offsets increase linearly with the coupling strength. How to design a reasonable circuit to optimize the measurement is thus an important issue.

A similar situation occurs when an ac radiation source is used to manipulate a qubit. To operate the qubit efficiently, the frequency range of the pass band of the source circuit needs to cover the qubit frequency; but this connection lets noise of the same frequency pass as well, which may induce strong qubit damping and decoherence. Therefore the problem of how to get best design of an external control source is also an important problem to study.

In this section we study the noise that is transmitted to the persistent-current qubit during the measurement by a underdamped dc SQUID. We apply the Caldeira-Leggett formalism to calculate the noise spectral density of the transmitted noise. In this formalism, the environment of the dc SQUID is modeled as a reservoir of bosonic modes with continuous spectral density. The dc SQUID circuit adds two discrete oscillator modes to this reservoir. The combined boson-oscillator system can be mapped to a linear circuit whose impedance determines the noise of the qubit. The mapping

to the circuit can be derived from the qubit-SQUID Hamiltonian straightforwardly. Discussions on a detailed study of the reservoir modes are given in the end together with the conclusions. Note that the study presented here were developed in the course of an ongoing collaboration with the Delft group. In particular, complimentary aspects of the problem were studied by F.K. Wilhelm, M. Grifoni[96], and C.H. van der Wal *et al.*[97]. The decoherence and relaxation of the qubit due to this noise will be studied in the next section following a master equation approach.

3.3.1 Effective environment

Now we investigate the environment of the qubit-SQUID system. In solid-state systems, decoherence warrants serious attention due to the many redundant degrees of freedom that interact with the qubit. Noise from the direct environment of the pc-qubit is presented in chapter IV of this thesis and in [41], and the decoherence time is estimated to be longer than $O(10^{-4})$ sec. However, during the ramping of current I_b, as the qubit and the SQUID become entangled, the noise from the environment of the SQUID affects the qubit via their inductive interaction. In this section, we calculate the spectral density of the noise transferred to the qubit from the environment of the SQUID and derive the decoherence and relaxation due to this noise. For simplicity we only discuss the environment of the external oscillator and neglect the environment of the inner oscillator[103]. Although we work on the example of pc-qubit measured by a SQUID, the framework of our discussion is general and can be applied to an arbitrary external system interacting with a qubit.

We use the Caldeira-Leggett approach for the reservoir where it is modeled as oscillator modes with a continuous spectrum[104]. Localized spin modes[105] can be mapped to oscillator modes when interaction with the reservoir modes is weak. With the reservoir included, we have:

$$\mathcal{H} = \mathcal{H}_t + \sum_\alpha \left[\frac{p_\alpha^2}{2m_\alpha} + \frac{1}{2} m_\alpha \omega_\alpha^2 (x_\alpha + \frac{c_\alpha}{m_\alpha \omega_\alpha^2} \varphi_p)^2 \right] \tag{3.3}$$

where $\mathcal{H}_t$ is the Hamiltonian of the qubit-SQUID system; x_α and p_α are the coordi-

nates and momenta of the reservoir modes. The c_α terms are the bilinear interaction between the external oscillator and its reservoir. The direct influence of the reservoir on the associated quantum system—the external oscillator—can be completely described by the spectral density: $J_0(\omega) = \frac{\pi}{2\hbar}\sum \frac{c_\alpha^2}{m_\alpha \omega_\alpha}\delta(\omega - \omega_\alpha)$.

The reservoir modes $\{x_\alpha\}$ have no direct interaction with the qubit. They affect the qubit via the interaction between the qubit and the SQUID. The qubit sees an effective reservoir which includes both the $\{x_\alpha\}$ modes and finite number of discrete modes from the external system. In this "larger" reservoir, different modes are not independent of each other: namely, modes from the detector interact with the $\{x_\alpha\}$ modes; meanwhile, the discrete modes of the detector interact with the qubit. In the qubit-SQUID system, the SQUID adds two oscillators to this "larger" reservoir. The external oscillator φ_p interacts with the $\{x_\alpha\}$ modes; the inner oscillator φ_m interacts with the external oscillator; and the qubit interacts with this effective reservoir by interacting with φ_m. The noise spectral density for the qubit J_{eff}, according to the standard approach[106, 107, 108], can be derived from the dissipation which is the imaginary part of the generalized susceptibility: $J_{eff}(\omega) = \lim_{\epsilon\to 0}\frac{1}{\hbar} Im[\hat{K}(z)]_{z=\omega-i\epsilon}$, where $\hat{K}(z)$ is the generalized susceptibility of the qubit when taking account of the SQUID.

Instead of calculating the susceptibility $\hat{K}(z)$ directly from the classical equations of motion, the noise can be derived from a simple but general linear circuitry approach which is easily applied to an arbitrary external system to derive the transferred noise. Given the Hamiltonian of a linear quantum system, different energy terms can be mapped to linear circuit elements such as inductances, capacitances, and resistors of a linear network. The classical equations of motion for the interacting system are the circuit equations of this linear circuit by Kirchoff's laws. The noise on any quantum variable can hence be calculated from the effective impedance of this circuit[64]: $J_{eff}^{(0)}(\omega) = \frac{\hbar}{(2e)^2}\omega Re[Y(\omega)]$ at zero temperature; for finite temperature, $J_{eff}^{(T)}(\omega) = J_{eff}^{(0)}(\omega)\coth\frac{\hbar\omega}{2k_BT}$, which is the Johnson-Nyquist noise at high temperature.

3.3.2 Classical equations of motion

First we are going to solve the noise spectrum following the method shown in [108]. We illustrate this method by working out the example of the persistent current qubit[20, 25] measured by a DC-SQUID. With Eq. 3.1 and Eq. 3.3 for the linearized qubit-SQUID-environment Hamiltonian and defining the qubit flux variable $q = \delta\varphi_0\sigma_z$ for the convenience of discussion, the classical equations of motion for the qubit-SQUID system are:

$$\begin{aligned} m_q\ddot{q} &= -\tfrac{\partial U_q}{\partial q} - m_m\omega_m^2(q+\varphi_m) \\ m_m\ddot{\varphi}_m &= -m_m\omega_m^2(q+\varphi_m) - J_1\varphi_p \\ m_p\ddot{\varphi}_p &= -m_p\omega_p^2\varphi_p - J_1\varphi_m - \textstyle\sum_\alpha \frac{c_\alpha^2}{m_\alpha\omega_\alpha^2}\varphi_p - \sum_\alpha c_\alpha x_\alpha \\ m_\alpha\ddot{x}_\alpha &= -m_\alpha\omega_\alpha^2 x_\alpha - c_\alpha\varphi_p \end{aligned} \tag{3.4}$$

where m_q is the effective mass of the qubit flux q and is determined by the capacitances of the qubit junctions; and U_q is the potential energy of q and is dominated by the self inductance of the qubit. The specific expressions of m_q and U_q will not affect our results. We then apply a Fourier transformation to these linear equations and derive the interdependence between the Fourier components of different variables. For example, we have $\bar{x}_\alpha(z) = \frac{c_\alpha}{M_\alpha(z^2-\omega_a^2)}\bar{\varphi}_p(z)$, where $\bar{x}_\alpha(z)$ and $\bar{\varphi}_p(z)$ are Fourier components of the corresponding variables at the complex frequency z. Using these relations, we can cancel the components of all the other variables and derive an equation for $\bar{q}$: $\hat{K}(z)\bar{q} = -\frac{\partial\bar{U}}{\partial q}$. Considering the environment of φ_p as an admittance $Y_0(\omega)$ with $J_0(\omega) = \frac{\hbar}{(2e)^2}Re[Y_0(\omega)]\omega$, we derive $\hat{K}(z)$ from:

$$\begin{aligned} \hat{L}_p(z) &= -m_p z^2 + i(\tfrac{\hbar}{2e})^2 Y_0(z) z \\ \hat{L}_m(z) &= -m_m z^2 - \frac{J_1^2}{\hat{L}_p(z)+m_p\omega_p^2} \\ \hat{K}(z) &= -m_q z^2 + \frac{m_m\omega_m^2\hat{L}_m(z)}{m_m\omega_m^2+\hat{L}_m(z)} \end{aligned} \tag{3.5}$$

which only depends on known parameters in the Hamiltonian $\mathcal{H}_t$ and the shunt admittance. The effective spectral density $J_{eff}^q(\omega)$ for the flux q can then be calculated from $\hat{K}(z)$. As a result, the current noise coupling to the operator σ_z of the qubit is

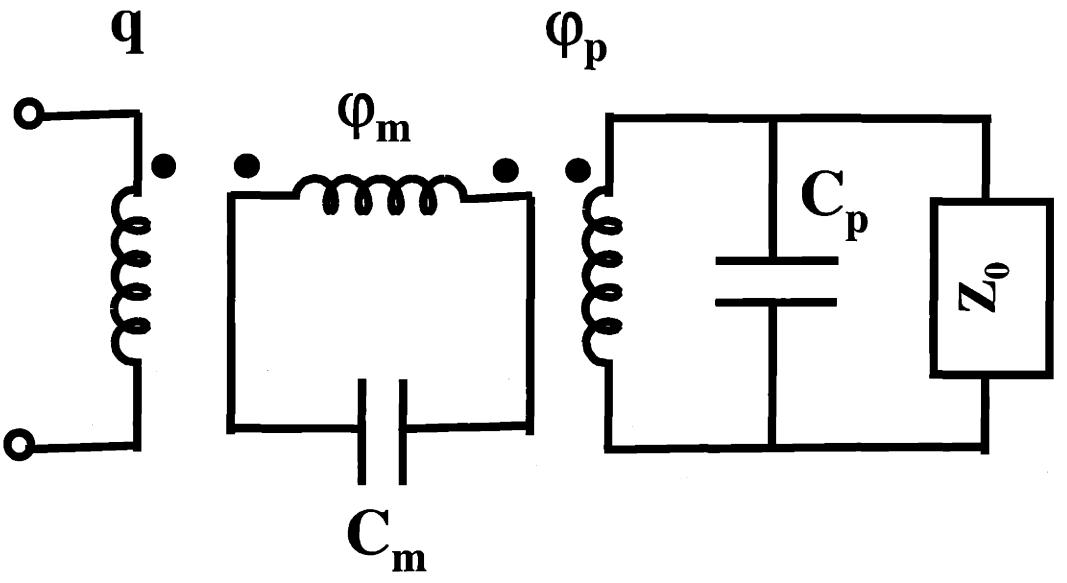

Figure 3-4: Equivalent circuit derived from the linearized Hamiltonian of the qubit-SQUID system. The phases q, φ_m and φ_p are chosen as the independent circuit variables of the three loops of the circuit. The capacitances of the φ_m loop and the φ_p loop are $C_m = 2C_J$ and $C_p = C_s + 2C_J$ respectively. The inductances in the three loops interact via mutual inductances as indicated by the paired dots near the inductances. Z_0 is the environment of the φ_p loop.

$J_{eff} = \delta\varphi_0^2 J_{eff}^q(\omega)$ which follows the relation $q = \delta\varphi_0 \sigma_z$.

Using the above results, we derive the effective noise spectrum on the qubit:

$$\begin{aligned} J_{eff}(\omega) &= \delta\varphi_0^2 \tfrac{4\hbar}{e^2\omega L_{dc}^2} Re[(2i\omega C_J + \tfrac{4}{i\omega L_{dc}} + \tfrac{[J_1 4\pi^2]^2}{\omega^2 \Phi_0^4 Y_p(\omega)})^{-1}] \\ Y_p(\omega) &= i\omega C_s + \tfrac{1}{i\omega L_J} + Y_0(\omega) \end{aligned} \tag{3.6}$$

where Y_p is the admittance of the dynamic inductance L_J, the shunt capacitance and the environmental admittance $Y_0(\omega)$ in parallel. This expression looks complicated, but it has a simple correspondence in terms of linear circuitry which will be shown in the next subsection.

3.3.3 Equivalent circuit

Now, we map the system described by Eq. 3.1 and Eq. 3.3 to an equivalent circuit. For each φ_i^2 term we introduce an inductance; for each P_j^2 term we introduce a capacitance in parallel to the inductance; the environment of φ_p is an impedance Z_0 (admittance $Y_0(\omega)$) in parallel to the inductance element φ_p^2. The circuit is shown in Fig. 3-4. It has three independent flux variables: $\Phi_q = \frac{\Phi_0}{2\pi}\langle q\rangle$, $(q = \delta\varphi_0\sigma_z)$, $\Phi_m = \frac{\Phi_0}{2\pi}\langle\varphi_m\rangle$, $\Phi_p = \frac{\Phi_0}{2\pi}\langle\varphi_p\rangle$.

From Fig. 3-4, the currents in the three loops are related to the flux by the inverse inductance matrix:

$$\begin{bmatrix} I_q \\ I_m \\ I_p \end{bmatrix} = \begin{bmatrix} \frac{1}{L_q} & \frac{4}{L_{dc}} & 0 \\ \frac{4}{L_{dc}} & \frac{4}{L_{dc}} & (\frac{2\pi}{\Phi_0})^2 J_1 \\ 0 & (\frac{2\pi}{\Phi_0})^2 J_1 & \frac{1}{L_J} \end{bmatrix} \begin{bmatrix} \Phi_q \\ \Phi_m \\ \Phi_p \end{bmatrix} \tag{3.7}$$

where L_q is determined by the self inductance of the qubit and will not affect our result. $I_j(j = q, m, p)$ are currents in each of the loops in the circuit. Let $v_j(j = q, m, p)$ be voltage of the corresponding inductance. The circuit equations are:

$$\begin{aligned} i\omega\Phi_p &= v_p = -I_p Z_p \\ i\omega\Phi_m &= v_m = -I_m Z_m \\ i\omega\Phi_q &= v_q = I_q Z_{eff} \end{aligned} \tag{3.8}$$

where Z_p is the impedance of C_p and Z_0 in parallel; Z_m is the impedance of C_m; and Z_{eff} is the effective impedance at the input where the qubit is located. The real part of Z_{eff}^{-1} determines the current noise on the qubit.

We derive the effective admittance $Y_{eff} = Z_{eff}^{-1} = I_q/v_q$ from circuit equations:

$$\begin{aligned} Y_{eff} &= \frac{1}{i\omega L_q} + \frac{16}{\omega^2 L_{dc}^2 Y_m} \\ Y_m &= i\omega C_m + \frac{4}{i\omega L_{dc}} + \frac{(4\pi^2 J_1)^2}{\omega^2 \Phi_0^4 Y_p} \\ Y_p &= i\omega C_p + \frac{1}{i\omega L_J} + \frac{1}{Z_0} \end{aligned} \tag{3.9}$$

where Y_m is the admittance of the circuit without the qubit loop; and Y_p is the admittance of the circuit without both the qubit and the inner oscillator loops. Plugging Y_{eff} into $J_{eff}^q(\omega)$ and putting the $2\delta\varphi_0$ factor back, the noise spectrum coupling to the qubit is[106, 107, 108]:

$$J_{eff}(\omega) = (2\delta\varphi_0)^2 \frac{4\hbar}{e^2 \omega L_{dc}^2} Re\left[\left(2i\omega C_J + \frac{4}{i\omega L_{dc}} + \frac{[J_1 4\pi^2]^2}{\omega^2 \Phi_0^4 \left(i\omega C_s + \frac{1}{i\omega L_J} + Y_0(\omega)\right)}\right)^{-1}\right]. \tag{3.10}$$

Note that this linear circuit does not have direct correspondence to the physical system, but comes from the linearized Hamiltonian. This equivalent circuit method is easier to apply to an arbitrary external system. Once the linearized Hamiltonian is known, a linear circuit can be obtained whose admittance determines the noise and can be calculated easily.

For the qubit-SQUID system, as $\omega_m \gg \omega_p, \omega_0$, the spectrum can be simplified for $\omega \ll \omega_m$ by ignoring the capacitance C_m term. Assuming an ohmic environment with resistance R_s and substituting $\delta\varphi_0$ with $\pi M_q I_{cir}/\Phi_0$, we have:

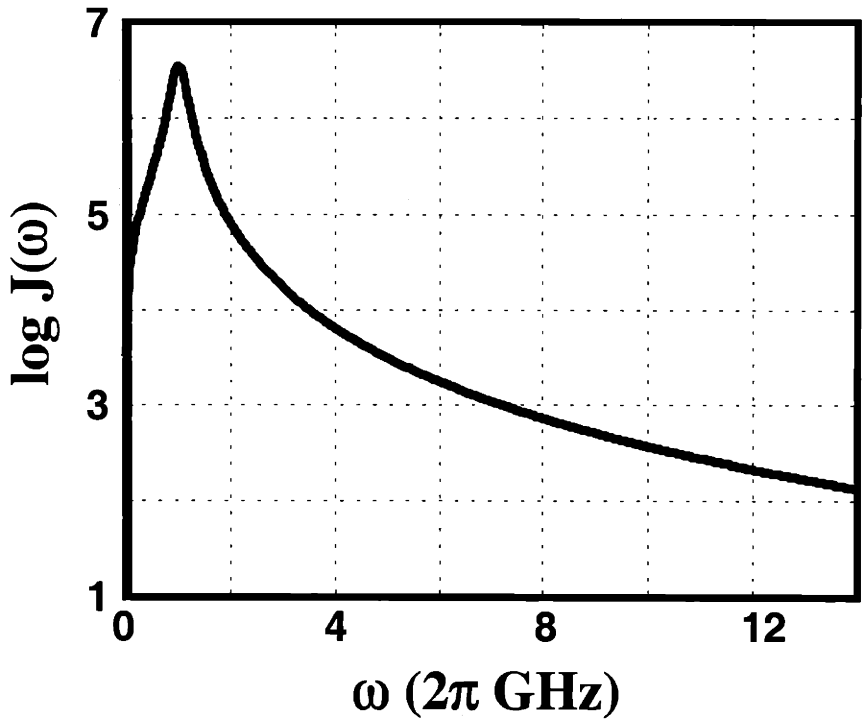

Figure 3-5: Effective noise spectrum verses frequency for ramping current $I_b = 0.8I_c^{eff}$, zero temperature and with an Ohmic environment of $R_s = 100\,\Omega$.

$$J_{eff}(\omega) \approx \frac{4(eI_{cir}I_bM_q)^2}{C_s^2\hbar^3R_s}\frac{\omega}{(\omega^2-\omega_p^2)^2+(\omega/R_sC_s)^2}. \tag{3.11}$$

$J_{eff}(\omega)$ increases with the square of the mutual inductance and the square of the ramping current; hence when the coupling between qubit and SQUID is stronger, the noise is also stronger. When the ramping current is off, the noise transferred to the qubit is negligible as the entanglement between the inner oscillator and the external oscillator is negligible. For finite ramping current, at low frequency when $\omega \ll \omega_p$, the spectrum increases linearly with ω; compared with the spectrum $J_0(\omega)$, $J_{eff}(\omega)$ is rescaled by a constant factor as $J_{eff} = J_0(2\delta\varphi_0\frac{2\pi I_bL_J}{\Phi_0})^2$. So at low frequency with I_b of the same order of I_c^{eff}, the noise transferred is reduced by an order of $\delta\varphi_0^2$. At high frequency when $\omega \gg \omega_p$, besides the rescaled linear term, another factor shows up as $J_{eff} = J_0\,(2\delta\varphi_0\frac{2\pi I_bL_J}{\Phi_0})^2(\frac{\omega_p}{\omega})^4$, and the spectrum decreases with ω^{-3} which further

reduces the noise at $\omega = \omega_0$. The SQUID thus acts as a filter that cuts off the high frequency noise transferred to the qubit. At $\omega \approx \omega_p$, a sharp Lorenzian peak appears in the spectrum with a width of $(R_s C_s)^{-1}$. This structure is due to the discrete external oscillator mode of the SQUID that interacts with the reservoir; when the interaction between the SQUID and the reservoir goes to zero ($R_s \to \infty$), the peak becomes a δ-function. The spectrum is plotted in Fig. 3-5.

3.4 Effect of noise

During a measurement, information about the measured system is obtained by entangling this system with a meter variable. In most discussions of measurement, entanglement is accomplished in a very short time during which the evolution of the measured system is neglected; in other words, the measurement basis is the basis of the pointer variable. Afterward, the meter variable is projected to macroscopically distinguishable states. Hence the dynamics of the measured system has no effect on the result of measurement once an initial state is selected. However, in the measurement of the pc-qubit, entanglement is a slow process (milliseconds) as the interaction between the system and the meter is much weaker than the qubit energy ω_0. At the same time, the pointer basis which is the eigenstates of the σ_z operator of the qubit is different from the qubit eigenstates as $[\mathcal{H}_q, \sigma_z] \neq 0$. As a result, we have to take the qubit dynamics into account, including relaxation and decoherence, when studying the measurement. In the following we study the decoherence and relaxation of the qubit due to the effective noise transferred to the qubit from the SQUID's environment.

3.4.1 Master equation approach

Here we introduce the master equation approach to discuss the effect of the environment with a noise spectral density $J(\omega)$ on the qubit dynamics. Compared with the qubit Hamiltonian, the interaction with the reservoir is much weaker; so the dynamics of the qubit can be described by the master equation which treats the environmental

perturbation to second order [110].

Consider a qubit interacting with a reservoir:

$$\mathcal{H}_{q,r} = \frac{\hbar\omega_0}{2}\sigma'_z + \sigma'_z\hat{X}'_z + \sigma'_x\hat{X}'_x \tag{3.12}$$

where σ'_z and σ'_x correspond to the Pauli matrices when choosing $|\sigma'_z = \pm 1\rangle$ as the qubit eigenstates. ω_0 is the qubit frequency. $\hat{X}'_z$ and $\hat{X}'_x$ are the transverse and longitudinal noise from the reservoir. The $\hat{X}'_z$ interaction creates random phase in the qubit state; and the $\hat{X}'_x$ interaction flips the qubit state. Let $J^{z'}(\omega)$ be the noise spectrum of $\hat{X}'_z$ and $J^{x'}(\omega)$ be the noise spectrum of $\hat{X}'_x$ at zero temperature.

The reduced density matrix of the qubit $\rho_s = tr_r(\rho)$, where the trace is taken over the reservoir modes on the total density matrix ρ of the qubit and the reservoir, evolves according to the master equation[110, 112]:

$$\begin{aligned}\frac{\partial\rho_s}{\partial t} = &-\gamma_p[\sigma'_z,[\sigma'_z,\rho_s]]/4 - \frac{\gamma_d}{2}(n(\omega_0)+1)(2\sigma'_-\rho_s\sigma'_+ - \sigma'_+\sigma'_-\rho_s - \rho_s\sigma'_+\sigma'_-) \\ &-\frac{\gamma_d}{2}n(\omega_0)(2\sigma'_+\rho_s\sigma'_- - \sigma_-\sigma'_+\rho_s - \rho_s\sigma_-\sigma'_+)\end{aligned} \tag{3.13}$$

where $n(\omega) = (e^{\hbar\omega/k_BT} - 1)^{-1}$ is the boson number distribution at frequency ω and temperature T. γ_p and γ_d are the transverse and the longitudinal relaxation rates determined by the noise spectrum: $\gamma_p = J^{z'}(\omega)\coth\frac{\hbar\omega}{2k_BT}|_{\omega\to 0}$ and $\gamma_d = J^{x'}(\omega_0)$. The decoherence time T_2 and damping time T_1 can be derived from the Bloch equations of $\rho_{\uparrow\uparrow} - \rho_{\downarrow\downarrow}$ and $\rho_{\uparrow\downarrow}$[111] by Eq. 3.13, where $T_1^{-1} = \gamma_d\coth\frac{\hbar\omega_0}{2k_BT}$ and $T_2^{-1} = \gamma_p + \frac{1}{2}\gamma_d\coth\frac{\hbar\omega_0}{2k_BT}$. In terms of the noise spectrum, we have:

$$\begin{aligned}T_1^{-1} &= \tfrac{1}{2}J^{x'}(\omega_0)\coth\tfrac{\hbar\omega_0}{2k_BT} \\ T_2^{-1} &= \tfrac{1}{2}J^{z'}(\omega)\coth\tfrac{\hbar\omega}{2k_BT}|_{\omega\to 0} + \tfrac{1}{4}J^{x'}(\omega_0)\coth\tfrac{\hbar\omega_0}{2k_BT}\end{aligned} \tag{3.14}$$

3.4.2 Effect of transmitted noise

The decoherence and relaxation are expressed in terms of the noise that couples to σ'_z and σ'_x. However, in the persistent-current qubit, physical noise couples with the

qubit by σ_z and σ_x:

$$\mathcal{H}_{q,r} = \mathcal{H}_q + \sigma_z \hat{X}_z + \sigma_x \hat{X}_x \tag{3.15}$$

where $\mathcal{H}_q = \frac{\epsilon_0}{2}\sigma_z + \frac{t_0}{2}\sigma_x$ is the qubit Hamiltonian; $\hat{X}_z$ and $\hat{X}_x$ are noise from the reservoir. Eq. 3.15 is a general form of the qubit-reservoir interaction. The effective noise transferred to the qubit from the SQUID's environment is also included. Examples of noise that give $\hat{X}_z$ are flux noise and nuclear spin fluctuations; example of noise that gives $\hat{X}_x$ are charge fluctuations on the gates. Let the noise spectrum of $\hat{X}_z$ be $J^z(\omega)$ and the noise spectrum of $\hat{X}_x$ be $J^x(\omega)$ at zero temperature. $J^z(\omega)$ and $J^x(\omega)$ can be calculated directly from the system coupling and geometry. To derive $J^{z'}$ and $J^{x'}$ from the physical noise, we rewrite $\mathcal{H}_{q,r}$ in the terms of σ_z' and σ_x', with

$$\sigma_z' = \cos\theta\sigma_z + \sin\theta\sigma_x \quad \text{and} \quad \sigma_x' = -\sin\theta\sigma_z + \cos\theta\sigma_x \tag{3.16}$$

where θ is the angle between the qubit eigenstate and the σ_z basis with $\cos\theta = \epsilon_0/\omega_0$ and $\sin\theta = t_0/\omega_0$. $\omega_0 = \sqrt{\epsilon_0^2 + t_0^2}$. Now the qubit-reservoir Hamiltonian is

$$\mathcal{H}_{q,r} = \frac{\hbar\omega_0}{2}\sigma_z' + \sigma_z'(\cos\theta\hat{X}_z + \sin\theta\hat{X}_x) + \sigma_x'(-\sin\theta\hat{X}_z + \cos\theta\hat{X}_x) \tag{3.17}$$

The comparison of Eq. 3.17 with Eq. 3.12 shows that $\hat{X}_z'$ has contributions from both $\hat{X}_z$ and $\hat{X}_x$; and so does $\hat{X}_x'$. The spectra $J^{x'}(\omega)$ and $J^{z'}(\omega)$ can be expressed in terms of J^x and J^z:

$$\begin{aligned} J^{z'}(\omega) &= \cos^2\theta J^z(\omega) + \sin^2\theta J^x(\omega) \\ J^{x'}(\omega) &= \sin^2\theta J^z(\omega) + \cos^2\theta J^x(\omega) \end{aligned} \tag{3.18}$$

The transmitted noise affects the qubit via σ_z coupling. As $[\sigma_z, \mathcal{H}_q] \neq 0$, which is generally the case, damping occurs as well as decoherence. We write:

$$\sigma_z' = \cos\theta\sigma_z + \sin\theta\sigma_x, \quad \sigma_x' = -\sin\theta\sigma_z + \cos\theta\sigma_x \tag{3.19}$$

where θ is the angle between the qubit eigenstate and the σ_z basis with $\cos\theta = \epsilon_0/\omega_0$ and $\sin\theta = t_0/\omega_0$. $\omega_0 = \sqrt{\epsilon_0^2 + t_0^2}$. σ_z' and σ_x' correspond to the Pauli matrices when choosing $|\sigma_z' = \pm 1\rangle$ as the qubit eigenstates. The qubit-reservoir Hamiltonian:

$$\mathcal{H}_{q,r} = \frac{\hbar\omega_0}{2}\sigma_z' + \cos\theta\,\hat{X}_z\sigma_z' - \sin\theta\,\hat{X}_z\sigma_x' \tag{3.20}$$

where $\hat{X}_z$ is the coupling between the qubit and the effective noise reservoir whose spectrum is $J_{eff}(\omega)$. In Eq. 3.20, we have both pure dephasing noise with spectrum $\cos^2\theta J_{eff}(\omega)$ and relaxation coupling with spectrum $\sin^2\theta J_{eff}(\omega)$. Once we know the noise spectrum, the relaxation and decoherence rates can be derived[109, 110, 111]. At finite temperature,

$$\begin{aligned} T_1^{-1} &= \frac{t_0^2}{2\omega_0^2} J_{eff}(\omega)\coth\frac{\hbar\omega}{2k_BT}|_{\omega=\omega_0} \\ T_2^{-1} &= \frac{\epsilon_0^2}{2\omega_0^2} J_{eff}(\omega)\coth\frac{\hbar\omega}{2k_BT}|_{\omega\to 0} + \frac{t_0^2}{4\omega_0^2} J_{eff}(\omega)\coth\frac{\hbar\omega}{2k_BT}|_{\omega=\omega_0} \end{aligned} \tag{3.21}$$

Due to the reduction factor ω_p^4/ω_0^4 in the spectral density, relaxation is slowed by the filtering of the SQUID. With the system parameters, we calculate the damping time as $\tau_r = 0.15\,\text{sec}$ and the decoherence time as $\tau_d = 2\,\mu\text{sec}$ at $I_b = 0.8I_c^{eff}$. The decoherence time is of the same order as was measured in the Delft experiment[29] and is much shorter than the estimated intrinsic decoherence[41], while relaxation is slow enough that it will not hinder the extraction of qubit information. The noise transferred to the qubit is negligible at $I_b = 0$ when no measurement is being conducted.

Note that the noise increases with the square of the inductive coupling; and so do the decoherence and relaxation rates. In contrast, α, the coherent state parameter that determines the information bound of this measurement, only increases linearly with the inductive coupling. When increasing α by 10 times by adjusting the mutual inductance, the relaxation rate is two orders faster. This puts an extra restriction on measurement optimization—to keep the noise low for a good enough signal-to-noise ratio.

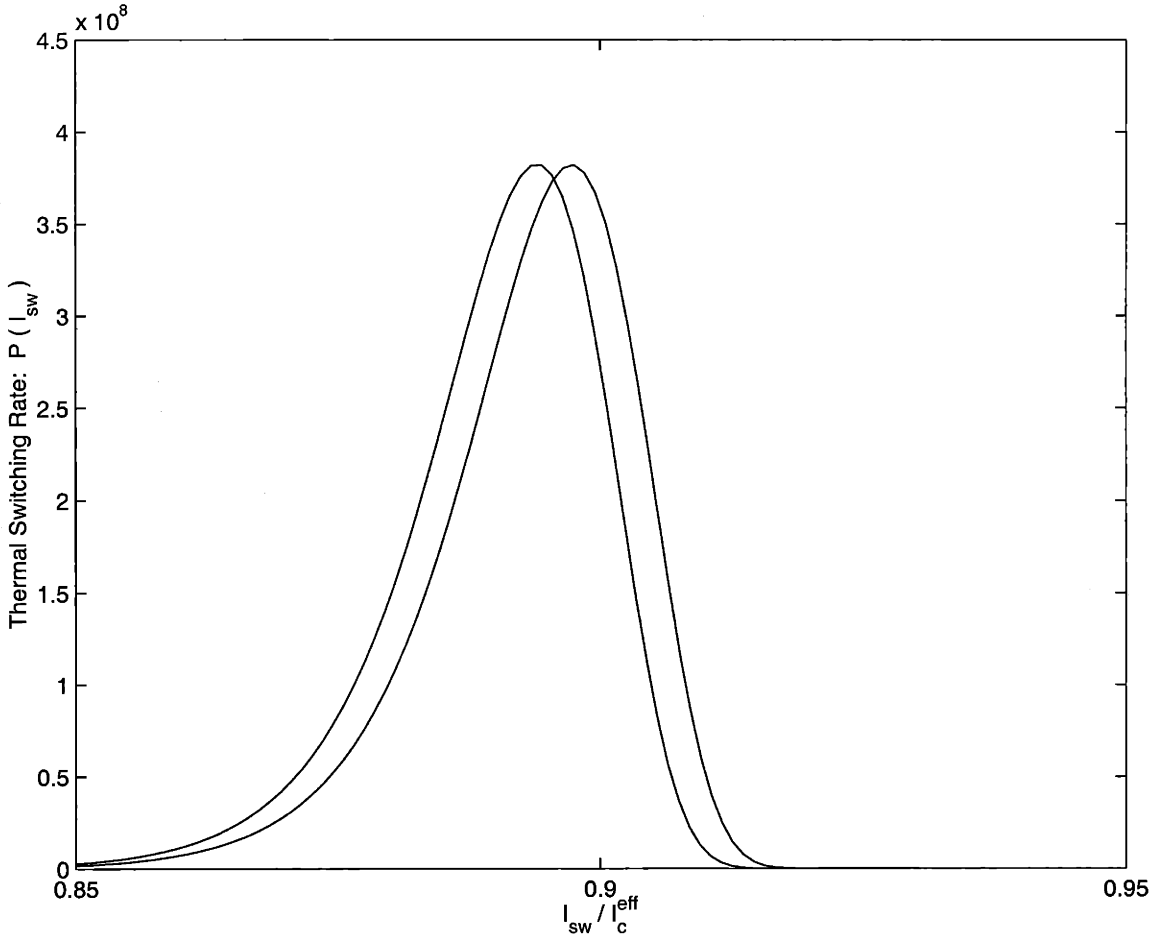

Figure 3-6: The thermal tunneling histograms for the dc SQUID at temperature above the crossover temperature. Left: qubit flux $\delta\varphi_0$; right: qubit flux $-\delta\varphi_0$.

3.5 Tunneling Rate of the DC SQUID

The switching current histogram of the dc SQUID can be calculated numerically. Much has been done on calculating the switching rate for a one-dimensional particle from a metastable washboard potential. When the temperature is higher than the crossover temperature $T_{cr} = \hbar\omega_p/2\pi k_B$ (ω_p, the plasma frequency of the metastable potential), the escape rate from the potential well is dominated by thermal activation rate: $\Gamma_t = \frac{a_t\omega_p}{2\pi}\exp(-\Delta U/k_BT)$, where $a_t = 4/[(1+\frac{Qk_BT}{1.8\Delta U})^{1/2}+1]^2$, with $Q = \omega_pRC$, where R is the resistance shunting the junction, C is the capacitance, and ΔU is the energy barrier of the potential. When the temperature is lower than the crossover temperature, the escape rate is dominated by quantum fluctuations: $\Gamma_q = \frac{a_q\omega_p}{2\pi}\exp(-\frac{7.2\Delta U}{\hbar\omega_p}[1+\frac{0.87}{\omega_pRC}])$, where $a_q \approx [120\pi(7.2\Delta U/\hbar\omega_p]^{1/2}$. In Fig. 3-6 and Fig. 3-7 the switching histogram by thermal rate and by quantum rate are plotted respectively. The normalized probability of the switching histogram at current I_b is $P(I_b) = \Gamma(I_b)|\frac{dI}{dt}|^{-1}(1-\int_0^{I_b}P(I)dI)$. This can be written as $P(I_b) = \Gamma(I_b)|\frac{dI}{dt}|^{-1}\exp(-|\frac{dI}{dt}|^{-1}\int_0^{I_b}dI'\Gamma(I'))$.

The dc SQUID in the qubit measurement works at a temperature slightly above the crossover temperature. Although the thermal rate dominates in this regime, the quantum fluctuations can modify the escape rate significantly. At the same time, as the dc SQUID is in fact a two-dimensional system, the escape from the potential can be affected by the second dimension. Here, we calculate the SQUID escape rate by taking account of both the quantum modification of the thermal rate and the effect of the second dimension. We follow the method in [113] which is briefly described below.

For a metastable system, the escape rate from the metastable state can be derived from the free energy as $\Gamma = -\frac{2T_0}{\hbar T}\mathrm{Im}F$ above the crossover temperature, and the free energy can be expressed as $F = -\frac{1}{\beta}\ln Z$. Here we extend the method to a two-dimensional system. The partition function Z can be derived with a path integral approach as $Z = \int \mathcal{D}\bar{q}e^{-S^E([\bar{q}])}$. In the saddle point approximation, the partition function Z consists of two parts: $Z = Z_0 + Z_b$, where Z_0 is the contribution from

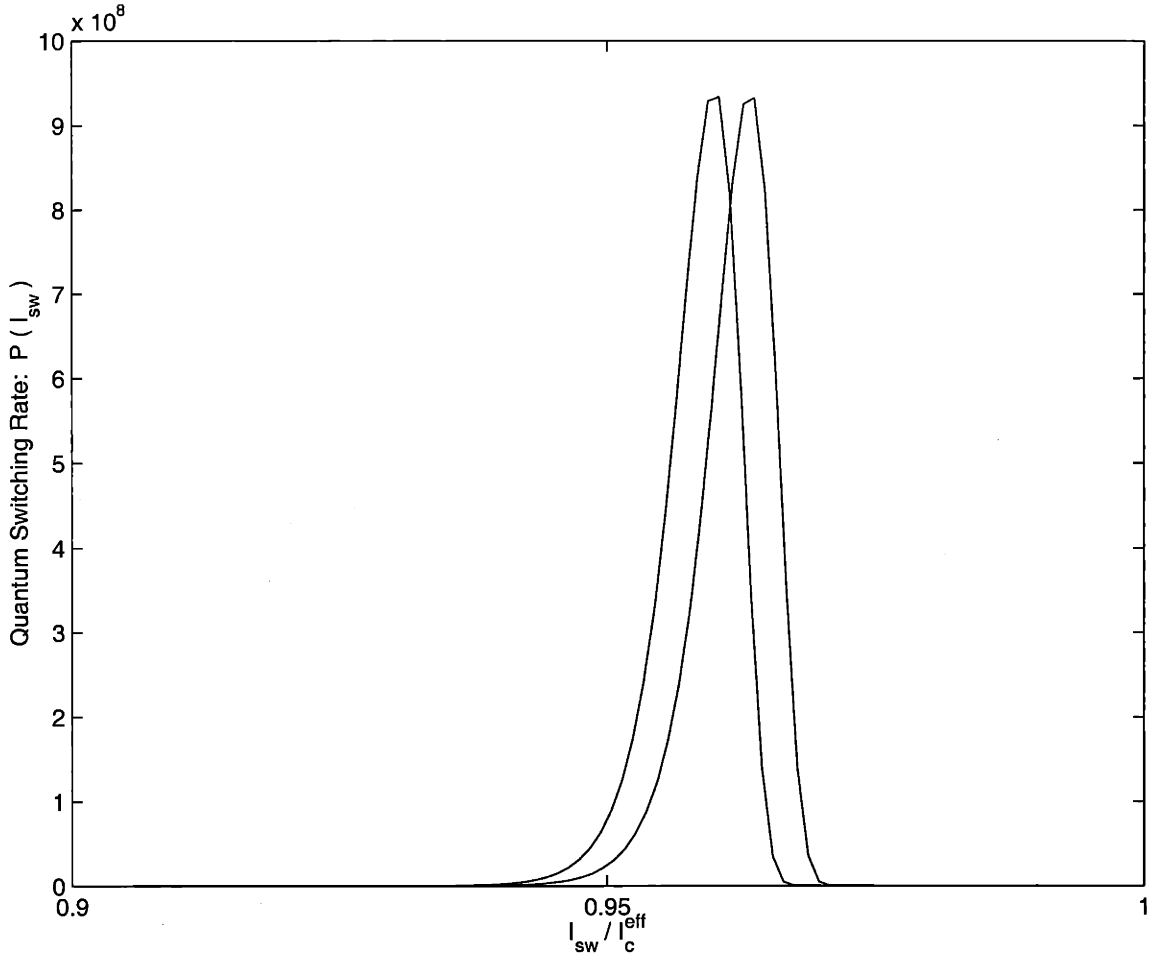

Figure 3-7: The quantum tunneling histograms for the dc SQUID at temperature below the crossover temperature. Left: qubit flux $\delta\varphi_0$; right: qubit flux $-\delta\varphi_0$.

the potential minimum and Z_b is the contribution from the potential maximum (the barrier). The action $S^E_{o,b}$ can be expressed as:

$$S^E_{o,b} = \hbar\beta V_{o,b} + \frac{\hbar\beta}{2}\sum_n(\lambda_{+n}|\xi_{+n}|^2 + \lambda_{-n}|\xi_{-n}|^2) \tag{3.22}$$

where λ_i are the roots of the following equations:

$$\begin{aligned} \lambda_\pm &= \tfrac{a_n+b_n)\pm\sqrt{(a_n-b_n)^2+4c_n^2}}{2} \\ a_n &= M_m(\nu_n^2 + |\nu_n|\gamma_m + \omega_m^2) \\ b_n &= M_p(\nu_n^2 + |\nu_n|\gamma_p \pm \omega_p^2) \\ c_n &= -2E_J^{dc}\sin\varphi_m \sin\varphi_p \end{aligned} \tag{3.23}$$

Here $\gamma_{m,p}$ are the spectral density of the inner variable and the external variable environments, respectively. $\nu_n = n2\pi/\hbar\beta$ is the Matsubara frequency. M_m and M_p are the masses of the harmonic oscillators; ω_m and ω_p are the frequencies. Substituting the equations into the partition function, we have:

$$\begin{aligned} Z_0 &= e^{-\beta V_{min}}\frac{k_BT}{\sqrt{\lambda^o_{+0}\lambda^o_{-0}}}\prod_{n=1}^{\infty}\frac{(k_BT)^2}{\lambda^o_{+n}\lambda^o_{-n}} \\ Z_b &= ie^{-\beta V_{max}}\frac{k_BT}{2\sqrt{\lambda^b_{+0}|\lambda^b_{-0}|}}\prod_{n=1}^{\infty}\frac{(k_BT)^2}{\lambda^b_{+n}\lambda^b_{-n}} \end{aligned} \tag{3.24}$$

Z_b is imaginary part from the contribution of the zeroth mode. Hence the final expression for the escape rate is:

$$\Gamma = \frac{k_BT_0}{\hbar}\sqrt{\frac{\lambda^o_{+0}\lambda^o_{-0}}{\lambda^b_{+0}|\lambda^b_{-0}|}}e^{-\beta\Delta U_b}\prod_{n=1}^{\infty}\frac{\lambda^o_{+n}\lambda^o_{-n}}{\lambda^b_{+n}\lambda^b_{-n}} \tag{3.25}$$

which can be derived with loop integration. T_0 is decided by the oscillator frequency ω_p and by the dissipation rate γ_p:

$$k_BT_0 = \frac{\hbar}{2\pi}\left(\sqrt{\omega_p^2 + (\frac{\gamma_p}{2})^2} - \frac{\gamma_p}{2}\right) \tag{3.26}$$

where $\gamma_p = (RC)^{-1}$ is the dissipation rate of the SQUID. With this equation, the

modification of the escape rate by quantum fluctuations and by the interference of the second dimension can be studied. It is shown that the effect on the escape rate is negligibly small.

3.6 Radiation Assisted Measurement

Among the various physical realizations of a quantum bit, solid-state qubits have the advantage of being easily scalable to large numbers and that their structures and quantum states can be easily manipulated. The study of solid-state quantum computing is a growing field [18, 20, 21, 22, 23, 24, 25, 114] and several mesoscopic systems have been implemented[115, 29, 28, 116, 117]. Most measurements of these solid-state qubits rely on the detection of the electromagnetic signal[30, 116, 118, 119, 120] of the qubit states which is usually a small signal. On the one hand, coupling with the detector is necessary to get information from the qubit; on the other hand, we want to keep the coupling weak so that the qubit be well isolated from the rest of the world.

Effective measurement of quantum bits is a crucial step in quantum information processing. An ideal measurement to resolve the qubit states is a projective measurement[100] that can project each state of the quantum bit onto a macroscopically resolvable state. In reality, it is often hard to design an experiment that can measure the qubit efficiently. The detectable signal of the qubits, which is usually an electromagnetic signal, is small compared with the detector's quantum state width. This is a major problem in the study of the flux-based persistent-current qubits (pc-qubit) [20, 25, 29].

The two qubit states of a pc-qubit have opposite circulating currents which generate a flux of a thousandth of a flux quantum. By inductively coupling this flux to a dc SQUID[29], which is one of the most sensitive flux detection devices, the qubit states are measured. As the flux from the qubit is much smaller compared with the width of the SQUID's wave function, the histograms for the two qubit states largely overlap with each other. Hence, the same measurement has to be repeated many times

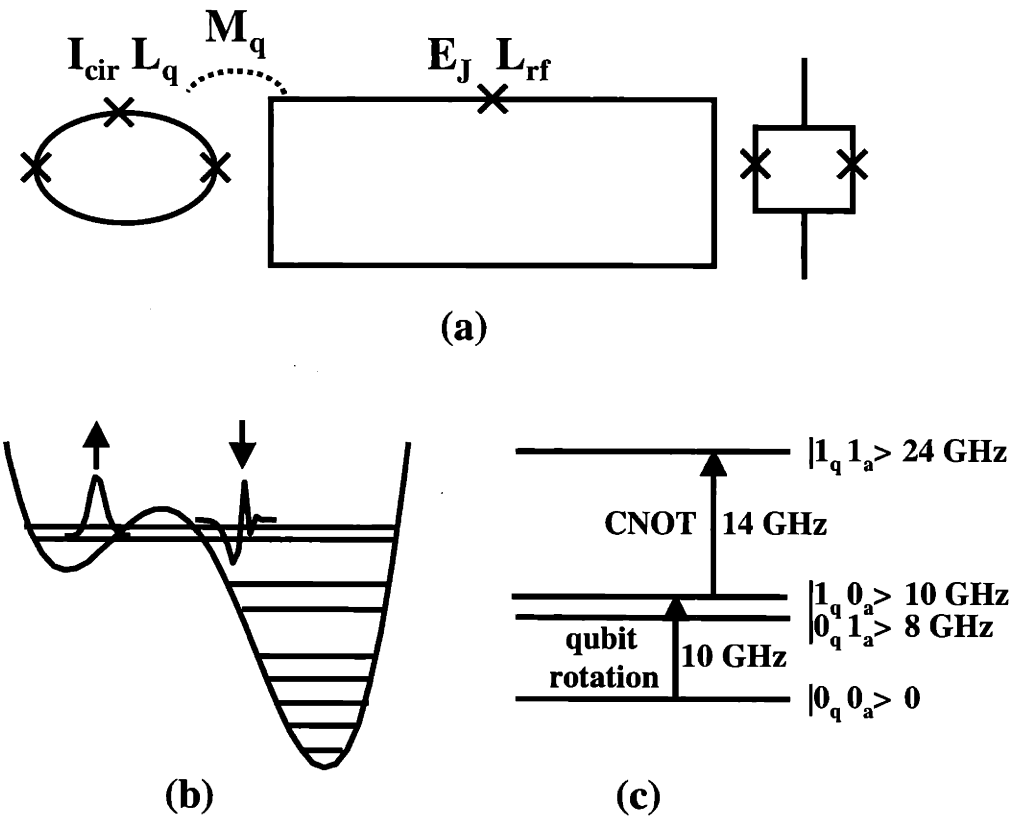

Figure 3-8: (a). The circuit for the coherent transition assisted measurement, from left to right: the qubit, the rf SQUID and the magnetometer. The pc-qubit is inductively coupled to the rf SQUID via the mutual inductance M_q. (b). Energy levels of rf SQUID with its potential energy when biased near 1/2 flux quantum. The ancilla qubit states are labeled with arrows and their wave functions are also shown. (c). The effective four level system for the interacting qubit and the rf SQUID. The states are labeled beside the energy levels with their energies in GHz.

to resolve the qubit states. However, considering the fact that the two qubit states are orthogonal to each other, it is in principle possible to construct a measurement operator that projects the two qubit states into perfectly distinguishable states.

In this section, we present a measurement scheme on the pc-qubit that projects the eigenstates of the qubit onto macroscopicly different results. The idea is to first entangle the qubit coherently to another quantum system which has much stronger coupling to the detector and then measure this supplementary system to infer the qubit states. We choose the supplementary system to be a rf SQUID which behaves as an effective two level system with the flux difference between these two levels being of order of a half flux quantum. This rf SQUID is of the same size as that in Ref.[56] and the operation can be easily implemented. This larger flux can then be easily measured by magnetometers such as a dc SQUID or an rf frequency tank circuit[121]. This design is not only closely related with the present experiments for the pc-qubit, but also brings a new way of effectively measuring solid-state qubits with small signals.

3.6.1 Limit of direct flux detection

The superconducting persistent-current qubit[20, 25] is a superconducting loop that has three Josephson junctions in series, Fig. 3-8 (a). One junction has a slightly different critical current from that of the others. The qubit is controlled by the magnetic flux $f_q\Phi_0$ in the loop, where Φ_0 is the flux quantum. The static flux is f_q near 1/2. Microwave radiation can be coupled to the loop to rotate the qubit. The lowest two energy levels of this quantum system are nearly localized flux states with opposite circulating currents, and are chosen as the qubit states. The two qubit states are analogous to spin states and can be described by $SU(2)$ algebra of Pauli matrices. By identifying the localized flux states as eigenstates of σ_z, the qubit Hamiltonian can be written as $\mathcal{H}_q = \frac{\epsilon_0}{2}\sigma_z + \frac{t_0}{2}\sigma_x$, where $\epsilon_0 \propto (f_q - 1/2)$ is controlled by the flux f_q in the qubit loop and t_0 is the coherent tunneling between the two localized flux states through potential energy barrier. In this chapter we assume $t_0 = 0$ to emphasis the discussion on the measurement process. t_0 can be calculated by the WKB approach.

Typically, the circulating current is $I_{cir} \approx 0.7 I_c$, where I_c is the critical current of the Josephson junction and $I_c = 200\,\mathrm{nA}$. With a loop inductance of $L_q = 10\,\mathrm{pH}$, the self induced flux of the qubit is $\delta\varphi_q = 10^{-3}\Phi_0$.

In the previous experiment[29], the pc-qubit was measured by a dc SQUID. By inductively coupling the qubit to the dc SQUID, the flux of the qubit affects the critical current of the SQUID by $\Delta I_c = \pm I_c^{eff}\delta\varphi_q \simeq \pm 10^{-3} I_c^{eff}$. During measurement, a bias current I_b is ramped through the dc SQUID; and the switching current, where the SQUID switches to a finite voltage state from the supercurrent state, is recorded. Due to quantum fluctuations and thermal activation, the switching current distribution has a finite width. The average of the switching current changes with I_c^{eff} and reflects the probability of the two qubit states. Due to quantum fluctuations and thermal activation, the switching current distribution has a finite width. The two qubit states result in two switching histograms that are only separated by order of ΔI_c, which is much less than the width of the histogram. As a result, the histogram is not perfectly correlated with the qubit states and the measurement has to be repeated many times to derive information the qubit.

To understand what prevents the effective measurement on the pc-qubit, we analyze the previous measurement in detail in Ref.[39]. The dc SQUID as a quantum system interacts with the qubit inductively and can be modeled as two oscillators: the inner oscillator φ_m that represents the circulating current of the SQUID loop; and the external oscillator φ_p that represents a quantum particle in a washboard potential tilted by the ramping current I_b. The external oscillator interacts with the inner oscillator through the ramping current. Only the inner oscillator interacts directly with qubit and limits the measurement efficiency. A detailed study of the quantization of the dc SQUID's Hamiltonian can be found in [98]. Considering the inner oscillator of the dc SQUID and the qubit interaction Hamiltonian

$$\mathcal{H}_1 = \frac{\hbar\omega_0}{2}\sigma_z^q + \frac{\hat{P}_m^2}{2m_m} + \frac{1}{2}m_m\omega_m^2(\varphi_m - \delta\varphi_0\sigma_z^q)^2 \tag{3.27}$$

where ω_0 is the qubit frequency, σ_z^q is the qubit Pauli matrix. $\hat{P}_m$ is the momentum

of the inner oscillator, m_m is the mass of the oscillator and ω_m is the frequency of the oscillator[39]. The inner oscillator offset $\delta\varphi_0\sigma_z^q$ originates from the inductive interaction with $\delta\varphi_0 = \pi M_q I_{cir}/\Phi_0 \approx 0.002$ with experimental parameters, where $M_q = 8\,\mathrm{pH}$ is the mutual inductance and $I_{cir} = \langle I_1 \rangle$ is the circulating current of the qubit state. Corresponding to the two qubit states, the lowest oscillator states are $\langle \varphi_m | \psi_g^{\pm} \rangle = e^{\pm i\delta\varphi_0 \hat{P}_m/\hbar}\psi_0(\varphi_m)$ respectively, where $\psi_0(\varphi_m) = (2\pi\langle\varphi_m^2\rangle)^{-\frac{1}{4}} e^{-\frac{\varphi_m^2}{4\langle\varphi_m^2\rangle}}$. The width of the wave functions of these states is $\sqrt{\langle\varphi_m^2\rangle} = \sqrt{\frac{\hbar}{2m_m\omega_m}} \approx 0.1$. These two states overlap with each other as $\langle\psi_g^-|\psi_g^+\rangle = e^{-\frac{\delta\varphi_0^2}{2\langle\varphi_m^2\rangle}} \approx 1 - 0.0002$. In this experiment, the measurement of the qubit becomes the detection and resolution of these two largely-overlapping, highly non-orthorgonal oscillator states. The consequence of the overlapping is the intrinsic limits to measurement efficiency (A quanlitative definition of the measurement efficiency is how many bits of information, which is always less than one, is derived from a measurement).

To measure the probability of each eigenstates in a qubit state, we study the density matrix of the dc SQUID when the qubit state is $|\psi_q\rangle = c_0|0_q\rangle + c_1|1_q\rangle$. With the inductive coupling, the density matrix of the dc SQUID quickly relaxes to $\rho_m = |c_0|^2|\psi_g^+\rangle\langle\psi_g^+| + |c_1|^2|\psi_g^-\rangle\langle\psi_g^-|$, which is a mixed state of the overlapping states $|\psi_g^{\pm}\rangle$. Let the desired measurement accuracy be A_m. For a von Neumann measurement, within N measurements, the average time we find $|0\rangle$ is $|c_0|^2 N$ and the deviation is $\Delta N/N = 1/(2\sqrt{N})$. The accuracy of the measured $|c_0|^2$ increases with the number of the measurements. $N_v = 1/(2A_m)^2$ repetitions are required to achieve accuracy A_m. For a measurement with overlapping distributions, we assume each distribution is a Gaussian to simplify the analysis. Let the Gaussians have slightly different averages y_0 and y_1 and a deviation σ with $|y_1 - y_0| \ll \sqrt{\sigma}$: $y = \frac{1}{\sqrt{2\pi\sigma}} e^{-\frac{(y-y_i)^2}{2\sigma}}$. With the given qubit state, the average of the measured distribution is $y_{ave}^{exp} = |c_0|^2 y_0 + |c_1|^2 y_1$. By measuring this average we can infer $|c_0|^2$ of the qubit state. The accuracy of the measured average y_{ave} is the accuracy we can achieve for the probability $|c_0|^2$. According to the Central Limit Theorem, with $y_{ave} = \frac{1}{N}\sum_{k=1}^{N} y_k$, the average y_{ave} in N measurements obeys a Gaussian distribution with an average y_{ave}^{exp} and a deviation σ/N. The relative accuracy with N measurements is $\Delta y_{ave}/|y_1 - y_0| = \sqrt{\sigma/N|y_1 - y_0|^2}$.

$N_p = \frac{4\sigma}{|y_1-y_0|^2}N_v$ repetitions are required to achieve accuracy A_m. In the previous experiment, $2\sqrt{\sigma}/|y_1 - y_0| = 50$, so $N_p/N_v = 2500$ is required to get satisfactory result.

This shows that the dc SQUID measurement on the pc-qubit is not an efficient measurement. The detection of the weak flux of the pc-qubit prevents the efficient derivation of qubit information. To get a more efficient measurement, we should either encode information in the pc-qubit in some other way or measure the qubit states with another method as described below.

3.6.2 Entanglement assisted measurement

Given two eigenstates of a Hamiltonian, a projective measurement that maps the two qubit states into distinct macroscopic states can always be constructed according to Newwark's theorem[100]. But in reality, the measurement is usually the direct detection of physical observables such as the flux or charge signal of the qubit states. It is not obvious that we can build a measurement that effectively measures the pc-qubit. In the following, we present a new measurement procedure for the pc-qubit that improves on the previous measurement significantly.

The idea is that instead of detecting the direct effect of the qubit's flux on the detector (splitting of the SQUID wave function as in Eq.3.27), we entangle the qubit with a second quantum system that behaves as an effective quantum two level system (ETLS). The flux or charge difference between these two levels is designed to be much larger than the quantum broadening of the quantum detector. Then we measure the second system which exactly reflects the qubit state.

Let the pc-qubit interacts with this supplementary system via inductive interaction. Assume the following Hamiltonian for the qubit and the ETLS,

$$\mathcal{H} = \frac{\hbar\omega_0}{2}\sigma_z^q + \frac{\hbar\omega_a}{2}\sigma_z^a + \frac{\hbar\omega_\Delta}{2}\sigma_z^q\sigma_z^a \tag{3.28}$$

where ω_0 is the energy splitting of the qubit states, ω_a is the energy splitting of the ETLS, and ω_Δ comes from the inductive interaction. σ_z^q and σ_z^a represent the two

level systems of the qubit and the ETLS respectively. The energy levels are shown in Fig.3-8 (c). During regular computation, we store the supplementary system at state $|0_a\rangle$. Due to the inductive coupling, the qubit energy is modified as $E_{1_q 0_a} - E_{0_q 0_a} = \hbar\omega_0 - \hbar\omega_\Delta$. By applying local oscillation of $\hbar\Omega_R \sigma_x^q$ at the qubit energy, single qubit gates can be achieved. In the process, the ETLS stays in its ground state and has trivial dynamics. To measure the qubit state, a local operation on the supplementary system is applied to entangle the two systems. With the presence of the qubit, we have: $E_{0_q 1_a} - E_{0_q 0_a} = \hbar\omega_a - \hbar\omega_\Delta$ and $E_{1_q 1_a} - E_{1_q 0_a} = \hbar\omega_a + \hbar\omega_\Delta$. By applying a pulse of $\hbar\Omega_X \sigma_x^a$ at the frequency $\omega_a + \omega_\Delta$, resonant transition between the ETLS occurs when the qubit is at state $|1_q\rangle$. The system is designed with $\omega_\Delta \gg \Omega_X$ so that off-resonant transitions at $|0_q\rangle$ are negligible. After a π-pulse, the ETLS becomes completely entangled with the qubit,

$$(c_0|0_q\rangle + c_1|1_q\rangle)\,|0_a\rangle \rightarrow c_0|0_q\,0_a\rangle + ic_1|1_q\,1_a\rangle \tag{3.29}$$

The density matrix of this system is $\rho_a = |c_0|^2|0_a\rangle\langle 0_a| + |c_1|^2|1_a\rangle\langle 1_a|$ and ρ_a is then measured by a detector. Note that the secondary system may not be a good qubit candidate itself as it couples strongly with the environment due to the large flux or charge signal, but the coupling can be measured easily due to its large flux or charge signal.

In this design, we choose an rf SQUID to be the supplementary system that inductively couples with the qubit. The circuit is shown in Fig. 3-8(a): the pc-qubit, the rf SQUID, and the magnetometer. In the following, we adopt the rf SQUID parameters as in Ref. [28, 56] where the coherent manipulation of the system states have been achieved. Typical SQUID parameters are: $L_{rf} = 154\,\text{pH}$, $I_c = 4\,\mu\text{A}$, $C_J = 40\,\text{fF}$, $E_J/E_C \approx 4000$. The inductance of the rf SQUID is much larger than that of the qubit, which has two consequences: the flux difference between the states localized at different potential wells is of order of half a flux quantum and can be resolved easily by a magnetometer; the coupling between the rf SQUID and environmental noise is strong, so that it is harder to keep the coherence of the rf SQUID and to choose

the rf SQUID as a qubit. At $\beta_L = 2\pi L_{rf} I_c/\Phi_0 \approx 1.9$, the rf SQUID has a double well potential with several eigenstates localized in each of the potential wells. The potential energy of the rf SQUID is shown in Fig. 3-8(b) with the eigen levels. By controlling the parameters of the rf SQUID, there exists an effective two level system as is indicated by the up and down arrows in the figure. The currents of these two states differ by $\Delta I \approx I_c$ which results in a flux difference of $\Delta\Phi_{rf} = \Delta I L_{rf} \approx 0.3\Phi_0$. For Eq. 3.28, we choose $\omega_0 = 13\,\mathrm{GHz}$ and $\omega_a = 11\,\mathrm{GHz}$. By adjusting the mutual inductance coupling to be $M_q/L_q = 1/4$, we have $\omega_\Delta = 3\,\mathrm{GHz}$. The equivalent four-level system is shown in Fig. 3-8(c) with their energies labeled beside each level. The complete energy spectrum of the rf SQUID over a large range of flux is plotted in Fig. 3-9.

The rf SQUID is stored at the state $|0_a\rangle$[28] by suddenly switching the flux in the loop. The qubit energy is $E_{1_q 0_a} - E_{0_q 0_a} = 10\,\mathrm{GHz}$ and single qubit operation is implemented with local rf pulse at this frequency. During this operation, the rf SQUID has trivial dynamics. In the beginning of a measurement, a local rf source with frequency $E_{1_q 1_a} - E_{1_q 0_a} = 14\,\mathrm{GHz}$ is applied to the rf SQUID for a π rotation. This pulse flips the SQUID state when the qubit is at $|1_q\rangle$. When the qubit is at state $|0_q\rangle$, $E_{0_q 1_a} - E_{0_q 0_a} = 8\,\mathrm{GHz}$ and is off-resonance with the pulse. With an amplitude of 0.0005 flux quantum, the π pulse takes 10 nsec with the rotating frequency $\omega_X = 50\,\mathrm{MHz}$. Hence the off resonant transition at $|0_q\rangle$ is at most 10^{-4}, and is negligible for the measurement. After the entanglement, the rf SQUID is measured by a magnetometer. A simple dc SQUID magnetometer is shown in Fig. 3-8 (a). The magnetometer can be improved by using radio-frequency devices[122].

In designing the rf SQUID, attention should be paid to several issues for the successful implementation of this measurement. First, the two states of the rf SQUID have an energy difference well below the gap energy of the superconductor so that no quasiparticle is excited during the CNOT operation. Also, the two level system should be well separated from other states so that no off-resonant leakage to other levels happens during the rf pulse. In our design, the two states are at least 40 GHz away from other states. And the off-resonant transitions can be ignored with the

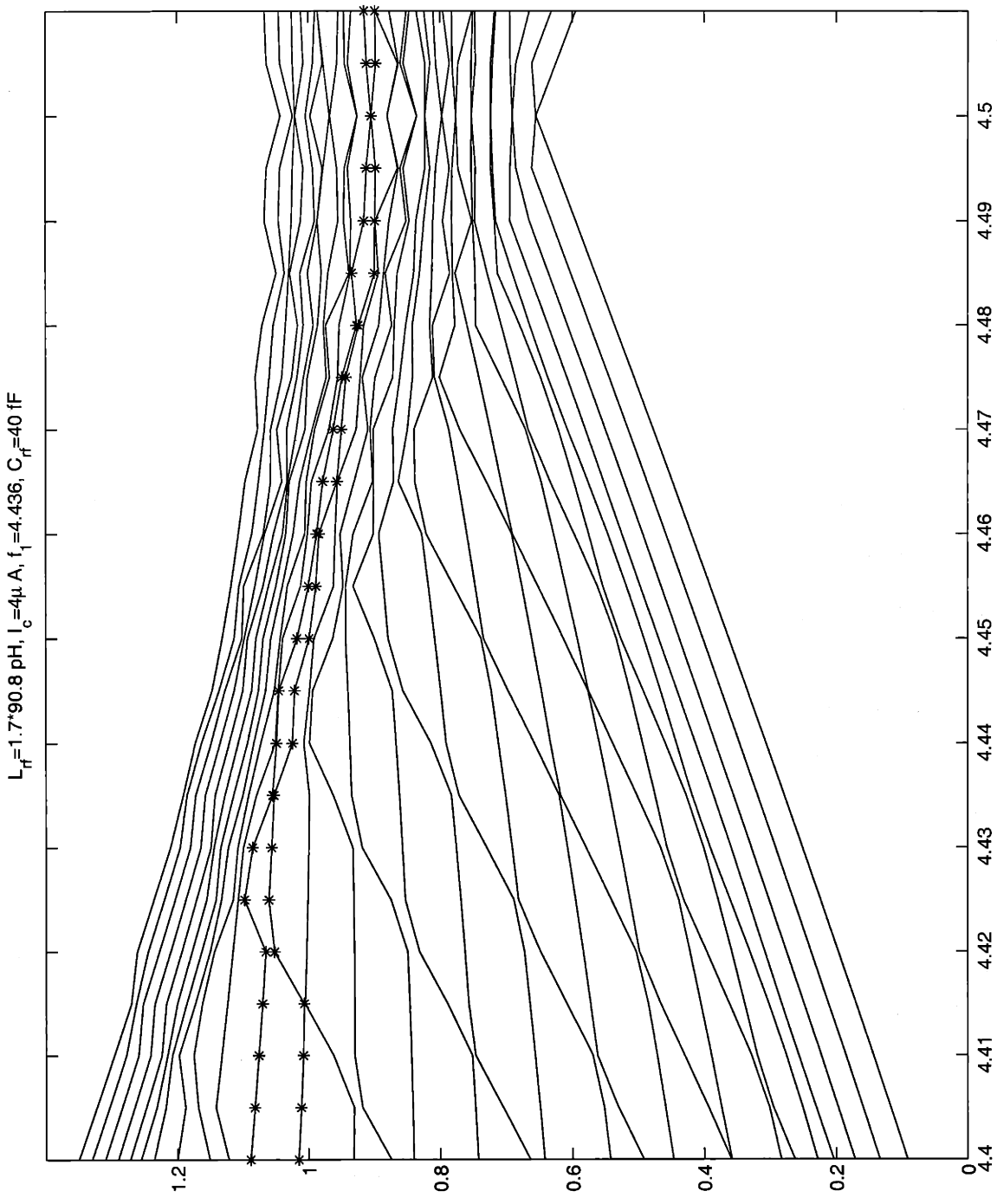

Figure 3-9: The energy of the rf SQUID versus flux. The parameters of the rf SQUID are on the top of the figure. The x axis is the flux in the rf SQUID loop; the y axis is the eigenenergies of the SQUID states versus the flux. The two energy bands labelled with stars are the ancilla qubit's states.

given rf pulse strength. Finally, a trivial but crucial point, the parameters have to be realistic for the sample. We base this design on existing experiments[28, 56].

3.6.3 Discussion on extra noise and conclusion

With the giant self-induced flux of 1 flux quantum, the rf SQUID is subjected to a strong perturbation by the environment, such as randomly trapped flux, impurity spins and nuclear spins. However, fortunately, the noise does not affect the qubit during regular qubit operations. The flux-like noise adds to Eq. 3.28 a term $\sigma_z^a f(t)$ which perturbs the energy levels of the SQUID up and down randomly. As the rf SQUID stays at $|0_a\rangle$ during the qubit operations, this term only contributes as an overall phase to the wave function of the interacting system and does not decohere the qubit. For environmental degrees that assume σ_x^a coupling with the rf SQUID, the environmental modes with the frequency around 10 GHz can flip the rf SQUID in principle. But in reality, this noise couples with the qubit much weaker than the σ_z^a noise. At the low temperature of 20 mK, there are no excitations in these modes to excite the rf SQUID from the ground state to the second level. During the entanglement operation, the rf SQUID makes transition from $|0_a\rangle$ to $|1_a\rangle$, and the noise affects the dynamics of the rf SQUID. To ensure the successful implementation of the measurement, it is important for the gate time to be shorter than the decoherence time of the rf SQUID[123].

In conclusion, we present the design for a measurement on the pc-qubit that significantly improves the measurement efficiency. By a qubit-controlled resonant transition of the rf SQUID, the qubit information is conveyed to the rf SQUID which has a flux signal of half a flux quantum. The subsequent measurement on the rf SQUID by a magnetometer can resolve its state with one measurement. This design projects the eigenstates of the qubit into macroscopically distinct states of the magnetometer and efficiently obtains qubit information. Compared with the previous experiment[29], this method avoids the difficulty of measuring 10^{-3} flux quantum by a quantum detector whose quantum width is 0.1 flux quantum. This measurement can also be regarded as a first attempt in implementing a CNOT gate on the superconducting

flux qubits to realize a quantum algorithm. Although we choose to couple the qubit inductively to an rf SQUID in this chapter, other supplementary systems can also be used with a different interaction mechanism and different detection technology.

3.7 Conclusions

In this chapter, we studied the measurement of the pc-qubit by a dc SQUID in terms of the quantized SQUID Hamiltonian. During the premeasurement entanglement process, the SQUID is modeled as two oscillators. Then, the SQUID switches to a finite voltage state via tunneling. We derived the upper limit to the mutual information that can be achieved in one switching event. This gives a natural limitation for the direct detection of the qubit flux. Besides information, the measurement process also transfers additional noise to the qubit from the SQUID's environment. We calculated the noise transferred to the pc-qubit with the Caldeira-Leggett formalism and estimated the relaxation and decoherence of the qubit due to this noise. This study suggests that a better readout circuit can be designed to optimize the measurement within the qubit-SQUID coupling scheme. Hence, we propose a radiation-assisted measurement at the end of this chapter which substantially improves the measurement efficiency.

When calculating the transferred noise, we map the linearized Hamiltonian of the interacting qubit-SQUID system to a linear circuit. By calculating the impedance of this circuit, the noise spectrum can be derived directly. This approach can be applied to an arbitrary external system, including a measurement circuit, control circuit *etc.* Note that this linear circuit can not be derived directly from the physical circuit of the interacting systems, but is derived from the linearized Hamiltonian. Several other impedance environments were examined from a direct circuit analysis[97] which is valid in the specific parameter range of the experiment[29] with $\omega_m \gg \omega_0$.

The inductive coupling between the qubit and the SQUID contributes σ_z noise to the qubit. As $[\sigma_z, \mathcal{H}_q] \neq 0$, this noise induces damping as well as decoherence. We found that when the measurement is on, relaxation is reasonably slow and will not prevent the collection of accurate information of the qubit; when the measurement is

off, the SQUID introduces negligible noise to the qubit. A more comprehensive study of this structured environment shows that when the qubit frequency is close to the plasma frequency of the external oscillator, the structure of the environment affects the relaxation and decoherence in a complex way[96].

This study also brings up a general question in quantum information processing: how to divide the system from the environment during any information exchange between the quantum system and an external control device, such as a detector, a controller or another qubit. To calculate the noise transferred to the qubit, the SQUID and its environment form an effective environment with spectrum J_{eff}. However, in order to determine the information obtained in the measurement, the qubit and the SQUID's inner oscillator must be treated as a joint quantum system in its own right.

Chapter 4

Environmental Fluctuations

The power of quantum logic[77] depends on the coherence of the qubit[10] and on the accurate manipulation of quantum logic. To successfully realize quantum algorithms, a quantum computer needs to be both very well isolated from the external world and to be very accurately controlled by an external program. Otherwise, quantum errors that are lethal to quantum computing will occur during the process of computation. Errors can occur during any process, even during the quantum storage process when the qubit network is supposed to have trivial dynamics. The errors can either come from environmental fluctuations that weakly couple with the qubit, or come from the imperfectness of the controlled operations.

The theory of quantum error correction provides a remedy to the decoherence effect. It was shown[124] that quantum errors can be corrected by encoding the qubits with certain linear codes based on group theory proofs. By measuring the error syndrome of the encoded qubit and applying state-recovering quantum operations according to the measured syndrome, any independent qubit errors can be corrected. To make sure this method works when the error also occurs during the error correction process, fault-tolerant design of the error correction is required. In the fault-tolerant quantum computing scheme, although error occurs in the error correction procedure, the error can not propagate to qubits in the same encoded block. As a result, as far as the probability of error is kept below a threshold, large scale quantum computing can be realized. This threshold requires that the so-called "quality factor" of the qubit,

the number of quantum operations performed during the qubit decoherence time, should be at least 10^4 to allow fault-tolerant quantum computation[124, 125, 126].

Decoherence is an especially vital issue in solid state qubit designs, due to many kinds of low energy excitations in the solid state environment that may couple to qubit states and cause dephasing. A solid-state system is a complicated many-body system. To construct the qubit state, we choose an effective two level system from the solid-state sample. There are many other degrees of freedom that interact with qubit states. The interaction, although designed to be weak, affects the qubit dynamics and acts as source of decoherence. It is important to study the effect of the environment on the qubit dynamics and to estimate the quality factor for a concrete qubit design.

In this chapter, we will first present a general formalism to study the environmental noise in solid state systems. Then we apply the formalism to estimate some of the main sources of decoherence in the supercondutcing persistent-current, including the background charge fluctuations, nuclear fluctuations, and quasiparticle conduction. The approach will be presented in a way making it easy to generalize it to other systems. We emphasize those decoherence mechanisms that illustrate this approach. We will also study the interaction between the pc-qubit and electromagnetic radiation. The interaction results in radiation decay of the qubit. The decay rate is calculated with a perturbation approach. Dipole interaction between qubits causes the oscillation of qubit energy and induces additional phase to the qubit dynamics. We will also study the effect of this interaction and introduce a method to reduce the interaction. Finally, we will summarize our results by categorizing different noise according to their dephasing times and their noise correlation time and discussing the potential method of controlling the noise in the different categories where it occurs.

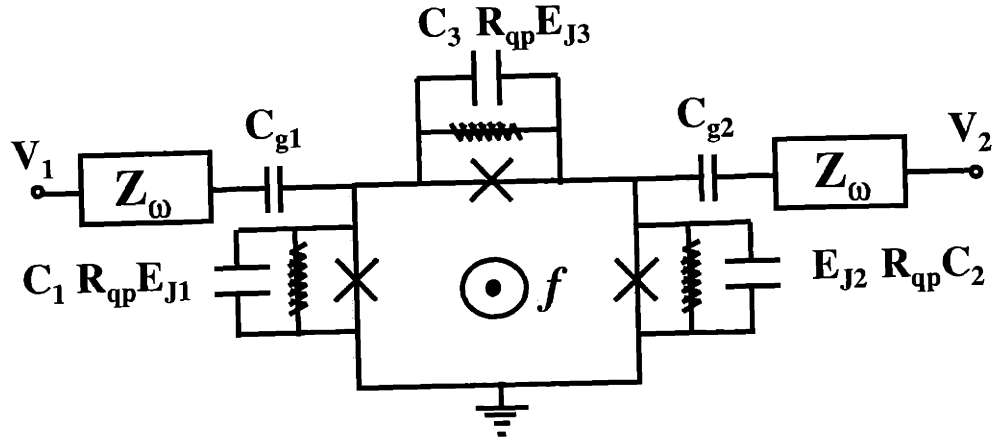

Figure 4-1: Schematic qubit design[20, 25] consisting of three Josephson junctions connected as shown. Josephson energy of one of the junctions (number 3 in the figure) is adjustable by varying the flux in the SQUID loop. The impedances Z_ω model the electromagnetic environment coupled to the qubit via gate capacitances $C_{g(1,2)}$. Shunt resistors model the quasiparticle subgap resistance effect.

4.1 Classical Fluctuations

4.1.1 Model

The pc-qubit[20, 25] consists of three small Josephson junctions which are connected in series, forming a loop, as shown in Fig. 4-1. The charging energy of the qubits $E_C = e^2/2C_{1,2}$ is ~ 100 times smaller than the Josephson energy $E_J = \hbar I_0/2e$, where I_0 is the qubit Josephson critical current. The junctions discussed in [20, 25] are 200 nm by 400 nm, and $E_J \approx 200$ GHz.

The qubit is realized by the two lowest energy states of the system corresponding to opposite circulating currents in the loop. The energy splitting of these states $\varepsilon_0 \approx 10$ GHz is controlled by the external magnetic field flux f, the barrier height is $\simeq 35$ GHz and the tunneling amplitude between the two states is $t \approx 1$GHz. The Hamiltonian derived in[20, 25] for the two lowest energy levels of the qubit has the

form

$$\mathcal{H}_0 = \begin{pmatrix} -\varepsilon_0/2 & t(q_1,q_2) \\ t^*(q_1,q_2) & \varepsilon_0/2 \end{pmatrix} , \tag{4.1}$$

where $t(q_1,q_2)$ is a periodic function of the gate charges $q_{1,2}$. In the tight binding approximation [20, 25], $t(q_1,q_2) = t_1 + t_2 e^{-i\pi q_1/e} + t_2 e^{i\pi q_2/e}$, where t_1 is the amplitude of the tunneling between the nearest energy minima and t_2 is the tunneling between the next nearest neighbor minima in the model[20, 25]. Both t_1 and t_2 depend on the energy barrier height and width exponentially. With the parameters of our qubit design, $t_2/t_1 < 10^{-3}$, the effect of the fluctuations of $q_{1,2}$ should be small.

Below, we consider a number of decoherence effects which seem to be most relevant for the design[20, 25], trying to keep the approach general enough, so that it can be applied to other designs.

4.1.2 Basic Approach

We start with a Hamiltonian of a qubit coupled to environmental degrees of freedom in the solid: $\mathcal{H}_{\rm total} = \mathcal{H}_{\rm Q}(\vec{\sigma}) + \mathcal{H}_{\rm bath}(\{\xi_\alpha\})$, where $\mathcal{H}_{\rm Q} = \mathcal{H}_0 + \mathcal{H}_{coupling}$:

$$\mathcal{H}_{\rm Q} = \frac{\hbar}{2}\left(\vec{\Delta}(t) + \vec{\eta}(t)\right)\cdot\vec{\sigma} , \qquad \vec{\eta} = \sum_\alpha \vec{A}_\alpha \hat{\xi}_\alpha , \tag{4.2}$$

where $\vec{\sigma} = (\sigma_x, \sigma_y, \sigma_z)$ is the vector of Pauli matrices acting on the qubit states, the vector $\vec{\Delta}$ represents an external control function, and $\vec{\eta}$ is the noise due to coupling to the bath variables ξ_α. In (4.1), $\Delta_z = -\varepsilon_0$, $\Delta_x - i\Delta_y = t(q_1,q_2)$.

The degrees of freedom that may decohere the qubit dynamics are:

- charge fluctuations in the gates coupling qubit states to other states;
- quasiparticles in the superconductor giving rise to subgap resistance;
- nuclear spins in the solid creating fluctuating magnetic fields;
- electromagnetic radiation causing damping of Rabi oscillations;
- coupling between qubits affecting operation of an individual qubit.

In all cases except the last one, the qubit is coupled to a macroscopic number of degrees of freedom $N \gg 1$ with about the same strength A_α to each. In such a situation, the qubit decoherence rate is much larger than the characteristic individual coupling frequency $A_\alpha/\hbar$. This means that dephasing happens on a shorter time scale than it would have taken to create an entangled state of the qubit with one particular element of the bath. In other words, on the decoherence time scale each element of the bath remains in its initial state with probability $1 - O(1/N)$, and it is only due to a large number of relevant degrees of freedom N that the state of the qubit is significantly affected on this time scale.

This observation makes the analysis quite simple, especially because the condition $N \gg 1$ allows one to replace quantum variables $\eta_{x,y,z}(t)$ by classical fields fluctuating in time. (Because all commutators $[\eta_i(t), \eta_j(t')] = O(1/N) \to 0$.) As a result, the problem becomes equivalent to that of longitudinal and transverse spin relaxation times T_1 and T_2 in NMR, corresponding to the noise $\eta_i(t)$ either flipping the qubit spin, or contributing a random phase to the qubit states evolution, respectively. Thus we can use the standard Debye–Bloch theory of relaxation in two-level systems.

To adapt this theory to our problem, we assume, without loss of generality, that $\vec{\Delta}(t) \parallel \hat{z}$ and is constant as a function of time. Then one can eliminate the term $\frac{1}{2}\vec{\Delta} \cdot \vec{\sigma}$ by going to the frame rotating around the $z-$axis with the Larmor frequency $\Delta = |\vec{\Delta}|$. In the rotating frame the Hamiltonian (4.2) becomes:

$$\widetilde{\mathcal{H}}_{\mathrm{Q}} = \frac{\hbar}{2}\left(\eta_{\parallel}(t)\sigma_z + e^{-i\Delta t}\eta_{\perp}(t)\sigma_+ + e^{i\Delta t}\eta_{\perp}^*(t)\sigma_-\right) , \tag{4.3}$$

where $\eta_{\parallel}(t)$ and $\eta_{\perp}(t)$ correspond to components of vector $\vec{\eta}(t)$ in (4.2) parallel and perpendicular to $\vec{\Delta}$, respectively.

The time evolution due to noise $\vec{\eta}(t)$ is given by the evolution operator

$$\mathrm{Texp}\left(-i\int \widetilde{\mathcal{H}}_{\mathrm{Q}}(t')dt'\right) \tag{4.4}$$

written in the rotating Larmor basis. However, for a simple estimate below, we ignore noncommutativity of different parts of the Hamiltonian (4.3), and consider a

c-number phase factor instead of an operator exponent.

Then the decoherence can be characterized using the function

$$R(t) = \max\left[\langle\phi_{\|}^2(t)\rangle,\, \langle|\phi_{\perp}(t)|^2\rangle\right] , \tag{4.5}$$

where $\langle ...\rangle$ stands for ensemble average, and

$$\phi_{\|}(t) = \int_0^t \eta_{\|}(t')dt' , \qquad \phi_{\perp}(t) = \int_0^t e^{-i\Delta t'}\eta_{\perp}(t')dt' . \tag{4.6}$$

The function $R(t)$ grows with time, and one can take as a measure of decoherence the time τ for which $R(\tau) \simeq 1$. It is easy to justify neglecting noncommutativity of evolution due to (4.3) at short times, when $R(t) \ll 1$. The condition $R(\tau) \simeq 1$ thus gives a correct order of magnitude estimate of the decoherence time τ. Note that this estimate is a result of an ensemble average over many qubits. Although this is usually a good lower bound for the decoherence of a single qubit, care needs to be taken in the interpretation of τ when the bath is "frozen" into a particular configuration so that the ensemble averaging does not apply, as in the case of coupling to the nuclear spins.

Since $\vec{\eta} = \sum_\alpha \vec{A}_\alpha \hat{\xi}_\alpha(t)$, it is the time evolution of $\hat{\xi}_\alpha(t)$ defined by $\mathcal{H}_{\rm bath}$ that is what eventually leads to decoherence. One can express quantities of interest in terms of the noise spectrum of the components of $\vec{\eta}$:

$$\langle\phi_{\|}^2(t)\rangle = \int d\omega \frac{|1-e^{i\omega t}|^2}{2\pi\omega^2}\langle\eta_{\|}(-\omega)\eta_{\|}(\omega)\rangle \tag{4.7}$$

$$\langle|\phi_{\perp}(t)|^2\rangle = \int d\omega \frac{|1-e^{i\omega t}|^2}{2\pi\omega^2}\langle\eta_{\perp}(-\omega-\Delta)\eta_{\perp}(\omega+\Delta)\rangle . \tag{4.8}$$

In thermal equilibrium, by virtue of the Fluctuation–Dissipation theorem, the noise spectrum in the RHS of (4.7) and (4.8) can be expressed in terms of the out-of-phase part of an appropriate susceptibility.

Here we discuss the above listed decoherence mechanisms and use the expressions (4.7) and (4.8) to estimate the corresponding decoherence times.

4.1.3 Charge Fluctuations

We start with the effect of **charge fluctuations on the gates** due to electromagnetic coupling to the environment modeled by an external impedance Z_ω (see Fig. 4-1), taken below to be of order of 400Ω, the vacuum impedance.

The dependence of the qubit Hamiltonian on the gate charges $q_{1,2}$ is given by (4.1), where the $q_{1,2}$ vary in time, in response to the fluctuations of gate voltages, $\delta q_{1,2} \approx C_g \delta V_{g(1,2)}$, where the gate capacitance is much smaller than the junction capacitance: $C_g \ll C_{1,2}$. The gate voltage fluctuations are given by the Nyquist formula: $\langle \delta V_g(-\omega)\delta V_g(\omega)\rangle = 2Z_\omega \hbar\omega \coth \hbar\omega/kT$.

In our design, $|t(q_1,q_2)| \ll \varepsilon_0$, and therefore fluctuations of $q_{1,2}$ generate primarily transverse noise $\eta_\perp$ in (4.3), $\eta_\perp(t) \simeq (\pi/\hbar e) t_2 C_g \delta V_g(t)$. In this case, according to (4.8), we are interested in the noise spectrum of δV_g shifted by the Larmor frequency Δ. Our typical $\Delta \simeq 10\,\mathrm{GHz}$ is much larger than the temperature $k_B T/h = 1\,\mathrm{GHz}$ at $T = 50\,\mathrm{mK}$, and thus one has $\omega \simeq \Delta \gg kT/\hbar$ in the Nyquist formula.

The Nyquist spectrum is very broad compared to the Larmor frequency and other relevant frequency scales, and thus in (4.8) we can just use the $\omega = \Delta$ value of the noise power. Evaluating the integral $\int |(1-e^{i\omega t})/\omega|^2 d\omega = 2\pi t$, we obtain

$$R(t) = \langle |\phi_\perp(t)|^2 \rangle = \frac{2t}{\hbar}\left(\frac{\pi}{e} t_2 C_g\right)^2 \Delta Z_{\omega=\Delta}\,. \tag{4.9}$$

Rewriting this expression as $R(t) = t/\tau$, we estimate the decoherence time as

$$\tau = \Delta^{-1} \frac{\hbar}{2e^2} Z^{-1}_{\omega=\Delta} \left(\frac{e^2}{\pi C_g t_2}\right)^2 \tag{4.10}$$

where $\hbar/2e^2 \simeq 4\,\mathrm{k}\Omega$. In the qubit design $e^2/2C_g \simeq 100\,\mathrm{GHz}$, and $t_2 \simeq 1\,\mathrm{MHz}$ when $t_2/t_1 \leq 10^{-3}$. With these numbers, one has $\tau = 10\,\mathrm{sec}$.

4.1.4 Quasiparticles

The next effect we consider is dephasing due to **quasiparticles on superconducting islands**. At finite temperature, quasiparticles are thermally activated above the

superconducting gap Δ_0, and their density is $\sim \exp(-\Delta_0/kT)$. The contribution of quasiparticles to the Josephson junction dynamics can be modeled as a shunt resistor, as shown in Fig. 4-1. The corresponding *subgap resistance* is inversely proportional to the quasiparticle density, and thus increases exponentially at small temperatures: $R_{\rm qp} \approx R_n \exp \Delta_0/kT$, where R_n is the normal state resistance of the junction. For a Josephson current $I_0 = 0.2\mu$A, $R_n \approx 1.3\,\mathrm{k}\Omega$. At low temperatures the subgap resistance is quite high, and thus difficult to measure[127]. For estimates below, we take $R_{\rm qp} = 10^{11}\Omega$ which is much smaller than what follows from the exponential dependence for $T = 50\,\mathrm{mK}$.

The main effect of the subgap resistance in the shunt resistor model is generating normal current fluctuations which couple to the phase of the junction. The Hamiltonian describing this effect is

$$\mathcal{H}^{\rm qp}_{\rm coupling} = \sum_i \frac{\hbar}{2e}\varphi_i I_i^{\rm qp}(t)\ , \tag{4.11}$$

where $i = 1, 2, 3$ labels the Josephson junctions. Projecting (4.11) onto the two qubit states, one obtains the Hamiltonian (4.2) with $\eta_z(t) = I_i^{\rm qp}(t)/2e$, $\eta_{x,y} = 0$.

The noise spectrum of the quasiparticle current is given by the Nyquist formula:

$$\langle I^{\rm qp}(-\omega) I^{\rm qp}(\omega)\rangle = 2R_{\rm qp}^{-1}\hbar\omega\coth(\hbar\omega/kT) \tag{4.12}$$

After rotating the basis and transforming the problem to the form (4.3) we have $\eta_\perp(t) \simeq (t_1/\varepsilon_0)\eta_\parallel(t)$, where $\eta_\parallel(t) \simeq I_i^{\rm qp}(t)/2e$ since $t_1 \ll \varepsilon_0$.

The analysis of $\langle|\phi_\perp(t)|^2\rangle$ and $\langle|\phi_\parallel(t)|^2\rangle$ is similar to that described above for charge fluctuations on the gates, and one obtains $R_\perp(t) = t(t_1/\varepsilon_0)^2\hbar\Delta/(2e^2R_{\rm qp})$, and $R_\parallel(t) = t\,kT/(2e^2R_{\rm qp})$ which gives

$$\tau = \min\left[\tau_\perp, \tau_\parallel\right] = \min\left[\frac{2e^2R_{\rm qp}}{\hbar\Delta}\left(\frac{\varepsilon_0}{t_1}\right)^2,\ \frac{2e^2R_{\rm qp}}{kT}\right] \tag{4.13}$$

Taking $R_{qp} = 10^{11}\,\Omega$, $T = 50\,\mathrm{mK}$, and $\varepsilon_0/t_1 = 100$, the decoherence times are $\tau_\parallel = 10\,\mathrm{msec}$ and $\tau_\perp = 10\,\mathrm{sec}$.

4.1.5 Nuclear Spins

The decoherence effect of **nuclear spins** on the qubit is due to their magnetic field flux coupling to the qubit inductance. Alternatively, this coupling can be viewed as a Zeeman energy of nuclear spins in the magnetic field $\vec{B}(r)$ due to the qubit. The two states of the qubit have opposite currents, and produce a magnetic field of opposite sign. The corresponding term in (4.2) is

$$\mathcal{H}_{\text{coupling}} = -\sigma_z \sum_{r=r_i} \mu \vec{B}(r) \cdot \vec{\hat{s}}(r) \tag{4.14}$$

where r_i are positions of the nuclei, μ is nuclear magnetic moment and $\hat{s}(r_i)$ are spin operators.

Nuclei are in thermal equilibrium, and their spin fluctuations can be related to the longitudinal relaxation time T_1 by the Fluctuation-Dissipation theorem. Assuming that different spins are uncorrelated, one has

$$\langle s_\omega(r) s_{-\omega}(r) \rangle = 2k_B T \frac{\chi''(\omega)}{\omega} = \frac{2k_B T_1 \chi_0}{1+\omega^2 T_1^2} , \tag{4.15}$$

where $\chi_0 = 1/k_B T$ is the static spin susceptibility.

The spectrum (4.15) has a very narrow width set by the long relaxation time T_1. This width is much less then $k_B T$ and Δ. As a result, only longitudinal fluctuations $\eta_{||}$ survive in (4.7) and (4.8). One has

$$\langle \phi_{||}^2(t) \rangle = \int d\omega \frac{|1-e^{i\omega t}|^2}{2\pi\hbar^2\omega^2} \sum_{r=r_i} \mu^2 B^2(r) \langle s_\omega(r) s_{-\omega}(r) \rangle . \tag{4.16}$$

Plugging the spectrum (4.15) in (4.16) and integrating, one obtains

$$R(t) = \frac{T_1}{\tau_0^2} \left(|t| - T_1 + T_1 e^{-|t|/T_1} \right), \tau_0 = \left(\int \frac{2\mu^2}{\hbar^2} n(r) B^2(r) d^3 r \right)^{-1/2} , \tag{4.17}$$

where $n(r)$ is the nuclei concentration. The **ensemble-averaged** decoherence time

that is defined by $R(\tau) \simeq 1$ is then estimated as:

$$\tau = \begin{cases} \tau_0, & \text{for} \quad T_1 > \tau_0 \\ \tau_0^2/T_1, & \text{for} \quad T_1 < \tau_0 \end{cases} . \tag{4.18}$$

In superconducting Al, nuclear spin relaxation time is strongly varying with temperature: $T_1 \simeq (300/T\,[K])e^{\Delta/k_BT}$ sec. At $T = 50\,\text{mK}$, the time T_1 is of order of minutes, which exceeds all time scales relevant for qubit operation. To estimate τ_0, we use the magneton $\mu \simeq e\hbar/Mc$, where M is proton mass, and $\int B^2(r)d^3r \simeq 10^{-5}\Phi_0^2/w$, where $w \simeq 0.5\,\mu\text{m}$ is the thickness of Al wires in the circuit, and $\Phi_0 = hc/2e$ is the flux quantum. The resulting $\tau_0 \simeq 3 \times 10^{-8}\,\text{sec} \ll T_1$.

According to (4.18), one apparently obtains a worryingly short time $\tau = \tau_0$. However, we note that this result corresponds to ensemble averaging, and one should be careful in applying it to an individual qubit.

The physical picture is that the nuclei spin configuration stays the same over times $\leq T_1$. At such times the perturbation $\vec{\eta}$ due to spins has essentially no time dependence, and so nuclei can be viewed as sources of random *static* magnetic field. The fluxes of this field induced on the qubits depend on initial conditions, and are uncorrelated for different qubits. A typical value of this flux corresponds to the change in the Larmor frequency of order of $\delta\Delta \simeq \tau_0^{-1} \simeq 30\,\text{MHz}$.

To summarize, for an individual qubit the effect of nuclear spins is equivalent to a random detuning caused by a random change in Δ. For an ensemble of qubits, there will be a distribution of Larmor frequencies of width $\delta\Delta \simeq 30\,\text{MHz}$, even if all qubits are identical. However, since the qubit phase can be kept coherent within a time $\leq T_1$, an indirect observation of Rabi oscillations is still possible by using the so-called "spin-echo technique."

A similar theory can be employed to estimate the effect due to magnetic impurities. The main difference is that for impurity spins the relaxation time T_1 is typically much shorter than for nuclear spins. If T_1 becomes comparable to the qubit operation time, the ensemble averaged quantities will describe a *real* dephasing of an individual qubit, rather than effects of inhomogeneous broadening, like for nuclear spins.

4.2 Radiation Decay of PC-Qubit

In the previous section , the environment is treated as a classical fluctuating field whose noise spectrum determines its effect on the qubit dynamics. In this section, we study the effect of a quantized electromagnetic field on the qubit. We use Fermi's Golden rule to study the radiation decay of the pc-qubit in the electromagnetic field. First, we are going to study the decay rate of a single pc-qubit in the electromagnetic filed. We study both the electrical dipolar radiation and the magnetic dipolar radiation, both of which increase with the size of the qubit (though with different orders). We will then apply the method to study the radiation decay of the rf SQUID circuit which has a much larger size than the persistent-current qubit and as a result, a much faster decay.

The electromagnetic field is given by

$$\begin{aligned} E(r) &= \textstyle\sum_{s,k} \hat{i}_s \sqrt{\frac{\hbar\omega_k}{2\epsilon_0 L^3}} \left[\hat{a}_{k,s} e^{ik\dot{r}} + \hat{a}^\dagger_{k,s} e^{-ik\dot{r}}\right] \\ H(r) &= -i \textstyle\sum_{s,k} \hat{i}_k \times \hat{i}_s \sqrt{\frac{\hbar\omega_k}{2\mu_0 L^3}} \left[\hat{a}_{k,s} e^{ik\dot{r}} - \hat{a}^\dagger_{k,s} e^{-ik\dot{r}}\right] \end{aligned} \tag{4.19}$$

where the summation is over all modes in the field, with s beingthe polarization and k being the wave vector. L is the size of the cavity where the sample stays. r is the spatial coordinate in the cavity. As the qubit frequency ω_0 is about 10 GHz, the relevant photon wavelength is much longer than the size of the qubit, and hence the dipole approximation can be applied when studying the transition between qubit states. So in the following, we neglect the field's dependence on the spatial coordinates.

The Hamiltonian of the pc-qubit depends on the external electromagnetic field as:

$$H_t = \frac{(P_p + \frac{\hbar}{2e} C_g V_p)^2}{2M_p} + \frac{(P_m + \frac{\hbar}{2e} C_g V_m)^2}{2M_m} + E_J(-2\cos\varphi_p \cos\varphi_m - \alpha\cos(2\pi f_{ex} + 2\varphi_m)) \tag{4.20}$$

where $P_p = P_1 + P_2$, $P_m = P_1 - P_2$ are the momenta corresponding to the phase variables φ_p and φ_m respectively. C_g is the gate capacitance and $C_g = \gamma C_J$. We have $M_p = 2C_J(1+\gamma)(\frac{\hbar}{2e})^2$ and $M_m = 2C_J(1+2\alpha+\gamma)(\frac{\hbar}{2e})^2$ in Eq. 4.20. The external

electromagnetic environment affects the qubit by causing fluctuations in the gate voltages V_p and V_m ($V_p = V_1 + V_2$, and $V_m = V_1 - V_2$) and in the magnetic flux f_1 in the qubit circuit. The fluctuations include both the zero-point fluctuations and the thermal fluctuations. These fluctuations cause the coherence of the qubit to decay which can be calculated with a perturbation approach.

4.2.1 Magnetic Radiation

The qubit interaction with the magnetic field introduces the following term the Hamiltonian:

$$\delta\mathcal{H}_M = 2\pi\alpha E_J \sin(2\varphi_m + 2\pi f_{ex})\delta f(t) = \hat{I}_{cir}\delta f(t)\Phi_0 = \hat{I}_{cir}R^2\delta B(t) \qquad (4.21)$$

where R is the size of the qubit loop and is about 5 times the size of the qubit junction p. The term $R^2\delta B(t)$ is the fluctuating flux in the qubit loop, and it will cause magnetic dipolar radiation of the qubit. From Fermi's Golden rule, the decay rate is:

$$\Gamma_M = \frac{2\pi}{\hbar}|\langle\Psi_1|\hat{I}|\Psi_2\rangle|^2 R^4 |\langle n=1|B|n=0\rangle|^2 \rho(\hbar\omega_0) = \frac{\mu_0\omega_0^3 R^4}{3\pi c^3\hbar}|\langle\Psi_1|\hat{I}|\Psi_2\rangle|^2 \qquad (4.22)$$

where $|\Psi_1\rangle$ and $|\Psi_2\rangle$ are the qubit states. $\rho(\hbar\omega_0)$ is the density of states at the qubit energy ω_0 and $\rho(\hbar\omega) = L^3\omega^2/3\pi^2\hbar c^3$ in a cavity of size L. The factor 3 comes from the mode in the direction of the coupling field z. Eqn. 4.22 shows that the magnetic dipolar radiation rate is proportional to the fourth square of the loop size R.

4.2.2 Electric Radiation

The electrical field also causes radiation decay. The interaction between the electrical field and the qubit is:

$$\delta\mathcal{H}_E = \frac{\hat{P}_p}{M_p}\frac{\hbar}{2e}C_g\delta V_p + \frac{\hat{P}_m}{M_m}\frac{\hbar}{2e}C_g\delta V_m = \frac{\gamma}{2(1+\gamma)}R\hat{Q}_p\delta E_p + \frac{\gamma}{2(1+2\alpha+\gamma)}R\hat{Q}_m\delta E_m \quad (4.23)$$

where we assume that $\delta V_p = R\delta E_p$ and $\delta V_m = R\delta E_m$, R being the size of the qubit loop. The electrical modes E_p and E_m can be written as the electrical modes in Eqn. 4.19. The charge operators are defined by $\hat{P}_p = \frac{\hbar}{2e}\hat{Q}_p$ and $\hat{P}_m = \frac{\hbar}{2e}\hat{Q}_m$, corresponding to the sum and difference of the charges on the superconducting islands 1 and 2 respectively ($\hat{Q}_p = \hat{Q}_1 + \hat{Q}_2$ and $\hat{Q}_m = \hat{Q}_1 - \hat{Q}_2$). With the Fermi-Golden rule, the spontaneous decay rates are:

$$\begin{aligned}
\Gamma_E^{(p)} &= \frac{2\pi}{\hbar}\left(\frac{\gamma}{2(1+\gamma)}\right)^2 |\langle\Psi_1|\hat{Q}_p|\Psi_2\rangle|^2 R^2 |\langle 1|E_p|0\rangle|^2 \rho(\hbar\omega_0) \\
&= \left(\frac{\gamma}{1+\gamma}\right)^2 \frac{4e^2\omega_0^3 R^2}{12\pi\epsilon_0\hbar^3c^3}|\langle\Psi_1|\hat{P}_p|\Psi_2\rangle|^2 \\
\Gamma_E^{(m)} &= \frac{2\pi}{\hbar}\left(\frac{\gamma}{2(1+2\alpha+\gamma)}\right)^2 |\langle\Psi_1|\hat{Q}_m|\Psi_2\rangle|^2 R^2 |\langle 1|E_m|0\rangle|^2 \rho(\hbar\omega_0) \\
&= \left(\frac{\gamma}{1+2\alpha+\gamma}\right)^2 \frac{4e^2\omega_0^3 R^2}{12\pi\epsilon_0\hbar^3c^3}|\langle\Psi_1|\hat{P}_m|\Psi_2\rangle|^2
\end{aligned} \quad (4.24)$$

both of these radiation rates increase with the square of the size of the qubit loop.

In the pc-qubit, the current operator almost commutes with the Hamiltonian as the qubit states are nearly localized flux states. As a result, the off-diagonal element of the current operator is much smaller than the diagonal element of the current operator which is average current of the eigenstate. This indicates a small magnetic dipolar radiation rate. On the other hand, the electrical dipolar radiation depends on the off-diagonal elements of the momentum operator $P_m/\hbar^2$ and $P_p/\hbar^2$ with $\langle P_p/\hbar^2\rangle = 0$ but $P_m/\hbar^2$ with $\langle P_p/\hbar^2\rangle$ of the order one. This indicates strong radiation by this electrical dipolar coupling. The ratio between electrical and magnetic radiation is:

$$\frac{\Gamma_E^{(m)}}{\Gamma_M} = \frac{(3\times10^8)^2(\gamma/(1+2\alpha+\gamma))^2}{(4\pi\times10^9)^2R^2\times10^{-12}E_J^2}\left|\frac{\langle 2|\hat{I}/I_c|1\rangle}{\langle 2|\hat{P}_m/\hbar^2|1\rangle}\right|^2 \quad (4.25)$$

where R is in units of μm, and E_J is in units of GHz. The electrical dipole radiation is reduced largely by the gate capacitances that are much smaller than the junction capacitances. The gates screen the pc-qubit from the electrical fluctuations.

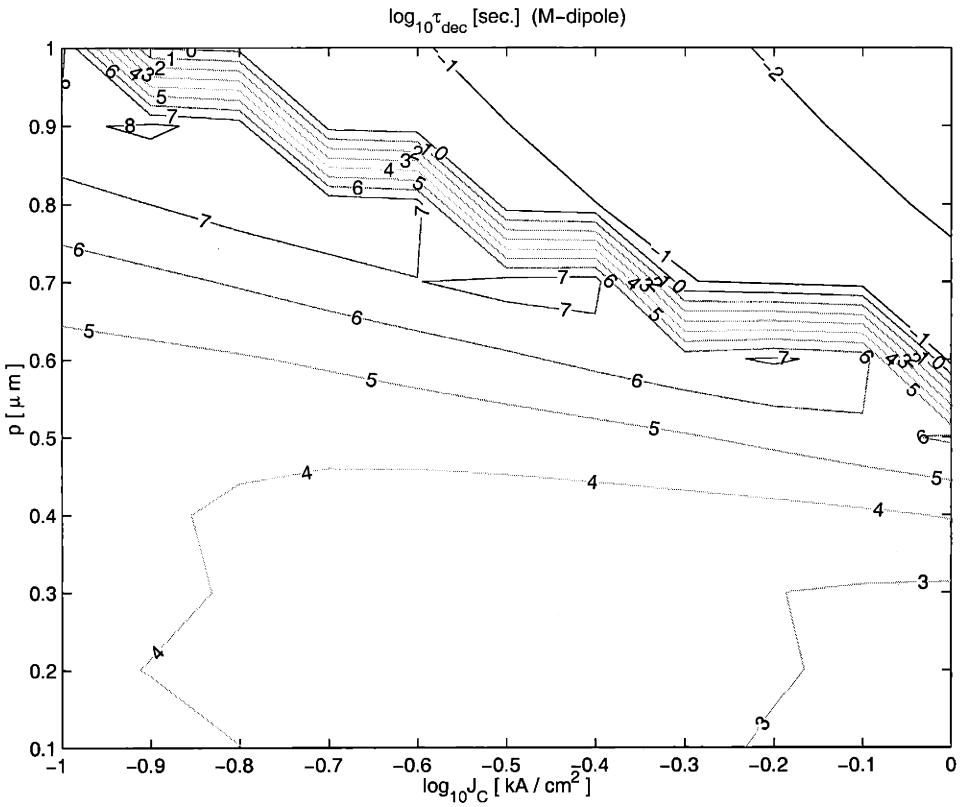

Figure 4-2: Contour map of logarithm of the decoherence time τ_{dec} of the pc-qubit due to the magnetic dipolar radiation. The numbers labelled in the contour are the 10-based logarithm of the decoherence time.

With the parameters of the pc-qubit: $E_J = 200\,\text{GHz}$, $R = 5p = 1.5\,\mu\text{m}$, $E_C = 2\,\text{GHz}$, and bias flux $f_{ex} = 0.495$, we estimate that the magnetic dipolar radiation rate is 1×10^{-5}/sec, and the electrical dipolar radiation rate is 1.5×10^{-4}/sec. This induces qubit decoherence by radiation decay with $\tau_{dec} = 1/\Gamma_E^m = 7\,\text{ksec}$.

4.2.3 Magnetic Radiation in an RF SQUID

As can be seen from eq. 4.22, the radiation rate depends on the cubic square of the Larmor frequency and the fourth square of the size of the qubit. As a result, the radiation increases dramatically when the qubit size is increased. In the rf SQUID qubit, the loop inductance has to be large enough ($1 < \beta = 2\pi L_s I_c/\Phi_0 < 4.6$) to have the double well potential. As a result, the circuit size has to be much larger than that of the pc-qubit under the same junction parameters. When $E_J = 200\,\text{GHz}$

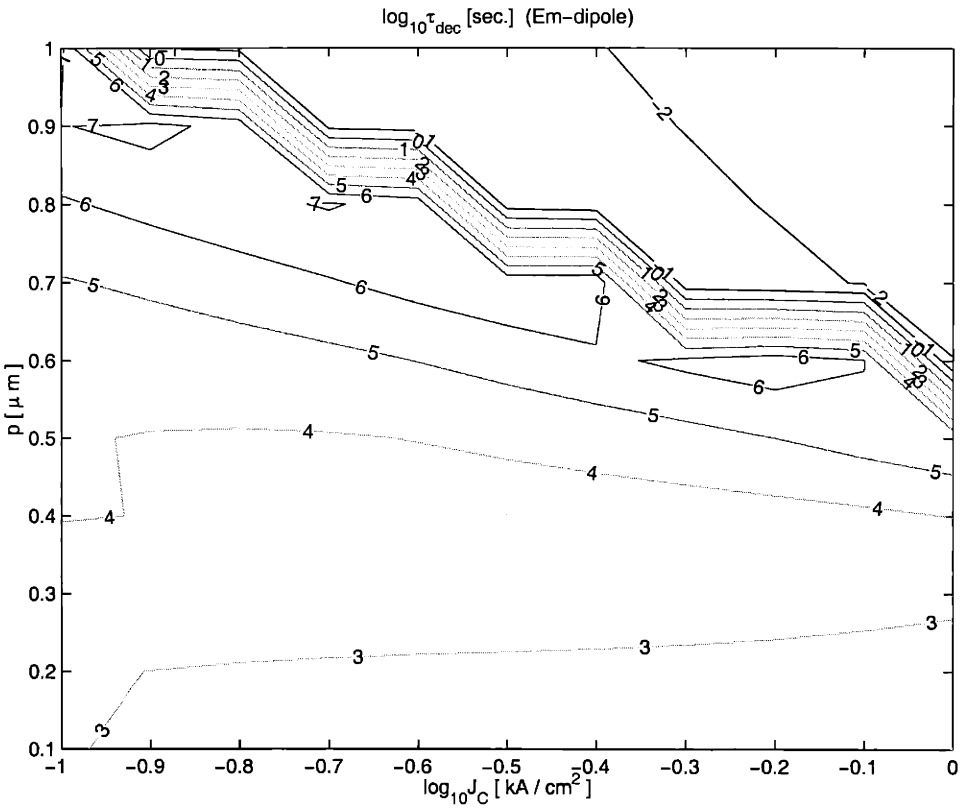

Figure 4-3: Contour map of logarithm of the decoherence time τ_{dec} of the pc-qubit due to the electric dipolar radiation. The numbers labelled in the contour are the 10-based logarithm of the decoherence time.

and $\beta = 2$, the loop size is 0.3 mm. This gives a magnetic dipolar radiation rate roughly 10^8 stronger than that of the pc-qubit, since the energy difference E_0 and the dipole matrix $< 1|\hat{I}|2 >$ don't change much in these two cases. This radiation kills the coherence of the rf SQUID in a very short time.

The junction parameters of the qubit are mainly decided by the junction size p and the critical current density J_c. We have the critical current $I_C = J_c p^2$, the junction capacitance $C_J = 40[\text{fF}/\mu\text{m}^2]p^2$, and $E_J/E_C \propto J_c p^4$. For the pc-qubit, the circuit size is usually $4 \sim 6$ times the junction size. For an rf SQUID, the circuit size is much larger in order to make $\beta \simeq 2$. We studied the dependence of the radiation decoherence time on the junction size and the junction current density. Fig. 4-2 shows the decoherence of the pc-qubit by magnetic dipolar radiation, and Fig. 4-3 shows the decoherence of the pc-qubit by electrical dipolar radiation and Fig. 4-4

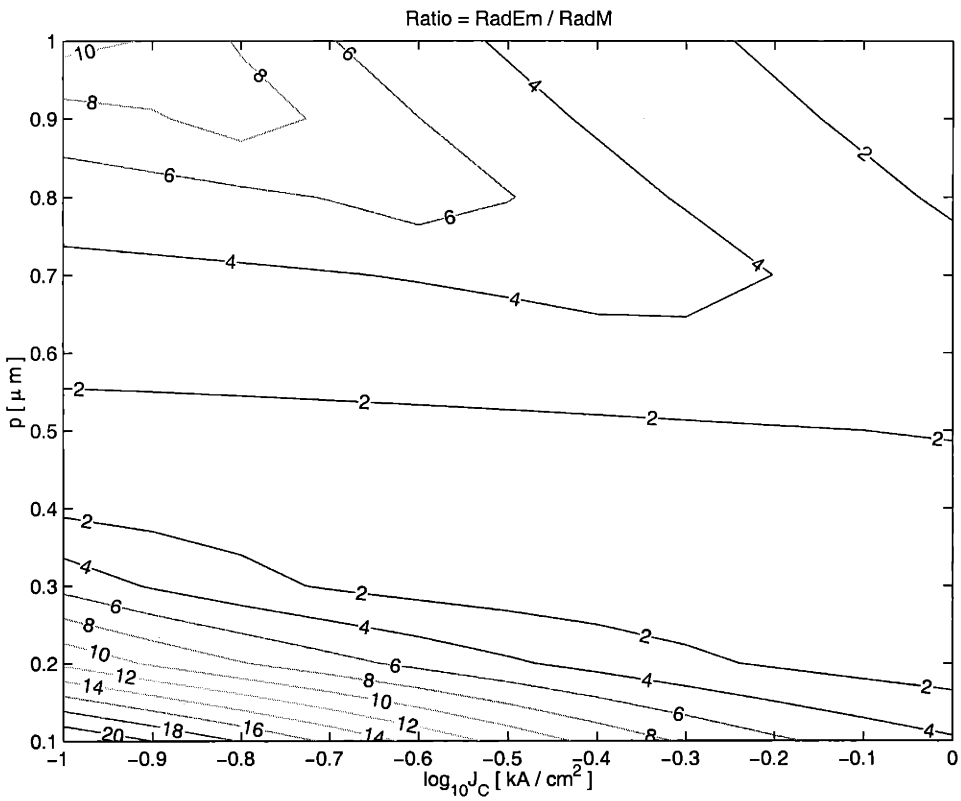

Figure 4-4: The ratio between the electric dipole radiation rate and the magnetic dipole radiation rate. The numbers labelled in the contour are the logarithms of the ratios.

is the ratio between the electrical dipolar radiation rate and the magnetic dipolar radiation rate. As is shown, the electrical dipolar radiation is about one order of magnitude stronger than the magnetic one in most regimes. Fig. 4-5 is the rf SQUID decoherence due to the magnetic dipolar radiation. As was analyzed in the previous paragraph, this radiation increases with the size quickly. As a result, the regime that can be designed as a flux qubit is very narrow. However, the rf SQUID can be designed with a gradiometer geometry which reduces the dipolar radiation of the SQUID significantly. With this geometry, the residual radiation is the higher order quadrupole radiation and is much weaker than that of the dipole radiation.

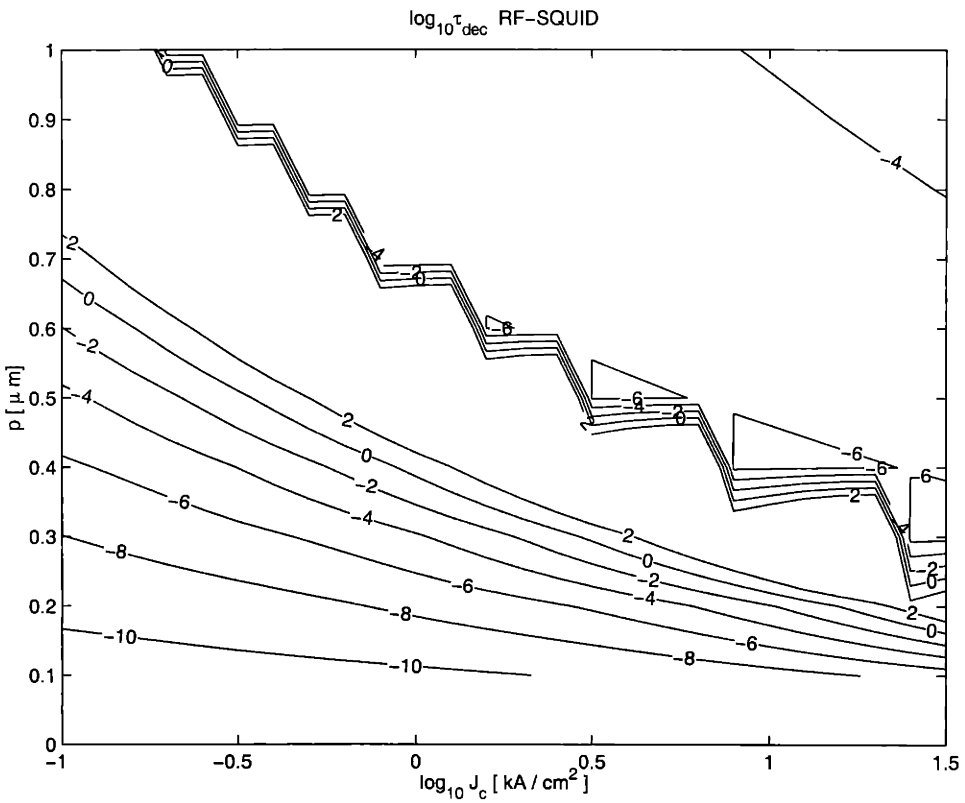

Figure 4-5: The decoherence time of the M-dipole radiation of the RF-SQUID.

4.3 Dipole Interaction between Qubits

In our previous discussion, we concentrated on the decoherence of the persistent-current qubit by environmental noise. Besides these random fluctuations, other sources of decoherence exist. These sources of decoherence are not amenable to the general approach considered in section 4.1. One of them is the interaction of the qubit with the other qubits in the Josephson network. Here we are going to study the effect of the qubit interactions on qubit decoherece.

4.3.1 Dipole Interaction

A qubit with a circulating current can be regarded as a magnetic dipole. For two qubits with a large distance, the lowest order interaction is the dipole-dipole coupling between the two magnetic momenta. Fig. 4-6 is a simple picture of this interaction. Let the dipolar moments of the two qubits be $\vec{\mu}_1$ and $\vec{\mu}_2$, this interaction is described

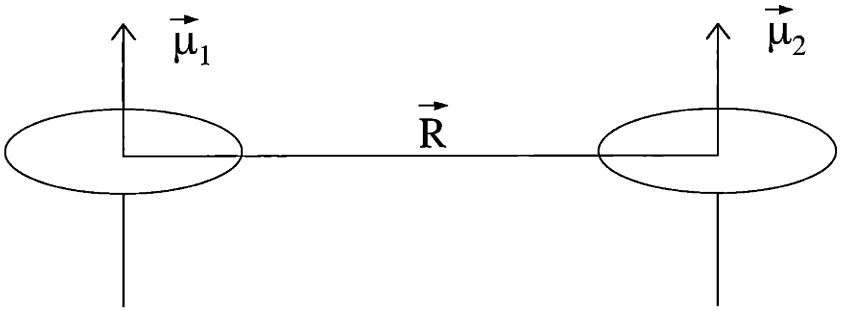

Figure 4-6: Dipole interaction between magnetic dipoles. $\vec{r}$ is the distance between the qubits.

by

$$\mathcal{H}_{\text{coupling}} = \sum_{i,j} \hbar\lambda_{ij}\sigma_z^{(i)} \otimes \sigma_z^{(j)} , \qquad \hbar\lambda_{ij} \approx \frac{\mu_i\mu_j}{|r_i - r_j|^3} \tag{4.26}$$

In our circuit, the circulating current is $I \approx 0.2\mu A$ and the area of the circuit loop is $A \approx 1\mu m^2$. (This is the critical current of the Josephson junction. The actual current is always smaller but of the same order.) The dipole moment is $\vec{\mu} = I.A \approx 0.2\mu A \times \mu m^2$. Taking the distance between qubits to be $R = 50\mu m$ as a first estimation, $E_{dipole} = 2 \times 10^{-9}K$ in units of temperature. For comparison, the tunneling energy is $\Delta \leq 0.01E_J = 0.06K$ and the operating time is proportional to the inverse of this energy $\tau_{op} = 1/\Delta$.

This interaction is strongest for nearest neighbors. For a square lattice of qubits with the spacing $R = 10\,\mu$m, one has the nearest neighbor coupling $\lambda \simeq 6\,$KHz. The corresponding decoherence time $\tau = \lambda^{-1} \simeq 0.2\,$msec is relatively short. The interaction energy in the worst case is:

$$\Delta E = \sum_{m,n,m+n\geq 1} \frac{E_0}{(n^2+m^2)^{3/2}} \tag{4.27}$$

where m and n are integers. The energy summation ΔE converges as the number of qubit increases and we have $\Delta E < 10E_0 = 60KHz$. The corresponding decoherence

time is $\tau_{int} = 16\mu s$ which means a quality factor of less than 10^4 when the Rabi frequency is $100MHz$. This is a short decoherence time for quantum computation.

4.3.2 Quadrupole Interactions

Several alternatives of the design can be implemented to reduce the effect of qubit-qubit interaction. One can arrange qubits in pairs with opposite signs of circulating currents. This will eliminate the dipole moment of a pair, and reduce the coupling between different pairs to a somewhat weaker quadrupole interaction. The same result can be achieved by using a superconducting base plane, in which magnetic dipoles will be imaged by dipoles of opposite sign, which will partially cancel the qubit-qubit coupling. Also, one can detune Larmor frequencies of neighboring qubits, moving them apart by more than λ, which will make the couplings (4.26) off-resonance and thereby reduce their effect.

Let us briefly discuss the pairing of the qubits. A qubit pair consists of two adjacent qubits that always have opposite currents. When one qubit in the pair has a state $|\Psi_1 >= \alpha_1|0 > +\alpha_2|1 >$, the other qubit in the same pair always has the state $|\Psi_1 >= \alpha_1|1 > +\alpha_2|0 >$. By introducing this pairing, the dipole interaction is cancelled and the interaction is a quadrupole coupling: $H_{int} = \frac{\mu_0}{4\pi}\frac{\mu_1\mu_2}{R^3}\frac{6r^2}{R^2}$, where r is the distance between the two qubits in the same pair. Let $r = 1\mu m$ and $R = 10\mu m$, and we then have $E_0 = 0.36KHz$. Summing over all the qubits, we have for a square lattice of qubit pairs:

$$\Delta E = \sum_{m,n,m+n\geq 1} \frac{E_0}{(n^2+m^2)^{5/2}} \tag{4.28}$$

which gives us the result that $\Delta E < 10E_0 = 3.kKHz$ and a decoherence time $\tau_{dec} = 300\mu s$. Now the quality factor is 6×10^4 and is improved from that of the dipole configuration. Other designs can be adopted to reduce the qubit interaction as well. At the same time, this will increase the complexity of the fabrication and might bring in decoherence from technical features such as inhomogeneity between different qubits. The more complicated the configuration is, the more difficult will be the

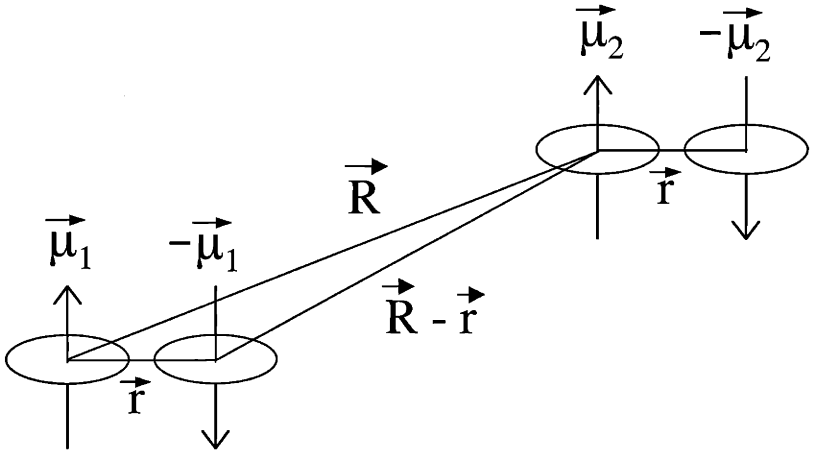

Figure 4-7: Quadrupole interaction between paired dipoles. When two dipoles with opposite dipole moments are paired closely together, their dipoles cancel each other. The residue interaction is the higher order quadrupole interaction.

fabrication. Fig. 4-7 is a simple picture of this interaction.

Unwanted coupling between qubits is a common problem in quantum computers. Sophisticated decoupling techniques that have been developed for NMR designs[16], could be used here too. The idea is to apply a sequence of single qubit operations that effectively average out the coupling Hamiltonian over time. Such methods would also be effective for reducing the coupling with the environment[128]. These techniques are fully compatible with quantum computation and could be used to lengthen significantly the effective coherence times.

4.4 Summary

In this chapter, we concentrated on investigating qubit decoherence from environmental fluctuations. Our method can be easily generalized to other qubit designs and other origins of noise. Our analysis shows that for the pc-qubit[20, 25] the decoherence time is limited by qubit-qubit coupling. By using methods discussed above, the decoherence time can be made at least 1 msec, which for $f_{\text{Rabi}} = 100\,\text{MHz}$ gives a quality factor of 10^5, passing the criterion for quantum error correction.

In addition to the effects we discussed, some other decoherence sources are worthy

of attention, such as low frequency charge fluctuations resulting from electron hopping on impurities in the semiconductor and charge configuration switching near the gates[129]. These effects cause $1/f$ noise in electron transport, and may contribute to decoherence at low frequencies. Also, we left out the effect of the *ac* field of coupling the two low energy states of the qubit to higher energy states. Results of our numerical simulations of the coupling matrix in the qubit[20, 25] show that Rabi oscillations can be observed even in the presence of the *ac* excitation mixing the states. For more details on this effect, see the next chapter.

In Fig. 4-8, we categorize quantum errors according to the dephasing time by this noise source and the correlation time of the noise fluctuations. The x axis is the correlation time τ_{cor} scaled to the qubit operation time $\tau_{op} \sim 10\,\text{nsec}$, and the y axis, also scaled to the qubit operation time τ_{op}, is the dephasing time τ_ϕ during which the qubit gains a random phase of order 2π. In the top area where $\tau_\phi > 10^4\tau_{op}$, large scale fault-tolerant quantum computation can be realized via quantum error correction[87, 124]. No additional pulse sequence is needed to further reduce the decoherence rate. Hence $\tau_{dec} = \tau_\phi$. The noise sources in this area are the charge noise, the quasiparticle tunneling, and the current noise from the external control line. In the area where $\tau_{cor} > N\tau_{op}$ but $\tau_\phi < 10^4\tau_{op}$, N is a number of order 10, direct quantum error correction can not result in fault-tolerant quantum computation. However, as $\tau_{cor} > N\tau_{op}$, an average Hamiltonian method can be applied to average out the random phase from the environment by exploiting the correlation between the fluctuations at different times. As a result, the real decoherence time is longer than the dephasing time $\tau_{dec} \gg \tau_\phi$ and the system can be modified to the quantum error correction regime. Both the interaction with the nuclear spins and the interaction with other qubits are in this area. In the area where the gate errors happen, including the single qubit gate and two qubit gates, the error accumulates very fast and $\tau_\phi < \tau_{op}$. Fortunately, these errors are coherent errors from the unitary dynamics of a multilevel quantum system. A dynamic pulse control method can be applied to reach the desired quantum operation. When both the dephasing time and the correlation time are short, both quantum error correction and dynamic control are not very helpful in keeping

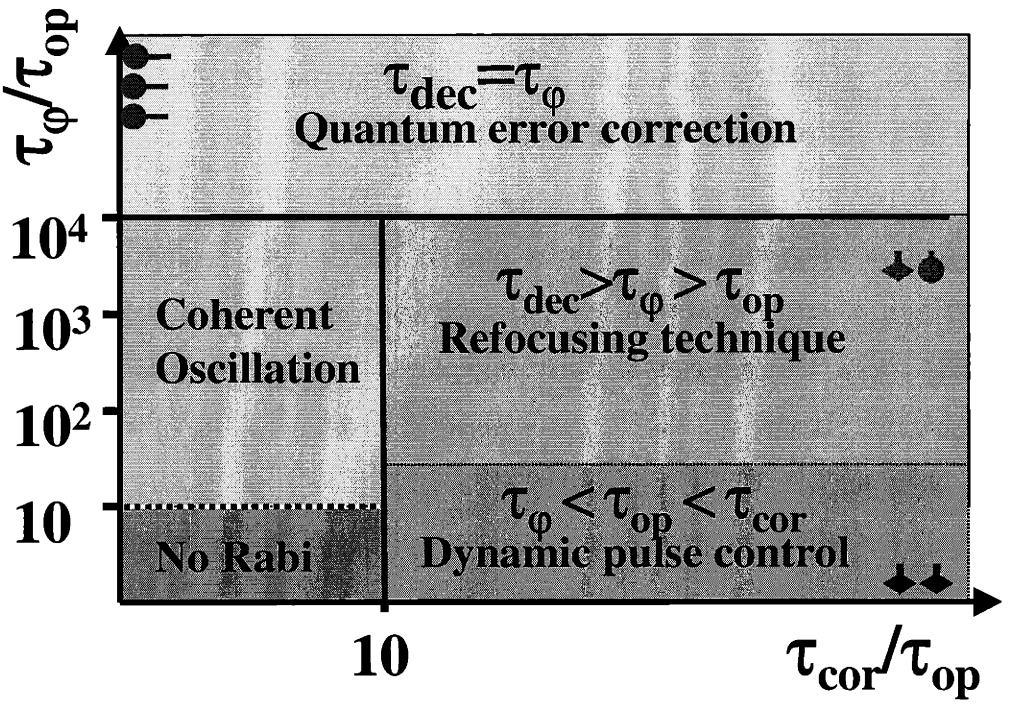

Figure 4-8: A summary of different noise sources and the control method applied to correct the errors.

the coherence of the qubit. Still, when the dephasing time is not too short, coherent dynamics between the qubit states can still be observed and some fundamental physics can be studied.

Some of these results are listed in Table 4.1.

error source	time scale	prevention
charge noise quasiparticle current noise	$\tau_\phi > 10^4 \tau_{op}$ $\tau_{cor} \ll \tau_{op}$	quantum error correction
nuclear spin dipole interaction	$\tau_\phi < 10^4 \tau_{op}$ $\tau_{cor} \gg \tau_{op}$	refocusing technique
higher levels two-bit gate error	$\tau_\phi < \tau_{op}$ *coherent error*	dynamic pulse control

Table 4.1: Major error sources with potential control methods. The errors are categorized according to two time scales: the dephasing time τ_ϕ and the correlation time τ_{cor}. At a different area, a potential error correction method is suggested.

In this study, we assume that the noise on different qubits is independent of each other, so that quantum error correction can be applied fault-tolerantly to deal with these independent errors. But in real life, the noise on different qubits is often spatially and temporally correlated. One example is the radiation decay. A general method for correcting strongly correlated error has been proposed [130, 131]. The effect of the correlated errors on entangled qubits has also been studied for superconducting charge qubits.

Chapter 5

Dynamic Control on A Multilevel Qubit

Successful quantum computation relies on accurate manipulation of the qubit states[5, 7]. In practice, qubits are subject to many sources of quantum errors including thermal fluctuations of the environment[132, 133, 134, 135], qubit-qubit interactions[136], and intrinsic redundant degrees of freedom within a qubit, such as the quasiparticle conduction in the superconducting qubits[20, 25, 22, 23, 24, 25], and the effect of the higher levels in many practicaL qubit designs[22, 23, 24, 137]. The dynamic control turns out to be a powerful tool to cope with the quantum errors during quantum computation. In this section, we present two applications of the dynamic control method: we propose a dynamic pulse control technique that efficiently eliminates unwanted off-resonance transitions and decouples the qubit from environmental noise; we also design a pulse sequence of a 24 nsec period for decoupling the pc-qubit from environmental noise.

Various schemes to protect the qubit from qubit errors have been proposed that can be divided into two categories. The first one is the quantum error correcting codes [87, 124, 125, 126, 131, 139, 140, 141, 142, 143, 144, 145] where the qubit state is encoded by redundant qubits. Different errors project the qubit-extra-qubit system into different subspaces that can be determined by measuring the extra qubits. By applying a transformation according to the measurement, the correct qubit state can

be restored. This approach relies on large numbers of extra qubits to keep the errors from propagating. The second approach exploits "bang-bang" control techniques[146, 147], where the dynamics of the qubit and its environment are manipulated by fast pulses that flip the qubit state. With the influence of the environment being averaged out, the qubit evolves in the error-free subspace. This method relies on the ability to apply the pulses rapidly compared with the correlation time of the environment. This is an open loop control method.

The persistent-current qubit is not a perfect two-level system. Higher energy states exist. During the gate operation, in addition to causing transitions between the two qubit states, the gate perturbation also causes transitions to the higher levels. This is the so-called leakage problem and is ubiquitous in many qubit designs. The leakage is a coherent quantum error during the gate operation. It can be shown that in many occasions this gate error has a much larger error rate than the environmental noise. Dynamic control turns out to be a good approach to correct or prevent this gate error. By applying the right sequence of pulses, this error can be completely prevented.

The dynamic control method is also a very effective way of manipulating environmental noise. A simple approach applies the average Hamiltonian method to decouple the qubit from the environmental noise. This method works for noise which has a finite correlation time. When the pulses can be applied sufficiently fast, the errors due to the environment can always be cancelled out to at least the third order in the interaction Hamiltonian. A practical problem is how to find the right pulse sequence with implementable pulse duration and pulse strength.

In this chapter, we will study two applications of the dynamic control method to the persistent-current qubit. Namely, the pulse control on a multilevel quantum system and the average Hamiltonian method to decouple the qubit from environmental noise. Both of these methods rely on the accurate manipulation of pulse sequences and have open problems remained to be solved. The discussion on these problems gives a different approach of correcting quantum errors from the quantum error correction method and can be a complementary approach to the standard quantum error

correction.

5.1 Off-resonant Transitions

A particularly important form of intrinsic qubit errors comes from the off-resonant transitions to the higher levels of a qubit during gate operation. Real qubits are not $S = 1/2$ spins that are perfect two level systems; redundant levels always exist that affect the information content of the qubit. The gate operation that is introduced to couple the lowest two states of a qubit almost always induces unwanted couplings between the lowest two states and the higher levels. When the interaction is applied with the frequency $\omega = \omega_2 - \omega_1$, a resonant transition occurs between the lowest two states; meanwhile, off-resonant transitions to the higher states are also switched on. These transitions cause deviations of the phase and amplitude of the qubit state from perfect Rabi oscillation. Numerical simulations on the superconducting persistent current qubit (pc-qubit)[20, 25, 148] show that this deviation can be severe when the unwanted couplings are of the same order as the Rabi frequency.

In this section, we study the off-resonant leakage from the qubit states to these higher states. we numerically simulate the dynamics of the lowest four energy levels of the qubit circuit and estimate the error rate of the process.

5.1.1 Unwanted Transitions

We simulate the dynamics of the lowest 4 eigenstates of the persistent-current qubit with a microwave pulse. The static qubit states are calculated from the Hamiltonian

$$\begin{aligned} H_t = \quad & \frac{1}{2}\frac{P_p^2}{M_p} + \frac{1}{2}\frac{P_m^2}{M_m} + E_J\{2+\alpha \\ & -2\cos\varphi_p\cos\varphi_m - \alpha\cos(2\pi f + 2\varphi_m)\} \end{aligned} \tag{5.1}$$

where the momenta can be written as $P_p = -i\hbar\partial/\partial\varphi_p$ and $P_m = -i\hbar\partial/\partial\varphi_m$. The mass terms are $M_p = (\Phi_o/2\pi)^2 2C(1+\gamma)$ and $M_m = (\Phi_o/2\pi)^2 2C(1+2\alpha+\gamma)$. Typical

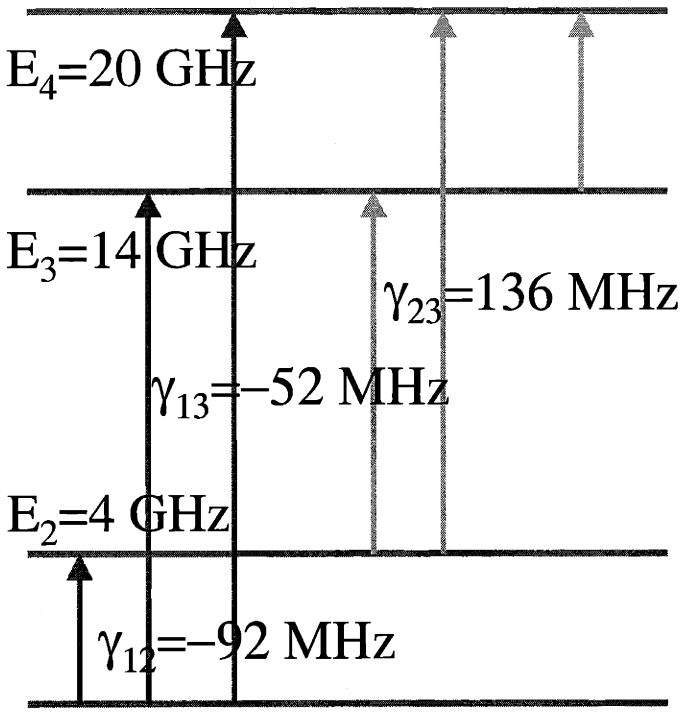

Figure 5-1: The lowest 4 energy levels of a pc-qubit circuit are plotted. The energy difference between the excited states and the ground state are labeled beside each energy level in units of GHz. When a radio-frequency perturbation is applied, transitions between different states are induced. The transition matrix elements are given as γ_{ij}.

parameters are: $E_J = 200\,\text{GHz}$, $E_J/E_c = 80$, $\alpha = 0.75$ and $\gamma = 0.02$. And the flux bias is $f = 0.495$ in our calculation. The energies of the lowest four states are: $E_1 = 1.5228E_J$, $E_2 = 1.5642E_J$, $E_3 = 1.6622E_J$, and $E_4 = 1.7193E_J$. The energy differences in terms of GHz are: $E_2 - E_1 = 4\,\text{GHz}$, $E_3 - E_1 = 14\,\text{GHz}$, and $E_4 - E_1 = 20\,\text{GHz}$.

Now apply a microwave pulse $\mathcal{H}_\mathcal{I} = 2\pi\delta f \sin(2\phi_m + 2\pi f_{ex}) \cos\omega_0 t$, where δf is the amplitude of the microwave pulse and $\hbar\omega_0 = E_2 - E_1$ is the pulse frequency. This pulse will induce transitions between the eigenstates. Ideally, we only want the transition between the ground state and first excited state for a single qubit rotation. But this simple pulse also induces unwanted transitions between the qubit states and the higher states. The transition matrix is

$$(\mathcal{H}_\mathcal{I})_{mn} = 2\pi\delta f \langle m| \sin(2\phi_m + 2\pi f_{ex}) |n\rangle \tag{5.2}$$

where m, n are labels of the states. The transition matrix is given by

$$\mathcal{H}_\mathcal{I}/E_J = \delta f \begin{bmatrix} 0 & -0.4578 & -0.2596 & 0.3195 \\ -0.4578 & 0 & 0.6766 & -0.0030 \\ -0.2596 & 0.6766 & 0 & 2.4314 \\ 0.3195 & -0.0030 & 2.4314 & 0 \end{bmatrix} \tag{5.3}$$

The matrix is written in units of E_J. With $E_J = 200\,\text{GHz}$ and $\delta f = 0.001$, the transition elements are $\gamma_{12} = -92\,\text{MHz}$, $\gamma_{13} = -52\,\text{MHz}$, and $\gamma_{23} = 136\,\text{MHz}$. The energy levels and the coupling matrix are shown in Fig. 5-1.

5.1.2 Simulation

Starting from the numbers given above, we simulate the dynamics of the four-level system with microwave radiation. The initial state of our simulation is the ground state. Ideally, without the unwanted couplings to the higher states, we should observe a Rabi oscillation between the two qubit states, with the Rabi frequency in proportion to the amplitude of the pulse. With the unwanted couplings, the transitions to the

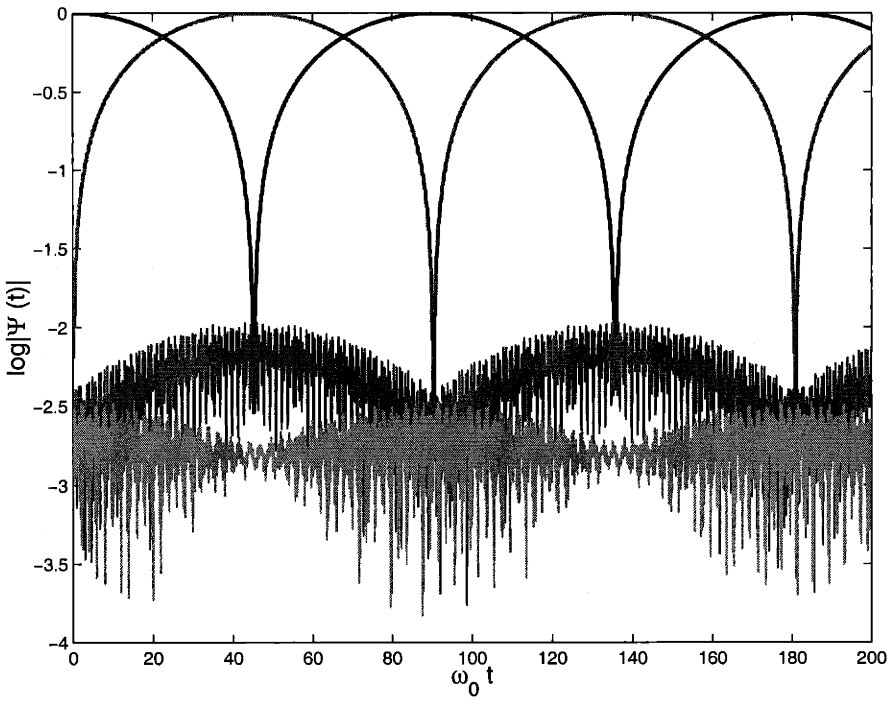

Figure 5-2: Numerical simulation on the 4 level system from the persistent-current qubit. The system starts from the ground state. Microwaves with a frequency of $\hbar\omega_0 = E_1 - E_0$ in resonance with the qubit frequency are applied. The x axis is the evolution time in terms of $\omega_0 t$. The total simulation lasts 200 periods of the applied pulse. The slower oscillation curves are the amplitudes of the ground state and the first excited state, which in an ideal situation, should go through Rabi oscillations. The fast oscillations are the amplitudes of the higher states and are the leakage from the qubit states.

higher states occur. As the probability for the leakage is small, we have following:

$$\begin{aligned} P(1 \to 2) &= \sin^2 \omega_{Rabi} t \\ P(1 \to 3) &= \frac{|\gamma_{13}|^2}{\omega_r^2} \sin^2 \omega_r t \\ \omega_r &= \sqrt{|\gamma_{13}|^2 + (\omega_{31} - \omega_0)^2} \end{aligned} \tag{5.4}$$

where the probability of the transition to the second level is approximately a Rabi oscillation with frequency ω_{Rabi}. So the probability of the leakage is determined by $(\gamma_{13}/\omega_r)^2$ and the off-resonant oscillation frequency is given by ω_r.

The simulated result is shown in Fig. 5-2. The x axis is the time of evolution in units of $\omega_0 t$ and the total simulation time is 200 periods of the rf pulse. The y axis shows the logarithm of the probability of the wave functions. The slow oscillations are the amplitudes of the ground state and the first excited state which behaves as a Rabi oscillation. The fast oscillations are the off-resonance oscillation of the higher states. The error rate from this simulation is 0.01/gate which is much higher than that of the environmental fluctuations.

The off-resonant leakage during gate operation has two significant characteristics. First, unlike the environmental fluctuations that affect the qubit only slightly (less than 10^{-4}) within one operation, the leakage changes the qubit dynamics by an amplitude of roughly $(\frac{\omega_{Rabi}}{\omega_0})^2$ and on a time scale $1/\omega_0$ that is much shorter than qubit operation time (about $1/\omega_{Rabi}$). Conventional quantum error correcting codes correct errors that occur with small probability and is not a suitable strategy to cancel these strong off-resonance transitions. Neither can we use the bang-bang method to average this effect out[149, 150] simply by flipping the qubit states as the flipping pulses induce the same transitions as well. Second, ignoring all interactions with external variables, the leakage is coherent, although the coherent oscillation will collapse since the revival time is too long to be observed due to the large number of transitions of different frequencies[110]. As will now be shown, the coherent nature of the leakage implies that this type of error can be corrected by applying a control sequence that coherently modifies the qubit dynamics.

5.2 Resonant Cancellation of Off-resonance Effects

In this section, we study the effect of the higher levels on qubit dynamics during qubit operation by a group theoretic approach. We prove that the errors can be completely avoided by applying a time varying operation Hamiltonian. Then we generalize this result to the qubit-qubit interaction problem which can be mapped exactly onto the first one. Extending the idea of dynamic pulse control[146], we design a pulse sequence that cancels the leakage to the higher levels to arbitrary accuracy with a $O(N)$ number of pulses, N being the number of higher levels.

The proposed method for protecting quantum information is complementary to quantum error correcting codes and the 'bang-bang' technique mentioned above. Like the bang-bang method, it has the advantage that it does not require extra qubits to enact. The proposed method protects against a different class of errors from those corrected by the methods of [146], however. Dynamic pulse control can be used in conjunction with quantum error correcting codes and the bang-bang decoupling method.

5.2.1 Lie Group Analysis

Consider a N level quantum system with Hamiltonian $\mathcal{H}_0$, the lowest two states of which are chosen as the qubit states $|\uparrow\rangle$ and $|\downarrow\rangle$. The unitary transformations on this N dimensional Hilbert space form the N^2 dimensional compact Lie group U(N). Without other interactions, the trajectory of the qubit follows the Abelian subgroup $\{e^{-i\mathcal{H}_0 t}, t \in R\}$.

Now apply to the qubit the perturbation $\mathcal{H}_I$, $[\mathcal{H}_0, \mathcal{H}_I] \neq 0$, to induce a desired transformation of the qubit. In most physical systems, unwanted transitions to the higher levels are simultaneously induced. For example, in the pc-qubit[20, 25] operation, $(\mathcal{H}_I)_{mn} = 2\pi\delta f \langle m| \sin(2\phi_m + 2\pi f)|n\rangle \cos\omega t$, when the bias flux is modulated with rf components of amplitude δf and frequency ω. This perturbation has couplings between all the energy levels. By successive commutation of $\mathcal{H}_0$, $\mathcal{H}_I$, and their commutators until no independent operator appears, a Lie algebra $\mathcal{A}_I$ is created. In

almost all cases, $\mathcal{A}_{\mathrm{I}} = \mathrm{u}(N)$[77], $\mathrm{u}(N)$ being the Lie algebra of $\mathrm{U}(N)$. The only exception occurs in a zero measure subspace of $\mathrm{u}(N)$ when $\mathcal{H}_I$ and $\mathcal{H}_0$ are both in the same subalgebra of $\mathrm{u}(N)$. Thus, with almost all perturbations, the evolution operator can be any element in $\mathrm{U}(N)$; and transitions to higher levels are unavoidable with an initial state that only occupies the lowest two levels.

To prevent transitions to the higher states at time t means to restrict the evolution operator $\mathcal{U}(t)$ to the submanifold of $\mathrm{U}(2) \oplus \mathrm{U}(N-2)$, $\mathrm{U}(2)$ being the unitary group on $\{|\uparrow\rangle, |\downarrow\rangle\}$ and $\mathrm{U}(N-2)$ on the remaining $N-2$ states. This applies $4(N-2)$ real domain restrictions on $\mathcal{U}(t)$: $\mathcal{U}(t)_{1k}, \mathcal{U}(t)_{2k} = 0, k = 3 \ldots N$. In contrast to a perfect qubit operation during which $\mathcal{U}(t)$ remains in the subspace $\mathrm{U}(2) \oplus \mathrm{U}(N-2)$ all the time, the qubit is allowed to stray away from this subspace if only it goes back to this subspace at the designated time t. The qubit dynamics can be manipulated by varying the strength and phase of the perturbation with time. As the N^2 dimensional Lie group $\mathrm{U}(N)$ is compact, any transformation can be reached at time t by adjusting the N^2+1 parameters in the following process[77]:

$$\mathcal{U}(t) = e^{-i\alpha\mathcal{H}_I t_{N^2}} e^{-i\alpha\mathcal{H}_0 t_{N^2-1}} \cdots e^{-i\alpha\mathcal{H}_0 t_1} \tag{5.5}$$

where α is introduced to ensure that $t = \sum t_i$. By playing with the N^2+1 real parameters, the $4(N-2)$ real numbers in $\mathcal{U}(t)_{1k}, \mathcal{U}(t)_{2k}$ can be set to zero so that the state of the qubit stays in the $\{\uparrow, \downarrow\}$ space without leakage. Hence by turning the perturbation on and off $O(N^2)$ times, the lowest two states are completely decoupled from the higher states. $O(N^2)$ pulses give a sufficient condition that is required to achieve an arbitrary transformation. As will be shown later in this chapter, with a proper arrangement, we can design a pulse sequence of $O(N)$ pulses to cancel the transitions to the higher levels. Furthermore, these pulses can be superposed to make a single shaped pulse as in [147, 150] that averages out the unwanted transitions. For a given driven power per unit frequency, the length of the shaped pulse is independent of the number of higher levels. Unlike that in the quantum Zeno effect[151] where measurement is used to prevent the system from evolving, the dynamics in this process

is described completely by unitary evolutions.

As the unwanted transitions are off-resonance transitions whose amplitudes decrease roughly as γ_{ij}/ω_i (ω_i is the energy of the ith level, γ_{ij} the coupling between level i and j), the influence of the levels with $\omega_i/\omega_0 \gg 1$ can be ignored. In the pc-qubit[20, 25] the energies of the lower levels increase fast enough ($\omega_{10} > 10\omega_0$) that levels beyond $|10\rangle$ can be ignored. The energy of the ith level of the charge state qubit increases as i^2; fewer states affect the qubit dynamics than that in the pc-qubit. Hence the number N of the higher states involved in the qubit dynamics in real designs can be reasonably small. As a result, the number of pulses in the previous analysis is also reasonable.

5.2.2 Generalization

One question to ask is whether there is any fundamental difference between the errors due to transitions to the higher levels and those due to the fluctuations of environmental variables. Putting it in another way: what is the difference between the intra-qubit coupling in a multilevel qubit and the qubit-external-system coupling? In the following we will show that the N-level qubit can be mapped into interacting subsystems, and vice versa.

Let the initial state of a N-level qubit be $|\Psi_0\rangle = \alpha_1^{(0)}|1\rangle + \alpha_2^{(0)}|2\rangle$, $|1\rangle$ and $|2\rangle$ being the lowest two states. To map the qubit into two subsystems, we divide the N states into two subspaces SP_1 and SP_2 by adding the vacuum states $|V_1\rangle$ and $|V_2\rangle$ to the respective subspaces as $SP_1 = \{|V_1\rangle, |1\rangle, |2\rangle\}$ and $SP_2 = \{|V_2\rangle, |3\rangle, \ldots, |N\rangle\}$. Now the N dimensional Hilbert space of the original qubit is embedded in the $3(N-1)$ dimensional direct product space $SP_1 \otimes SP_2$. The states in the expanded space are $|\overline{\Psi}\rangle = \sum_{i,j} \beta_{i,j}|b_i^{(1)}\rangle|b_j^{(2)}\rangle$, where $b_i^{(1)}$ and $b_j^{(2)}$ are basis of the two subspaces respectively. The initial state is $|\overline{\Psi}_0\rangle = (\alpha_1^{(0)}|1\rangle + \alpha_2^{(0)}|2\rangle)|V_2\rangle$ in the expanded form. The unitary transformations in this expanded space form the group U($3(N-1)$).

Perturbation introduces couplings between different states. When mapped to the expanded space, the perturbation $\overline{\mathcal{H}}_I$ connects states in the N dimensional subspace spanned by $\{|1\rangle|V_2\rangle, |2\rangle|V_2\rangle, |V_1\rangle|3\rangle, \ldots, |V_1\rangle|N\rangle\}$. So $\overline{\mathcal{H}}_I$ and $\overline{\mathcal{H}}_0$ create N^2

dimensional subalgebra u(N) in the expanded space. Under the perturbation, wave functions in the expanded space can be described as $|\overline{\Psi}\rangle = (\alpha_1|1\rangle + \alpha_2|2\rangle)|V_2\rangle + \sum_{i=3}^{N} \alpha_i|V_1\rangle|i\rangle$, where α_i are time dependent parameters evolving with the perturbation.

From this analysis, the higher levels in the qubit form an effective environment that interferes **strongly** with the lowest two levels. Interaction strength and spectrum density are the major differences between this effective environment and a real one[20, 25]. The couplings between SP_1 and SP_2 are strong and comparable to the Rabi coupling that realizes qubit operation. In contrast, the interactions between the environmental oscillators and the qubit are weak due to the $O(1/\sqrt{V})$ factor that originates from the normalization of the extended modes. So the thermal fluctuations are not enslaved to the qubit dynamics and can be treated classically. The strong interaction with the higher levels also explains why the error due to leakage occurs at such a short time that a particular strategy other than the bang-bang technique is required to correct this error. The spectrum density of a real environment is continuous with macroscopic degrees of freedom, while for the higher states, the spectrum is discrete. Another thing to mention is that this effective environment only comes with qubit operation, while the real environment affects the qubit all the time. Hence we worry about the leakage only during qubit operation and choose to correct the leakage by controlling the operation process.

Note that interacting qubits can be modeled as one multilevel quantum system by reversing the above mapping. This implies that errors due to qubit-qubit interactions[136] can be treated with the proposed method. Off-resonant effects are significant in existing NMR quantum computers, and techniques analogous to the ones suggested have been developed to correct unwanted transitions[150]. Although the number of levels grows exponentially with the number of qubits[152], because the two-qubit couplings in NMR are relatively weak, effective decoupling procedures only require that the number of pulses be polynomial in the number of qubits and the complexity of a single shaped pulse also be polynomial in the number of qubits.

5.2.3 Example

To illustrate the general idea of dynamic pulse control, we give an example of a pulse sequence that completely cancels the transitions to the higher levels with $O(N)$ pulses. Let us start from a three level system with eigenvalues $\omega_i, i = 1, 2, 3$. The energy difference between level i and j is shorthanded as ω_{ij}. An interaction $\mathcal{H}_I$ that couples level i and j by γ_{ij} is applied to the qubit. When the third level is not present, γ_{12} is the Rabi frequency of the lowest two states. For simplicity, we ignore the diagonal couplings γ_{ii} since $\gamma_{ii} \ll \omega_i$. As will become clear, the effectiveness of the designed pulse sequence depends on the condition $|\gamma_{ij}/\omega_{ij}| \ll 1$ which is satisfied in most qubits.

The Hamiltonian in the interaction picture is $\mathcal{H}_{int} = e^{i\mathcal{H}_0 t}\mathcal{H}_I e^{-i\mathcal{H}_0 t}\cos(\omega t + \phi)$, ω being the pulse frequency. The wave function $\Psi(t) = [u\, v\, w]^T$ evolves according to the equation $i\frac{\partial\Psi(t)}{\partial t} = \mathcal{H}_{int}\Psi(t)$. When the perturbation is weak, this equation is integrated order by order as:

$$\begin{aligned} \Psi(t) &= \Psi(0) + \textstyle\int_0^t dt' \mathcal{H}_{int}(t')\Psi(0) \\ &+ \textstyle\int_0^t dt' \int_0^{t'} dt'' \mathcal{H}_{int}(t')\mathcal{H}_{int}(t'')\Psi(0) + \cdots, \end{aligned} \tag{5.6}$$

The cosine function is used in the rf pulse instead of a single frequency wave. In many systems, no physical correspondence of the transversal polarized wave exists. For example, the circuit of the pc-qubit is biased by the z direction magnetic flux and the perturbation is the high frequency modulation of the z flux.

Our strategy to reduce the unwanted transitions is to divide the qubit operation into short intervals of t_0 and attach additional pulses to each operation pulse to correct errors from this short interval. The operation pulse is in resonance with ω_{21} of the lowest two states. Besides rotating the qubit between the level 1 and 2, it brings up off-resonant transitions between the third level and these two levels by the couplings γ_{13} and γ_{23}. Then the same perturbation is applied in two other pulses with different frequencies, amplitudes and phases as: $\alpha_{31}\mathcal{H}_I\cos(\omega_{31}t + \phi_{31})$ and $\alpha_{32}\mathcal{H}_I\cos(\omega_{32}t + \phi_{32})$, both for time t_0, to cancel the unwanted transitions to the third level. This three-piece sequence is repeated τ_{op}/t_0 times to finish the qubit

operation. The time t_0 satisfies $1/\omega \ll t_0 \ll 1/\gamma_{ij}, i,j = 1,2,3$ with both $1/\omega_{21}t_0$ and $\gamma_{ij}t_0$ being small parameters of the same order. Thus we have two small parameters in this procedure. This is crucial for this simple pulse sequence to work.

Starting with an initial wave function $\Psi(0) = [u_0\, v_0\, w_0]^T$, $w_0 = 0$, after the ω_{21} pulse, the third level has the component:

$$\begin{aligned} w = \;& u_0\left(\frac{\gamma_{13}^*(e^{-i(\omega_{21}-\omega_{31})t_0}-1)}{\omega_{21}-\omega_{31}} - \frac{\gamma_{13}^*(e^{i(\omega_{21}+\omega_{31})t_0}-1)}{\omega_{21}+\omega_{31}}\right) \\ +\; & v_0\left(\frac{\gamma_{23}^*(e^{-i(\omega_{21}-\omega_{32})t_0}-1)}{\omega_{21}-\omega_{32}} - \frac{\gamma_{23}^*(e^{i(\omega_{21}+\omega_{32})t_0}-1)}{\omega_{21}+\omega_{32}}\right) , \\ +\; & u_0\theta_u + v_0\theta_v \end{aligned} \tag{5.7}$$

where θ_u and θ_v are of third order. The main components in w are second order terms that depend on the initial conditions u_0 and v_0 linearly. With t_0 satisfying $e^{2i\omega_{21}t_0} = 1$, u and v have third order deviations from the desired two-level rotation. The other two pulses are applied to cancel the w component. The ω_{31} pulse induces a resonant transition between level one and three to cancel the u_0 term; the ω_{32} pulse induces a resonant transition between level two and three to cancel the v_0 term. The amplitudes and phase shifts of these two pulses can be expanded in ascending order as:

$$\begin{aligned} \alpha_{31}e^{i\phi_{31}} &= \alpha_{31}^{(1)}e^{i\phi_{31}^{(1)}} + \alpha_{31}^{(2)}e^{i\phi_{31}^{(2)}} + \cdots \\ \alpha_{32}e^{i\phi_{32}} &= \alpha_{32}^{(1)}e^{i\phi_{32}^{(1)}} + \alpha_{32}^{(2)}e^{i\phi_{32}^{(2)}} + \cdots \end{aligned} , \tag{5.8}$$

The first order coefficients cancel the second order terms in w and modify the higher order terms θ_u and θ_v when:

$$\begin{aligned} \alpha_{31}^{(1)}e^{i\phi_{31}^{(1)}} &= \frac{e^{-i(\omega_{21}-\omega_{31})t_0}-1}{i(\omega_{21}-\omega_{31})t_0} - \frac{e^{i(\omega_{21}+\omega_{31})t_0}-1}{i(\omega_{21}+\omega_{31})t_0} \\ \alpha_{32}^{(1)}e^{i\phi_{32}^{(1)}} &= \frac{e^{-i(\omega_{21}-\omega_{32})t_0}-1}{i(\omega_{21}-\omega_{32})t_0} - \frac{e^{i(\omega_{21}+\omega_{32})t_0}-1}{i(\omega_{21}+\omega_{32})t_0} \end{aligned} , \tag{5.9}$$

It turns out that the nth order terms of w after the correction pulses include linear terms of $\alpha_{31}^{(n-1)}$ and $\alpha_{32}^{(n-1)}$, and complicated terms that depend on $\alpha_{3i}^{(k)}e^{i\phi_{3i}^{(k)}}$ ($k = 1 \ldots (n-2)$). So, for any n, $\alpha_{31}^{(n-1)}$ and $\alpha_{32}^{(n-1)}$ can be determined by the lower order components of α_{31} and α_{32} to cancel the nth order of w. As a result, transitions to

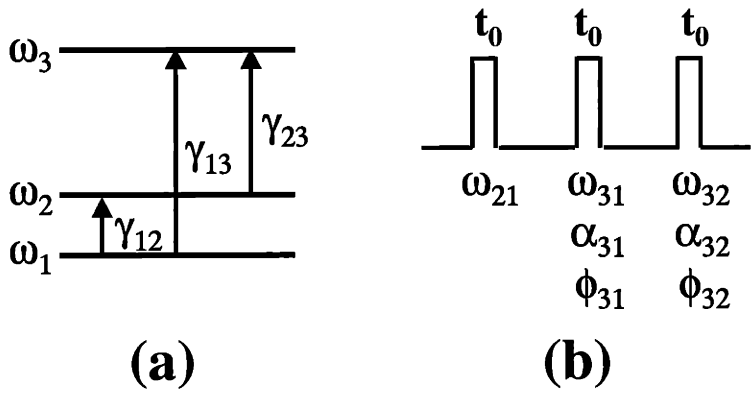

Figure 5-3: The pulse sequence that prevent leakage in the three level system. (a). the three level system that is coupled by transition matrix; (b). the pulse sequence that prevents the leakage. Each pulse has a duration of t_0 and in resonant with ω_{ij} as labeled under the pulse. Their amplitude and phase shift are determined by the parameters in the three level system and are given in the text. The amplitude and phase provide 6 free parameters that can be adjusted. And the consequence is that the unitary transformation is made block diagonal.

the third level can be completely erased. The parameters α_{31} and α_{32} do not depend on the initial condition u_0 and v_0. This is similar to solving the wave function in the perturbation theory where the higher order terms are derived after the lower order ones.

After the kth pulse sequence, with $w = 0$, the wave function is:

$$\begin{bmatrix} u_{k+1} \\ v_{k+1} \end{bmatrix} = \begin{bmatrix} \cos\bar{\varphi} + \bar{s}_u & -i\sin\bar{\varphi} + \bar{t}_u \\ -i\sin\bar{\varphi} + \bar{t}_v & \cos\bar{\varphi} + \bar{s}_v \end{bmatrix} \begin{bmatrix} u_k \\ v_k \end{bmatrix}, \tag{5.10}$$

where $\bar{\varphi} = \gamma_{12}t_0$ is the phase rotation of the two-level qubit; the $\bar{s}$ and $\bar{t}$ terms are of third order. As $w = 0$, this is a unitary transformation that deviates from the Rabi oscillation by third order corrections. The matrix can be written as $\mathcal{U}(t_0) = \exp\left(-i(\gamma_{12}\sigma_x + \delta_0 + \sum_i \delta_i\sigma_i)t_0\right)$, where δ_i are third order small numbers that can be determined by known parameters and do not depend on the index k. This is a renormalization of the qubit operation γ_{12} with the third level decoupled.

This correction strategy is easily generalized to an $N(N \geq 3)$ level system. By applying rf pulses with frequencies $\omega_{i1}, \omega_{i2}, i = 3...N$, the transitions to the higher

levels are completely erased. Assuming no particular symmetry between the states, $2(N-2)$ pulses are required in this process.

One may wonder why this simple pulse sequence works so well to correct the off-resonant transitions to the higher states. For $N-2$ higher levels, to decouple these levels is to exert $4(N-2)$ real domain restrictions on the transformation matrix: $\mathcal{U}_{1i}, \mathcal{U}_{2i} = 0, i = 3...N$. Our tools are the Hamiltonians $\mathcal{H}_0$ and $\mathcal{H}_I$ that create the whole u(N) algebra by commutation. Our pulse sequence

$$\mathcal{U}(t_0) = \prod_{i,\beta} P(\alpha_{i\beta}, \phi_{i\beta}) e^{-i \int \mathcal{H}_I \cos \omega_{21} t' dt'} \tag{5.11}$$

where $i = 3 \ldots N$ and $\beta = \uparrow, \downarrow$. $P(\alpha_{i\beta}, \phi_{i\beta}) = e^{-i \int \mathcal{H}_I \alpha_{i\beta} \cos(\omega_{i\beta} t' + \phi_{i\beta}) dt'}$, includes $4(N-2)$ free parameters. By choosing proper pulse sequences, we can achieve the decoupling with proper pulse parameters.

The proposed method is illustrated in Fig. 5-3 where the energy states and the pulse sequence are plotted schematically.

5.2.4 Ending Remark

In conclusion, we discussed the errors due to unwanted transitions to the higher states of a qubit during qubit operation. It was shown by a group theoretic argument that these errors can be completely prevented in principle. Then we generalized the result to the errors due to qubit interactions, which can also be prevented when the number of coupled qubits is not too large. A simple pulse sequence that modifies the qubit dynamics and cancels off-resonant transitions to arbitrary accuracy with $O(N)$ pulses was proposed to illustrate the general analysis. Our results showed that the idea of dynamic pulse control[146] also works for the fast gate errors due to off-resonant transitions to the higher states of a qubit. These results suggest that dynamic pulse control, together with conventional quantum error correcting codes, can function as a powerful tool for performing accurate quantum computation in the presence of errors.

5.3 Average Hamiltonian Approach

Another application of the dynamical control method is to control the qubit's coupling with environmental noise by the so-called average Hamiltonian method. In this method, fast pulses are applied in a systematical way that after one period of the pulse sequence, the evolution of the qubit is characterized by an average Hamiltonian in which the unwanted coupling between qubit and noise is averaged out. As a result, at the end of each period, the noise has no effect on qubit dynamics. This method provides stroboscopic windows where noise is effectively corrected. This method can correct noise that has a finite correlation time longer than the period of the pulse sequence. When pulses are applied to the Hamiltonian, the noise at a later time has memory of the noise from a previous time so that the averaging is possible. The average Hamiltonian has been widely used in NMR experiments [149] where the pulses are used to selectively turn on or turn off certain terms in the Hamiltonian.

The advantage of the dynamic control method for error correction is that no additional qubit resource is required. Standard quantum error correction relies on large number of extra qubits to encode quantum information and realize syndrome testing. Sometimes, the requirements on a large number of extra qubits can be a very difficult condition to be fulfilled in physical realization. The dynamic control method, instead, is a open loop control method, where no additional information is required of the qubit and hence no extra qubit is required either. At the same time, the decoherence from the environment can be very fast so that it is beyond the ability of the quantum error correction method to deal with these noise. An example is the coupling with the nuclear spins for a persistent-current qubit which has a decoherence time on the order of 10 nsec. This is where the dynamic control method steps in.

In this section, we apply the average Hamiltonian method to the decoupling of the persistent-current qubit from environmental noise. We will first describe the method in general. Then we will design a specific pulse sequence with realistic parameters. We also discuss the limitations of this method.

5.3.1 Average Hamiltonian Method

The goal of the average Hamiltonian method is to average out unwanted terms in the static Hamiltonian $\hat{\mathcal{H}}_0$ by fast pulse sequences that are represented by the interaction Hamiltonian $\hat{\mathcal{H}}_1(t)$. These fast pulses are usually very strong and dominate the dynamics of the quantum system. The pulses have a periodic structure with a finite period of T_c.

Let the total Hamiltonian be

$$\hat{\mathcal{H}} = \hat{\mathcal{H}}_0 + \hat{\mathcal{H}}_1(t) \tag{5.12}$$

The time evolution of this Hamiltonian can be studied in the "toggling" frame. By a toggling frame, we mean that the static Hamiltonian $\hat{\mathcal{H}}_0$ is treated as a perturbation and the evolution is studied in the interaction picture with this perturbation. The unitary evolution can be written as:

$$\begin{aligned} U(t) &= U_1(t)U_{int}(t) \\ U_1(t) &= \hat{T}e^{-i\int_0^t ds\hat{\mathcal{H}}_1(s)} = U_1(t+T_c) \\ U_{int} &= \hat{T}e^{-i\int_0^t ds\widetilde{\mathcal{H}}_0(s)} \\ \widetilde{\mathcal{H}}_0(s) &= U_1^\dagger(s)\hat{\mathcal{H}}_0U_1(s) \end{aligned} \tag{5.13}$$

where U_{int} is the unitary transformation in the toggling frame and $U(t)$ is the unitary transformation in the Schrödinger picture. They are different by a unitary transformation $U_1(t)$ that can be determined from the pulse sequence. With the periodic condition, $U_1(t)$ is also periodic with a period of T_c. This also shows that $U_1(T_c) = I$. Hence at the end of one pulse period, the dynamics of the quantum system is described by the transformation $U(t) = U_{int}(t)$.

Assume the pulse sequence has n fast pulses at time $t_i, i = 1 \cdots n$ respectively. The duration of each pulse is very short and can be ignored. Each pulse generates a transformation $P_i = e^{-i\int ds\hat{\mathcal{H}}_1(s)}$. Hence, the $U_1(t)$ operators and the $\widetilde{H}_0(t)$ operators are

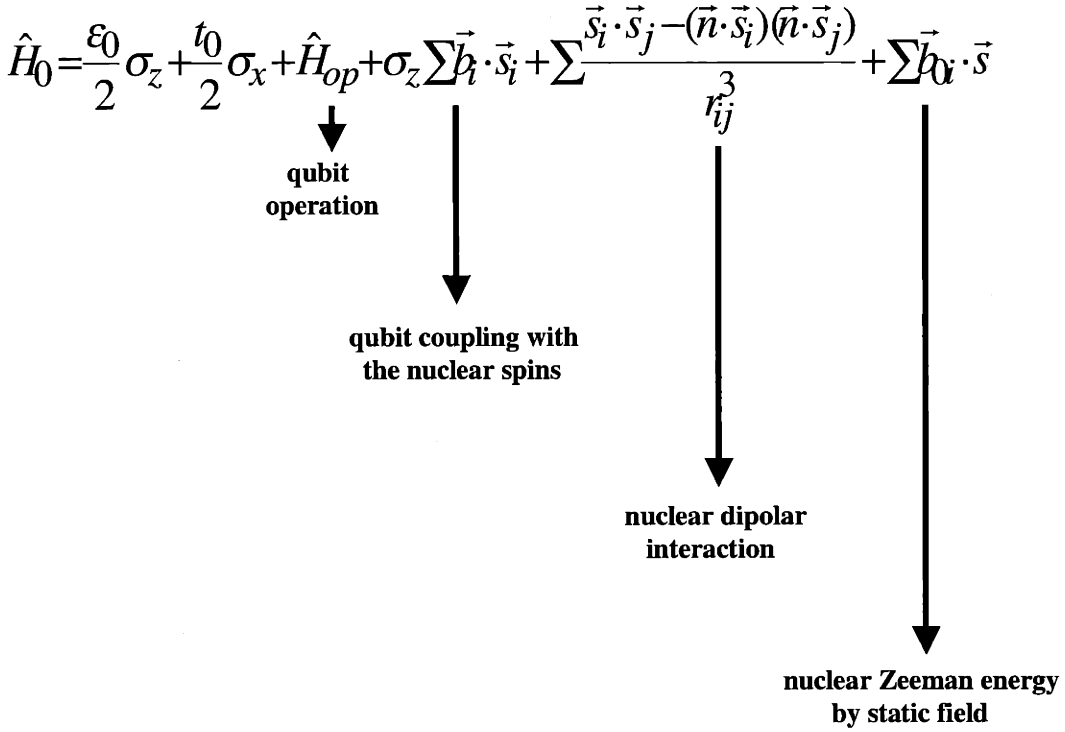

Figure 5-4: The interaction between a qubit and the nuclear spins. The first two terms are the qubit static Hamiltonian. $\hat{\mathcal{H}}_{op}$ is the single qubit operation. Then there is the magnetic interaction between the qubit and the nucleus, followed by the dipolar interaction between the nucleus. The last term is the nuclear spin Zeeman energy. $\vec{b}_{0i}$ is the local magnetic field on the ith spin.

$$
\begin{aligned}
&t < t_1, && U_1(t) = I, && \widetilde{\mathcal{H}_0}(t) = \hat{\mathcal{H}}_0 = \widetilde{\mathcal{H}_0} \\
&t_1 < t < t_2, && U_1(t) = P_1, && \widetilde{\mathcal{H}_0}(t) = P_1^\dagger \hat{\mathcal{H}}_0 P_1 = \widetilde{\mathcal{H}_1} \\
&t_2 < t < t_3, && U_1(t) = P_2 P_1, && \widetilde{\mathcal{H}_0}(t) = P_1^\dagger P_2^\dagger \hat{\mathcal{H}}_0 P_2 P_1 = \widetilde{\mathcal{H}_2} \\
&\ldots
\end{aligned}
\tag{5.14}
$$

which shows that the effect of the pulses is to transform the Hamiltonian $\hat{\mathcal{H}}_0$ into $\widetilde{\mathcal{H}_i}$ with the product of the P_i operators. After one period of the pulses, $\prod_{i=1}^{n} P_i = I$ and $\widetilde{\mathcal{H}_n} = \hat{\mathcal{H}}_0$. As a result, we can write the time evolution of the qubit as

$$
U(t) = e^{-i\widetilde{\mathcal{H}}_n \Delta t_n} \cdots e^{-i\widetilde{\mathcal{H}}_1 \Delta t_1} e^{-i\widetilde{\mathcal{H}}_0 \Delta t_0} = e^{-i\bar{\mathcal{H}} T_c} \tag{5.15}
$$

where Δ_i is the time between pulse i and pulse $i+1$ with $\sum \Delta_i = T_c$. $\bar{\mathcal{H}}$ in the last term is the average Hamiltonian of the pulse sequence. To the lowest order, $\bar{\mathcal{H}}^{(0)} = \frac{1}{T_c}(\widetilde{\mathcal{H}_0}\Delta t_0 + \widetilde{\mathcal{H}_1}\Delta_1 + \cdots + \widetilde{\mathcal{H}_n}\Delta t_n)$. At times NT_c (N: integer), the dynamics is determined by the average Hamiltonian. And when the higher order contribution can be neglected, $\bar{\mathcal{H}}^{(0)}$ is the only important term of the system. By manipulating the sequence of the fast pulses, the average Hamiltonian can be selectively controlled and the system dynamics can be manipulated.

When this method is applied to the decoupling of a quantum system from its environment, the operators that appears in the coupling terms are average out by the pulses. At the same time, the environment is required not to fluctuate too fast—- the correlation time of the environment can not be too short. Otherwise, the randomness of the environmental operator will destroy the averaging process.

This method can decouple the persistent-current qubit from the nuclear spin fluctuations, for example. Fig. 5-4 shows the Hamiltonian of the qubit-nuclear spin interaction. The first two terms are the qubit Hamiltonian, followed by a gate operation term on the qubit. The next term is the coupling between the qubit and the nuclear spins. The magnetic interaction generates a σ_z coupling to the qubit. The next term is the dipolar interaction between the nucleus, followed by the Zeeman energy of the nuclear spins. As T_1 can be very long in the superconducting system

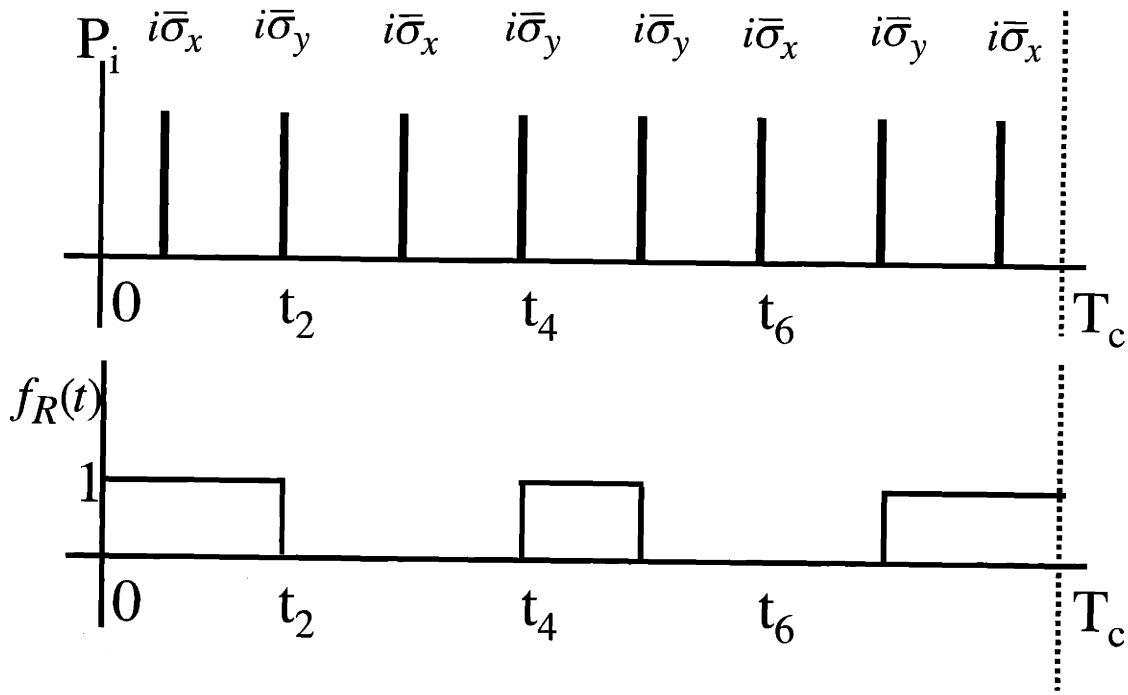

Figure 5-5: The pulse sequence designed to average noise of the persistent current qubit. x axis: the time of the pulse sequence with duration T_c. Top: the pulse sequence that can average out any temporally correlated noise with σ_z, σ_x and σ_y couplings. Bottom: gate pulse that has non-trivial dynamics even with the fast control pulses.

at a temperature well below the critical temperature, the nuclear spin fluctuation time is determined by the dipolar interaction: $T_{cor} \sim 1/E_{dipole} = 10\,\mu$sec. To apply the average Hamiltonian method, the pulse sequence needs to be shorter than this correlation time. As will be shown later, this is indeed possible.

5.3.2 Pulse Decoupling for PC-Qubit

Now we apply the average Hamiltonian method to the persistent-current qubit. We propose a pulse sequence that can decouple the qubit from any Pauli noise. This requires that the correlation time of the noise spectrum is longer than the period of

the pulse sequence. This also requires that the pulse is sufficiently fast so that during the pulses, the qubit original dynamics can be neglected. We will present the pulse first, then we will discuss whether the proposed pulse is practical or not. As the pulse sequence averages all the Pauli matrices to zero, attention should be paid when we want to generate a qubit operation at the same time as the decoupling pulses. We will discuss how the decoupling will affect the gate operation.

We start from the Hamiltonian:

$$\hat{\mathcal{H}}_0 = \frac{\omega_0}{2}\sigma_z + f_R(t)\Omega_R\sigma_x \cos\omega_0 t + \sigma_z\hat{X}_z + \sigma_x\hat{X}_x + \sigma_y\hat{X}_y + \hat{\mathcal{H}}_B \tag{5.16}$$

where σ_i, $i = x, y, z$ are the Pauli matrices of the qubit, ω_0 is the qubit eigen frequency, Ω_R is the Rabi frequency of qubit operation, and f_R is an envelope function of the gate pulse and needs to be modified when the decoupling pulses are on. The $\hat{X}_i$, $i = x, y, z$ is the operators of the environment. These terms are the coupling between the qubit and the environment. $\hat{\mathcal{H}}_B$ is the Hamiltonian of the environment.

To decouple the qubit from the most general type of noise, we need to average all the Pauli matrices to zero. The decoupling pulse is plotted in Fig. 5-5. This is an eight-pulse sequence with equal spacing between each pulse. The pulse labeled by $i\sigma_x$ and the pulse labeled by $i\sigma_y$ can be implemented by the same microwave source with a $\frac{\pi}{2}$ shift: $\hat{\mathcal{H}}_1 = \alpha\sigma_x \cos\omega_0 t$ for $i\sigma_x$ and $\hat{\mathcal{H}}_1 = \alpha\sigma_x \sin\omega_0 t$ for $i\sigma_y$, where α is the pulse amplitude.

The unitary transformation after one period of pulses is

$$\begin{aligned} U(T_c) &= \sqrt{U_0}(i\sigma_x)U_0(i\sigma_y)U_0(i\sigma_x)U_0(i\sigma_y)U_0(i\sigma_y)U_0(i\sigma_x)U_0(i\sigma_y)U_0(i\sigma_x)\sqrt{U_0} \\ &= \sqrt{e^{-i\hat{\mathcal{H}}_0\Delta t}}e^{-i\hat{\mathcal{H}}_0^x\Delta t}e^{-i\hat{\mathcal{H}}_0^z\Delta t}e^{-i\hat{\mathcal{H}}_0^y\Delta t}e^{-i\hat{\mathcal{H}}_0\Delta t}e^{-i\hat{\mathcal{H}}_0^y\Delta t}e^{-i\hat{\mathcal{H}}_0^z\Delta t}e^{-i\hat{\mathcal{H}}_0^x\Delta t}\sqrt{e^{-i\hat{\mathcal{H}}_0\Delta t}} \end{aligned} \tag{5.17}$$

where Δt is the spacing between the pulses and $e^{-i\hat{\mathcal{H}}_0^i\Delta t}$, $i = x, y, z$, is the Hamiltonian after transformation. The signs of the Pauli matrices in each of these Hamiltonians are shown in Table 5.1. As a result, the average Hamiltonian of the lowest orders is: $\bar{\mathcal{H}} = \bar{\mathcal{H}}^{(0)} = \bar{\mathcal{H}}_{op} + \mathcal{H}_B + O([\mathcal{H}_0\Delta t]^4)$. As the sequence is designed to have time

	σ_x	σ_z	σ_z
$\hat{\mathcal{H}}_0$	+	+	+
$\hat{\mathcal{H}}_0^x$	+	−	+
$\hat{\mathcal{H}}_0^y$	−	+	−
$\hat{\mathcal{H}}_0^z$	−	−	+

Table 5.1: The effective Hamiltonian during the pulse sequence. The signs of the Pauli matrices at different Hamiltonian are listed with + or −. When adding up to the zeroth order of the average Hamiltonian, these terms cancel each other and decouple the qubit from the environment.

reversal symmetry, all odd order contributions are zero. It can also be proved that the second order term is also zero.

In the Hamiltonian, we write $\bar{\mathcal{H}}_{op}$ instead of $\mathcal{H}_{op}$ as the gate operation. The decoupling sequence modifies the gate operation as well as decoupling the noise. As in Fig. 5-5, the envelope function is designed according to the decoupling pulse to give a non-trivial operation on the qubit and $\bar{\mathcal{H}}_{op} = \frac{\Omega_R}{4}\sigma_x$.

For the average Hamiltonian method to work, several conditions need to be satisfied. First, the duration of the pulse needs to be much shorter than the spacing between the pulses. Second, the period of the sequence needs to be much shorter than the correlation time of the noise. So we have $T_c = 8\Delta t \ll \tau_{cor} \sim 10\,\mu$sec. Third, during gate operation, the pulse needs to be faster than the gate operation. Considering all these restrictions, we have $\Delta t = 2.5\,$nsec, $\alpha = 2\pi \times 1\,$GHz and $\Omega_R = 5\,$MHz. In the superconducting persistent-current qubit, this design can be achieved with existing technology.

In this pulse sequence, the pulses are ideal square pulses. In reality, pulses of more complicated shape might do better, taking into account the higher level of the qubit and the rotating wave approximation in this analysis. As the applied pulses are very strong, $\alpha = 1\,$GHz, the dynamics of the qubit is expected to have significant deviation from a perfect Rabi flip. Numerical derivation of the pulse shape and phase is necessary to get the desired decoupling pulses.

5.4 Summary

In this chapter, we studied the application of dynamic control approach to deal with quantum gate error and environmental noise. We first applied a group theoretical analysis to the accurate control of a multilevel quantum system. We proved that given a pair of non-commuting operators, any unitary transformation on the Hilbert space can almost always be constructed within n^2 pulses, where n is the number of states in the Hilbert space. We used our analysis to prove that the leakage to the higher qubit states during a gate operation can be completely prevented by applying the right pulse sequence to the qubit. The problem is equivalent to the designing of the right pulses to generate a unitary operation that is block diagonal. We further proved that for the specific problem of preventing leakage, only $O(n)$ pulses are required. We calculated the pulse sequence for a 3-level system to illustrate the method.

Then, we applied the dynamic control method to the decoupling of a qubit from environmental noise under the average Hamiltonian approach. The crucial point of this method is that by applying fast pulses to the qubit, the Hamiltonian evolution can be represented by an average Hamiltonian in which terms in the original Hamiltonian are selectively cancelled out. The method has been widely used in the NMR experiment. In the model we used, the qubit interacts with a general environment with couplings to all the Pauli operators. We designed a pulse sequence that can average out any Pauli noise of the qubit. The sequence includes eight pulses of either σ_x or σ_y operations. The sequence averages out the qubit Hamiltonian as well. By applying an envelope function to the gate pulse, we can achieve non-trivial qubit dynamics even when the decoupling pulses are on.

The dynamic control approach turns out to be a very powerful tool in combination with the quantum error correction method. This method can correct the fast gate error without using extra qubit resources as it is an open loop control method. To be successfully applied, this method relies either on the correlation between errors at different times or on the coherence of a larger quantum system. The reliable application of the method requires accurate control of the pulses. It has been shown

that a shaped pulse is a better solution for many experimental systems, such as the NMR experiment[150]. A numerical method to derive the pulse shapes is required to implement this method and is not yet available for general problems.

Chapter 6

Conclusions and Future Work

6.0.1 Conclusions

The superconducting flux qubits are macroscopic quantum systems and are promising candidates for large-scale quantum computation. The flexibility in fabricating these qubits makes it possible to adjust the qubit's characteristics and to control the quantum operation on the qubits.

In this thesis, various aspects of a superconducting flux qubit—the persistent-current qubit—are investigated in detail. The problems studied include: characterization and manipulation of qubit states, measurement efficiency and the back-effect, decoherence by environmental fluctuations, and a dynamic control approach for accurate gate operation and noise decoupling. This research covers major problems in the physical implementation of the persistent-current qubit and is a first step in realizing superconducting quantum computation.

The persistent-current qubit is made of three nano-scale Josephson junctions connected in a superconducting loop. The system is a phase particle in a two-dimensional periodic potential. By discretizing the phase space, the energy spectrum and the average current of the qubit eigenstates versus the magnetic flux and versus the gate voltage are calculated numerically. It is shown that this qubit behaves as a giant magnetic dipole in a magnetic field, and the field provides a Zeeman splitting for the qubit states. Only near $f_1 = 1/2$ where the Zeeman term is zero, quantum tunnel-

ing between flux states starts to dominate and an anticrossing appears in the energy spectrum. The qubit states have opposite circulating currents which generate a flux of 10^{-3} flux quantum. The qubit can be manipulated by the external magnetic field or microwave radiation in the superconducting loop. Qubits interact with each other via inductive coupling due to the qubit circulating current. This provides a natural means for implementing controlled qubit operations. The calculation also shows that the qubit spectrum versus gate voltage is almost a flat band. This indicates the insensitivity of the qubit to charge fluctuations on the gate.

Measurement of the qubit is an important step in quantum information processing. By inductively coupling the qubit to a dc SQUID magnetometer, the qubit is measured. During measurement, a ramping current is increased until the dc SQUID switches to the finite voltage state and the switching current is recorded. The switching current histogram is affected by the flux of the qubit and is recorded to decide the qubit state. The detector is another quantum system with two degrees of freedom. The interaction between the qubit and the detector induces a displacement between the wave functions of the two detector states regarding the two qubit states. It is shown that this displacement is much smaller than the quantum width of the detector's wave packet. This puts an intrinsic limit to the measurement efficiency and explains the fact that many repetitions are required for the measurement. To improve this efficiency, a coherent transition assisted scheme is designed that is a projective measurement on the qubit. During the measurement, the noise from the environment of the detector is transmitted to the qubit and causes qubit decoherence. This noise can be calculated with a generalized spin-boson approach by adding the detector's degrees of freedom to the boson bath. A general method to calculate this noise from an equivalent circuit approach is developed that by mapping the qubit-detector Hamiltonian to a linear circuit, the noise can be directly derived from the circuit impedance. The method can be easily applied to other interacting quantum systems.

The solid-state qubits are subjected to stronger environmental noise than other qubit systems. A general approach for studying the qubit decoherence due to environ-

mental fluctuations is developed. As the coupling between the qubit and environmental modes is weak, the noise is described as classical fluctuation fields that interact with the qubit through the Pauli matrices. The decoherence of qubit can be studied by integrating the noise spectral density over the whole frequency range according to the fluctuation-dissipation theorem. This approach is applied to study intrinsic qubit noise such as the charge fluctuations on the substrate, the nuclear spin fluctuations and the quasiparticle tunneling. The study shows that the decoherence time due to these noise sources is longer than 10^4 gate-operation times. The decoherence due to electromagnetic decay is studied by a perturbation approach. The electromagnetic field is written into the Hamiltonian of the qubit as the gate voltage and the magnetic flux. The decay rate is calculated by Fermi's Golden rule and is of order of seconds. The decoherence due to the interaction between different qubits is also studied. It turns out this is the major decoherence source. This interaction can be manipulated by adjusting the qubit geometry and by a pulse decoupling method.

Dynamic control is a powerful method in coping with quantum errors in quantum computation. In this approach, quantum operations are studied in a group theoretical framework in the qubit Hilbert space. One application of dynamic control is to construct accurate gate operations with available Hamiltonian operators. In the pc-qubit, during the gate operation, the qubit makes transitions to higher states of the circuit through off-resonance transitions. This leakage is a serious and ubiquitous problem in quantum computation. By a Lie algebra analysis, it is proved that gate operation only between the two qubit states can be realized by controlling the time dependence of the operation. A pulse sequence is developed that can prevent the leakage to arbitrary accuracy. Another application of the dynamic control is to decouple the qubit from environmental noise by pulse sequences. Fast pulses are applied to the qubit and are equivalent to transformations of the qubit operators. Hence, the dynamics of the qubit and the environment is described by different effective Hamiltonians at different moments during the pulse sequence. After one period, the evolution operation is determined by an average Hamiltonian. In the lowest orders of this average Hamiltonian, the unwanted coupling to the environment is cancelled out. This

method is applied to the pc-qubit and a pulse sequence of 24 nsec is designed. Noise with a correlation time of the order of longer than 1 μsec. can be decoupled from the qubit with this pulse sequence.

6.0.2 Future Work

Many problems are left unanswered for building the superconducting flux qubit, such as the effect of the $1/f$ noise, the effect of the fabrication inaccuracy for devices and the calibration of accurate control on the qubit dynamics. These problems deserves serious study in the path of realizing superconducting quantum computing. It will take the join effort and both theoretical and experimental studies on these issues to overcome the decoherence problem in the pc-qubit.

The study in this thesis concentrated on the properties of a single qubit. To realize large scale quantum computation, however, qubit network with many qubits is required. The designing of qubit geometry in the network is a complicated issue and is related to the accurate and optimal control of the multi-qubit dynamics. Universal control over the complete Hilbert space of the multi-qubit system is required in the qubit network. To have simple yet universal control is a trade-off between the complication of circuit fabrication and the complication of temporal manipulation.

Another interesting question is that given the basic operation set, how to physically implement function calls in the quantum algorithms. In the mathematical models, the function call is applied to the qubits by an oracle. To test the theory experimentally, it is necessary to figure out how to achieve the quantum operation in the oracle with available control over the system. Due to the complicated form of many of the function calls, it is a difficult task to implement them physically and hence, a challenging question to answer.

Appendix A

Classical Stability

In this appendix we find the eigen values of the stability matrix for the three junction potential and the range of frustration around $f = 1/2$ where there are two stable classical solutions with opposite circulating currents.

The potential energy of the Josephson energy of the three junction qubit is given by Eqn. 2.1

$$\tilde{U} = \frac{U}{E_J} = 2 + \alpha - \cos\varphi_1 - \cos\varphi_2 - \alpha\cos(2\pi f + \varphi_1 - \varphi_2) \tag{A.1}$$

We are interested in minimum energy phase configurations; that is, stable solutions of the following system of equations:

$$\begin{aligned} \frac{\partial\tilde{U}}{\partial\varphi_1} &= \sin\varphi_1 + \alpha\sin(2\pi f + \varphi_1 - \varphi_2) = 0 \\ \frac{\partial\tilde{U}}{\partial\varphi_2} &= \sin\varphi_2 - \alpha\sin(2\pi f + \varphi_1 - \varphi_2) = 0\,. \end{aligned} \tag{A.2}$$

The solutions $(\varphi_1^*, \varphi_2^*)$ comply with: $\sin\varphi_1^* = -\sin\varphi_2^* = \sin\varphi^*$. Then

$$\sin\varphi^* = -\alpha\sin(2\pi f + 2\varphi^*) \tag{A.3}$$

In order to check the character of the solution we compute the eigen values of the

stability matrix, $\frac{\partial^2 \tilde{U}}{\partial\varphi_i \partial\varphi_j}$, where

$$\begin{aligned}
\frac{\partial^2 \tilde{U}}{\partial \varphi_1^2} &= \cos\varphi_1 + \alpha\cos(2\pi f + \varphi_1 - \varphi_2) \\
\frac{\partial^2 \tilde{U}}{\partial \varphi_2^2} &= \cos\varphi_2 + \alpha\cos(2\pi f + \varphi_1 - \varphi_2) \\
\frac{\partial^2 \tilde{U}}{\partial \varphi_1 \partial \varphi_2} &= -\alpha\cos(2\pi f + \varphi_1 - \varphi_2)\,.
\end{aligned} \tag{A.4}$$

For the states with $\cos\varphi_1^* = \cos\varphi_2^* = \cos\varphi^*$ (these are the ones we are interested here), the eigen values are

$$\begin{aligned}
\lambda_1 &= \cos\varphi^* \\
\lambda_2 &= \cos\varphi^* + 2\alpha\cos(2\pi f + 2\varphi^*)\,.
\end{aligned} \tag{A.5}$$

When $f \neq 0, 1/2$ we have used relaxation methods for computing φ^*. Both eigen values are greater than zero which assures the minimum energy condition. Fig. 2-2 shows the energy of the minimum energy configurations for $\alpha = 0.8$. We find that there exists a region of values of the field for which two different minimum energy phase configurations coexist.

Next we calculate the critical values of the external field for this coexistence. We can restrict our analysis to the region around $f = 0.5$; that is, $[0.5 - f_c, 0.5 + f_c]$ (where $f_c \geq 0$). These extrema values of the field correspond to solutions for which one of the eigen values is positive and the other equals zero. The inset of Fig. 2-2 shows $f_c(\alpha)$.

We first calculate f_c when $\alpha \geq 1.0$. The first eigen value which equals zero is λ_1. Then at $f = 0.5 \pm f_c$, $\lambda_1 = 0$ which implies $\varphi^* = \mp\pi/2 \bmod 2\pi$ (here and below we associate the sign in f_c with the sign of the phase in order to have $f_c \geq 0$). Then, going to Eqn. A.3 we get

$$\begin{aligned}
\sin(\mp\pi/2) &= -\alpha\sin(\pi \pm 2\pi f_c \mp \pi) \\
\pm 1 &= \pm\alpha\sin(2\pi f_c)
\end{aligned} \tag{A.6}$$

and

$$f_c = \frac{1}{2\pi} \arcsin \frac{1}{\alpha} . \tag{A.7}$$

We now calculate f_c when $0.5 \leq \alpha \leq 1.0$. Now the first eigen value to equal zero is λ_2, and we have to solve:

$$\begin{aligned} \sin\varphi^* &= -\alpha \sin(2\pi f + 2\varphi^*) = \alpha \sin(\pm 2\pi f_c + 2\varphi^*) \\ \cos\varphi^* &= -2\alpha \cos(2\pi f + 2\varphi^*) = 2\alpha \cos(\pm 2\pi f_c + 2\varphi^*) . \end{aligned} \tag{A.8}$$

We will use $\Delta = \pm 2\pi f + 2\varphi^*$, so that

$$\begin{aligned} 1 &= \sin^2\varphi^* + \cos^2\varphi^* \\ &= \alpha^2 \sin^2\Delta + 4\alpha^2 \cos^2\Delta \\ &= \alpha^2 + 3\alpha^2 \cos^2\Delta . \end{aligned} \tag{A.9}$$

Then

$$\begin{aligned} \cos\Delta = \sqrt{\frac{1-\alpha^2}{3\alpha^2}} \quad &; \quad \Delta = \mp \arccos(\sqrt{\frac{1-\alpha^2}{3\alpha^2}}) \\ \cos\varphi^* = 2\sqrt{\frac{1-\alpha^2}{3}} \quad &; \quad \varphi^* = \mp \arccos(2\sqrt{\frac{1-\alpha^2}{3}}) . \end{aligned} \tag{A.10}$$

Here we have followed the solution corresponding to $\cos(\varphi^*) \geq 0$. Finally we have the solution for f_c ($\Delta = \pm 2\pi f_c + 2\varphi^*$)

$$f_c = \frac{1}{2\pi} \left[2\arccos(2\sqrt{\frac{1-\alpha^2}{3}}) - \arccos(\sqrt{\frac{1-\alpha^2}{3\alpha^2}}) \right] . \tag{A.11}$$

Appendix B

Tight-Binding Estimate of Coefficients of Change

Recall that $f_a = f_2$ and $f_b = f_1 + f_2/2$. Assume that we change f_a and f_b independently. The minima in U occur at $\varphi_p^* = 0$ and $\varphi_m^* = \pm\varphi_m^o$ Therefore, the energy due to the potential energy is for each of the minima

$$\frac{U}{E_J} = 2 + 2\beta - 2\cos\varphi_m^* - 2\beta\cos(\pi f_a)\cos(2\pi f_b + 2\varphi_m^*)\,. \tag{B.1}$$

The change in the magnetic flux f_a by δf_a causes a change in U of

$$\frac{\partial U}{\partial f_a}\,\delta f_a = -2\pi\beta\sin\pi f_a\cos 2\varphi_m^o\,\delta f_a \tag{B.2}$$

which is the same for the minimum at $\pm\varphi_m^o$. Whereas, the flux f_b causes a change

$$\frac{\partial U}{\partial f_b}\,\delta f_b = \mp 4\pi\beta\cos\pi f_a\sin 2\varphi_m^o\,\delta f_b \tag{B.3}$$

which has opposite signs for the two minimum. Therefore,

$$\frac{\Delta U}{E_J} = -2\pi\beta\sin\pi f_a\cos 2\varphi_m^o\,\delta f_a\,\mathbf{1} - 4\pi\beta\cos\pi f_a\sin 2\varphi_m^o\,\delta f_b\,\sigma_z\,. \tag{B.4}$$

Recall that ΔF is the change in the energy between the two states when there

is no tunneling. This is the second term in Eqn. B.4, since the first term is only a constant for both levels, so that

$$\frac{\Delta F}{E_J} = -4\pi\beta \cos \pi f_a \sin 2\varphi_m^o \, \delta f_b \, \sigma_z \, . \tag{B.5}$$

For this change $\Delta F = r_1\delta_1 + r_2\delta_2$; and since $\delta f_b = \delta_1 + \delta_2/2$, we have $r_1 = 2r_2$ and

$$\frac{r_1}{E_J} = 4\pi\beta \cos \pi f_a \sin 2\varphi_m^o \, . \tag{B.6}$$

We have found previously that $\cos \varphi_m^o = 1/2\alpha$ where $\alpha = 2\beta \cos \pi f_a$ so that with $f_a = 1/3$,

$$\frac{r_1}{E_J} = 2\pi\sqrt{1 - 1/(4\beta^2)} \, . \tag{B.7}$$

To find the changes in Δt, we see that the changes in $t_1 = (\hbar\omega_m/2\pi)e^{-S_1/\hbar}$ are dominated by changes in S_1, so that

$$\Delta t = -\frac{t}{\hbar} \sum_{i=a,b} \frac{\partial S_1}{\partial f_i} \delta f_i \, . \tag{B.8}$$

The changes in f_b do not change S_1 to first order. Hence, changes in t come from changes in $f_a = f_2$ only, so that $s_1 = 0$. But changes in f_a are equivalent to changes in α in the three junction problem, so we can use Eqns. B.8 and 2.17 and the fact that $2\beta\cos(\pi f_a)$ plays the role of α to find

$$\Delta t = \frac{\pi t}{\hbar} \frac{\partial S_1}{\partial \alpha} (2\beta \sin \pi f_a) \, \delta f_a \, . \tag{B.9}$$

This allows us to write $s_2 = \eta t\sqrt{E_J/E_c}$ where η is of the order of unity. For the operating point we find $\eta \sim 3.5$. Therefore, changes in H due to changes in t_1 go like σ_x. These tight-binding estimates for $\beta = 0.8$ and $f_a = 1/3$ give $s_1 = 0$ and $s_2 = 0.03$.

Appendix C

Simulation of Coupled Qubits

The qubits interact with each other through their mutual inductive coupling. The qubit flux is 10^{-3} flux quantum. When two qubits are adjacent to each other, the interaction energy is about 2 GHz. The effect of self inductance is omitted in this discussion[153]. As the interaction is weak, the self-consistent mean field approach is applied to solve the interaction Hamiltonian.

We start by discussing the Hamiltonian of two kinds of interacting circuits. An appropriate approximation is made to simplify the Hamiltonian. The numerical method is then described. In this method, the qubit states are calculated with a self-consistent mean field approach. The influence of qubit coupling on the energy and current is analyzed according to the numerical results.

C.1 Hamiltonians

In this part, we study two kinds of qubit coupling circuits which can implement a Controlled-Not gate. The coupling circuits are plotted in Fig. C-1. In (a), flux $f_1^{(A)}$ of circuit A is modulated by the circulating current of circuit B $I_1^{(B)}$ through mutual inductance M_{A_1,B_1}. Similarly, the flux $f_1^{(B)}$ of circuit B is changed by current $I_1^{(A)}$. The roles of the two qubits are symmetric in the interaction. In (b), flux $f_1^{(A)}$ of circuit A is affected by the squid loop current $I_2^{(B)}$ of circuit B, and flux $f_2^{(B)}$ of circuit B is affected by the circulating current $I_1^{(A)}$ of circuit A. In this case, the

mutual inductance between these two loops is M_{A_1,B_2} and the two qubits are not symmetric. The self inductance of both circuits is neglected in this discussion.

C.1.1 The First Kind of Coupling

The discussion in this part starts from the Lagrangian of this coupling circuit, then the mean field approximation is applied for the simplification of the Hamiltonian. First, we write down the Lagrangian as:

$$\mathcal{L} = T_A + T_B - U_A - U_B - H_{int} \tag{C.1}$$

where

$$\begin{aligned}
T_A &= \tfrac{1}{2}C_g(V_{g1}^{(A)} - \tfrac{\Phi_0}{2\pi}\tfrac{d\varphi_{A,1}}{dt})^2 + \tfrac{1}{2}C_g(V_{g2}^{(A)} - \tfrac{\Phi_0}{2\pi}\tfrac{d\varphi_{A,2}}{dt})^2 \\
&\quad + \tfrac{1}{2}C_1(\tfrac{\Phi_0}{2\pi}\tfrac{d\varphi_{A,1}}{dt})^2 + \tfrac{1}{2}C_1(\tfrac{\Phi_0}{2\pi}\tfrac{d\varphi_{A,2}}{dt})^2 + \tfrac{1}{2}C_3(\tfrac{\Phi_0}{2\pi}\tfrac{d\varphi_{A,1}}{dt} - \tfrac{\Phi_0}{2\pi}\tfrac{d\varphi_{A,2}}{dt} + M_{A_1,B_1}\tfrac{dI_1^{(B)}}{dt})^2 \\
U_A &= E_J(-\cos\varphi_{A,1} - \cos\varphi_{A,2}) \\
&\quad + \alpha E_J(-2\cos\pi f_2^{(A)}\cos(\varphi_{A,1} - \varphi_{A,2} + 2\pi(f_1^{(A)} + f_2^{(A)}/2) + \tfrac{2\pi}{\Phi_0}M_{A_1,B_1}I_1^{(B)})) \\
I_1^{(A)} &= I_c\sin\varphi_{A,1} \\
I_1^{(B)} &= I_c\sin\varphi_{B,1} \\
\begin{matrix} T_B \\ U_B \end{matrix} &= \begin{matrix} T_A \\ U_A \end{matrix} \quad byreplacing \quad \varphi_{A,1}\to\varphi_{B,1} \quad \varphi_{A,2}\to\varphi_{B,2} \quad I_1^{(B)}\to I_1^{(A)} \\
H_{int} &= M_{A_1,B_1}I_1^{(A)}I_1^{(B)}\,.
\end{aligned} \tag{C.2}$$

In this equation, the parameters of circuit A and B are labeled by subscripts or superscripts A and B respectively. The T_A and T_B terms are charge energies for circuits A, B, and U_A, U_B are potential energies for the Josephson Junctions. The last term $\mathcal{H}_{int}$ is the mutual inductive coupling between the two circuits. The effect of the mutual inductance appears in the charging energy, potential energy and the interaction terms. A simple estimation shows that $M_{A_1,B_1}I_1^{(B)}/\Phi_0 \approx 10^{-3}$, which enables us to apply the mean field approach to individual circuits. We substitute the

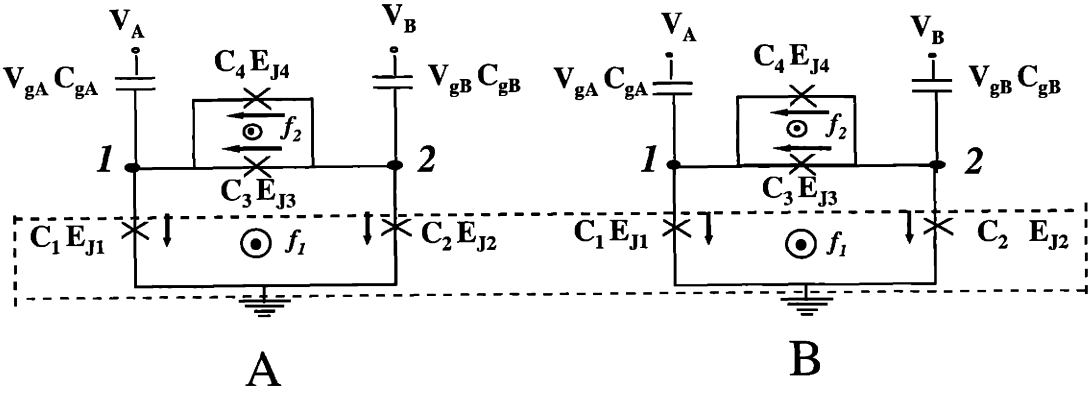

(a)

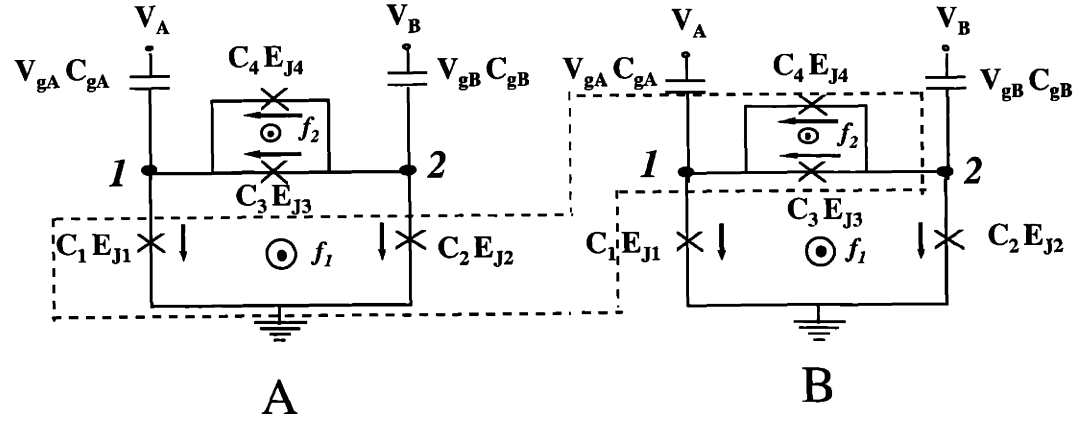

(b)

Figure C-1: The two-qubit coupling circuits. The qubits interact via mutual inductance of neighbour circuits.

operator $I_1^{(B)}$ and $dI_1^{(B)}/dt$ with the quantum averages $< I_1^{(B)} >$ and $< dI_1^{(B)}/dt >$ respectively. It turns out that the additional term $M_{A_1,B_1}\frac{dI_1^{(B)}}{dt}$ inside the charge energy has no influence on the kinetic energy of the Hamiltonian except for a constant term and a shift of wave vector $\vec{k}_m$, as this term only adds a full-differentiation which has no effect on the dynamics. This constant term is:

$$-C_3(M_{A_1,B_1}\langle\frac{dI_1^{(B)}}{dt}\rangle)^2 \tag{C.3}$$

which is of second order of $M_{A_1,B_1}\langle\frac{dI_1^{(B)}}{dt}\rangle)/\Phi_0$, and $\approx 10^{-6}E_J$. It is neglected in the calculation. In the last term H_{int}, we have

$$I_1^{(A)}I_1^{(B)} \approx I_1^{(A)} < I_1^{(B)} > + < I_1^{(A)} > I_1^{(B)} - < I_1^{(A)} >< I_1^{(B)} > . \tag{C.4}$$

Under this approximation, we obtained the following Hamiltonian:

$$\begin{aligned}
H &= H_A + H_B - M_{A_1,B_1}\langle I_1^{(A)}\rangle\langle I_1^{(B)}\rangle \\
H_A &= \tfrac{(P_{A,p}+B_{A,p})^2}{2M_p} + \tfrac{(P_{A,m}+B_{A,m})^2}{2M_m} - 2E_J\cos\varphi_{A,p}\cos\varphi_{A,m} \\
&\quad -2E_J\cos\pi f_2^{(A)}\alpha_A\cos(2\varphi_{A,m} + 2\pi(f_1^{(A)} + f_2^{(A)}/2) + \frac{2\pi}{\Phi_0}M_{A_1,B_1}\langle I_1^{(B)}\rangle) \\
&\quad +M_{A_1,B_1}I_1^{(A)}\langle I_1^{(B)}\rangle \\
H_B &= \tfrac{(P_{B,p}+B_{B,p})^2}{2M_p} + \tfrac{(P_{B,m}+B_{B,m})^2}{2M_m} - 2E_J\cos\varphi_{B,p}\cos\varphi_{B,m}) \\
&\quad -2E_J\cos\pi f_2^{(B)}\alpha_B\cos(2\varphi_{B,m} + 2\pi(f_1^{(B)} + f_2^{(B)}/2) + \frac{2\pi}{\Phi_0}M_{A_1,B_1}\langle I_1^{(A)}\rangle) \\
&\quad +M_{A_1,B_1}\langle I_1^{(A)}\rangle I_1^{(B)}
\end{aligned} \tag{C.5}$$

$B_{A,p}$ and $B_{A,m}$ are wave vector shifts due to the external voltage and the mutual inductance:

$$\begin{aligned}
B_{A,p} &= \frac{\Phi_0}{2\pi}C_g(V_{g1}^{(A)} + V_{g2}^{(A)}) \\
B_{A,m} &= \frac{\Phi_0}{2\pi}(C_g(V_{g1}^{(A)} - V_{g2}^{(A)}) - 4C_3M_{A_1,B_1}\langle I_1^{(B)}\rangle)
\end{aligned} \tag{C.6}$$

so for $B_{B,p}$ and $B_{B,m}$, the inductance causes a shift in the $B_{A,m}$ and $B_{B,m}$ with no other effect. Therefore, H_A and H_B are essentially the same as that without the interaction, except for the corrections to the flux in the coupled loops. More explicitly, flux $f_1^{(A)}$ and $f_1^{(B)}$ are replaced by:

$$\begin{aligned} f_1^{(A)} &\to f_1^{(A)} + \frac{M_{A_1,B_1}\langle I_1^{(B)}\rangle}{\Phi_0} \\ f_1^{(B)} &\to f_1^{(B)} + \frac{M_{A_1,B_1}\langle I_1^{(A)}\rangle}{\Phi_0} \end{aligned} \tag{C.7}$$

C.1.2 The Second Kind of Coupling

The analysis of the second coupling circuit is similar to that of the first. Now the mutual inductance is between the circulating current $I_1^{(A)}$ and the squid loop current $I_2^{(B)}$ which is equal to the current in the upper branch of the squid:

$$\begin{aligned} I_1^{(A)} &= I_c \sin(\varphi_{A,p} + \varphi_{A,m}) \\ I_2^{(B)} &= I_c \sin(\varphi_{B,p} + \varphi_{B,m}) + \alpha I_c \sin(2\varphi_{B,m} + 2\pi f_1^{(B)}) \end{aligned} \tag{C.8}$$

.

$I_2^{(B)}$ modifies flux $f_1^{(A)}$ in the first qubit, and $I_1^{(A)}$ changes flux $f_2^{(B)}$ as:

$$\begin{aligned} f_1^{(A)} &\to f_1^{(A)} + \frac{M_{A_1,B_2}\langle I_2^{(B)}\rangle}{\Phi_0} \\ f_2^{(B)} &\to f_2^{(B)} + \frac{M_{A_1,B_2}\langle I_1^{(A)}\rangle}{\Phi_0} \end{aligned} \tag{C.9}$$

.

Therefore the effective Josephson energy of the squid in circuit B is modified to $2\alpha E_J \cos\pi(f_2^{(B)} + \frac{2\pi}{\Phi_0} M_{A_1,B_2}\langle I_1^{(A)}\rangle)$. The other difference from the first coupling is that the wave vector shift $B_{B,m}$ is half of the shift of the first coupling:

$$B_{B,m} = \frac{\Phi_0}{2\pi}(C_g(V_{g1}^{(B)} - V_{g2}^{(B)}) - 2C_3 M_{A_1,B_2}\langle I_1^{(A)}\rangle) \tag{C.10}$$

while $B_{A,m}$ is the same as that of the first circuit.

This circuit is not symmetric for the two qubits and the dependence on the qubit

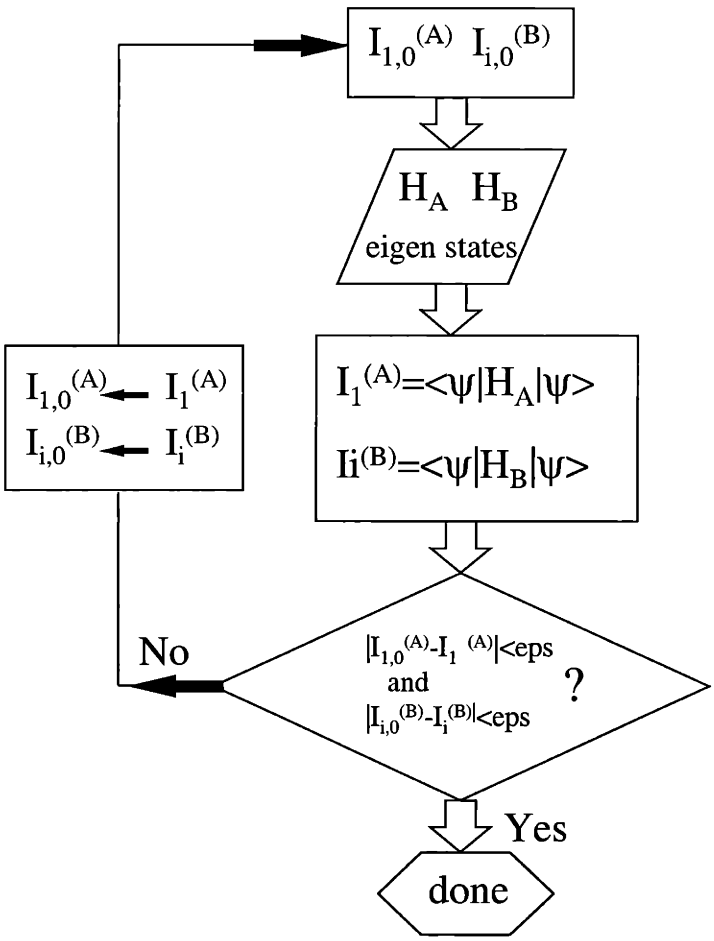

Figure C-2: The self-consistent process for solving the Hamiltonian in the mean field approximation. $i = 1$ in $I_i^{(B)}$ for the first kind of circuit and i=2 for the second kind.

state (especially qubit B) is more complicated than the first circuit. Numerical calculation shows that it is an advantage for implementing the CNot gate.

C.2 Simulation of the Circuits

In this section, we simulate the coupled qubit circuit. In the Hamiltonian of qubit A and B, there are terms that depend on the average current in the other qubit. By an iterative process, we can solve this system self-consistently. The process is shown in Fig. C-2. The initial values $I_{1,0}^{(A)}$ and $I_{1,0}^{(B)}$ (or $I_{2,0}^{(B)}$ in the second circuit) are set as zero. The Hamiltonian for both qubits are solved with the initial current, and eigen values and eigen wave functions are calculated. Then, the currents $\langle I_1^{(A)} \rangle$ and

$\langle I_1^{(B)} \rangle$ are calculated and compared with the initial value. If the two sets of currents are close enough, stop the process. Otherwise, the average currents $\langle I_1^{(A)} \rangle$ and $\langle I_1^{(B)} \rangle$ are put into the Hamiltonian again and the process is repeated until the calculation converges.

In our system, the current is about 1 μA. The qubit size is of μm. As a result, the induced flux is about $10^{-3}\Phi_0$. In the simulation, we assume $M_{A_1,B_i} I_c \frac{2\pi}{\Phi_0}$ to be 10^{-3} for $i = 1, 2$.

C.2.1 Average of Operators

To get the matrix elements of the Hamiltonian, we need to calculate the average of operators such as $I_1^{(A)}$ and $dI_1^{(A)}/dt$. The average of the current operators are straightforward. For example, we have $I_1^{(A)} = I_c \sin(\varphi_p + \varphi_m)$, and the matrix is:

$$\langle n_1, m_1, \vec{k} | I_1^{(A)} | n_2, m_2, \vec{k} \rangle = I_c \delta_{n_1,n_2} \delta_{m_1,m_2} \sin \Delta(n_1 + m_1) \tag{C.11}$$

where n_i and m_i are index for the phase space basis. $\vec{k}$ is the wave vector related to the gate voltage. Δ is the distance between adjacent basis and is a measure of the discreteness.

Another operator in the Hamiltonian is the time derivative of the coupling current, $dI_1^{(A)}/dt = I_c \cos\varphi_1 \frac{d\varphi_1}{dt}$, which can be expressed as momentum operators:

$$\frac{dI_1^{(A)}}{dt} = I_c \cos(\varphi_p + \varphi_m)\left(\frac{P_{A,p} + B_{A,p}}{M_p} + \frac{P_{A,m} + B_{A,}}{M_m}\right) \tag{C.12}$$

In a discrete basis, the momentum operator is

$$P|n> = \frac{i\hbar}{2\Delta}(|n+1> - |n-1>) \tag{C.13}$$

So we have

		E_1	E_2	I_1	I_2
$\|00>$	A	1.5171	1.6144	-0.7155	0.7274
	B	1.5171	1.6144	-0.7155	0.7274
$\|01>$	A	1.5236	1.6078	-0.7210	0.7222
	B	1.5171	1.6144	-0.7155	0.7275
$10>$	A	1.5171	1.6144	-0.7155	0.7275
	B	1.5236	1.6078	-0.7210	0.7222
$\|11>$	A	1.5236	1.6078	-0.7209	0.7222
	B	1.5236	1.6078	-0.7209	0.7222
$M_{A_1,B_1}=0$	A	1.5203	1.6111	-0.7182	0.7248
	B	1.5203	1.6111	-0.7182	0.7248

Table C.1: The eigen values and currents for states of the first coupling circuit. The first two rows are the lowest two energies of the quantum states with the corresponding occupation configuration, followed by the average currents of these two states.

$$\langle n_1, m_1, \vec{k}|\frac{dI_1^{(A)}}{dt}|n_2, m_2, \vec{k}\rangle = I_c \cos\Delta(n_1+m_1)\frac{i\hbar}{2\Delta}(\delta_{m_1,m_2}\frac{e^{-ik_p\Delta}\delta_{n_1,n_2+1}-e^{ik_p\Delta}\delta_{n_1,n_2-1}}{M_p} + \delta_{n_1,n_2}\frac{e^{-ik_m\Delta}\delta_{m_1,m_2+1}-e^{ik_m\Delta}\delta_{m_1,m_2-1}}{M_m}) \tag{C.14}$$

C.2.2 Numerical Results

With this method, the eigen values and currents of states can be derived self-consistently. The results are listed in Table. C.2.2 and Table C.2.2.

In the first circuit, the coupling currents are $I_1^{(B)}$ and $I_1^{(A)}$ which are the circulating currents that relate to the magnetic moments directly. The lowest two states of the qubit have opposite currents and moments, which resembles the $|\uparrow>$ and $|\downarrow>$ states of 1/2 spin. These two states have opposite effect on the flux $f_1^{(A)}$ (or $f_1^{(B)}$ in the other coupling circuit). Hence, when qubit B is in the states $|0>$, the effective flux $f_1^{(A)}$ is lowered, and the first eigen level is lowered, the second eigen level raised; when qubit B is in the states $|1>$, the effective flux $f_1^{(A)}$ is raised, and the first eigen level is raised, the second eigen level lowered. The same is true for the effect of qubit A on qubit B. This can be seen clearly from the numerical results. So the first coupling

		E_1	E_2	I_1	I_2	$I_{2,1}^{(B)}$	$I_{2,2}^{(B)}$
$\|00>$	A	1.5180	1.6135	-0.7163	0.7267		
	B	1.5180	1.6123	-0.7155	0.7275	-0.5134	0.2616
$\|01>$	A	1.5215	1.6099	-0.7192	0.7239		
	B	1.5180	1.6123	-0.7155	0.7275	-0.5134	0.2616
$\|10>$	A	1.5180	1.6135	-0.7163	0.7268		
	B	1.5227	1.6099	-0.7210	0.7222	-0.5253	0.2615
$\|11>$	A	1.5215	1.6099	-0.7192	0.7239		
	B	1.5227	1.6099	-0.7209	0.7222	-0.5253	0.2615
$M_{A_1,B_1}=0$	A	1.5203	1.6111	-0.7182	0.7248		
	B	1.5203	1.6111	-0.7182	0.7248		

Table C.2: The eigen values and currents for states of the second coupling circuit. The first two rows are the lowest two energies of the quantum states with the corresponding occupation configuration, followed by the average currents of these two states.

can be treated as:

$$\begin{aligned} H_{AB} &= \sqrt{F^2+t^2}\sigma_z^A + (r_1\delta f_{1,ext}^{(A)} + r_2\delta f_{2,ext}^{(A)})\sigma_z^A + s_2\delta f_{2,ext}^{(A)}\sigma_x^A \\ &+ \sqrt{F^2+t^2}\sigma_z^B + (r_1\delta f_{1,ext}^{(B)} + r_2\delta f_{2,ext}^{(B)})\sigma_z^B + s_2\delta f_{2,ext}^{(B)}\sigma_x^B \\ &+ \epsilon r_1\sigma_z^A\sigma_z^B \end{aligned} \tag{C.15}$$

where ϵ is small constant about 10^{-3} and r_1 is equal to 4.90. The total energy of the system can be obtained which is the sum of the energy of the two qubits and the magnetic energy in the inductance that differs when the qubit state is different. This energy levels are plotted in Fig. C-3 (a). State $|0,1>$ and $|1,0>$ are degenerate due to the symmetry of the circuit.

The coupling currents in the second circuit are $I_2^{(B)}$ and $I_1^{(A)}$, where $I_2^{(B)}$ is the loop current of the squid in qubit B. It can be proved that this current is equal to the current in the outer branch of the squid. From our calculation, $I_2^{(B)}$ for the lowest two levels always have opposite direction, but different value, $|<0|I_2^{(B)}|0>| \approx 2|<1|I_2^{(B)}|1>|$. Therefore, the states $|0,1>$ and $|1,0>$ are not symmetric and not degenerate any more. In Fig. C-3 (b), there are four levels with different energies. This indicates an easy way to perform a CNOT gate. If a rf pulse with $\hbar\omega = E_{|11\rangle} - E_{|10\rangle}$

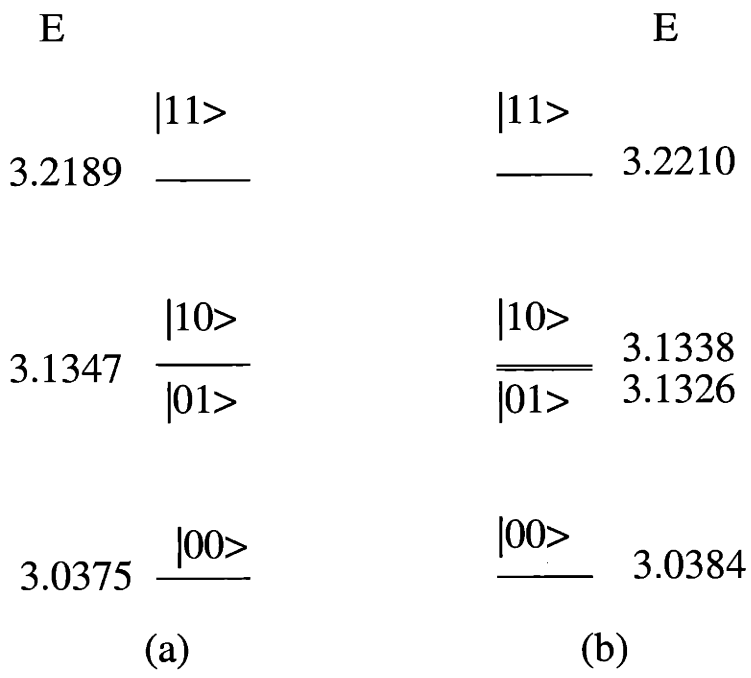

Figure C-3: The total energy of the coupled qubits, including the magnetic energy in the mutual inductance. The levels in (a) are levels for the first kind of coupling circuit; that in (b) are for the second kind circuit. The energy for each level is labeled beside the corresponding level. The states are labeled as $|lk>$, for state in level l of qubit A and level k of qubit B.

is applied to the circuit, the qubit B will flip only when qubit A is in state $|1>$. Now the interaction Hamiltonian can not simply be $\epsilon' r_2 \sigma_z^A \sigma_z^B + \epsilon'' s_2 \sigma_z^A \sigma_x^B$, as there is no obvious relation between $I_2^{(B)}$ and the magnetic moment.

Appendix D

Hamiltonian of Qubit-SQUID Interaction

In this appendix, we detail the quantization of the qubit-SQUID interaction Hamiltonian. For simplicity, we only discuss the situation for symmetric Josephson junctions in the dc SQUID. General results on SQUID quantization can be found in [98].

D.1 SQUID Quantization

The qubit-SQUID system is shown in Fig 3-1. The DC-SQUID has two Josephson junctions which have gauge invariance phases $\tilde{\varphi}_1$ and $\tilde{\varphi}_2$ respectively. For convenience of discussion, we assume the two junctions are identical. A difference in the junction critical currents will not affect the main results in this appendix. When the self inductance of the SQUID is considered, the flux quantization relation gives:

$$\tilde{\varphi}_1 - \tilde{\varphi}_2 + 2\pi\frac{\Phi_L}{\Phi_0} = -2\pi(f_{ext} + f_s) \tag{D.1}$$

where Φ_L is the flux from the self inductance, f_{ext} is the external applied frustration in the SQUID loop, and f_s is the induced frustration from the qubit loop. The Lagrangian of the SQUID is, in terms of $\tilde{\varphi}_1$ and $\tilde{\varphi}_2$,

$$\begin{aligned}
\mathcal{L}_{dc} &= \tfrac{1}{2}C_J\left(\tfrac{\Phi_0}{2\pi}\dot{\widetilde{\varphi}}_1\right)^2 + \tfrac{1}{2}C_J\left(\tfrac{\Phi_0}{2\pi}\dot{\widetilde{\varphi}}_2\right)^2 + \tfrac{1}{2}C_s\left(\tfrac{\Phi_0}{4\pi}(\dot{\widetilde{\varphi}}_1+\dot{\widetilde{\varphi}}_2)\right)^2 - U(\widetilde{\varphi}_1,\widetilde{\varphi}_2) \\
U &= -E_J^{dc}\cos\widetilde{\varphi}_1 - E_J^{dc}\cos\widetilde{\varphi}_2 + \tfrac{\Phi_L^2}{2L_{dc}} - I_b\tfrac{\Phi_0}{4\pi}(\widetilde{\varphi}_1+\widetilde{\varphi}_2)
\end{aligned} \tag{D.2}$$

where C_J is the junction capacitance, and C_s is the shunt capacitance parallel to the SQUID. $E_J^{dc} = I_c^{dc}\frac{\Phi_0}{2\pi}$ is the Josephson energy of the junctions in the SQUID. The first three terms in the Lagrangian depend on the time derivatives of the phase variables and are the charge energies of the capacitances. $U(\widetilde{\varphi}_1,\widetilde{\varphi}_2)$ is the potential energy of the SQUID, including the Josephson energies of the junctions, the energy of the self inductance and the work done by the ramping current I_b.

The Hamiltonian of the qubit-SQUID system can be derived from the Lagrangian by adding the qubit Hamiltonian $\mathcal{H}_q$ to the total energy. We choose the independent variables of the SQUID to be: $\widetilde{\varphi}_p = \frac{\widetilde{\varphi}_1+\widetilde{\varphi}_2}{2}$ and $\widetilde{\varphi}_m = \frac{\widetilde{\varphi}_1-\widetilde{\varphi}_2}{2}$. $\widetilde{\varphi}_p$ is the external variable that directly correlates with the ramping current I_b, and $\widetilde{\varphi}_m$ is the inner variable that corresponds to the circulating current of the SQUID. $\widetilde{\varphi}_m$ inductively couples with the qubit flux. The total Hamiltonian of the qubit-SQUID system is:

$$\begin{aligned}
\mathcal{H}_t &= \mathcal{H}_q + \mathcal{H}_m + \mathcal{H}_{int} \\
\mathcal{H}_q &= \tfrac{\epsilon_0}{2}\sigma_z + \tfrac{t_0}{2}\sigma_x \\
\mathcal{H}_m &= \tfrac{\mathrm{P}_p^2}{2m_p} + \tfrac{\mathrm{P}_m^2}{2m_m} - 2E_J^{dc}\cos\widetilde{\varphi}_p\cos\widetilde{\varphi}_m + 2E_J^{dc}\tfrac{(\widetilde{\varphi}_m+\pi f_{ext})^2}{\beta_{dc}} - I_b\tfrac{\Phi_0}{2\pi}\widetilde{\varphi}_p \\
\mathcal{H}_{int} &= \tfrac{4\pi f_s E_J^{dc}}{\beta_{dc}}(\widetilde{\varphi}_m+\pi f_{ext})\sigma_z
\end{aligned} \tag{D.3}$$

which includes the qubit Hamiltonian $\mathcal{H}_q$, the SQUID Hamiltonian $\mathcal{H}_m$ under external flux f_{ext}, and the qubit-SQUID interaction $\mathcal{H}_{int}$. P_p and P_m are the conjugate variables of the corresponding phases. $m_m = 2C_J(\frac{\Phi_0}{2\pi})^2$ is the mass of the inner variable; $m_p = (C_s+2C_J)(\frac{\Phi_0}{2\pi})^2$ is the mass of the external variable. For convenience we introduce $\beta_{dc} = \frac{2\pi L_{dc}I_c^{dc}}{\Phi_0}$ to represent the self-inductance. f_s is the qubit's contribution to the flux in the SQUID loop and $f_s = M_q I_{cir}/\Phi_0$, where M_q is the mutual inductance between the qubit and the SQUID and I_{cir} is the circulating current of the

qubit state. Note that the qubit parameters ϵ_0 can be adjusted by the external flux in the qubit circuit, and is also affected by the back action of the inductive interaction.

Typical parameters of the experiments are: $E_J^{dc} = 40\,\mathrm{GHz}$ with $I_c^{dc} = 80\,\mathrm{nA}$, $C_J = 2\,\mathrm{fF}$, $C_s = 5\,\mathrm{pF}$, $L_q = 10\,\mathrm{pH}$, $L_{dc} = 16\,\mathrm{pH}$ and $M_{12} = 8\,\mathrm{pH}$. The circulating current of the qubit gives a flux of $f_q \approx 10^{-3}$ flux quanta, which is coupled to the SQUID by mutual inductance. The external frustration in the DC-SQUID loop is $f_{ext} = 3/4$ to ensure maximum sensitivity of $dI_{sw}/d\varphi_m^0$.

To linearize the Hamiltonian in Eq. D.3, we expand the potential energy to second order terms near the potential energy minimum $(\tilde{\varphi}_m^0, \tilde{\varphi}_p^0)$ which is determined by $\partial U/\partial\tilde{\varphi}_m = 0$ and $\partial U/\partial\tilde{\varphi}_p = 0$. When $\beta_{dc} \ll 1$, the inductive energy of $\tilde{\varphi}_m$ dominates; so $\tilde{\varphi}_m^0 \approx \pi f_{ext}$. The minimum of $\tilde{\varphi}_p$ is determined by the relation $2I_c^{dc}\cos\tilde{\varphi}_m^0 \sin\tilde{\varphi}_p^0 = I_b$. Deriving the second derivatives at the potential energy minimum, we then obtain the oscillator frequencies and the coupling between the two oscillators as in Eq. 3.1, with $\omega_m = \sqrt{2/L_{dc}C_J}$, $\omega_p = \omega_p^0[1 - (\frac{I_b}{I_c^{eff}})^2]^{1/4}$ where $\omega_p^0 = \sqrt{2\pi I_c^{eff}/C_s\Phi_0}$, and $J_1 = |\tan\tilde{\varphi}_m^0| I_b\Phi_0/2\pi$.

D.2 Numerical Results

To study the dynamics of the qubit-SQUID system, it is necessary to know the energy structure of the system. The Hamiltonian in Eq. 3.1 can be solved numerically by choosing the direct product space of the qubit states and the lowest harmonic oscillator number states as the numerical basis. Because the interaction between the qubit and the SQUID is weak, so is the interaction between the two corresponding harmonic oscillators; hence only small number of basis states are required to solve the low energy states of the Hamiltonian to high accuracy. By varying the σ_z component ϵ_0 from $-20\,\mathrm{GHz}$ to $20\,\mathrm{GHz}$, we can study the system in the full range of the qubit bias flux of $0.49 < f_q < 0.51$.

Calculation shows that the lowest levels of the system can be described as the product states of a spin and an harmonic oscillator: $\{|s, n_{\bar{p}}\rangle, s = \uparrow, \downarrow, n_{\bar{p}} = integer\}$, with the oscillator frequency $\bar{\omega}_p \approx \omega_p$ and the spin energy $\bar{\omega}_0(\epsilon_0) \approx \sqrt{\epsilon_0^2 + t_0^2}$. Let the

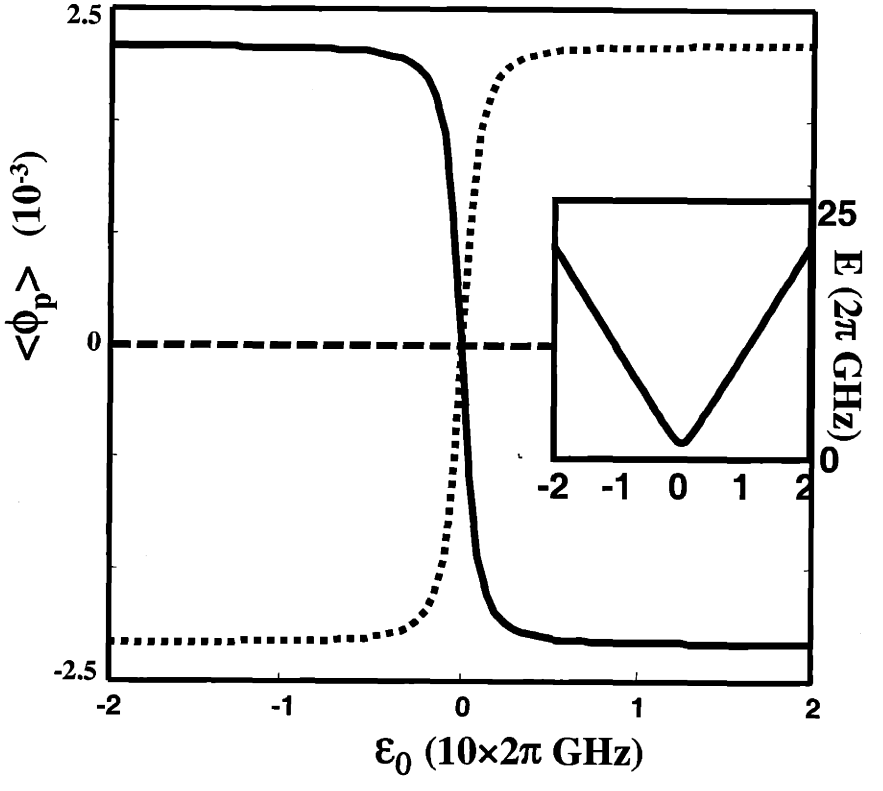

Figure D-1: The average of the external oscillator coordinate $\langle\varphi_p\rangle$ for the ground state and the state $|\bar{s}_g, 0\rangle$ verses ϵ_0. $\epsilon_0 \propto (f_q - 1/2)$ is the σ_z component of the qubit. Solid line: for the ground state at $I_b = 0.8I_c^{eff}$; dashed line: for the ground state at $I_b = 0$; dotted line: for the state $|\bar{s}_g, 0\rangle$ at $I_b = 0.8I_c^{eff}$. The inset is the energy difference between the ground state and the state $|\bar{s}_g, 0\rangle$.

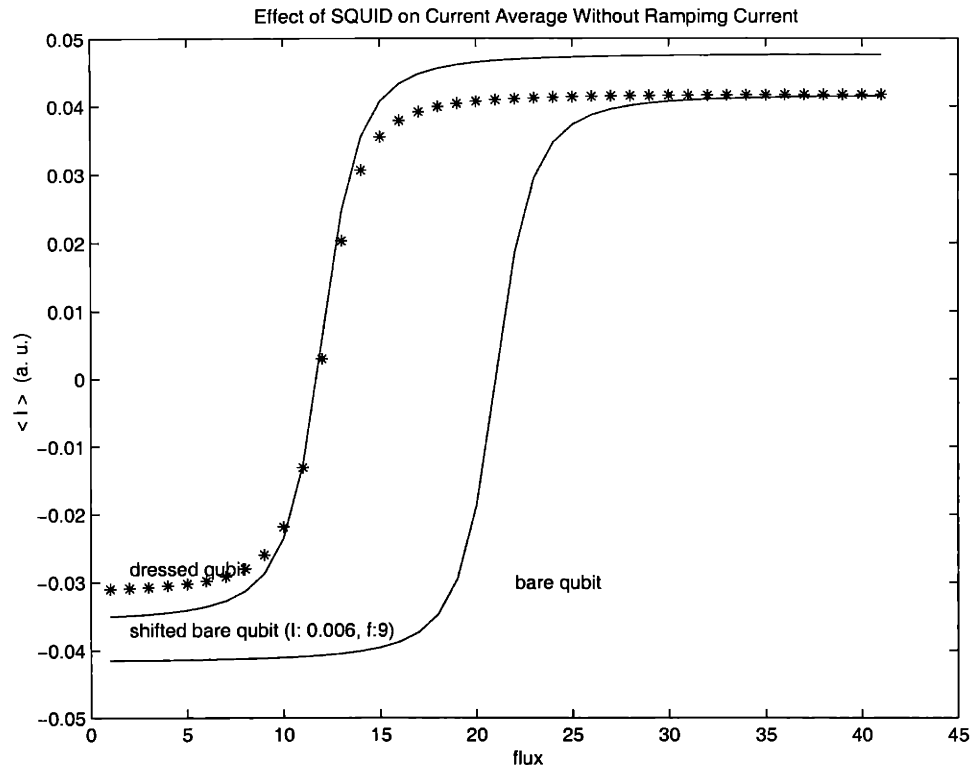

Figure D-2: More detail on the average current of the ground state of the qubit and the corresponding response from the dc SQUID's external oscillator mode, at $I_b = 0.8I_c^{eff}$.

ground state be $|s_g, 0\rangle$. Then, the state $|\bar{s}_g, 0\rangle = |-s_g, 0\rangle$ is the lowest state that has opposite spin to that of the ground state. $\bar{\omega}_0$ is the energy difference between the ground state and $|\bar{s}_g, 0\rangle$, and is plotted in the inset of Fig. D-1. The qubit's effect on the SQUID when the ramping current I_b is turned on is manifested in the operator averages of the external oscillator coordinate $\langle\varphi_p\rangle$ for both the ground state and $|\bar{s}_g, 0\rangle$. We plot $\langle\varphi_p\rangle$ at $I_b = 0.8I_c^{eff}$ and $I_b = 0$ respectively in Fig. D-1. We found that, at $I_b \neq 0$, $\langle\varphi_p\rangle$'s dependence on ϵ_0 follows that of $\langle\sigma_z\rangle$; while at $I_b = 0$, $\langle\varphi_p\rangle$ is negligible. The calculated average currents for the qubit states are shown in Fig. D-2 in comparison with the expected current of the qubit. The $\langle\varphi_p\rangle$ of the state $|\bar{s}_g, 0\rangle$ is plotted in Fig. D-3, which shows sharp peaks due to the degeneracy between the state $|\bar{s}_g, 0\rangle$ and the state $|s_g, 1\rangle$.

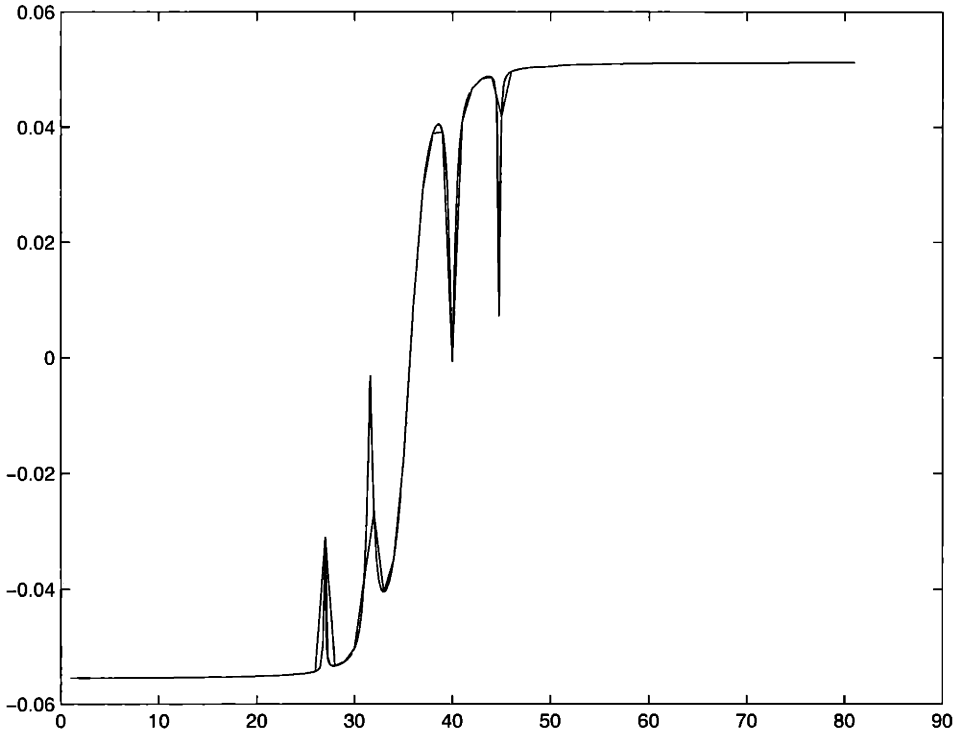

Figure D-3: The average of the external oscillator coordinate $\langle \varphi_p \rangle$ for the state $|\bar{s}_g, 0\rangle$ verses ϵ_0. $\epsilon_0 \propto (f_q - 1/2)$ is the σ_z component of the qubit at better numerical resolution. The peaks come from the degeneracy between the state $|\bar{s}_g, 0\rangle$ and the state $|s_g, 1\rangle$ and *etc.*

Bibliography

[1] P. Shor, "Algorithms for Quantum Computation: Discrete Log and Factoring", in *Proceedings of the 35th Annual Symposium on Foundations of Computer Science*, S. Goldwasser, Ed., IEEE Computer Society, Los Alamitos, CA, 1994, pp. 124-134.

[2] L.K. Grover, "Quantum computers can search arbitrarily large databases by a single query", Phys. Rev. Lett. **79**, 4709 (1997).

[3] L.K. Grover, "Quantum Mechanics Helps in Searching for a Needle in a Haystack", Phys. Rev. Lett. **79**, 325-328 (1997).

[4] D.P. DiVincenzo, "The physical implementation of quantum computation", Fortchr Phys. **48**: 771-783 (2000).

[5] S. Lloyd, "A Potentially Realizable Quantum Computer", Science **261**, 1569 (1993).

[6] C. H. Bennett, "Quantum Information and Computation", *Physics Today* **48** (10), 24 (1995)

[7] D. P. DiVincenzo, "Quantum Computation", Science **270**, 255 (1995).

[8] T. P. Spiller, "Quantum information processing: Cryptography, computation, and teleportation", *Proc. IEEE* **84** 1719 (1996).

[9] S. Lloyd, "Envisioning a Quantum Supercomputer", Science **263**, 695 (1994).

[10] R. Landauer, "Uncertainty Principle and Minimal Energy-Dissipation in the Computer", Int. J. Theor. Phys. **21**, 283 (1982); "Computation and Physics - Wheeler Meaning Circuit" Found. Phys.**16**, 551 (1986); "Dissipation and Noise-Immunity in Computation and Communication", *Nature* **335**, 779 (1988); *"Nanostructure Physics and Fabrication"*, M.A. Reed and W.P. Kirk, eds. (Academic Press, Boston, 1989), pp. 17-29; "Can We Switch by Control of Quantum Mechanical Transmission", Physics Today **42**, 119 (October 1989); Proc. 3rd Int. Symp. Foundations of Quantum Mechanics, Tokyo, 407 (1989); "Advanced Technology and Truth in Advertising", Physica A **168**, 75 (1990); "Information is Physical", Physics Today **44**, 23 (1991); Proc. Workshop on Physics of Computation II, D. Matzke ed., 1,*IEEE* Press, (1992).

[11] J. I. Cirac and P. Zoller, "Quantum Computations with Cold Trapped Ions", Phys. Rev. Lett. **74**, 4091 (1995).

[12] C. Monroe, D.M. Meekhof, B.E. King, W.M. Itano, D.J. Wineland, "Demonstration of a Fundamental Quantum Logic Gate", Phys. Rev. Lett.**75**, 4714 (1995).

[13] Q.A. Turchette, C.J. Hood, W. Lange, H. Mabuchi, H.J. Kimble, "Measurement of Conditional Phase Shifts for Quantum Logic", Phys. Rev. Lett.**75**, 4710, (1995).

[14] Loss and D. P. DiVincenzo, "Quantum computation with quantum dots", Phys. Rev. A **57**, 120 (1998).

[15] N. A. Gershenfeld and I. L. Chuang, "Bulk spin-resonance quantum computation", Science **275**, 350 (1997).

[16] D. G. Cory, A. F. Fahmy, T. F. Havel, PhysComp96, Proceedings of the Fourth Workshop on Physics and Computation, edited by T. Toffoli, M. Biafore, J. Leao, New England Complex Systems Institute, pp. 87-91.

[17] A. Steane, "Quantum computing", Rep. Prog. Phys. **61**, 117 (1998).

[18] B. E. Kane, "A silicon-based nuclear spin quantum computer", Nature **393**, 133 (1998).

[19] J. E. Mooij, "Possible design for a quantum computer with superconducting tunnel junctions," Conference on Quantum Coherence and Decoherence, Santa Barbara, California, December 15—18, 1996.

[20] J. E. Mooij, T. P. Orlando, L. Levitov, Lin Tian, Caspar H. van der Wal, and Seth Lloyd, "Josephson persistent-current qubit", Science **285**, 1036 (1999).

[21] M. F. Bocko, A. M. Herr, and M.F. Feldman, "Prospects for quantum coherent computation using superconducting electronics", IEEE Trans. Appl. Supercond. **7**, 3638 (1997).

[22] A. Shnirman, G. Schön, and Z. Hermon, "Quantum Manipulations of Small Josephson Junctions", Phys. Rev. Letts. **79**, 2371 (1997).

[23] D. V. Averin, "Adiabatic quantum computation with Cooper pairs", Solid State Commun. **105**, 659 (1998).

[24] Y. Makhlin, G. Schön and A. Shnirman, "Quantum-state engineering with Josephson-junction devices" Rev. Mod. Phys. **73**, 357 (2001).

[25] T.P. Orlando, J.E. Mooij, L.Tian, C.H. van der Wal, L.S. Levitov, S. Lloyd and J.J. Mazo, "Superconducting persistent-current qubit", Phys. Rev. B **60**, 15398 (1999).

[26] A.J. Leggett and A. Garg, "Quantum mechanics versus macroscopic realism: Is the flux there when nobody looks?", Phys. Rev. Lett. **54**, 857 (1985).

[27] A.J. Leggett, "Macroscopic Quantum Tunneling and Related Matters", Jpn. J. Appl. Phys. (1) Supplement **26-3**, 1986 (1987).

[28] J.R. Friedman, V. Patel, W. Chen, S.K. Tolpygo, and J.E. Lukens, "Quantum superposition of distinct macroscopic states", Nature **406**, 43 (2000).

[29] C.H. van der Wal, A.C.J. ter Haar, F.K. Wilhelm, R.N. Schouten, C.J.P.M. Harmans, T.P. Orlando, S. Lloyd and J.E. Mooij, "Quantum superposition of macroscopic persistent-current states", Science **290**, 773 (2000).

[30] S.Y. Han, Y. Yu, X. Chu, S.I. Chu, Z. Wang, " Time-resolved measurement of dissipation-induced decoherence in a Josephson junction", Science **293**, 1457 (2001).

[31] M. Grifoni and P. Hänggi, "Driven quantum tunneling", Phys. Rep. **304**, 229 (1998).

[32] P. Hänggi, P. Talkner, and M. Borkovec, "Reaction-rate theory: fifty years after Kramers", Rev. Mod. Phys. **62**, 251 (1990).

[33] M.H. Devoret, J.M. Martinis, and J. Clarke, "Measurements of Macroscopic Quantum Tunneling out of the Zero-Voltage State of a Current-Biased Josephson Junction", Phys. Rev. Lett. **55**, 1908 (1985).

[34] J.M. Martinis, M.H. Devoret, and J. Clarke, " Energy-Level Quantization in the Zero-Voltage State of a Current-Biased Josephson Junction", Phys. Rev. Lett. **55**, 1543 (1985).

[35] M.H. Devorett, J.M. Martinis, D. Esteve and J. Clarke, "Resonant Activation from the Zero-Voltage State of a Current-Biased Josephson Junction", Phys. Rev. Lett. **53**, 1260 (1984).

[36] N.P. Suh, "The Principles of Design", Oxford University Press, Oxford (1990).

[37] K.G. Segall, in preparation (2002).

[38] L. Tian, S. Lloyd and T.P. Orlando, "Radiation Assisted Measurement on the Superconducting Persistent-Current Qubit", preprint (2002).

[39] L. Tian, S. Lloyd and T.P. Orlando, "Decoherence and relaxation of a superconducting quantum bit during measurement", Phys. Rev. B **65**, 144516 (2002).

[40] T.P. Orlando, L. Tian, D.S. Crankshaw, S. Lloyd, C.H. van der Wal, J.E. Mooij, F. Wilhelm, "Engineering the quantum measurement process for the persistent current qubit", Physica C **368**, 294 (2002).

[41] L. Tian, L.S. Levitov, C.H. van der Wal, J.E. Mooij, T.P. Orlando, S. Lloyd, C.J.P.M. Harmans, and J.J. Mazo, "Decoherence of the Superconducting Persistent Current Qubit", cond-mat/9910062, *Proceedings of NATO-ASI on Quantum Mesoscopic Phenomena and Mesoscopic Devices in Microelectronics*, Kluwer Academic Publishers, ed. I.O. Kulik, R. Ellialtioglu (2000).

[42] L. Tian and S. Lloyd, "Resonant cancellation of off-resonant effects in a multilevel qubit", Phys. Rev. A. **62**, R050301 (2000).

[43] M. Tinkham, *"Introduction to Superconductivity"*, Second Ed., McGraw-Hill, New York, (1996).

[44] *"Single Charge Tunneling*, edited by H. Grabert and M. Devoret, Plenum, New York (1992).

[45] P. Carruthers and M. M. Nieto, "Phase and Angle Variables in Quantum Mechanics", Rev. Mod. Phys. **40**, 411 (1968).

[46] P. Joyez, A. Pilipe, D. Esteve, and M. H. Devoret, "Observation of parity-induced suppression of Josephson tunneling in the superconducting single electron transistor", Phys. Rev. Lett. **72**, 2458 (1994).

[47] M. Matters, W. J. Elion, and J. E. Mooij, "Influence of Controlled Quantum-Mechanical Charge and Phase Fluctuations on Josephson Tunneling", Phys. Rev. Lett. **75**, 721 (1995).

[48] V. Bouchiat, D. Vion, P. Joyez, D. Esteve, and M. Devoret, "Quantum coherence with a single Cooper pair", Physica Scripta **T76**, 165 (1998); and V. Bouchiat, Ph.D. Thesis, Université Paris, (1997).

[49] D. V. Averin and K. K. Likharev, in *"Mesoscopic Phenomena in Solids"*, eds. B.L. Altshuler, P. A. Lee and R. A. Webb, North-Holland, Amsterdam (1991).

[50] P. Lafarge, M. Matters, and J. E. Mooij, "Charge representation of a small two-dimensional Josephson-junction array in the quantum regime", Phys. Rev. B **54**, 7380 (1996).

[51] W. J. Elion, M. Matters, U. Geigenmüller, and J. E. Mooij, "Direct Demonstration of Heisenbergs Uncertainty Principle in a Superconductor", Nature **371**, 594 (1994).

[52] A. van Oudenaarden, S. J. K. Vàrdy, and J. E. Mooij, "Bloch vortices in one-dimensional Josephson junction arrays", Czech. J. Phys **46**, suppl. s2, 707 (1996).

[53] L. J. Geerligs, V. F. Anderegg, and J. E. Mooij, "Tunneling Time and offset Charging in Small Tunnel-Junctions", Physica B **165**, 973 (1990).

[54] G. Zimmerli, T. M. Eiles, R. L. Kautz, and John M. Martinis, "Noise in the Coulomb Blockade Electrometer", Appl. Phys. Lett. **61**, 237 (1992).

[55] S. Han, J. Lapointe, J. E. Lukens, in *"Activated Barrier Crossing"*, eds. G.R. Fleming and P. Hanggi, World Sci., pp. 241—267, 1993.

[56] R. Rouse, S. Han, and J. E. Lukens, "Observation of Resonant Tunneling between Macroscopically Distinct Quantum Levels", Phys. Rev. Lett. **75**, 1614 (1995).

[57] J. Diggins, T. D. Clark, H. Prance, R. J. Prance, T. P. Spiller, J. Ralph, and F. Brouers, "Limits to the Observation of Coherent Oscillations in a SQUID Ring", Physica B **215**, 367 (1995).

[58] M. G. Castellano, R. Leoni and G. Torrioili, "Switching dynamics of Nb/AlOx/Nb Josephson junctions: Measurements for an experiment of macroscopic quantum coherence", J. Appl. Phys. **80**, 2922 (1996).

[59] T. P. Orlando and K. A. Delin, *"Introduction to Applied Superconductivity"*, Addison and Wesley (1991).

[60] S. Doniach, in *"Nato Advanced Study Institute on Localization, Percolation, and Superconductivity"*, edited by A. M. Goldman and S.A. Wolf, Plenum, New York (1984), p.401.

[61] In fact, Likharev has pointed out that replacing the third junction by an inductor also will give a similar functional form for U. We choose the three junction system instead because the inductor values needed are not as accessible with our technology. We have also carried out quantum mechanical simulations with the inductor and do indeed find that it has similar properties to what is reported here.

[62] D. A. Wells, *"Theory and Problems of Lagrangian Dynamics"*, McGraw-Hill, New York (1967).

[63] D. C. White and H. H. Woodson, *"Electromechanical Energy Conversion"*, Wiley and Sons, New York (1959).

[64] M. H. Devoret, "Quantum Fluctuations in Electrical Circuits", Chapter 10 in *"Quantum Fluctuations"*, S. Reymaud, E. Giacobino, and J. Zinn-Justin, eds., Elsevier Science, B.V. (1997).

[65] T. P. Orlando, to be published.

[66] S. P. Yukon and N.C. H. Lin, *"Macroscopic Quantum Phenomena and Coherence in Superconducting Networks"*, World Scientific, Singapore (1995); S. P. Yukon and N. C. H. Lin, IEEE Trans. Appl. Supercond. **5**, 2959 (1995).

[67] U. Geigenmüller, "Dynamics of a ring with three Josephson junctions", J. Appl. Phys. **80**, 3934 (1996).

[68] M.Barahona, E. Trías, T. P. Orlando, A. E. Duwel, H.S.J. van der Zant, S. Watanabe, and S. H. Strogatz, "Resonances of dynamical checkerboard states in Josephson arrays with self-inductance ", Phys. Rev. B **55**, 11989 (1997).

[69] P. Caputo, A. E. Duwel, T. P. Orlando, A. V. Ustinov, N.C. H. Lin, and S. P. Yukon, ISEC (1997).

[70] G. Schön and A. D. Zaikin, "Distinguishing Phases in Josephson-Junctions and the Choice of States", Physica B **152**, 203 (1988).

[71] T. P. Spiller, T. D. Clark, R. J. Prance, and A. Widom, Chapter 4 in *"Progress in Low Temperature Physics"* Volume XIII, Edited by D. F. Brewer, Elsevier (1992).

[72] K.K. Likharev and A.B. Zorin, "Theory of the Bloch-Wave Oscillations in Small Josephson-Junctions", J. Low Temp. Phys. **59**, 347 (1985).

[73] E. U. Condon, "The Physical Pendulum in Quantum Mechanics", Phys. Rev. **31**, 891 (1928).

[74] Note that H_t could be have been found directly by not making the Legendre transformation in the Lagrangian. Then the canonical momentum would not be proportional to the charges on the nodes. Although this canonical momentum and Hamiltonian are clearer mathematically, we use instead the more physical canonical momentum which proportional to the charge so as to make better contact with the literature, such as in Refs. [64], [70], and [71].

[75] H. S. J. van der Zant, D. Berman, K. A. Delin , T. P. Orlando, "Fiske modes in one-dimensional parallel Josephson-junction arrays", Phys. Rev. B **49**, 12945 (1994).

[76] L. D. Landau and E. M. Lifshitz, *"Quantum Mechanics"*, pp. 183–184.

[77] S. Lloyd, "Almost Any Quantum Logic Gate is Universal", Phys. Rev. Lett. **75**, 346 (1995).

[78] A. Barenco, C.H. Bennett, R. Cleve, D.P. DiVincenzo, N. Margolus, P. Shor, T. Sleator, J.A. Smolin, H. Weinfurter, "Elementary gates for quantum computation", Phys. Rev. A, **52**, 3457 (1995).

[79] D. Deutsch, A. Barenco, A. Ekert, Proc. R. Soc. "Universality in Quantum Computation", London Ser. A **449**, 669 (1995).

[80] C. D. Tesche, "Superconducting Measurement Circuit for an EPR Experiment with an rf SQUID", Physica B **165**, 925, 1990; "Measurement Scheme for the Macroscopic Quantum Coherence Experiment", Japanese J. Appl. Phys. Suppl.bf 26, 1409 (1987).

[81] C. D. Tesche, "Can a noninvasive measurement of magnetic flux be performed with superconducting circuits?", Phys. Rev. Lett. **64**, 2358 (1990).

[82] A.T. Johnson, C.J. Lobb and M. Tinkham, "Effect of leads and energy gap upon the retrapping current of Josephson junctions", Phys. Rev. Lett. **65**, 1263 (1990).

[83] S. Lloyd, "Quantum-mechanical Computers", *Scientific American*, **273**, 140 (1995).

[84] G. P. Berman, G. D. Doolen and R. Mainieri, *"Introduction to Quantum Computers"*, World Scientific (1998).

[85] C. Ahn, S. Lloyd, B. Rahn, "Robust quantum computation via simulation", to be published.

[86] A. Y. Kitaev, "Fault-tolerant quantum computation by anyons", quant-ph/9707021.

[87] J. Preskill, "Fault-tolerant quantum computation", quant-ph/9712048.

[88] D.R. Simon, "On the Power of Quantum Computation", in *Proceedings of the 35th Annual Symposium on Foundations of Computer Science*, S. Goldwasser, Ed., IEEE Computer Society, Los Alamitos, CA, 1994, pp. 116-123.

[89] P. Shor, "Fault Tolerant Quantum Computation", *Proceedings of the 37th Annual Symposium on the Foundations of Computer Science,* IEEE Computer Society Press, Los Alamitos, 1996, pp. 56-65.

[90] A. Steane, "Multiple-Particle Interference and Quantum Error Correction", *Proceedings of the Royal Society of London A*, Vol. **452**, pp. 2551-2577 (1996).

[91] D.P. DiVincenzo and P.W. Shor, "Fault Tolerant Error Correction With Efficient Quantum Codes", Phys. Rev. Lett.**77**, 3260 (1996).

[92] J.I. Cirac, T. Pellizzari, and P. Zoller, "Enforcing Coherent Evolution in Dissipative Quantum Dynamics", Science **273**, 1207-1210 (1996).

[93] E. Knill and R. Laflamme, "Theory of Quantum Error-Correcting Codes", Phys. Rev. A **55**, 900 (1997).

[94] A. Stern, Y. Aharonov and Y. Imry, "Phase uncertainty and loss of interference: A general picture", Phys. Rev. A **41**, 3436 (1990).

[95] Caspar H. van der Wal and J.E. Mooij, "Controlled single-Cooper-pair charging effects in a small Josephson junction array", J. Supercond. **12**, 807 (1999).

[96] F.K. Wilhelm and M. Grifoni, preprint (2001).

[97] C.H. van der Wal, F.K. Wilhelm, C.J.P.M. Harmans and J.E. Mooij, preprint (2001).

[98] Y-C. Chen, "Macroscopic Quantum Tunneling in a dc SQUID", J. Low Temp. Phys. **65**, 133 (1986).

[99] J.M. Martinis, M.H. Devoret, & J. Clarke, "Experimental tests for the quantum behavior of a macroscopic degree of freedom: The phase difference across a Josephson junction", Phy. Rev. B **35**, 4682 (1987); We use the thermal escape rates to calculate the probabilities and histogram of switching; detailed calculation on the escape rate near the thermal-to-quantum crossover temperature shows very small difference.

[100] A. Peres, *"Quantum theory : concepts and methods"*, Kluwer Academic (1993).

[101] T.M. Cover and J.A. Thomas, *"Elements of information theory"*, Wiley series in telecommunications, New York, Wiley (1991).

[102] A.S. Holevo, Probl. Inform. Transmission **9**, 177 (1973).

[103] Similar to the qubit's intrinsic noise, the most significant noise on the inner oscillator comes from nuclear spins and flux fluctuation. As the size of the SQUID loop is of the same order as that of the qubit, the direct noise on the inner oscillator is of the same order as the direct noise on the qubit. When transferred to the qubit, this noise is reduced by a factor of $\delta\phi_0^2$ ($\ll 1$) and is negligible. The external oscillator is exposed to a much more noisy environment as it interacts directly with external electronics.

[104] A.O. Caldeira and A.J. Leggett, "Quantum Tunneling in a Dissipative System", Annals of Physics **149**, 374-456 (1983).

[105] N.V. Prokof'ev and P.C.E. Stamp, "Theory of the spin bath", Rep. Prog. Phys. **63**, 669 (2000).

[106] A.J. Leggett, "Quantum tunneling in the presence of an arbitrary linear dissipation mechanism", Phys. Rev. B **30**, 1208 (1984).

[107] A.J. Leggett, "Macroscopic Quantum Tunneling - An Overview of the Background", J Appl. Phys. **73**(10), 6715 (1993).

[108] A. Garg, J.N.Onuchic, and V. Ambegaokar, "Effect of Friction on Electron-Transfer in Biomolecules", J. Chem. Phys. **83**(9). 4491 (1985).

[109] M. Grifoni, E. Paladino, and U. Weiss "Dissipation, decoherence and preparation effects in the spin-boson system", Eur. Phys. J. B **10**, 719-729 (1999).

[110] D.F. Walls and G.J. Milburn, *"Quantum Optics"*, Springer (1994).

[111] C.P. Slichter, *"Principles of magnetic resonance"*, 3rd ed., Springer-Verlag (1990).

[112] C.W. Gardiner and P. Zöller, *" Quantum noise : a handbook of Markovian and non-Markovian quantum stochastic methods with applications to quantum optics"*, Berlin ; New York : Springer (2000).

[113] G. Ingold, "Dissipative Quantum System", chap. 4 in *"Quantum Transport and Dissipation"*, Thomas Dittrich *et al*, Weinheim; New York: Wiley-VCH (1998).

[114] L.B. Ioffe, V.B. Geshkenbein, M.V. Feigel'man, A.L. Fauchere, G. Blatter, "Environmentally decoupled sds-wave Josephson junctions for quantum computing", Nature **398**, 679 (1999).

[115] Y. Nakamura, Y.A. Pashkin, J.S. Tsai, "Coherent control of macroscopic quantum states in a single-Cooper-pair box", Nature **398**, 786 (1999).

[116] Y. Nakamura, Y.A. Pashkin, J.S. Tsai, "Rabi Oscillations in a Josephson-Junction Charge Two-Level System", Phys. Rev. Lett. **87**, 246601 (2001)

[117] Y. Nakamura, Y.A. Pashkin, T. Yamamoto, and J.S. Tsai, "Charge Echo in a Cooper-Pair Box", Phys. Rev. Lett. **88**, 047901 (2002).

[118] M.H. Devoret, R.J. Schoelkopf, "Amplifying quantum signals with the single-electron transistor", Nature **406**, 1039 (2000).

[119] A. Aassime, G. Johansson, G. Wendin, R. J. Schoelkopf, and P. Delsing, "Radio-frequency single-electron transistor as readout device for qubits: Charge sensitivity and backaction", Phys. Rev. Lett. **86**, 3376 (2001).

[120] Jens Siewert and Rosario Fazio, "Quantum Algorithms for Josephson Networks", Phys. Rev. Lett. **87**, 257905 (2001).

[121] T. van Duzer and C.W. Turner, *" Principles of superconductive devices and circuit"*, 2nd ed. Upper Saddle River, N.J. : Prentice Hall, c1999.

[122] The simplest choice of a magnetometer is a dc SQUID, but better way to measure the rf SQUID exists by using rf tank circuit: K.G. Segall, unpublished result.

[123] The CNOT gate can be replaced with incoherent transition gate to get information of the qubit. With an rf frequency $E_{1_q 1_a} - E_{1_q 0_a}$ and strong decoherence on the rf SQUID, the incoherent transition results in a density matrix of

$(1 - \frac{|c_1|^2}{2})|0_a\rangle\langle 0_a| + \frac{|c_1|^2}{2}|1_a\rangle\langle 1_a|$ for the rf SQUID. This density matrix is also uniquely determined by the qubit state probabilities.

[124] P. Shor, *Proceeding of the 37th Annual Symposium on the Foundations of Computer Science*, 56, IEEE Computer Society Press, Los Alamos, 1996; D. P. DiVincenzo and P. W. Shor, "Fault-Tolerant Error Correction with Efficient Quantum Codes", Phys. Rev. Lett. **77**, 3260 (1996).

[125] E. Knill and R. Laflamme, "Theory of quantum error-correcting codes", Phys. Rev. A**55**, 900 (1997).

[126] A. Steane, "Multiple-particle interference and quantum error correction", Proceedings of the Royal Society of London A **452**, 2551 (1996).

[127] J. R. Kirtley, C. D. Tesche, W. J. Gallagher, A. W. Kleinsasser, R. L. Sandstrom, S. I. Raider, and M. P. A. Fisher, "Measurement of the Intrinsic Subgap Dissipation in Josephson Junctions", Phys. Rev. Lett. **61**, 2372 (1988); A. T. Johnson, C. J. Lobb, and M. Tinkham, "Effect of leads and energy gap upon the retrapping current of Josephson junctions", Phys. Rev. Lett. **65**, 1263, (1990).

[128] L. Viola and S. Lloyd, "Dynamical suppression of decoherence in two-state quantum systems", Phys. Rev. A**58**, 2733 (1998); L. Viola, E. Knill, and S. Lloyd, "Dynamical Decoupling of Open Quantum Systems", Phys. Rev. Lett. **82**, 2417 (1999).

[129] T. Henning, B. Starmark, T. Claeson, and P. Delsing, "Bias and temperature dependence of the noise in a single electron transistor", Eur. Phys. J. B **8**. 627 (1999); V. A. Krupenin, D.E. Presnov, M.N. Savvateev, H. Scherer, A.B. Zorin, and J. Niemeyer, "Noise in Al single electron transistors of stacked design", J. Appl. Phys. **84**, 3212 (1998); N. Zimmerman, Jonathan L. Cobb, and Alan F. Clark, "Modulation of the charge of a single-electron transistor by distant defects", Phys. Rev. B **56**, 7675 (1997); E. H. Visscher S.M. VerBrugh, J. Lindeman, P. Hadley and J.E. Mooij, "Fabrication of Multilayer Single-Electron Tunneling Devices", Appl. Phys. Lett. **66**, 305 (1995).

[130] D.A. Lidar, I.L. Chuang, and K.B. Whaley, "Decoherence-Free Subspaces for Quantum Computation", Phys. Rev. Lett. **81**, 2594 (1998).

[131] L.M. Duan and G.C. Guo, "Reducing decoherence in quantum-computer memory with all quantum bits coupling to the same environment", Phys. Rev. A **57**, 737 (1998).

[132] A. J. Leggett, S. Chakravarty, A. T. Dorsey, Matthew P. A. Fisher , Anupam Garg, and W. Zwerger, "Dynamics of the dissipative two-state system", Rev. Mod. Phys. **59**, 1 (1987).

[133] H. Grabert, P. Schramm, and G.L. Ingold, "Quantum Brownian-Motion - The Functional Integral Approach", Phys. Rep. **168**, 115 (1988).

[134] P.C.E. Stamp, in *"Tunneling in Complex Systems"*, pp.101–197, edited by T. Tomsovic, World Sci. (1998).

[135] S. Schneider & G.J. Milburn, "Decoherence and fidelity in ion traps with fluctuating trap parameters", Phys. Rev. A **59**, 3766 (1999); "Decoherence in ion traps due to laser intensity and phase fluctuations", **57**, 3748 (1998); M. Murao & P.L. Knight, "Decoherence in nonclassical motional states of a trapped ion", *ibid* **58**, 663 (1998).

[136] J. Gea-Banacloche, "Qubit-qubit interaction in quantum computers", Phys. Rev. A **57**, R1 (1998); "Qubit-qubit interaction in quantum computers. II. Adder algorithm with diagonal and off-diagonal interactions", *ibid.* **60**, 185 (1999).

[137] M.B. Plenio and P.L. KnIght, "Realistic lower bounds for the factorization time of large numbers on a quantum computer", Phys. Rev. A **53**, 2986 (1996); "Decoherence limits to quantum computation using trapped ions", Proc. Roy. Soc. A 453, 2017 (1997).

[138] J. Preskill, "Reliable quantum computers", Proc. Roy. Soc. Lond. A **454**, 385 (1998).

[139] M. Grassl and Th. Beth, "Codes for the quantum erasure channel", Phys. Rev. A **56**, 33 (1997).

[140] P. Shor, "Scheme for reducing decoherence in quantum computer memory", Phys. Rev. A **52**, R2493 (1995).

[141] A. Steane, "Simple quantum error-correcting codes", Phys. Rev. A **54**, 4741 (1996); A. Steane, "Error Correcting Codes in Quantum Theory", Phys. rev. Lett. **77**, 793 (1996).

[142] R. Laflammei, C. Miquell, J. P.Paz, and W. H. Zurekl, "Perfect Quantum Error Correcting Code", Phys. Rev. Lett. **77**, 198 (1996);

[143] D. Gottesman, "Class of quantum error-correcting codes saturating the quantum Hamming bound", Phys. Rev. A **54**, 1862 (1996).

[144] A.R. Calderbank, E. M. Rains, P. W. Shor, and N. J. A. Sloane, "Quantum Error Correction and Orthogonal Geometry", Phys. Rev. Lett. **78**, 405 (1997); A.R. Calderbank & P. Shor, "Good quantum error-correcting codes exist", Phys. Rev. A **54**, 1098 (1996).

[145] L.M. Duan & G.C. Guo, "Preserving coherence in quantum computation by pairing quantum bits", Phys. Rev. Lett. **79**, 1953 (1997).

[146] L. Viola, S. Lloyd, and E. Knill , "Universal Control of Decoupled Quantum Systems", Phys.Rev. Lett.**83**, 4888 (1999).

[147] P. Zanardi, "Symmetrizing evolutions", Phys. Lett. A **258**, 77 (1999); M. Rasetti & P. Zanardi, "A possible strategy to defeat decoherence in quantum computation: The role of symmetries, dynamical algebras, and all that", Fortschr Phys. **48**, 559 (2000).

[148] We simulated the dynamic evolution of pc-qubit under rf magnetic field of $\delta f = 0.002$ for $t = T_{Rabi}$. With an initial state $|0\rangle$, the final state has components from many higher levels. Details to be published elsewhere.

[149] U. Haeberlen, *"High Resolution NMR in Solids - Selective Averaging"*, Academic Press (1976).

[150] D.G. Cory *et al.*, R. Laflamme, E. Knill, L. Viola, T.F. Havel, N. Boulant, G. Boutis, E. Fortunato, S. Lloyd, R. Martinez, C. Negrevergne, M. Pravia, Y. Sharf, G. Teklemariam, Y.S. Weinstein, and W.H. Zurek, "NMR based quantum information processing: Achievements and prospects", Fortschr Phys. **48**, 875 (2000).

[151] C. Presilla, R. Onofrio, and U. Tambini, "Measurement quantum mechanics and experiments on quantum zeno effect", Ann. Phys. (NY) **248**, 95 (1996); D. Home and M. A. B. Whitaker, "A conceptual analysis of quantum zeno; Paradox, measurement, and experiment", *ibid.* **258**, 237 (1997).

[152] S. Lloyd, "Quantum search without entanglement", Phys. Rev. A **60**, 010301 (2000).

[153] D.S. Crankshaw and T.P. Orlando, "Inductance effects in the persistent current qubit", IEEE T Appl Supercon **11**, 1006 (2001).

Publications and Preprints

J. E. Mooij, T. P. Orlando, L. Levitov, Lin Tian, Caspar H. van der Wal, and Seth Lloyd, "Josephson persistent-current qubit", Science **285**, 1036 (1999).

T.P. Orlando, J.E. Mooij, L.Tian, C.H. van der Wal, L.S. Levitov, S. Lloyd and J.J. Mazo, "Superconducting persistent-current qubit", Phys. Rev. B **60**, 15398 (1999).

L. Tian, L.S. Levitov, C.H. van der Wal, J.E. Mooij, T.P. Orlando, S. Lloyd, C.J.P.M. Harmans, and J.J. Mazo, "Decoherence of the Superconducting Persistent Current Qubit", cond-mat/9910062, *Proceedings of NATO-ASI on Quantum Mesoscopic Phenomena and Mesoscopic Devices in Microelectronics*, Kluwer Academic Publishers, ed. I.O. Kulik, R. Ellialtioglu (2000).

L. Tian and S. Lloyd, "Resonant cancellation of off-resonant effects in a multilevel qubit", Phys. Rev. A. **62**, R050301 (2000).

T.P. Orlando, L. Tian, D.S. Crankshaw, S. Lloyd, C.H. van der Wal, J.E. Mooij, F. Wilhelm, "Engineering the quantum measurement process for the persistent current qubit", Physica C **368**, 294 (2002).

L. Tian, S. Lloyd and T.P. Orlando, "Decoherence and relaxation of a superconducting quantum bit during measurement", Phys. Rev. B **65**, 144516 (2002).

L. Tian, S. Lloyd and T.P. Orlando, "Radiation Assisted Measurement on the Superconducting Persistent-Current Qubit", preprint (2002).